Microsystems Platforms for Array-based Single-cell Biological Assays

by

Brian M. Taff

B.S. Electrical Engineering, North Carolina State University, 2002
B.S. Mechanical Engineering, North Carolina State University, 2002
S.M. Electrical Engineering, Massachusetts Institute of Technology, 2004

Submitted to the Department of Electrical Engineering and Computer Science in partial fulfillment of the requirements for the degree of

DOCTOR OF PHILOSOPHY

at the

MASSACHUSETTS INSTITUTE OF TECHNOLOGY
SEPTEMBER 2008

Signature of Author _____
Department of Electrical Engineering and Computer Science
July 18, 2008

Certified by _____
Joel Voldman
Associate Professor of Electrical Engineering
Thesis Supervisor

Accepted by _____
Terry P. Orlando
Chairman, Department Committee on Graduate Students

Microsystems Platforms for Array-based Single-cell Biological Assays

by

Brian M. Taff

Submitted to the Department of Electrical Engineering and Computer Science on July 18, 2008
in partial fulfillment of the requirements for the degree of Doctor of Philosophy

Abstract

For much of the past century, plated cell cultures have served investigations regarding a variety of fundamental biological processes. Though this *in vitro* approach has been fruitful, for surveying topics including cell cycle effects[3, 8], pro-survival[4, 7, 9, 10] and apoptotic[2, 11] signaling networks, gene regulation[12, 13], and stress dynamics[14, 15] (among others), it caters best to harvesting the averaged responses from binned populations of cells and offers only limited avenues for tracking individual cell behaviors. Microsystems-based initiatives[16-28] are beginning to aid this investigative shortcoming by offering a variety of strategies for handling individual cells. Such efforts, may ultimately serve studies of cross-population heterogeneity[29-33], an effect often masked when tracking responses via averaged population-based means. As it is believed that small subpopulations of cells may be responsible for determining the fate of various diseases and developmental processes[34-36], this new paradigm for probing cell function will likely offer key insights.

In my dissertation, I offer a unique suite of microsystems-based tools[37-42] for servicing novel biological assays centered on cross-population dynamics. This work leverages the investigative potential enabled by arrayed groupings of precisely-spaced single cells and presents innovations in active and passive cell trapping architectures, packaging design, and the use of novel materials for microfabrication[41, 43]. From proof-of-concept forays, where I discuss the first reported row/column-based electrically-addressable platform[40] for trapping, imaging, and releasing collections of individual cells, to scaled implementations that employ frequency modulation to assign unique forcing effects to in-system constructs, I outlay fundamentals for designing, building, and evaluating dielectrophoresis-reliant (DEP) microsystems architectures. I further present matured platforms that, for the first time, parallelize single-cell manipulations within microfluidic devices by combining hydrodynamic weir-based cell capture with DEP-based actuation[37-39]. In progressions toward functional on-chip bioassays, I experimentally validate conditions for in-device cell viability and offer a novel means for tracking mitosis in individual cells. Ongoing work, related to the developments presented here, offers the hope of new empirical approaches to drug discovery, the assignment of gene function in the aftermath of the human genome project, and enhanced understandings of cell communication-linked dynamic responses.

Thesis supervisor: Joel Voldman, Ph.D.
Title: Associate Professor of Electrical Engineering

Acknowledgements

Over the course of my six year involvement in this work, I have learned to appreciate the crucial role that intellectual adaptability and a willingness to reconsider project planning can play in aiding development and maintaining a focus toward efforts that serve overall research progress. I also learned the importance of aiming high, for without a lofty set of goals to drive my focus, I doubt I would have realized as many successes as I in fact did. Though I had hoped to provide more of a generalized architecture for servicing a variety of assay needs, I also came to understand that, as in most works, optimizing designed systems for one purpose often arrives at the expense of precluding functionalities in other domains. The good news for microsystems designers is that this circumstance will likely ensure many more years of development needs. As goals changed and technical limits were faced, I realized that combining challenging and complex engineered systems with challenging and complex matters in cell biology could synergistically meld to simply remind me of my small place in this beautiful but daunting world. I hope that this document may prove useful for those who are patient enough to work their way through it. It is my effort for trying to leave one tiny footprint in the sand.

While undertaking my doctoral work, a great number of individuals have led cheers, stayed up late, offered valuable feedback, and even sometimes simply helped to remind me exactly why I had chosen to spend six years of my life with a seemingly dedicated focus toward ensuring that monthly stipends would amount to pay well below minimum wage. Without this collective of individuals, some whose names I never knew, some whose interactions were little more than a fleeting smile on a short-lived T ride or a "wicked pissah" to point out that I was not "in Kansas anymore," you made "Beantown" my home and you made it all a bit less acute when "cowboy up" had to stand in as the adopted mantra.

To my research advisor, Dr. Joel Voldman, I offer many thanks for providing the opportunities and resources to spend a portion of my life pursuing the development of ideas that would have been too risky to indulge outside of the blessing of an academic setting. My committee, as a whole, deserves the highest of acclaim for taking the time to understand my work and to help me grapple with complexities spanning many disciplines. Beyond his inspirational lecture style, Dr. Alan Grodzinsky, always knew how to point to the heart of all matters by sifting through layers of detail to outline fundamentals in readily understood terms. Dr. Peter Sorger, despite a trek across the muddy waters of the Charles, was kind enough to keep me in his Cambridge-side network while welcoming me within the Harvard Systems Biology community. He always grounded my work with an appreciation for aspects of both engineering and biology while offering the much-appreciated perspective of a realist.

In my tenure at MIT, I was fortunate to work under the purview of the Research Laboratory of Electronics and, furthermore, to be surrounded by the "neighborhood block" appeal native to the "8th floor" in building 36. Dialogues, conversations, collaborations, and courtesies shared with Dr. Jacob White, Dr. Jongyoon Han, and Dr. Dennis Freeman and their affiliate bands of graduate students and postdocs gave a personal touch to an institute that, at times, could feel like a strange bedfellow. Dave Foss and Sukru Cinar you, too, sheltered others and me from many woes.

My added ties to the Microsystems Technology Laboratories, the Singapore-MIT Alliance, the Cell Decision Process Center, and the Edgerton Center helped diversify my time here in ways that would have been challenging to replicate by alternative means. I met wonderful staff members who helped debug equipment and offered valued feedback (special "thank yous" go out to Eric Lim, Bob Bicchieri, Vicky Diadiuk, Dennis Ward, Paul Tierney, Debb Hodges-Pabon and Fred Cote); I was privileged to travel to parts of the world that I had never seen before; and I ingested a steady diet of worldly perspective on the work that kept me busy.

Serving in the trenches along with me, my colleagues in the Voldman lab, at times loved me, at times hated me, but could usually laugh along with me, when all was said and done. To Mike Vahey, Salil Desai, Somponnat Sampattavanich (a.k.a. "Pat" or in trying times "Somponasty") I owe special thanks as both collaborators and friends. May you all learn to carry less weight some day. To Joseph Kovac, Nikhil Mittal, Dr. Alison Skelley, Laralynne Przybyla, Dr. Lily Kim, Dr. Adam Rosenthal, Hsu-Yi Lee, Dr. Katarina Blagović, Rikky Muller, Nitzan Gadish, and Dr. Wei Mong Tsang thanks for tolerating this southern man.

A true note of gratitude goes to Dr. Suzanne Gaudet, Dr. John Albeck, Dr. John Burke, and Sabrina Spencer. Despite being biologists, they all treated me as an equal and did everything in their capacity to help others within their community understand that an engineer's perspective could offer something of value.

In true cross-disciplinary style, Dr. Karen Willcox and her students, Dr. Theresa Robinson and Boon Hooi Ooi, offered efforts that have been pivotal in tackling refined simulation-based understandings of much of my work. It has been a true pleasure, and also a humbling experience, to learn how easily a microsystems designer can step away from the path illuminated by validated modeling tools. I can only imagine that collaborations such as the one we enjoyed will necessarily become more of a "gold standard" for those wishing to provide meaningful impact with novel small-scale multiphysics-based platforms.

My two UROPs, Theresa Guo and Hari Singal, deserve to take a bow for their tireless efforts in helping me to cram more work than one person alone could manage into a six-year stint. For Hari's willingness to travel from India to the States only to be driven as hard as any undergraduate researcher could, I am indebted. He was naive enough to not only work for me, but also to try and generate data that met the highest of standards.

If any of this document's presentational style rings true to my roots, then I owe my junior year high school English professor Dr. Sally Humble and my parents, Michael and Louise Taff, major credit. They were all tough on me beyond comfort and loved me enough to be as hard as was essential to enable the effective communication of ideas in written form. If I write with an aim to satisfy anyone, it is this team of three that I hope to serve.

To the dignity and excellence that is UNC Tar Heel basketball, I take my hat off. Through the tradition and discipline of Dean Smith, Roy Williams, and many teams whose work ethic is perhaps best exemplified by the drive of Tyler Hansbrough, I model my academic endeavors, my work ethic, and commitment to quality upon the examples that you have set. Thank you for

showing us that the beauty of a simple game can serve as a microcosm for approaching all matters personal, public, and otherwise.

To all of my friends, especially Tyrone Hill and Amil Patel, the levity you added made rolling out of bed on even the worst of days a duty that was always buffeted with something other than keeping one's chin to the grindstone. Good times, good beers, and good laughs.

Last, I must thank my family. My mother, Louise Taff, was always in the wings to providing supportive messages and a positive outlook. Without her help, none of this work would have been possible. My late father, Michael Taff, was here for more of the ride than he may know. I just wish I could have shared more of this experience with him through first-hand conversations, as I know he would have "gotten it." Having both my brother, Kevin, and my sister-in-law, Meredith, nearby for the past several years has been an added comfort that has helped enable the occasional, much-needed, escape. To my wonderful woman, Vivian Chen, your tolerance and understanding has amassed a debt of love and generosity I can only hope to someday repay.

A general note to the reader

In developing the overarching story outlined in my dissertation, I made a dedicated effort to employ a visual approach. As such, I have attempted to incorporate every major point and/or result in some figure-based form throughout the document. In general, I approached each chapter as if it was a Science- or Nature-style discussion that focused on the core issues in the body of the chapter, while leaving more ancillary concerns to the chapter-specific appendices. This structuring is aimed toward enhancing the overall readability while at the same time providing a comprehensive outlay. For those left short on time, who would like to obtain a cursory understanding of this work, simply reading the figure captions and thumbing through the in-text images and chapter-specific appendices should prove instructional. To those who read this document in comprehensive fashion, your added attention is most certainly appreciated.

Table of contents

Chapter 1: Introduction, Background, and Project Focus

In this dissertation, I present a number of distinct technologies that enable unique micron scale particle manipulations and offer templates for addressing heretofore unapproachable experimental investigations in the cellular biology and life science domains. To frame my work, Chapter 1 outlines details relevant to the primary motivations, both technological and application specific, that have guided my work and propelled it to the state covered in explicit detail throughout the remainder of this document. By discussing the context of my research and key elements of the approaches adopted using a generalized presentation format at the onset, it is my hope that as the reader progresses through subsequent chapters he/she will appreciate specific design details from a more contextual perspective.

Conventional cell culture - its flexibilities and its limitations

For much of the past century, efforts by research groups worldwide have leveraged plated cell cultures, where collections of sample cells are grown on polystyrene or glass Petri dish surfaces, as test beds for investigating a variety of fundamental biological processes. Using these template *in vitro* culture systems, investigators often extract lysates or measure secretions from bulk groupings of cells and over time have shed light on topics as diverse as the cell cycle[3, 8], the balance of pro-survival[4, 7, 9, 10] and apoptotic[2, 11] (programmed cell death) signaling, inflammation[9, 44], wound healing[45], gene regulation[12, 13], and even stress dynamics[14, 15].

Despite these gains, in contexts other than those dedicated to the analysis of either single-celled organisms or small-scale multicellular organisms, surveying cell behaviors in such environments only serves as a surrogate for analyzing responses in cases where tracking such effects *in vivo* would face overwhelming moral stigmas and/or technological challenges. These dish-based investigational efforts though historically fruitful, especially in light of their abstractions from the systems they aim to represent, cater best to harvesting the averaged responses from binned populations of cells and present only limited avenues for tracking individual cell behaviors. Technologies targeting expanded single-cell analysis could thus further progress approaches to biological discovery.

In recent years, studies at the single-cell level, in mammalian and other living systems, have uncovered a wide variety of cross population heterogeneity[29-33] that is often masked when tracking dynamics via averaged population-based measurements. These cross population differences have motivated revised understandings of pathways relevant to prosurvival NFAT[10, 44] and NF-kappaB[4, 7] signaling, p53 oscillations stimulated by gamma irradiation[33], synthetic biological constructs[46-48], various types of biological noise regulation[31, 32, 49-54], and even drug-induced apoptotic responses[2, 35, 55-62]. Monitoring the unique dynamics affiliated with various cell subpopulations compared to the averaged behaviors of the surrounding bulk populace has gained the devoted attention of many researchers in part because it is believed and/or known, in many contexts, that small groupings of cells may be/are responsible for dictating the fate of various diseases and developmental processes[34-36].

Despite the relevance of such investigations, the available suite of experimental tools for probing such effects is somewhat limited, and, for many biological laboratories, often amounts to either analyses of standard cell platings via automated microscopy or fluorescence-activated cell

sorting (FACS) approaches to cell manipulation. Though such avenues regularly provide new insights, manipulating and organizing cell subpopulations within cultured microenvironments based upon imaged-cues could readily augment surveys of this type.

From a signaling standpoint both autocrine and paracrine effects play important roles in cell behaviors[63-71]. Such dynamics relate to the communication occuring between a cell and itself (autocrine) as well as that which occurs between disparate cells (paracrine). Such effects are intimately tied to cell placement and clustering within a culture environment as the spatial locations of neighboring cells directly affects the extracellular signaling network topology and its mechanics. Controlling this complexity using conventional techniques has generally leveraged variable-density dish platings as a crude means for regulating signaling effects. Such approaches present non-uniform cell-cell spacings throughout the culture and can therefore confound opportunities to observe the potentially subtle effects associated with the highly regulated cell organization endemnic to *in vivo* systems. A need therefore exists to provide *in vitro* manipulation capabilities well suited to the organization and patterning of multiple cell types on a common surface. Such efforts would need to direct individual cells to distinct locations within the culture and thus explicitly modulate communication dynamics using prescribed cell-cell distances.

Probing complex phenotypes via "full stream" assays

Globally, a cell's interactions with its surroundings can be parsed into three, perhaps artificial, but distinct components[64, 72]. As outlined in Figure 1, the culture environment can present upstream activating ligands that stimulate receptors on the cell's membrane. This stimulation can in turn motivate the translocation and/or activation of various intracellular proteins that drive the upregulation of various genes. The activated genes can then stimulate the production of

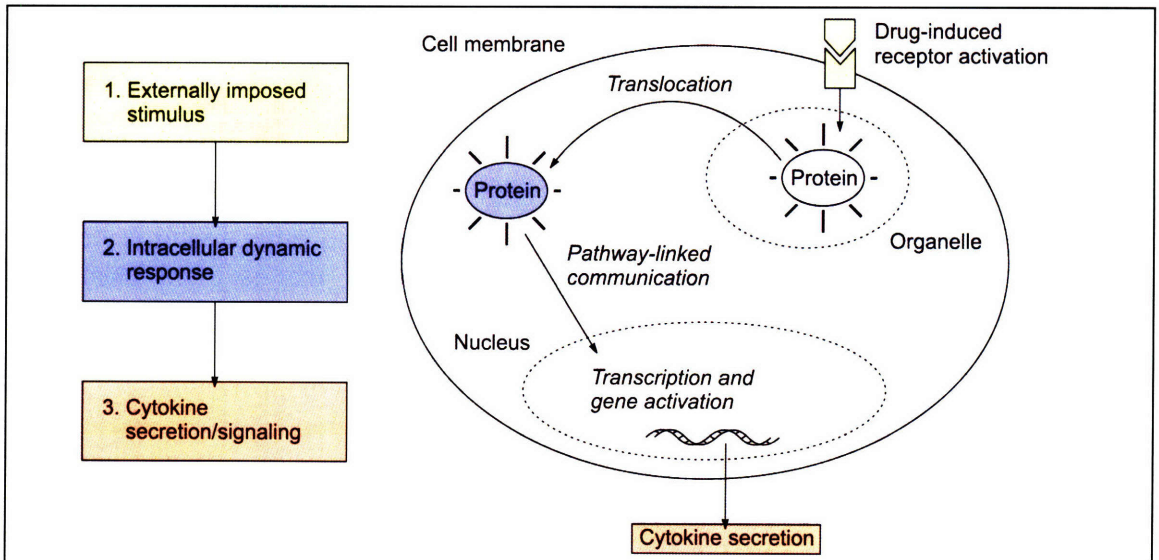

Figure 1: A generalized outline of the interactions and signaling dynamics that individual cells present as part of their life-cycle processes. In essence, the outside world can interact with individual cells via receptor mechanics that can in turn motivate intracellular signaling dynamics, gene activation and eventually downstream decision processes that often result in secretions of various cytokines and/or determinations of cell fate.

various downstream responses. Such responses can take the form of cytokine secretions (as shown explicitly) or manifest as other specific cell decision processes. These downstream processes typically regulate cell fate and/or details affiliated with a cell's interactions with its environment.

Though I have presented a generalized three-tier approach to understanding the interactions and signaling dynamics of individual cells and significant works have readily probed portions of this communication topology, few, if any, technologies offer robust avenues for surveying all portions of such "full stream" (a moniker for the cascaded response from upstream inputs to downstream responses) interactions. As an example, many assays may explore a variety of drug dosage treatments and then monitor either the intracellular dynamic response or the downstream decision process alone. This circumstance arises because many of the standardized analysis techniques (Western blots, immunofluorescence staining, IP) used in biology laboratories are inherently "endpoint" style methods where taking the measurement requires the destruction of the biological sample under study. As a result, if one wants to monitor effects after such "endpoint" routines, or track dynamic effects occurring over time, it proves essential to run multiple copies of an assay condition and truncate each instance at different point to later assemble a composite time course[4, 73]. Such composites may not fully reflect the true behavior of any one grouping of cells had they been monitored separately over time. Combining this complication with the fact that many such efforts demand sizeable cell counts for reliable readouts, we once again face the averaging effect where, the behaviors of distinct cell populations become occluded by the nature of the measurements being recorded.

Of special interest to my work was the notion of expanding the potential to survey complex phenotypes via "full stream" analyses. In general, a phenotype amounts to any observable physical or biochemical characteristic expressed by an organism[64, 74]. Complex phenotypes include cell characteristics and behaviors that demonstrate both temporal and/or spatial variance within the cell. To elaborate, proteins within the cell often translocate between various compartments within the cell during signaling responses. Monitoring the dynamics of such processes within the context of upstream drug stimuli and downstream cell output has proven elusive using most standard technologies, especially when autocrine and paracrine effects additionally demand effective management. Examining intracellular processes in real-time from a "full stream" perspective could leverage the information provided by the suite of fluorescence-based tags and reporter gene technologies developed in recent years[75, 76] to catapult biological discovery to a new realm. From a less technologically involved perspective, complex phenotypes can also include whole-cell characteristics affiliated with morphology. Oftentimes just knowing the eventual shape of cell after monitoring intracellular dynamics has proven challenging in formats other than those used to track small numbers of cells.

Array-based technologies

The types of studies targeted in my work, require a functional technology for handling large numbers of individual cells simultaneously. Avenues for servicing such demands have been made with increasing frequency in recent years through the use of microfabrication techniques [77, 78]. This approach has leveraged many of the recipes and processes originally motivated by the need for developing low-cost, highly-integrated microprocessors to instead pattern cell-scaled flow channels, electrodes, manipulators, barriers, and even substrate affixed chemical stamps.

By using tools originally developed for integrated circuit manufacturing or by leveraging tangential technologies that service wafer-based processing (aligned bonders, deep reactive ion etchers, etc.), a large class of biological microelectromechanical systems (bioMEMS or biological microsystems) have emerged offering functional capabilities surpassing those addressed by conventional cell culture means. A common footprint that has arisen in many bioMEMS platforms centered on parallelized manipulations of individual cells is the array. A multitude of applications ranging from patterned neural network[79, 80], to coculture systems[81-83], cell-based biosensors[84-86], secretion measurement tools[87, 88], cellular force measurements[89], drug delivery systems[90, 91], and even transfection platforms[92, 93] for monitoring gene expression have benefited from this type of organizational format.

From a basic standpoint, arrays offer clean and simple avenues for organizing and indexing assayed collections of cells by assigning unique, known positions to every cell under study[94-96]. Information about variations in the behavioral responses across populations of cells is easily obtained using arrays as they present a functional probe for investigating the heterogeneous responses of nominally isogenic cells[84, 88, 97]. Through precise control of cellular position and environment, arrays can additionally enhance the reliability and statistical significance of collected data through redundancy. Furthermore, though it is not the specific focus of the work presented here, by assaying libraries of distinct mutants[92, 93, 98] or by examining arrays where different stimuli are directed to different subpopulations of similar cells[99-101], it is possible to simultaneously monitor large collections of distinct assay conditions in a single experiment.

Microfabricated arrays for biological applications fall loosely into a small set of subclassifications. One type is passive and simply serves to hold objects in specific locations. Such arrays generally operate either by presenting patterned adhesive regions[81, 83] or by defining mechanical structures that serve as small containers to physically confine biomaterial to specified positions[94, 95]. Others are globally active, enabling dynamic simultaneous control over all sites in the array. Arrays of this type include devices where the surface features[102, 103] or even the trapping capabilities[24, 104] of all sites in the array can be switched from one state to another in a parallel fashion. Last, active addressable arrays present avenues for changing or mapping different conditions to specific sites[19, 105, 106]. The mechanisms for switching individual sites in this sort of array are often similar to those used in globally active arrays, but modified to permit individual site control. In general, the intended application of a

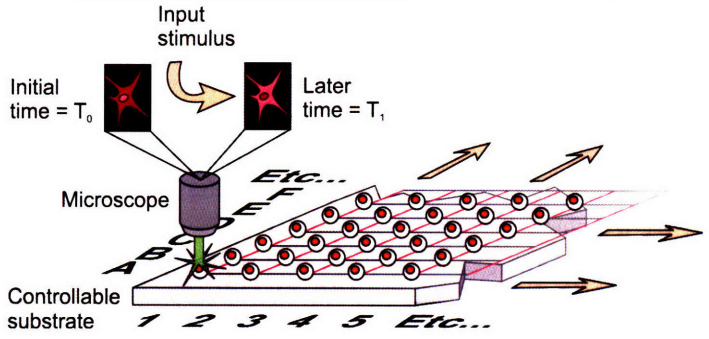

Figure 2: A template of the types of active addressable arrays explored as a part of my doctoral work. In this setup, individual cells are held in specified locations on a row/column organized trapping grid. We can stimulate the populace and then interrogate cell function in individual cells using microscopy methods. In some context we may opt to monitor individual "downstream" cell fates while in other we can elect to release targeted cells for further study. The specific configuration of individual "pixels" within the array is intentionally obscured at this stage in the discussion and will be expanded in subsequent chapters through an exploration of details pertinent to their design evolution and application demands.

given array mandates its associated levels of functionality and complexity. As detailed more explicitly further on in this document, my work incorporates various assortments of active addressable arrays for trapping, holding, visualizing, and, in certain contexts, sorting subpopulations of individual cells[39, 40]. In Figure 2 I present an overarching generalized perspective on the types of active addressable arrays explored as a part of my doctoral work. As noted by the indexing scheme on the periphery of the device, all array locations are organized in specific rows and columns. The connections (shown in red and black), which I will discuss in more detail further along in this chapter, prove to be a pivotal component of array activation mechanics and their management is crucial for effective array-based biological microsystems design.

Single-cell manipulations

To date, numerous methods have been employed to enable single-cell placement and manipulation in various exploratory bioMEMS contexts. Most applications have incorporated physical, optical, or electrical forces either in isolation or in some appropriate combination. Illustrative examples of physical means have included various microwell structures with fabrication methods ranging from silicon bulk micromachining[107] to the selective wet etching of the cores of bundled, extruded fiber optic cables[17]. Patch clamping devices have likewise proven beneficial for electroporation, transfection, bioprocess monitoring, and even controlled cell-fusion studies[91, 108, 109]. Furthermore, numerous methods for micropatterning substrates such that different spatially defined regions present distinct surface chemistries capable of promoting varying degrees of attachment for different cell types have shown broad use[81, 83]. Micro-bubble generation[110] through controlled, localized fluid boiling has also shown promise. In complementary fashion, optical tweezing technologies have benefited studies ranging from the analysis of mechanically-induced growth mechanisms in individual single bone and cartilage cells[111] to the establishment of optical lattices capable of separating distinct cell populations based upon size considerations[112]. Electrical strategies have relied heavily upon dielectrophoretic (DEP) techniques[24, 104, 113, 114]. This approach uses the intrinsic electrical polarizability of various cell types as a means for exerting ponderomotive forces. Since this strategy can employ frequency-modulated voltages, it is possible to avoid complications associated with direct current (DC) fields in on-chip liquid-based environments. Concerns tied to bubble formation and induced transmembrane potentials are thus less problematic when compared to other electric field-based approaches.

Dielectrophoresis

In my work I too implement DEP methods either in isolation or in concert with other mechanisms to exert cell-scale forces at each "pixel" within my developed device arrays. In general, DEP forces result when spatially non-uniform electric fields induce oriented charge distributions in electrically polarizable bodies[115]. The specific properties of the media, the polarizable body, and the in-system electric fields determine whether the body (from now on referred to as "the particle" – for our purposes can denote, beads, cells, or a more general term for both) will migrate toward sites of maximum field intensity (positive DEP or p-DEP) or away from sites of maximum field intensity (negative DEP or n-DEP)[116].

Both p- and n-DEP based forcing strategies honor a number of distinct advantages and disadvantages. For many biological applications, operations in cell culture medias, present

highly conductive on-chip buffers (~1.5 S/m) that enable n-DEP manipulations alone. This imbalance in particle and media conductivities assigns a negative value to the DEP force by means of an internal fractional relation known as the Clausius-Mossoti (CM) factor (discussed in more detail below.) Conversely p-DEP trapping demands low-conductivity in-system buffers that own the risk of creating unsuitable environmental conditions for investigating cell function but can reduce in-system Joule heating effects and demand reduced current input to maintain a given in-buffer voltage drop. Here the conductivity imbalance is reversed such that the CM factor contributes a positive sign to the DEP force equation. For a given electric-field gradient, a p-DEP force can be twice as strong as a comparable n-DEP force, a direct consequence of the specific formulation of the CM factor ratio. N-DEP's weaker magnitudes, its heightened propensity for inducing Joule heating, and its aptitude for providing repulsion-based forcing suggest, as has been supported by a great deal of simulation work explored in my Master's thesis and efforts since, that it may be fundamentally more difficult to create a stable n-DEP trap geometry with holding characteristics comparable to a p-DEP design. As the reader progresses though the work presented in this dissertation, I will demonstrate a series of devices that use both negative and positive forcing strategies to approach the "full stream" assay platforms targeted in our approach.

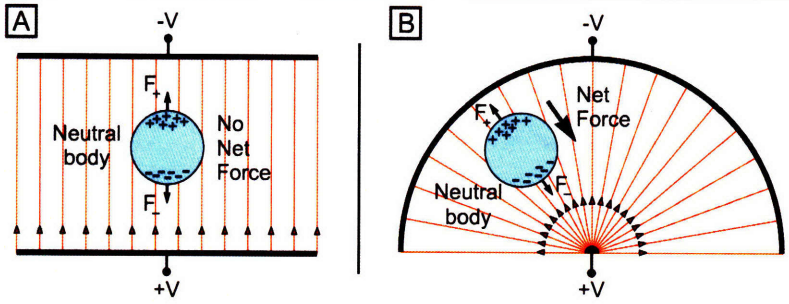

Figure 3: In a uniform electric field **(A)**, neutral bodies form balanced distributions of charge that exerts no net electromotive forces. In contrast **(B)**, within spatially non-uniform fields neutral bodies witness unbalanced charge accumulations that produce net forces. The direction of this net DEP force is determined by a range of components including the drive frequency of the activating electrodes and the relative complex permittivity of the particle and in-system buffer. To simply indicate that a net force exists we have illustrated a p-DEP directed (up the field gradient) toward the +V electrode in our depiction. We could have just as easily drawn the net force in the opposite direction and indicated the presence of an n-DEP force down the field gradient.

To best understand many of the specifics underlying DEP forcing mechanics, it is instructional to survey the presiding physics involved as well as some of the basics of their associated mathematical formulations. In Figure 3 we explore two example electrode configurations. In part A, we position a neutral particle between a set of parallel plates driven with opposing voltages. In this setup, the neutral body experiences no net force since the in-particle induced charges perfectly balance one another generating a case where $F_+ = F_-$. In such contexts, either the upper electrode attracts positive charges to the top portion of the particle that mirror the negative charges attracted by the lower electrode to the bottom side of the particle or the in-system field orients internal dipoles in ways that provide no translational effects. With no net force the particle simply maintains its position between the electric plates with no tendency to migrate toward one or the other. In part B however, we have a neutral particle position within a spatially non-uniform electric field. This non-uniform field is a direct consequence of the mismatch in sizing seen when comparing the dimensions of the positive (+V; small) and negative (-V; large) in-system electrodes. Once again the electrodes induce charge accumulation within the neutral body. Subject to this context however, such

induced charges present an asymmetry and an associated net electromotive force. Within this environment the particle progresses either up or down the electric field gradient depending upon the relative permittivity of the particle compared to its surrounding buffer and the frequencies at which the electrodes are driven.

If the particle inside the non-uniform field is spherical and only influenced by induced dipole effects, then the mathematical expression, as originally developed by Pohl[117] for the affiliate DEP force is as follows[115]:

$$\bar{F}_{DEP} = 2\pi\varepsilon_{media} R^3 \,\mathrm{Re}\left[\widehat{CM}\left(\hat{\varepsilon}_{body}, \hat{\varepsilon}_{media}\right)\cdot\nabla\left|\bar{E}\right|^2\right] \qquad \textbf{Equation 1}$$

Here, ε_{media} represents the electrical permittivity of the fluid surrounding the particle, R is the radius of the particle, $\widehat{CM}$ presents the complex Clausius-Mossoti (CM) factor, $\hat{\varepsilon}_{body}$ and $\hat{\varepsilon}_{media}$ are the complex electrical permittivity of the particle and media, respectively, and $\bar{E}$ is the electric field generated between the electrodes. This simplified formulation of the DEP force presents several interesting features. First, the force scales with the cube of the particle radius and the gradient of the electric field squared. Larger particles will thus experience greater DEP forces and simply doubling the voltage applied across a set of activating electrodes will produce a fourfold increase in the net DEP force.

The CM factor is the only term in the equation that presents a functional dependency upon the driving frequency of the electrodes in the system. For a spherical body of uniform composition, this term is expressed as follows[115]:

$$\widehat{CM} = \frac{\hat{\varepsilon}_{body} - \hat{\varepsilon}_{media}}{\hat{\varepsilon}_{body} + 2\hat{\varepsilon}_{media}} \qquad \textbf{Equation 2}$$

This relation is derived from an evaluation of the Laplace equation for the particle-media system. The frequency dependence of this factor arises from the presence of both real and imaginary components in the denoted complex permittivities central to this mathematical description. In general, these complex permittivities are expressed as:

$$\hat{\varepsilon}_x = \varepsilon_x + \frac{\sigma_x}{j\omega} \qquad \textbf{Equation 3}$$

Here, ε_x marks the electrical permittivity corresponding to a generalized x-labeled in-system component (ie. media or particle) while σ_x denotes the electrical conductivity of that same generalized element. The j indicates the imaginary portion of this term and ω equates to the drive frequency of the field motivating the DEP forcing. The magnitude of the CM factor, can mathematically vary between values of -0.5 and 1. When this term is positive for a given setup, we witness positive dielectrophoretic forcing. When it is negative, we see negative dielectrophoretic forcing. It is typical for discussions on positive and negative DEP forcing to

lump concerns pertaining to the relative complex permittivities of the media and the body into categorizations of their relative (real) electrical conductivities. This approach stems from the fact that for many experimentally relevant cases it is the second term on the right hand side of Equation 3 that dominates over contributions from the first.

Though this initial discussion is useful for understanding DEP basics, biological cells are not homogeneous in nature and we therefore demand a more involved description of the CM factor to link force mechanics to details of the in-system electric field gradient. As a simple model, cells can be thought of as structures with a central core owning one set of electrical characteristics (effectively a description of the cell cytoplasm and organelles) and an outer shell demonstrating an alternative set of characteristics (effectively a description of the cell membrane). Once again, applying the Laplace equation to match boundary conditions across the composite model, we can develop a single effective permittivity term to describe the nested dielectric structure of a mammalian cell. The revised CM-factor description amounts to the following[115]:

$\hat{\varepsilon}_{body,eff} = \frac{\hat{C}_{mem} R \hat{\varepsilon}_{media}}{\hat{C}_{mem} R + \hat{\varepsilon}_{media}}$	**Equation 4**

We simply insert this relation into the position occupied by the $\hat{\varepsilon}_{body}$ variable in the homogeneous spherical model to obtain the updated dipolar description of the DEP force exerted on a cell. In this relation, $\hat{C}_{mem}$ is the complex membrane capacitance defined by

$\hat{C}_{mem} = C_{mem} + \frac{G_{mem}}{j\omega}$	**Equation 5**

where C_{mem} and G_{mem} represent the cell membrane capacitance and conductance, each in turn described by

$C_{mem} = \frac{\varepsilon_{mem}}{\Delta}$ and $G_{mem} = \frac{\sigma_{mem}}{\Delta}$	**Equation 6**

where ε_{mem} and σ_{mem} are the (real) electrical permittivity and conductivity of the membrane and Δ represents the membrane thickness.

Equation 1, is typically an accurate desciptor of DEP forcing mechanics, but it occasionally proves insufficient for adequately describing the actual dielectrophoretic forces experienced by particles submerged in fluid microenvironments. Discrepancies between this model and experimental behaviors sometimes arise from the assumptions made when deriving Equation 1 which only account for the presence of electrically-induced dipoles. In reality, electric fields induce a variety of higher order charge multipoles in the particle whose contributions to the overarching DEP forces can depend intimately upon the topology in the electric field. When the electric field presents spatial variations over length scales comparable to those of the particles

subjected to DEP manipulations (as is often the case for microfabricated electrode-reliant system configurations) or when the dipole term is zero (as is seen at the center of quadrupole trap designs[118]), the induction of higher order multipoles in those particles becomes more relevant.

Despite initial theoretical postulations of DEP electromechanics in the 1970s, a complete mathematical description of the multipole contributions to DEP force was only formalized in last fifteen years[119]. Neglecting the specifics of its derivation, I provide here[120].

$\bar{F}_{DEP}^{(n)} = \frac{\vdots\!\!=^{(n)}[\cdot]^n(\nabla)^n \bar{E}}{n!}$	**Equation 7**

the tensor notational description of the multipolar DEP force. In this relation, $\vdots\!\!=^{(n)}$ represents a multipolar induced-moment tensor and n indexes the force term corresponding to a given pole ($n=1$ for a dipole, $n=2$ for a quadrupole, etc.). The specific implementation used in the simulation work done for this dissertation (a subset and partially revised form of the coding originally developed by Dr. Rebecca Maxwell and my advisor Dr. Joel Voldman) utilized a more easily interpreted form of this extended DEP force relation dependent upon sinusoidal excitations and time averaging as detailed, for the sake of completeness, below[120].

$\left\langle \bar{F}_i^{(1)} \right\rangle = 2\pi\varepsilon_{media} R^3 \operatorname{Re}\left[\widehat{CM}^{(1)} E_m \frac{\partial}{\partial x_m} E_i^* \right]$	**Equation 8**
$\left\langle \bar{F}_i^{(2)} \right\rangle = \frac{2}{3}\pi\varepsilon_{media} R^5 \operatorname{Re}\left[\widehat{CM}^{(2)} \frac{\partial}{\partial x_m} E_n \frac{\partial^2}{\partial x_n \partial x_m} E_i^* \right]$	**Equation 9**
$\vdots$	

The numerically indexed superscripts in these expressions pertain to specific higher-order multipole terms while the i-indexed subscripts denote the specific Cartesian coordinate directions in which those forces act. The m and the n represent separate indices in a matrix-based discretization of space, and the * represents a complex conjugate form. In this context, the CM factor adopts the following form:

$\widehat{CM}^{(n)} = \frac{\hat{\varepsilon}_{body} - \hat{\varepsilon}_{media}}{n\hat{\varepsilon}_{body} + (n+1)\hat{\varepsilon}_{media}}$	**Equation 10**

in this enhanced system description. As I have documented in published form[5] and will explain further in the work presented in Chapter 3 of this dissertation, including higher order terms during modeling and analysis efforts can greatly narrow distinctions between predicted and observed device behaviors.

On-chip hydrodynamics

Perhaps the most popular actuation and manipulation strategies employed in biology- and chemistry-focused microsystems rely upon what is known as microfluidic control[100, 121, 122]. In essence this type of on chip dynamics amounts to scaled down plumbing networks that push fluids from one location to another by means of various flow channels. In all of the designs presented in this work, I too use microscale fluid flows as a means for introducing cells into my analysis arrays. Through carefully patterned in-flow constructs some of my array designs even provide hydrodynamic means for localizing individual particles at discrete on-chip locations[37, 39]. To provide a basic descriptor of the key mechanics involved in such flow-based configurations it is beneficial to discuss the Navier-Stokes equation and some of the simplifying assumptions made possible by geometric effects native to microscale environments.

The Navier-Stokes equation describes the physics of motions within fluids[77, 123]. Though complex in form it is simply a relation that maps the conservation of momentum, described in Newton's second law, to fluid elements of infinitesimal volume. In this balance momentum affiliated with such volumes amounts to the sum of various non-conserved viscous forces, changes in pressure, and other body forces that act upon the fluid. In its most general form, the Navier-Stokes equation is a nonlinear partial differential equation whose solution or velocity field is at best difficult and often impossible to solve analytically. Nonlinearity arises in this equation by means of convective acceleration. In other words, an acceleration tied to a change in velocity as a function of position within the system. Fortunately, for many microscale fluid environments creeping flow reduces the mathematical complexities necessary to describe in-system physics. Creeping (otherwise known as Stokes) flow exists in cases where a system descriptor known as the Reynolds number (Re) is substantially less than one. The Reynolds number is a ratiometric comparison of the in-system inertial and viscous forces. For the creeping flows common to microsystems settings the viscous effects therefore dominate over the inertial contributions.

In its full, generalized, form the Navier-Stokes equation is expressed as follows:

$\rho\left(\frac{\partial \bar{v}}{\partial t}+\bar{v}\cdot\nabla\bar{v}\right)=-\nabla p+\nabla\cdot\bar{\bar{T}}+\bar{F}$	**Equation 11**

Here ρ denotes the fluid density, $\bar{v}$ represents the flow velocity vector, p is the pressure, $\bar{\bar{T}}$ amounts to the deviatoric stress tensor, and $\bar{F}$ marks the body forces acting on a unit volume of fluid. Using a concept known as the substantive derivative, we can rewrite this formulation as follows:

$\rho\left(\frac{D\bar{v}}{Dt}\right)=-\nabla p+\nabla\cdot\bar{\bar{T}}+\bar{F}$	**Equation 12**

This substantive derivative, $\frac{D}{Dt}$, (also sometimes referred to as the convective derivative) is a derivative taken along a path moving at velocity $|\bar{v}|$ and provides a description of the time rate of

change of any quantity transported by the fluid. In the case of the Navier-Stokes relation, that quantity is momentum per unit volume, $\rho\bar{v}$, and Equation 12 thus makes it easier to interpret the composite system equation as a direct application of Newton's second law.

As a statement of conserved momentum, the Navier-Stokes equation alone generally demands further supplemental information to fully describe all aspects of in-system hydrodynamics. Such information may include boundary conditions, or other conservative formulations. It is typical that the mass continuity equation proves essential. I provide both its general form and one using the substantive derivative here:

$\frac{\partial \rho}{\partial t} + \nabla \cdot (\rho \bar{v}) = 0$	**Equation 13**
$\frac{D\rho}{Dt} + \rho(\nabla \cdot \bar{v}) = 0$	**Equation 14**

In many cases, and certainly all work done to model and understand the behaviors of systems developed in my doctoral work, we adopt the assumption that on-chip fluids are incompressible and Newtonian in nature. An incompressible flow is one in which the divergence of the velocity is zero. In mathematical form, this condition amounts to the following relation:

$\nabla \cdot \bar{v} = 0$	**Equation 15**

Inserting this condition into the substantive derivative form of the mass continuity equation from Equation 14 we arrive at the following relation:

$\frac{D\rho}{Dt} = 0$	**Equation 16**

In other words, the mass density of incompressible flows are constant when following any given in-flow fluid element.

Newtonian fluids such as water present mechanical stress-strain relations that are linear and pass through the origin. A simplified relation describing this effect is given as:

$\tau = \mu \frac{du}{dx}$	**Equation 17**

In this relation, τ represents the shear stress, μ is the fluid viscosity, and $\frac{du}{dx}$ is the velocity gradient perpendicular to the incident stress. Here, no matter how fast the fluid moves it continues to behave as a fluid and thus flows in concert with the forces acting upon it.

The incompressibility and Newtonian fluid assumptions allow a revised consideration of the original, admittedly overwhelming, generalized Navier-Stokes formulation. Below I explicitly list the simplified form.

$$\rho\left(\frac{\partial \bar{v}}{\partial t}+\bar{v}\cdot\nabla\bar{v}\right)=-\nabla p+\mu\nabla^2\bar{v}+\bar{F} \qquad \textbf{Equation 18}$$

In most cases this form only demands a mass continuity equation which, subject to incompressibility, is outlined in Equation 15. Though still a differential relation, only the convective terms in Equation 18 are nonlinear and a multitude of numerical techniques are well suited to evaluate and solve system equations of this type. The velocity fields that emerge from such solutions can then serve as a design feedback for developing various in-system hydrodynamic components.

Revisiting the context of creeping flows, we can further simplify this relation to the Stokes equation as denoted through the following formulation:

$$\nabla p=\mu\nabla^2\bar{v}+\bar{F} \qquad \textbf{Equation 19}$$

Again, Equation 15 typically completes the system description. This equation form is even more straightforward to evaluate and has, in part, been a major motivator for the progress made in fluid-based microsystems over the course of the past 20 or more years.

Managing addressable site control

With a generalized understanding of both DEP electromechanics and hydrodynamics in hand, we can begin considering a multitude of strategies for developing microsystems platforms to begin servicing the types of "full stream" biological assays motivating my work. With lithography techniques, it is feasible to use combinations of UV radiation and chrome-plated glass masks to pattern various electrode footprints onto silicon substrates. With high resolution on-chip wiring, it is then possible to connect individual array "pixels" in our devices to of chip peripheral control signaling.

As I will detail throughout the remainder of my dissertation, the design of individual "pixels" within

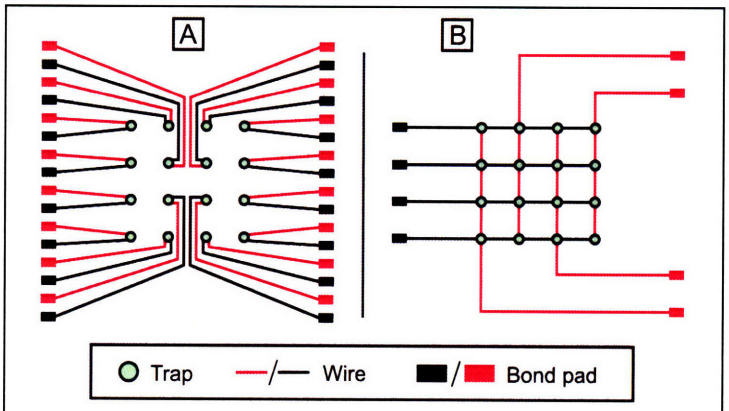

Figure 4: The conventional means **(A)** for enabling addressable site control in array-based microsystems demands unique sets of wires or control lines that link off-chip peripherals to on-chip cell traps. Unfortunately in scaled implementations this approach arrives at the expense of crowded on-chip electrode routing and a need for large numbers of chip-to-world connections. In contrast **(B)** row/column linked geometries eliminate the crowding contingency and substantially reduce the number of interconnects necessary for linking off-chip signals to designated on-chip locations.

the array-based platforms developed in my work will take on various forms that change to suit different assay-specific needs. In general however, whether I choose to use DEP in isolation or in concert with other means to perform on-chip cell manipulations, all of my design efforts rely upon electrical activation to address either individual sites within the arrays or designated subclasses of sites. While this level of control presents great flexibility, managing it effectively demanded a reexamination of methods for routing in-system control lines. As illustrated in Figure 4A the conventional approach to enabling addressable site control in microsystems platforms has leveraged a relatively simplistic effort that pairs an individual "positive" activating electrode and an individual "negative" activating electrode with each and every site in an array. While this type of effort does in fact provide the type of control targeted in my efforts, it suffers from the complication that as the array grows in size so too do woes related to on-chip control line crowding and the number of interconnects necessary to connect to off-chip peripherals.

To circumvent these limitations I examined and developed a revised site addressing approach as shown in Figure 4B which relies upon row/column connections that link to each on-chip trap. This approach is modeled upon strategies regularly employed in display technologies for television and other similar application domains where individual "pixel" locations are switched through varying red, green, and blue color patterns using row and column connected circuitry. In these more mature technologies it is common to include active transistor-based switching elements for each of the pixels in the system. With this setup, unique combinations of input signals directed to the row and column connections known as words can index and modify the condition of any site in the array. Contrasting this approach, my site addressing routine does not incorporate transistor elements that link to each of the on-chip cell traps, but it instead modifies the localized electric fields at targeted intersecting row and column electrodes to enable switching. Without on-chip transistor elements I offer a comparatively passive actuation scheme that eliminates electrode control line crowding and

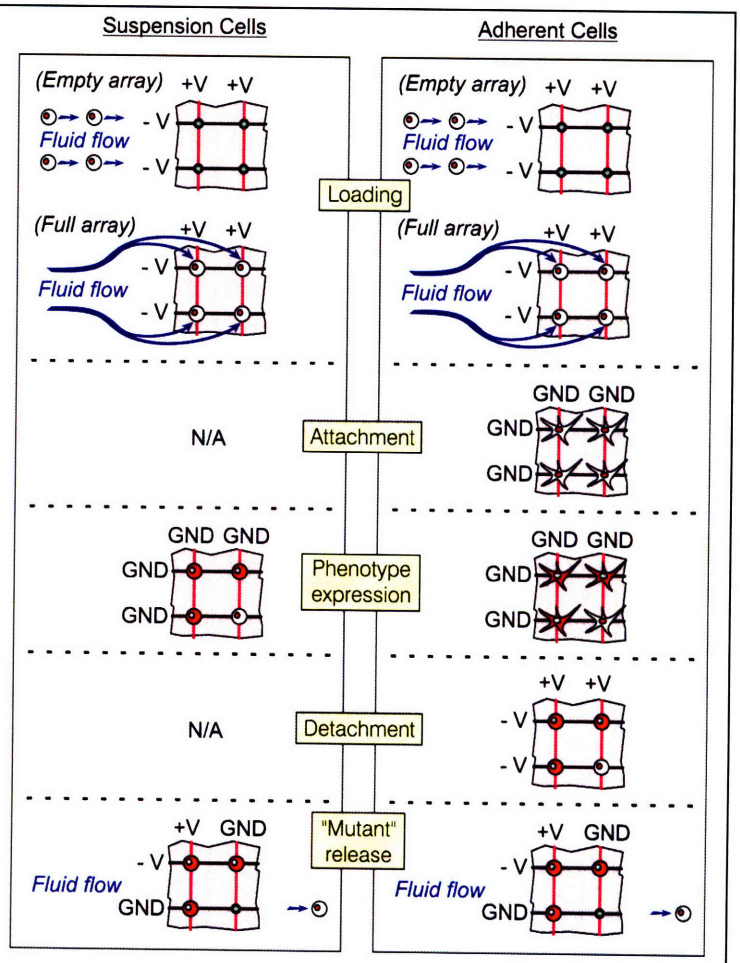

Figure 5: In sequential fashion I outline the most general form possible the basic steps required for the types of sorting assays that motivated much of the initial work for my doctoral thesis. At left we examine routines using suspension cell lines and at right I offer the equivalent protocols needed for operations with adherent cell lines.

greatly reduces the number of world-to-chip interconnects necessary for addressability at all array locations.

Though the fabrication processes necessary to manufacture such wiring footprints demand effective patterning of two separate levels of orthogonally-oriented conductive traces and thereby presents complexities surpassing the single-metal-level approach typically employed with conventional methods (as highlighted in Figure 4A), by not including on-chip transistors, our system complexity (from a fabrication standpoint) is still greatly reduced when compared to display-based addressing formats. In the end, our row/column addressing approach scales as $2\sqrt{n}$, where n represents the number of sites in the array, versus conventional efforts that scale as $2n$. For a 400 site array this sort of savings would mean that we could utilize 40 world-to-chip connections to manipulate any "pixel" as opposed to a need for 800 interconnects.

Sorting versus on-chip endpoint assays

In light of the "full stream" assays described earlier in this chapter, two basic categorizations of such investigations emerged as dominant motivators in my efforts to develop functional technology platforms. On the one hand, much of my early work focused upon the idea of sorting targeted subpopulations of cells from larger background groupings. With this approach the arrays were designed to function as a temporary docking station where image-based data could be extracted from surveyed cell populations via automated microscopy techniques and on-chip addressability functioned solely to direct specific cells off-chip for subsequent culture and study. Alternatively, on-chip endpoint assays provided another impetus for design development. In on-chip endpoint assays, the primary focus centers on positioning either one or more cell types in specified locations on a shared substrate and, based upon this initial organization, surveying both the intracellular dynamics and the ultimate downstream responses. This setup means that the chip arrays serves a role more closely matching that of a baseline culture environment where cells ideally remain viable and on-chip site addressing capabilities function solely to organize the initial cell groupings prior to surveying their responses. With such an approach, cells are never moved off-chip for continued analyses.

To illustrate an example sorting sequence, Figure 5 provides a generalized outline of an example of a on-chip routine that leverages my presented array-based row/column addressing scheme. Though, in idealized cases, adherent lines would demand both attachment and detachment steps, loading, observation, and release sequences are common to any cell type treated with such an approach. During loading routines we indiscriminately capture cells at all array "pixel" sites by activating all on-chip electrodes (column connections set to +V and row connections set to -V). We then image the dynamics of held cell responses in the aftermath of a given system input (in the shown case, a translocation of orange fluorescently-tagged proteins from the nucleus to the cytoplasm) and look for targeted subpopulations of cells to sort (the cell whose proteins fail to translocate as expected). With the targeted cells located, we reactivate in-system electrodes and then, in serial fashion, selectively deactivate the row and column electrodes affiliated with targeted cell locations. We use on-chip fluid flow in concert with these electrode signaling events to sweep only the desired cells out of the system.

For endpoint assays the initial cell organization can serve as a means for directly regulating diffusible cell signaling. It can also provide unique avenues for examining the isolated efficacy

of various dose-dependent treatments at a single-cell level surveyed across a multitude of different cell types. As the array-based format of the work provided in my dissertation presents unique surfaces to the culture environment, they too own the potential to play an active role in detecting downstream secretion responses using a host of different enzymatic and/or fluorescence-based means.

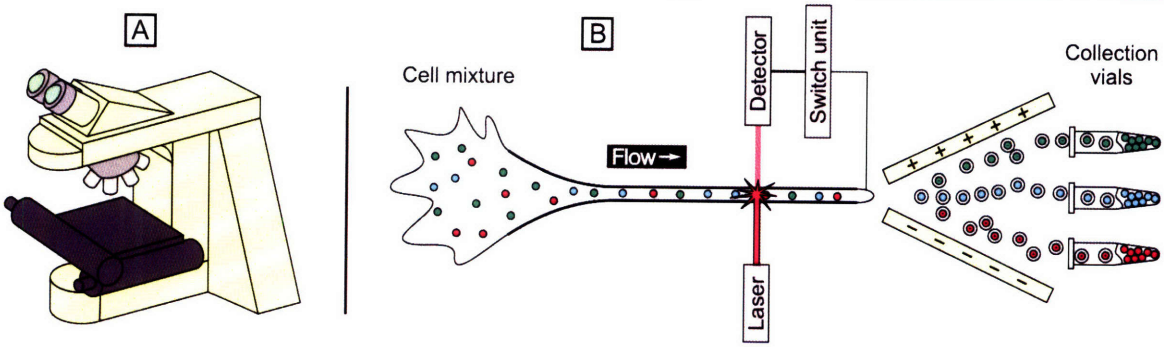

Figure 6: Automated microscopy **(A)** provides the dominant experimental technique for extracting image-based data from cultured cell systems. Though it renders a "window" to the goings-on in a given living microenvironment, in standard form, it lacks an equivalent ability to manipulate and maneuver observed in-culture entities. Alternatively, flow-assisted cell sorting (FACS) **(B)** offers the most widely used approach to manipulating and sorting cells, but it lacks an equivalent flexibility to image the cells that it sorts.

As a final wrap up and framing for the work I present in the coming chapters, Figure 6 solidifies the application space of my efforts by setting side-by-side the dominant imaging and manipulation platforms that are standardized as investigative tools in the biological community at-large. Automated microscopy offers the best available avenue for collecting image-based data from a cultured microenvironment. Aspects of morphology, protein localization, binding, and dissociation events, as well as, the general visual appearance of a culture provide rich information regarding cell function. Despite the ability to observe such valued content, standard automated microscopy platforms lack the ability to, in turn, directly exert manipulative forces upon observed cell cultures. To contrast this condition, the dominant means for selectively manipulating cells, fluorescence-activated cell sorting FACS, pushes suspended cultures through a narrow conduit and uses a simple yes/no detection-based decision tree to charge a series of activating plates that subsequently direct cells into various collection vials. Though this type of manipulation is rapid, there is no imaging involved. This caveat means that, at best, the in-system detector can only sort cells based upon the presence or absence of specific in-cell constructs. For example, it can not bin cells based upon whether or not a given protein is localized to a specific region within the cell. The organization of different cell types into different collection bins is furthermore an endpoint process with FACS. Though it is feasible to separate distinct cell populations it is not possible to use such manipulations to position cells on a shared culture substrate as an initial constraint for their collective growth. In this dissertation, I will present several distinct designed, fabricated, and tested platforms for merging many of the currently non-overlapping benefits of both automated microscopy and FACS cell manipulations. Through efforts to enhance the flexibility of both sorting and on-chip endpoint assays my work will provide a template for servicing all components of "full stream" functional cell investigations.

Chapter 2: A proof-of-concept trapping and sorting design

With a global understanding of the project focus in hand, I will present here details of my initial forays into array-based technology designs for single-cell biological assays. In this chapter, I use the terminus of my Masters thesis studies[124] as the starting point cultivating a continued dialogue with the reader. I will outlay complications faced with my developed first-generation devices and detail steps taken to produce both functional devices and outline design challenges for on-going matured work.

Developing a functional process for p-DEP "ring-dot" cell traps

In my Masters work I made extended efforts to design and develop on-chip traps for positioning individual mammalian cells at discrete locations within microscale flow chambers. The design pursued most aggressively relied solely upon positive dielectrophoretic means as the cell manipulation strategy.

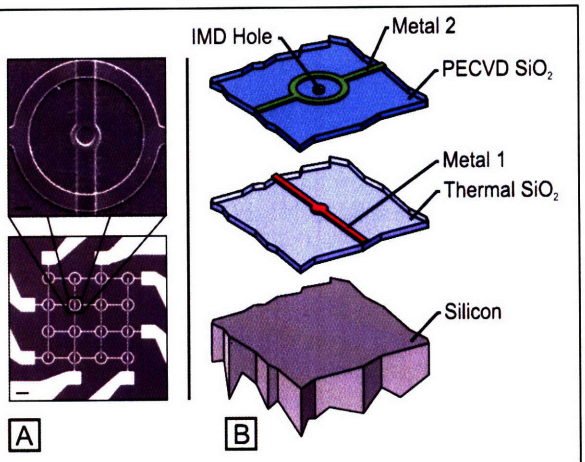

Figure 7: In both scanning electron micrograph **(A)** and schematic **(B)** form, I present the basic "ring-dot" single-cell p-DEP trapping geometry initially designed and developed as a part of my Master's thesis. This setup utilizes a two-level metal stack of aluminum layers to produce arrays of traps that attract cells to the central "dot" regions in the design footprint. (Scale bar in the enlarged image ≈10 μm. Scale bar in the array image ≈80 μm.)

As shown in Figure 7 the electrode footprint comprising such designs amounted to a central "dot" geometry surrounded by a peripheral "ring". I link the "ring" to a sinusoidal voltage input and the "dot" to a similar input that is phase shifted by 180°. This activation protocol produces a localized non-uniform electric field that, according to modeling efforts, should exert DEP forces for positioning individual cells over the central "dots".

To link into the row/column wiring scheme detailed in Chapter 1, I needed a two-level-metal fabrication process to form these traps (see Fabrication Methods Appendix - "Original 2-level metal non-via-based process for wafers presenting p- and n-DEP designs"). In brief, I first grew an insulating oxide layer onto a silicon substrate. I then sputter-deposited a thin aluminum layer and patterned it using plasma-based BCl_3 and Cl_2 etch chemistries. Next, I deposited a PECVD oxide layer and repeated the metal patterning sequence to produce a second level of on-chip metal. As a final step I used a timed Silox Vapox III (Transene Company, Inc., Danvers, MA) wet-etch chemistry to etch the intermetal dielectric (IMD) holes that produced the central "dot" features in thedesigns.

Unfortunately, after fabricating and packaging (methods detailed in my Masters thesis as well as in a comparative discussion found in Chapter 3) a series of devices using this processing sequence I failed to witness the anticipated single-particle trapping at the central "dot" location. As I show in Figure 8A, preliminary functional tests using silver-coated polystyrene beads (such

beads ensure on-chip p-DEP forcing as they are much more conductive than essentially any possible surrounding on-chip buffer) demonstrated a delocalized trapping response where particles migrated toward electrode edge across the entire chip surface instead of rendering a clean 16-site filled bead array. It was even common to find "pearl chaining" effects where extended clusters of beads bridged spans between oppositely polarized electrodes.

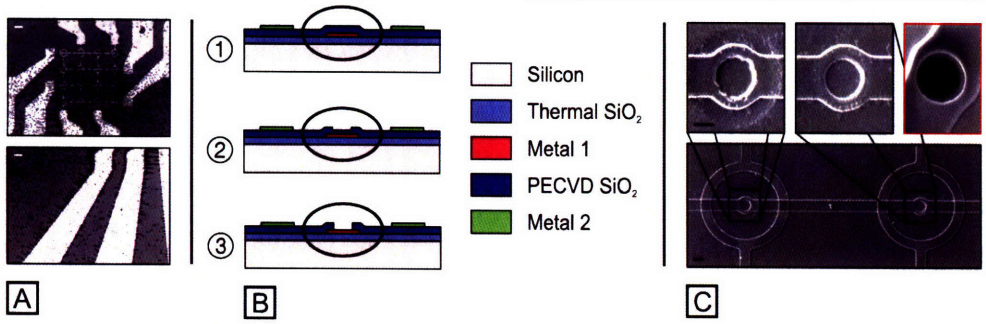

Figure 8: Despite front-end DEP force modeling efforts in the design of my "ring-dot" cell trapping geometries, using silver-coated polystyrene test beads, the loading response did not match well with anticipated behaviors. Rather than localizing to central "dot" regions in each trap, beads migrated to the edges of all on-chip electrodes and in some cases develop "pearl-chain" linkages between on-chip conductive traces **(A)**. (Scale bars ≈80 μm.) The suspected cause of this behavior was ill-patterned "dots" resulting from ineffective PECVD oxide etch sequences **(B)**. Though we aimed to expose the underlying Metal 1 layer **(3)**, reaching such an endpoint often proved elusive **(2)**. Even subject to uncoated SEM imaging **(C red outline)** the central "dots" in non-functional traps appeared etched and did not display anticipated charging effects. (Scale bar in the enlarged image ≈5 μm. Scale bar in the perspective image ≈10 μm.)

The suspected cause of such response dynamics centered on challenges faced in detecting an endpoint during our IMD etch sequences. While in-fab optical microscopy surveys showed, what seemed to be, properly formed central "dots", in reality it was likely that a partial etching, as highlighted in Figure 8B-2, more adequately described the device profile. Suspicious that the underlying metal layer was not being exposed to enable electric field communication between the "ring" and the "dot" I opted to examine a non-functional device using scanning electron microscopy (SEM). If a residual insulating oxide layer remained at the central "dot" covering the underlying metal, I anticipated that the electron bombardment used to form SEM images would charge the non-conductor such that it would image as a bright white patch. (Normally one coats SEM samples with a thin gold layer just prior to imaging to reduce this effect.) As shown in Figure 8C (red border) even neglecting a gold-coating sample treatment, the central "dots" did not charge and as a result did not produce a bright white signal. This effect was somewhat surprising, but in similar coated-samples (non-red borders) we did witness etch non-uniformities across array footprints. Some samples overetched, and others appeared as one might imagine they should.

Lacking a sound non-destructive (one could imagine actually sectioning the chip and attempting to image from a side-on perspective) metrology-based avenue for determining the cross-sectional profile of the on-chip trap designs, I revisited the idea of simulating "ring-dot" DEP electromechanics. In initial design efforts[124], I utilized a simplified modeling technique that did not include considerations of the on-chip electrical connections. In other words, the manner by

which the "ring" and the "dot" tied into the row- and column-oriented wiring was not a part of the design simulation. In this refocused effort I imagined that by including such effects I might witness different trapping responses. Additionally, all initial modeling efforts patently assumed that the central "dots" were reliably etched to completion, fully exposing the underlying Metal 1 layer. As I show in Figure 9, my revised efforts additionally included considerations of the two extremes for on-chip "dot" etching. In one case no IMD hole is formed and in the other the "dot" exists as desired.

By examining the square of the electric field magnitude ($|E|^2$) 1 μm above the plane of the array for various DEP-relevant frequencies (Figure 9B) (on-chip buffer set to 0.1S/m), we witness a rather remarkable effect. In the case where no IMD hole exists, the dominant DEP trapping occurs as a non-"dot"-specific behavior where cells can localize to the edges of all on-chip electrodes. This circumstance directly echoes the observed experimental results seen during our runs with silver-coated polystyrene beads and lends support to the notion that ineffective "dot" etching was indeed the cause for the particle loading responses seen in our fabricated designs. Even in the case where a proper "dot" exists, at higher frequencies, DEP trapping effects arise around the periphery of the "ring".

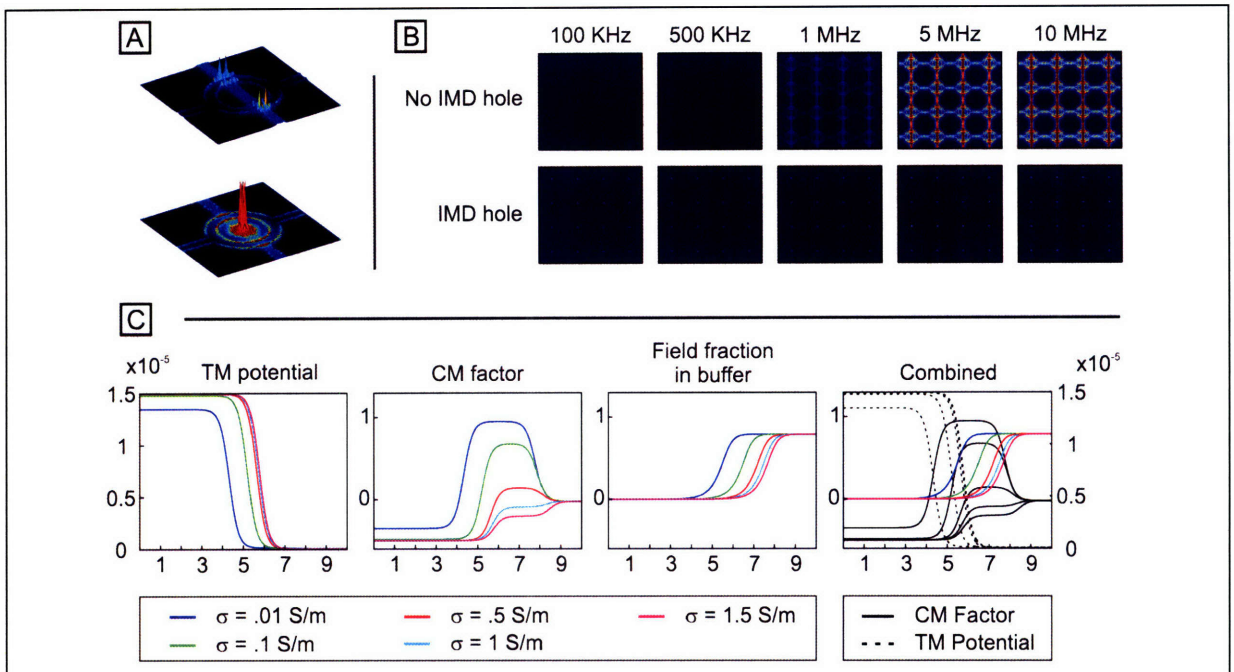

Figure 9: To understand the trapping responses detailed in Figure **8**, I revisited my initial modeling efforts. In the developmental stages, I did not include the interconnect footprints when modeling DEP trapping mechanics. Additionally I always assumed that the central "dot" feature could be effectively etched to the Metal 1 layer. By including interconnects and simultaneously examining the responses of traps with **(A bottom)** and without **(A top)** etched central "dots", I explored the frequency dependent on-chip DEP forcing resulting from fabrication "mishaps" **(B)**. (For each geometry the color maps adopt the dynamic range defaulted for the 1MHz case. Red indicates high values for the square of the magnitude of the electric field while blue indicates low values.) Without effectively etched "dots" dominant DEP forces arise along all electrode edges reflecting the behaviors seen experimentally. By then including the frequency-dependent transfer function describing the fraction of the applied voltage arriving in the on-chip buffer, effective p-DEP trapping faces another consideration beyond concerns pertaining to the induced transmembrane potential and CM factor issues alone **(C)**. (In all plots the x-axis indicates the drive frequency in Hz as a power of ten index - ie. $\times 10^n$ where n is listed on the x-axis.)

The presence of electric fields in non-designated regions witnessed at higher frequencies begged for further consideration of its impact on the potential to safely trap mammalian cells using p-DEP methodologies. In Figure 9C I developed a frequency-dependent template for understanding what factors needed management. As discussed in more expanded detail in my Masters thesis, I provide here a mathematical model for tracking the induced transmembrane voltages that arise for cells positioned within electric fields[125].

$$|V_{tm}| = \frac{1.5|\overline{E}|R}{\sqrt{1+(\omega\tau)^2}} \qquad \textbf{Equation 20}$$

Here V_{tm} equates to the transmembrane potential, R indicates the radius of the cell, and τ represents a system time constant expressed as follows:

$$\tau = \frac{RC_{mem}\left(\rho_{cyto} + \frac{\rho_{media}}{2}\right)}{1+RG_{mem}\left(\rho_{cyto} + \frac{\rho_{media}}{2}\right)} \qquad \textbf{Equation 21}$$

In this relation, C_{mem} and G_{mem} are the respective capacitance and conductance of the cell membrane, while ρ_{cyto} and ρ_{media} describe the electrical resistivity of the cytoplasm and the surrounding culture media.

By examining the transmembrane voltage induced by a normalized field of 1V/m as a function of frequency (see first plot in Figure 9C), we see that as we move to higher and higher frequencies the induced potential drops. Based upon this response, it would thus seem beneficial to always operate at high frequencies when performing DEP manipulations.

We must also consider the real component of the CM factor to bound functional regimes for viable DEP forcing. As shown in the second plot of Figure 9C the CM factor varies non-monotonically with frequency. To exert p-DEP forces (as mandated for holding cells at the central "dots" in our trap configurations) we must operate in frequency ranges where the real component of the CM factor is greater than zero. We therefore need to carefully calibrate our in-system buffer conductivities and remain within a mid-band frequency range spanning, at best, from ~10^4-10^8 Hz.

In my initial work modeling "ring-dot" traps, the transmembrane potential and the CM factor were the sole components considered when mapping out the frequency and conductivity spaces where viable DEP manipulations could occur. Based upon the delocalized field effect witnessed during my attempts to understand the non-ideal trapping effects observed in experimental contexts, I developed a simplified model for an additional component further impacting available cell-compatible device operation regimes. Sparing the details of the formulation (in part because I will develop similar concepts further in Chapter 4) I established a transfer-function-based

description for the fractional component of the applied voltages that produce in-buffer voltage drops for traps lacking a properly patterned central "dot". In general terms, this description amounts the following relation:

$H = \frac{V_{in\_buffer}}{V_{applied}}$	**Equation 22**

I track the magnitude of this expression in the third plot of Figure 9C and we observe that, as in the mappings from Figure 9B, at higher frequencies larger fractions of the applied potential breaches into the on-chip buffer environment. Though this dynamic maps the worst case scenario where an ill-pattern "dot" exists, it highlights the idea that in certain frequency regimes on-chip particles can witness parasitic DEP effects from portions of the array footprint that were not specifically intended to exert manipulative forces. Combining this consideration with transmembrane and CM factor effects owns the potential to highly constrain the viable operation regime for a given design.

With a strong belief that the IMD etching process was failing to expose the underlying Metal 1 layer, I explored an extended variety of options to develop a protocol that could guarantee proper processing. After running a multitude of timed wet etch sequences on sample chips with the Silox Vapox III product, undercutting of the photoresist arose as a dominant issue. To reliably etch to the Metal 1 layer at all "dot" locations meant that some portions of the array became overetched and thus the radii of the "dots" became grossly enlarged. The eventual solution utilized a combined dry and wet etch sequence. After patterning my wafers with a revised AZ9260 thick resist (MicroChemicals, GmbH, Ulm Germany), I used the EML Plasmatherm (Plasma-Therm, Inc., St. Petersburg, FL) etcher delivering 40 sscm HC23 and 5 sscm O_2 to etch individual die for 84 minutes. This sequence preserved the sidewalls of the resist as most of the IMD layer was removed via isotropic processing. I then dipped individual chips into Silox Vapox III for 4.5 minutes to guarantee that the etch had progressed to the underlying metal. Before fully packaging any chip I would then functionally test it by placing a bead suspension onto its top surface and in this state I would apply activating on-chip voltages using micromanipulator affixed probe tips. By observing such setups under a microscope I could monitor whether or not beads in the suspension localized to the on-chip "dots". Devices that could satisfy this end were classified as functional and prepped for further packaging.

Proof-of-concept loading and sorting operations

With a functional process in hand, I revisited my attempts to load 4×4 arrays in single-bead fashion. As shown in Figure 10, properly processed chips enabled the anticipated bead localization at the centers of my on-chip "ring-dot" geometries by performing assays using 0.01 S/m buffers (comprised of 10.25% w/v sucrose/deionized water solutions). Moreover the resultant operational chips provided a means for evaluating the feasibility of non-transistor-dependent row/column site addressability. In Figure 10 I provide the first demonstration of this design flexibility by extracting a diagonal from an initially fully loaded 16-site array[40] (silver-coated polystyrene beads injected as described in the Biological Methods Appendix - "Sample loop injection procedure"). In this five frame depiction, I remove individual beads (yellow circles highlight locations unloaded since the preceding frame) by grounding both the specific

row and the specific column electrodes linked to a given trap. As in-chamber flow progresses over the array, it selectively sweeps away only the targeted particle. This effect arises because the targeted traps present no DEP retention forces for the originally held particle. To contrast, other sites along the same column or row still witness one half of the original in-trap voltage drop and thus experience 1/4 of the original DEP retention forces. As long as the on-chip "1/4 strength" traps are strong enough to overcome drag forces from passing fluid flow they will remain loaded. Since I only turn OFF a single row and a single column at any one time all other sites in the array remain ON and at full strength.

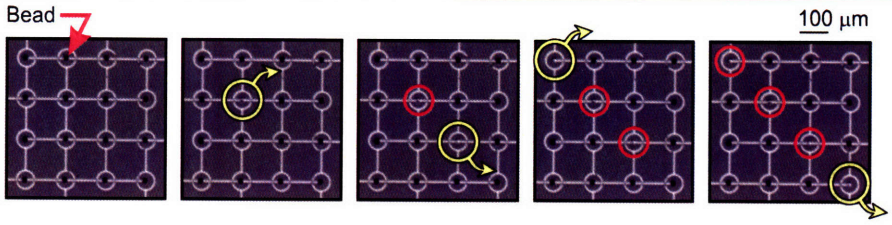

Figure 10: After "debugging" the PECVD oxide etching complication, I produced a functional "ring-dot" 4×4 array. Using silver-coated polystyrene beads, I successfully loaded the device in single-bead fashion and then, using sequential row/column deactivation, extracted all beads along a designated diagonal.

I chose to demonstrate the removal of a diagonal within my sample trapping arrays as an initial test because doing so, highlights a key component of the sorting mechanics associated with this type of addressing. The tradeoff in not including on-chip transistor elements arrives in the fact that most of the sorting operations made possible must occur in serial fashion. In other words, to remove the diagonal, I had to do so one particle at a time. If I had instead attempted to release the entire diagonal in parallel fashion by deactivating all of the row and column electrodes linked to each of the four targeted extraction sites simultaneously I would have inadvertently released every bead in the 16-site array. This response would occur because deactivating the electrodes linked to the four sites along the diagonal would amount to turning OFF all rows and all columns. With no rows or columns active, no on-chip DEP forces exist to hold any of the particles in the array. Despite this limitation, in certain contexts the numbers of particles that one might desire to sort could amount to only a small fraction of the total. In such cases, sequential sorting would not be a strong limitation. Additionally, there are certain patterns that can be extracted using parallelized electrode activation. If, for example, I wanted to simultaneously remove the four corner beads in the array it would be possible to do so.

Targeting cell-based operations

When I first attempted to transition to cell-based operations I confronted two fundamental complicating factors. First, it was unclear whether or not there would be any difference in the cell/array interactions for assays reliant upon adherent versus suspension culture cells. As show in Figure 11A, over the course of several test runs, it became clear that suspension culture cell lines could exhibit substantially less non-specific binding and typically fouled devices to a much less notable extent. For adherent lines it proved challenging to even load the arrays in single-cell fashion and thus for all subsequent cell-based work I exclusively utilized suspension culture lines.

After determining which cell classes seemed best suited for operations in my p-DEP-reliant devices, a second complication emerged when I attempted to observe site-addressable release.

Though I could readily trap HL60s and other non-adherent cell types in single-cell fashion, they seemed to remain attached in place after loading such that it became impossible to selectively remove targeted cells from the trapping array.

All microfluidic assay environments present high surface-area-to-volume ratios. If there is a given probability that interactions between a unit footprint of surface area and in-system particulates (biological, chemical, or otherwise) will result in an adsorption response, then within such contexts the propensity for witnessing such effects grows substantially since a given particulate has far more opportunities to interact with a surrounding surface. As a result, effectively managing and mitigating the adhesion of proteins and other biomolecules becomes a central focus for essentially all efforts in the microfluidic setting. By exerting p-DEP forces that could trap cells at the central "dots", I was seemingly enhancing the cell/surface interactions to an extent that they became bound in place. Circumventing this difficulty became a rather protracted enterprise.

The most basic approach to minimizing surface interactions typically involves the flow-based delivery of bovine serum albumin (BSA) to on-chip surfaces. This strategy coats the device surfaces with a protein that, not unlike proteins found internal to the body for preventing organ fusion, ideally presents a repellant surface to subsequent impinging biomolecules. Unfortunately, this fairly standardized technique, which typically amounts to flushing 1% BSA solutions (in either PBS or deionized water) through a system flow chamber for 1 hour or more timespans, failed to successfully address these release-related complications.

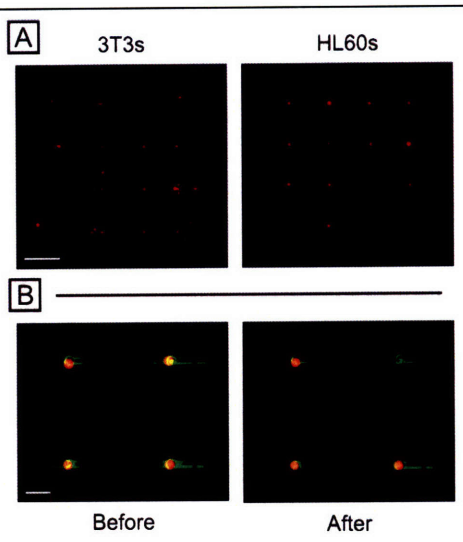

Figure 11: In cell-based efforts, non-adherent HL60s demonstrated reduced non specific binding **(A)** and loaded effectively as single-cells when compared to adherent lines. The challenge for sorting applications then centered on effective release following capture. Using PLL-g-PEG (shown in **(B)** via GFP) surface treatments I did witness small-scale release behaviors, but such work did not enable reliable release across arrays. (Scale bar in A ≈120 μm. Scale bar in B ≈40 μm.)

Beyond BSA-based efforts, perhaps the second most commonplace surface passivation method relies upon poly(ethylene glycol) (PEG) treatments[126-128]. PEG readily adsorbs to hydrophobic surfaces and acts as a water-binding hydrogel-like brush that prevents non-specific binding. Its protein resistant properties are highly dependent upon the length, flexibility, and density of chains which are often modified to exhibit specific behaviors. One of the more common forms of the polymer is its tri-block polyethyleneoxy-polyoxypropylene-polyethyleneoxy form sold commercially as Pluronic (BASF GmbH, Germany). The primary molecular mechanisms producing protein resistance for such molecules are not fully understood, but steric repulsions associated with the brush structures and hydration shells around the PEG moities are believed to be the dominating contributors. I too attempted to use various forms of Pluronic (F108 and F127) to remedy the release complications in my devices by performing such routines as flushing my

device surfaces with 1% w/v solutions (in deionized water) for spans of 1 hour. Despite numerous runs, trapped cells remained firmly in place following capture. Additionally, since Pluronic best adsorbs to hydrophobic surfaces I typically relied upon silane pretreatments for my devices (either via 10 second submersions in a 5% dimethyl dichlorosilane in dichlorobenzene[129] or via 24-hour vapor phase exposure to tridecafluoro-1,1,2,2-tetrahydrooctyl-1-trichlorosilane[24]). These treatments often attacked on-chip electrodes in detrimental ways[130, 131].

In my hands, the most promising PEG-based option, as presented in Figure 11B, leveraged a poly-L-lysine-g-poly(ethylene glycol) (PLL-g-PEG) construct[132-135] (Susos AG, Dübendorf, Switzerland) (the version shown has an added fluorescent tag to enable visualization on targeted surfaces). This grafted PEG formulation does not demand hydrophobic surfaces for adsorption and thus bypasses the complications that arose for many silane-based surface pretreatments. The PLL component directly links to the in-chip surface and leaves a PEG chain pointing outward that effectively hinders subsequent protein attachment. I explored this option for surface treatment by soaking device surfaces for 1 hour in 1% w/v solutions of PLL-g-PEG in phosphate buffered saline. As shown in Figure 11B, the upper right-hand trap in the 2×2 array successfully rendered a release. Though I was successful in sorting cells from arrays with this approach, it never proved to be a reliable strategy and as such I could never produce images where I extracted more than a few cells from a given loaded configuration.

In light of my limited success with adsorbed surface chemistry treatments for aiding release mechanics, my work demanded a more reliable and robust avenue for enabling effective site addressing and sorting. After scouring the literature, I discovered the common theme of deposited silicon nitride surfaces as a potential avenue for serving my needs. In various neuronal growth and cell-in-device technologies[136, 137] such films seemed to display an enhanced propensity beyond adsorption treatments for eliminating undesired binding effects. In short, after calibrating a nitride deposition of 250 Å (dies processed individually - bond pads protected by covering with glass coverslips - See Fabrication Methods Appendix - "Functional 2-level metal non-via-based process for p-DEP trap fabrication") and flushing my devices with a 1% Bovine Serum Albumin solution (in deionized water) for 30 minutes prior to on-chip assays, I produced functional cell-manipulation chips

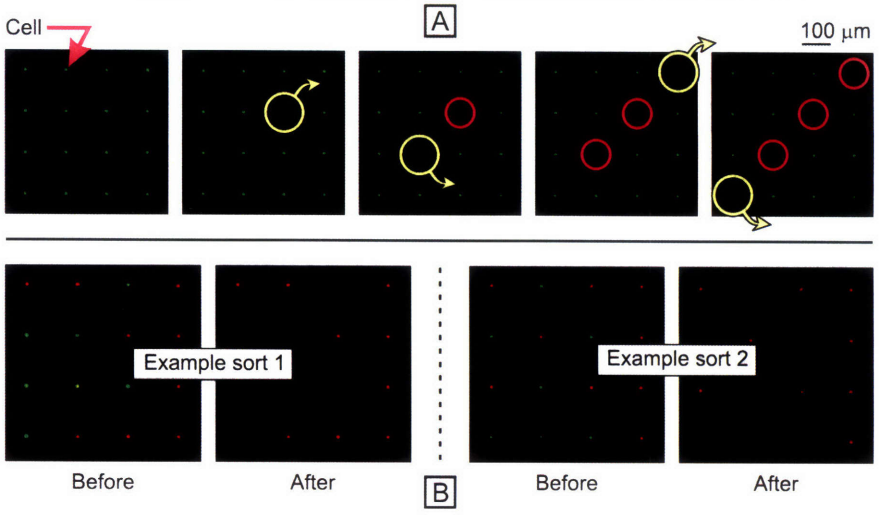

Figure 12: After successfully incorporating deposited nitride films as an end-point in my fabrication process row/column release for cells became feasible **(A)**. As a basic assay I then stained two independent cell populations, loaded them into my device, and sorted our targeted subpopulations **(B)**.

with effective site addressing capabilities.

As shown in Figure 12, I was successfully mirrored the bead-based extraction of a diagonal and furthermore demonstrated an image-based sort from an array originally loaded with two distinct cell populations[40]. In these sorting routines I used whole-cell CellTracker stains to color separate populations of HL60s either red or green. I then mixed the two cell populations and ported them onto my in-chip arrays (See Biological Methods Appendix for "CellTracker staining procedures", "Passaging techniques", and again "Sample loop injection procedures"). Because the initial loading sequence for row/column-linked arrays involves the activation of all sites, the organization of individual cells subpopulations within the array occurs subject to chance. In my assays, I therefore saw a variety of different red and green cell patterns emerge when loading my devices. The specifics of an initial pattern were not important since the basis for the designs was to selectively sort individual cells located anywhere on the chip using image based analyses. In the two presented assays in Figure 12B I elected to release only the green-dyed cells. Admittedly, since the sort shown only separated cells on the basis of a whole-cell response, an equivalent and faster sort could have been done using FACS methods. This simple demonstration simply aimed to show that it would be feasible to parse cell targeted subpopulations using imaging as a high-resolution detection means. Thus, though I did not demonstrate it here, I could have just as easily separated two groupings of cells on the basis of distinct internal protein localizations, unique secretion responses, or even on the basis of whole-cell morphology. All of these avenues would challenge the flexibility of even the most sophisticated FACS sorters.

Complications in need of consideration for on-going efforts

Despite the remarkable success in demonstrating the feasibility of engineering a cell manipulation and sorting device leveraging non-transistor-dependent row/column site addressing techniques several residual system complexities remained. As I outline in Figure 13, such effects owned the potential to confounded progressions toward designs dedicated to expanded imaging and sorting efforts.

Related to fabrication, two dominant issues demanded further attention. First, despite the significant effort involved in rendering a functional IMD etch protocol for proper "dot" formation it lacked a general robustness that prevented attempts toward full-wafer processing. Its finicky nature demanded that I individually treat and process individual device chips one at a time and even take the pains of placing coverslips over the bond pads along die edges to avoid coating the bond pads with an insulator. I needed a reliable in-process metric for detecting when the "dots" had been etched to completion. Initial thoughts as shown in Figure 13A&B adopted two distinct yet compatible approaches. In one case, I envisioned placing sizeable test features onto my wafers that would present layered Metal 1, IMD, and Metal 2 stacks. These designs would include a multitude of "dot" features that when etched to completion would shift the impedance response measured at the affiliate bond pads. Initial attempts to measure such shifts across row and column components on my initial chip set did not produce a overtly dramatic readout, but I imagined it might be possible to design a dedicated on-chip feature that would in fact provide a stark thru verses not-thru comparison.

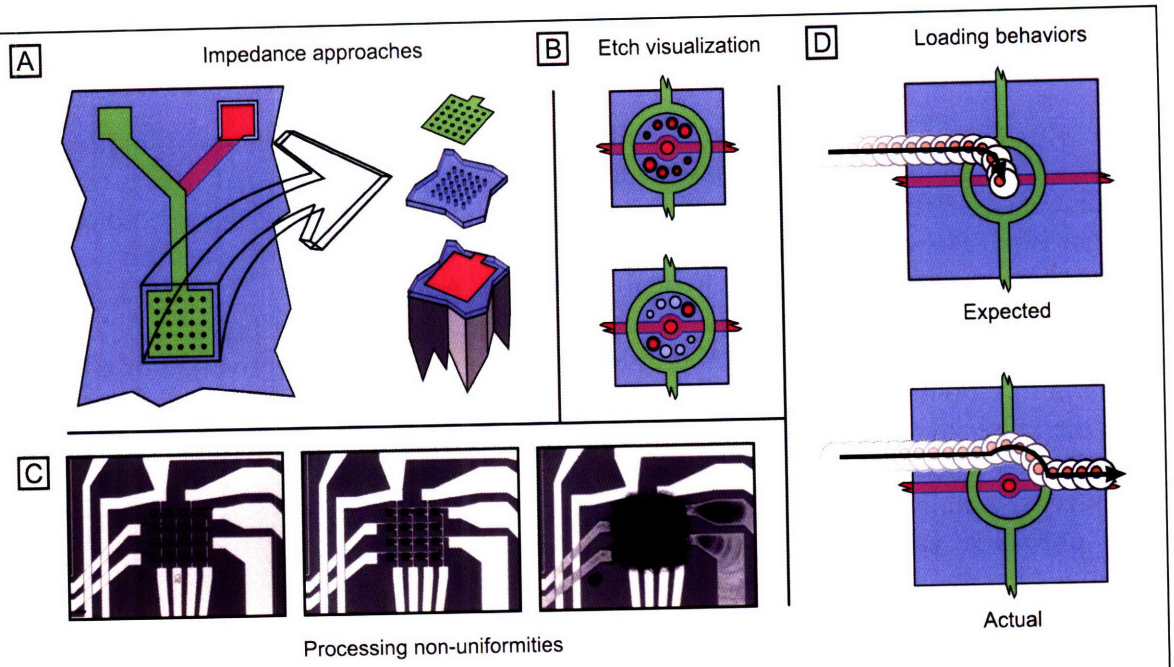

Figure 13: Despite developing a process for functional array manufacture, in future designs I envisioned possibilities for better detecting the endpoint in the PECVD oxide etch step. One consideration was to include a set of "spatula-like" electrodes separated by a series of "dot" features in an interleaved oxide **(A)**. In cases where the "dots" etched through to the Metal 1 layer I could potentially witness a measurable on-chip impedance change. Another thought was to include a more visual marker **(B)**. By including successively smaller and smaller Metal 1 "dot" features near the functional central "dot" in the DEP traps, I imagined I could watch the smallest features etch away (due to undercutting) until it was known that the central "dots" were exposed and thus functional. Despite these envisioned improvements in on-going work, the processing non-uniformities across etched chips and subsequent runs suggested that continued complications would arise **(C)** (Scale bar $\approx$50 μm.). Additionally, the loading behaviors during many observed experimental runs highlighted another need for revised designs **(D)**. I expected that any particle in close proximity to the central "dot" would trap at a given "pixel" unfortunately, the outer "ring" often served to deflect incoming particles around the traps thereby hindering or even preventing site loading.

Additionally (see Figure 13B), I imagined including a better visual readout where I could use a series of on-chip "dots" (in the Metal 1 layer) with gradually decreasing radii. The idea was that smaller "dots" in the Metal 1 layer would be attacked more aggressively since less surface area needed to be eroded before they became damaged. As a result, I could visually inspect the chips and stop etching after the small features had been damaged but before those matching the sizes of functional central "dots" became impacted. Unfortunately though both of these techniques might have helped the situation in on-going work, the overall processing uniformity across runs and even across individual dies (see Figure 13C) posed serious challenges.

During functional tests with both beads and mammalian cells an additional unanticipated response emerged (see Figure 13D). Based upon initial modeling efforts, I expected that any particle approaching a "ring-dot" structure would trap at the central "dot" location. Unfortunately, I often observed cells approach a trap; meander around the outer ring; and completely bypass the on-chip "pixels" without providing a capture response. In effect, the outer "ring" that helped provide the spatially non-uniform on-chip field needed for DEP trapping, was

instead encouraging cells to do anything but hold in place. Tackling this oddity and the process-related concerns detailed earlier in this section will be a major focus of Chapter 3.

An alternative n-DEP-reliant "pixel" design

Though I will avoid an extended discussion here, my Masters thesis provides enhanced details describing design considerations that enabled the manufacture of a series of n-DEP-reliant "pixel" implementations on wafers sharing the p-DEP "ring-dot" configurations (See Fabrication Methods Appendix - "Original 2-level metal non-via-based process for wafers presenting p- and n-DEP designs" for a comprehensive outlay of this fabrication sequence). In a step following the patterning of the Metal 2 layer, I selectively etched (using Bosch-style methods) wells into the silicon substrate at key locations to render an alternate cell-trap design as detailed in Figure 14. These n-DEP-based designs presented cell-sized wells flanked at their top edges by a set of row- and column-connected oppositely polarized electrodes.

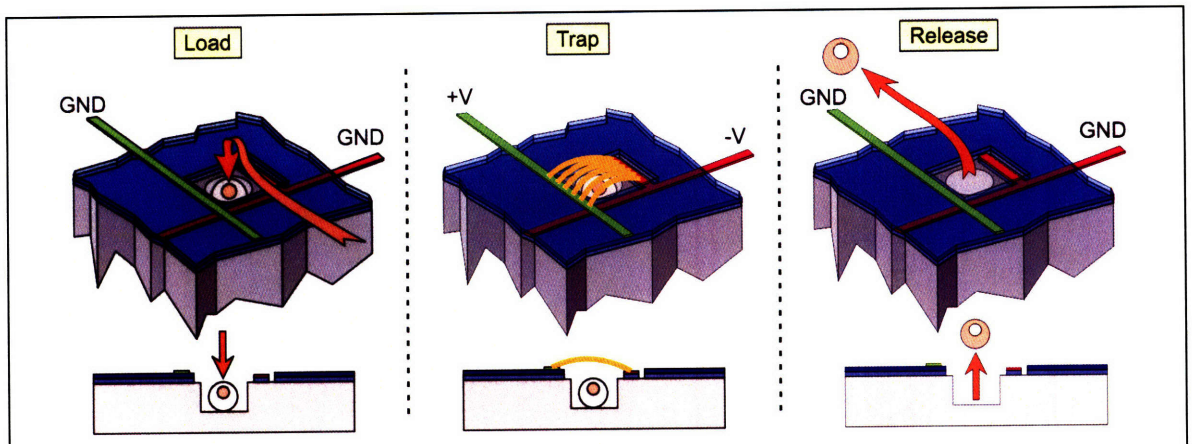

Figure 14: Our n-DEP "pixel" geometries attempted to utilize wells to contain individual cells. These wells would load by introducing cells into an overriding fluid flow from which settling could occur **(A)**. Cells would remain held inside the wells by activating flanking row- and column-connected electrodes that could establish DEP trapping "lids". Like the p-DEP configuration, release would occur via row/column site deactivation and the introduction of an overriding fluid flow that could "pry" targeted cells out of the array.

The envisioned operation of such designs involved first filling an array of the wells with single cells via on-chip fluid flow. The cells would settle, via gravitational effects and halted fluid flow, into the wells. To hold the cells in place, I would then activate all on-chip electrodes to establish DEP barriers that would exert downward forces on the in-well cells. This downward DEP forcing would arise because on-chip buffers would amount to high-conductivity cell culture media and the highest in-system electric fields would exist over the top opening of the wells. Cells under such conditions would be pushed down the field gradient such that they would experience downward retention forces. With such forces in place, I could activate on-chip flows once again to sweep untrapped cells out of the array. With a fully loaded chip I could then use row/column addressing tactics, identical to those demonstrated with my "ring-dot" geometries, to selectively deactivate target sites and hopefully sweep individual cells out of the array. I thus hoped to provide an array-based single-cell manipulation platform with site addressability that could operate with standard, high-conductivity, cell media.

Challenges in rendering functional n-DEP traps

I successfully fabricated a number of such designs and, as is the first step for many cell-based platforms, began testing their responses using bead assays. As I highlight in Figure 15, during such performance evaluations, two distinct complications arose. On the one hand, for particles sized below a certain threshold it was common to load multiple beads into each on-chip well. To try and gauge which well diameters would best minimize this effect for cell-based work, I used a suspension of NIH 3T3 (ATCC, Manassas, VA) fibroblasts to test a sample chip that presented multiple wells with diameters ranging in size from 10-50 μm. (The Biological Methods Appendix provides details pertainent to all cell culture media types used in my doctoral studies as well as handling techniques for both suspension and adherent lines. See subsections entitled "Standard cell culture medias" and "Passaging techniques" among others.) As I show in plotted form in Appendix 1, wells with diameters in the 25-30 μm range demonstrated a preference for loading individual 3T3 cells (black bars) as compared either two (red bars) or three (white bars) cells. Admittedly I only performed this assay once and therefore cannot provide a strong empirical indicator of the reliability of this cut-off response. As many cell types own unique sizes, the ideal well diameter for a given line could additionally vary.

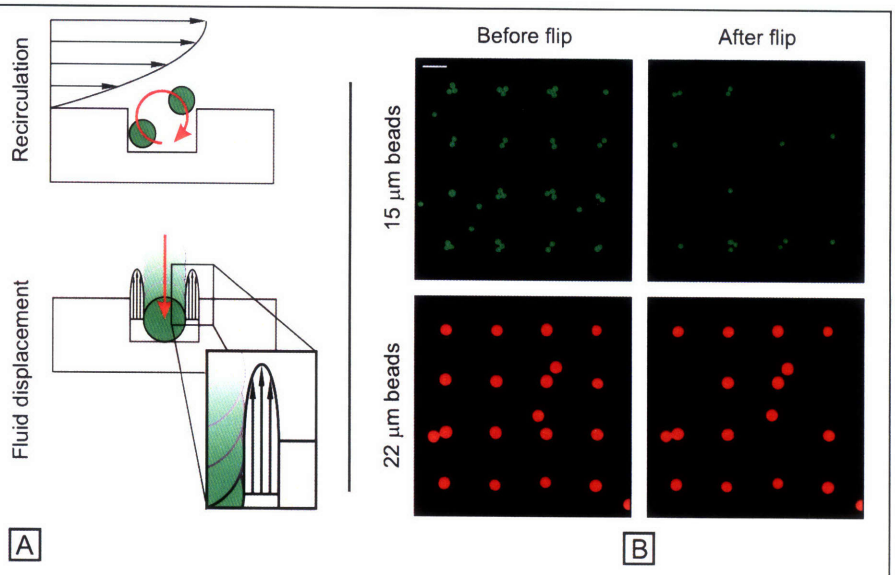

Figure 15: Two primary complications arose when testing my n-DEP trap designs **(A)**. In cases where loaded particles were substantial smaller than the retention wells it often occurred that multiple particles loaded and when they were targeted for release they simply recirculated in the well instead of sweeping out of the array (top). Alternatively, particles with sizes more closely matching the wells were slow to displace the in-well fluid and as a result remained in the wells via vacuum-like mechanics during release efforts. To remedy these challenges I attempted to turn the chip upside down during release operations such that gravitational effects could assist in unloading **(B)**. Unfortunately, such routines typically extracted additional particles beyond those specified. (Scale bar ≈60 μm.)

The second complication linked to the bead assays performed in this evaluation stemmed from challenges associated with effectively unloading targeted sites within the arrays. Though I could fairly routinely produce a fully loaded chip using our standard particle injection protocols (See Biological Methods Appendix), when I attempted to deactivate the row and column electrodes associated with an individual "pixel" and then ramp on-chip fluid flow, it proved exceptionally challenging to release held particles. In cases where many particles filled the on-chip wells, it was common to witness a recirculating effect within the well where beads rotated and translated in loops without ever reliably cascading out of the array. Beads sized comparable to the well diameter would regularly produce single-bead loading, but particles remained within the wells nearly unaffected by the overriding fluid flow.

As a cursory attempt to offset this challenge (see Figure 15B), I ran functional sorting tests where after deactivating targeted sites I would physically turn my devices upside down in an effort to use gravitational forces to aid release mechanics. In a vast majority such runs, I could generally unload the targeted cell of interest, but the handling required for such exercises typically caused other off-target sites to unload. Even if this release routine had proven functional, it did not lend itself to scaling efforts that would necessitate turning the chip upside down numerous times. Additionally by pulling the chip off from the microscope stage to perform such protocols, handling on-chip cells, at least momentarily, became a "blind" routine.

For beads displaying larger diameters, a squeezed-film damping-like response appeared to play a pivotal role in challenges associated with targetted site release. With dimensions comparable to the well diameters, loading operations meant that displacing in-trap fluids would require escaping liquids to pass through the narrow gap between the particle and the well edge. As such, once beads of this type settled into place, they faced substantial resistance to forces motivating extraction efforts. Extracting targeted particles out of such wells would mean that an equal volume of liquid would need to fill its place and the only avenue for its delivery was again through the small gap separating the particle from the well edge.

To highlight this effect from a generalized standpoint, we can consider a few basics related to a discipline known as near-field lubrication theory. This discipline specifically focuses upon the interactions and forcing mechanics that describe the motions of closely spaced solid particles submerged in surrounding fluids. For a submerged spherical body of known radius, the following relation presents a generalized description of the in-axis force needed to translate with respect to an in-fluid wall[138].

$$F = 8\pi\mu u R \sinh\alpha \sum_{n=1}^{\infty} \frac{n(n+1)}{(2n-1)(2n+3)} \left[\frac{2\sinh(2n+1)\alpha + (2n+1)\sinh 2\alpha}{4\sinh^2\left(n+\frac{1}{2}\right)\alpha - (2n+1)^2 \sinh^2\alpha} - 1 \right] \qquad \textbf{Equation 23}$$

Here $\alpha = \cosh^{-1}\left(\frac{z}{R}\right)$, where z represents the distance between the particle midpoint and the in-fluid plane surface. We can reduce an alternative matrix-based formulation[139] describing the forces necessary to move individual spherical bodies within colloidal suspensions by examining

the case of two spherical bodies of radii R and R' with an affiliate edge-to-edge axial distance of δ as follows:

$F = \frac{-6\pi\mu(RR')^2}{(R+R')^2} \cdot \frac{u}{\delta}$	**Equation 24**

Here again, u denotes the rate at which the two particles are separated or forced together. In the limiting case where $R' \to \infty$ (a mimic of the plane wall case explicitly accounted for in Equation 23), we obtain the following expression:

$F = \frac{-6\pi\mu R^2 u}{\delta}$	**Equation 25**

This equation describes the force needed to either push a particle toward or pull it away from a neighboring flat surface. As is seen by the presence of the δ in the denominator, for short separation distances, the force magnitude becomes substantial. While this relation does not fully describe the geometry of my n-DEP wells, it does provide a conservative and holistic motivation for the near-field effects seen during device testing. If we were to include additional tangential frictional forcing terms to characterize the presence of wall effects in the wells of my n-DEP designs, we would face even more substantial hydrodynamic challenges to releasing prescribed in-array particles.

Well design modifications to aid n-DEP "pixel" performance

With their affiliate complications presenting a roadblock for continued array-based assays, I attempted to reconsider design options for implementing well topologies that might render functional n-DEP "pixels". The primary challenge with the original n-DEP designs was the lack of proper simulation tools for determining whether or not given geometries would operate as desired. Unlike the p-DEP "ring-dot" traps which use creeping flows to exert near-wall compensated Stokes drag forces[140, 141] (detailed in Equation 26) on in-array particles, the flow mechanics of the well-based n-DEP designs are much more complex.

$F = \Omega 6\pi\mu R\dot{\gamma} z = \Omega 6\pi\mu R\left(\frac{6Q}{h^2 w}\right) z$ where: Ω = a non-dimensional factor accounting for wall effects $\dot{\gamma}$ = the shear rate at the wall in a parallel plate flow chamber Q = the flow rate h = the flow chamber height w = the flow chamber cross-sectional width	**Equation 26**

Unfortunately, considering such effects was not something easily adapted to the coding originally developed for analyzing in-system DEP forces. As a result, interactions between the

localized flow within the wells and the particles contained therein were not accounted for, which meant that we had few avenues for fully understanding device function prior to manufacture.

Because on-chip flows failed to release deactivated on-chip sites, I envisioned the possibility of including "finger"-like constructs on the upstream sides of all cell-trapping wells. As I show in Figure 16, the basic footprint of such design would operate such that the front-side "finger" would be too narrow to serve as a location where cells might settle. This "finger"-like extension

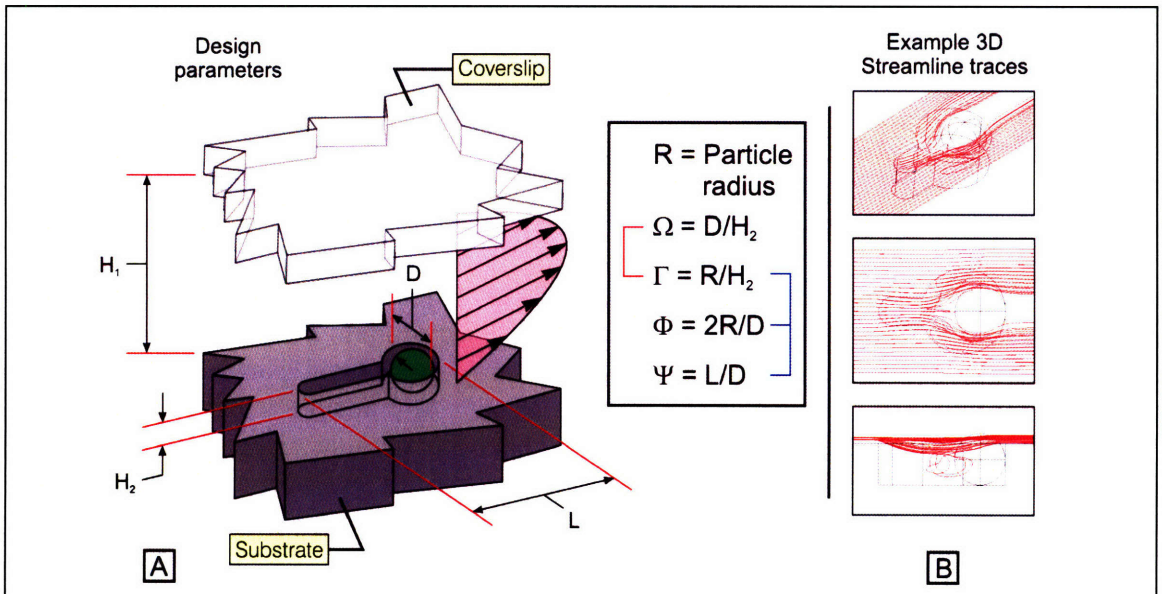

Figure 16: To remedy the challenges associated with release efforts in the originally designed n-DEP "pixel" geometries, I proposed the inclusion of etched "fingers" on the "windward" side of the wells. To analyze such features I developed a crude model with several key non-dimensional parameters **(A)**. The idea was that the front-side "finger" would be too narrow for cells but it would allow streamlines to enter the well and potentially unload retained particles more readily than a simple well configuration **(B)**.

would simply serve to allow streamlines to enter the well sooner than in cases lacking such features and provide an enhanced opportunity for overriding fluid flows to motivate targeted addressable particle extractions.

As a partial surrogate for an admitted lack of simulation-based resources, I attempted to develop a rudimentary numerical analyses technique for better understanding flow mechanics within such structures. To prepare for such modeling work, I developed a suite of non-dimensional terms (as listed explicitly in Figure 16A) to describe key features of the well designs. The basic sequence used for analyzing well behaviors relied upon the COMSOL (Burlington, MA) multiphysics environment to evaluate the Navier-Stokes equation for various presented designs. After running such simulations to completion, I would then integrate the total drag forces acting upon particles positioned within the well and subsequently examine both their magnitude and their phase.

To calibrate this model, I first examined 2D representations of basic (no "finger"-like extensions) well geometries and varied either their Ω or their Γ descriptors (see Appendix 1 for example geometries and on-particle force relations). For all cases, I set the flow chamber height H_1 to

250 μm, the flow chamber width to 4 mm, and positioned in-well particles at either a center or edge location. I used these two distinct cell positions to evaluate the behaviors of the designs, because there is no unique location within the trap where particles are forced to localize. They could essentially settle anywhere and therefore by examining two example locations I hoped to obtain what would be a more complete understanding of the trap response. In truth table fashion (again see Appendix 1), I hoped that I could then determine by virtue of a combined center and edge response matrix the likely behavioral mechanics of individual particle-well pairings. If the integrated drag forces for both positions presented positive phase values (ie. pointing above the horizontal) then I could score the particle-well pairing as likely to produce a release response. If, on the other hand, the integrated drag forces for the center and edge locations both returned negative phase values (ie. pointing below the horizontal) then I could rank the particle-well pairing as unlikely to produce a release dynamic. For cases where one position produced a positive phase and the other produced a negative forcing phase the resultant behavior could be scored as unknown or indeterminate.

For the sake of completeness, I provide a full set of the 2D responses in Appendix 1. For cases where Γ is held constant at 0.5 and Ω is increased, we witness a monotonically rising (as indicated by the phase values for both center and edge positioned particles) propensity for extraction. Alternatively, for cases where Ω is held stable at 3 and Γ is elevated, we too see a generally increasing (though non-monotonic) preference for particle extraction. Both of these test runs agree with intuition. As we increase the diameter of the well for a given particle size it does seem likely that streamlines could more effectively sweep in and dislodge loaded particles; and as we increase the size of the particle for a fixed well size it too seems likely that extractions would become more probable as streamlines would gain enhanced access to the underside of the contained particle.

With these 2D results in hand, I began a series of 3D simulations to try and evaluate the behaviors of wells patterned with "finger"-like extensions. I examined a variety of different designs (see the top of) but eventually settled upon the designs presented in explicit detail in Figure 16. I made this decision from a practicality standpoint. The designs encouraged single-particle trapping and they were both aesthetically pleasing geometrically and straightforward to draw in AutoCAD. Again I examined both center and edge positioned particles. I present the full set of simulation results in Appendix 2. In one case, I varied ψ while pinning Φ at 0.6 and Γ at 0.5. In another, I varied Φ while setting ψ to 1.5 and Γ 0.5. Finally, I examined changes in Γ after setting ψ to 1.5 and Φ to 0.6. Sparing the details in written form, I did find combinations of different designs that suggested including "finger"-like extensions in the well designs could motivate enhanced particle extractions.

To attempt to validate and further explore these simulation-based results, I fabricated a sample series of wafers (etched 20-μm-deep wells in a silicon substrate with no on-chip electrodes - See Fabrication Methods Appendix "Etching recipes: STSHAL-A" and steps 30-34 in "Original 2-level metal non-via-based process for wafers presenting p- and n-DEP designs") to functionally test the empirical performance of various "finger"-based well revisions. In Figure 17 I offer results gathered from three separate runs on one of the sample chips where I first saturated its surface with suspensions of 20-μm-diameter polystyrene beads (in 1% Triton X-100 solutions in DI) and subsequently flushed out the on-chip flow chamber (cross-sectional dimensions: 250 μm high × 4 mm wide) using a syringe pump (10 μL/min for a span of 40 minutes). I imaged the chip surfaces and then assessed what percentage of each well type remained filled with one or more polystyrene beads. In many cases statistically significant differences (as evaluated by Student's t-test) in the filling percentages arose when comparing wells with "finger"-like additions to control cases without such features. It was not uncommon to find that, as desired, wells with additions tended to retain beads less effectively than simple cylindrical wells. In other words, one could conclude that the "finger"-based well revisions were, at least to some extent, enhancing the potential to use bulk on-chip flows as a means for extracting targeted particles from array "pixel" sites and that it might further be possible to develop an n-DEP-based sorting platform reliant upon such topologies.

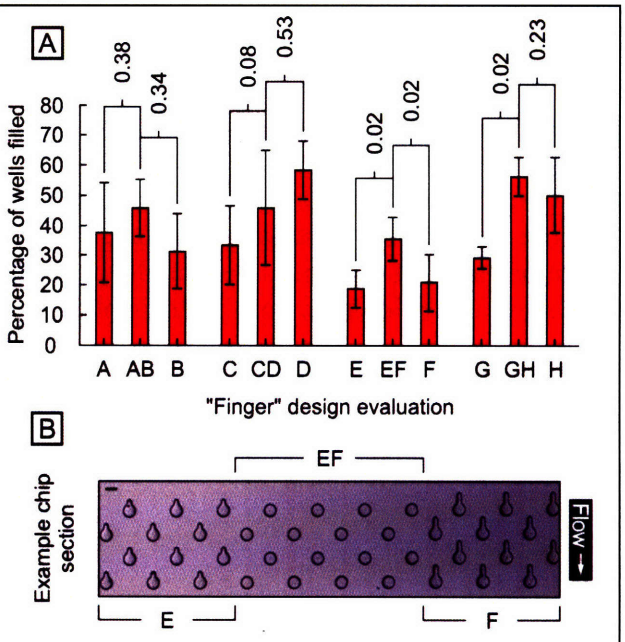

Figure 17: In functional tests of "finger" performance I observed, in many cases, a significant improvement in unloading responses when compared to control well geometries **(A)**. Bars labeled with a single letter indicate a specific "finger" geometry and those labeled with two letters denote the comparative control geometry. (Student t-test values provided). In **(B)**, I highlight an example section from one of the test chips. (Scale bar ≈30 μm.)

Though these experimental results were quite encouraging, I did not develop this type of trap geometry any further. Lacking a complete description of the in-system flows still left me without a true means for gaining *a priori* knowledge of its behaviors before fabrication. Several doctoral dissertations recently emerging from the Massachusetts Institute of Technology have made dedicated efforts to develop modeling tools to aid in understanding the mechanics of complex flows similar to those found in my n-DEP-based well style architectures. Using a variety of techniques including immersed boundary solvers[142] (which work well for 2D cases but have proven challenging to implement efficiently for 3D cases) and Green's function evaluations of the Navier-Stokes equation[1], there may yet be a way to someday design well-based array "pixels" that would be both functional and reliable. The contributions of some of these modeling efforts will become relevant for other matters discussed further in subsequent chapters.

In this chapter we explored model-based efforts to gain enhanced understandings of process challenges ultimately serving the development of functional p-DEP-based "ring-dot" designs. We used devices of this type to demonstrate small-scale sorting of both silver-coated polystyrene beads and cells. With well-reliant topologies for n-DEP-based manipulations, we explored non-cylindrical footprints, inspired by simple flow-based modeling efforts, to produce empirically-validated improvents of release mechanisms that aimed to serve particle sorting routines. With all of these demonstration efforts (both "ring-dot" and n-DEP well) encapsulated as a single body of work I leave the reader with several successes and several challenges. In the coming chapters the importance of my initial design, development, and experimentation forays will gain enhanced relevance and guide many of the decisions made in ongoing work.

Appendix 1

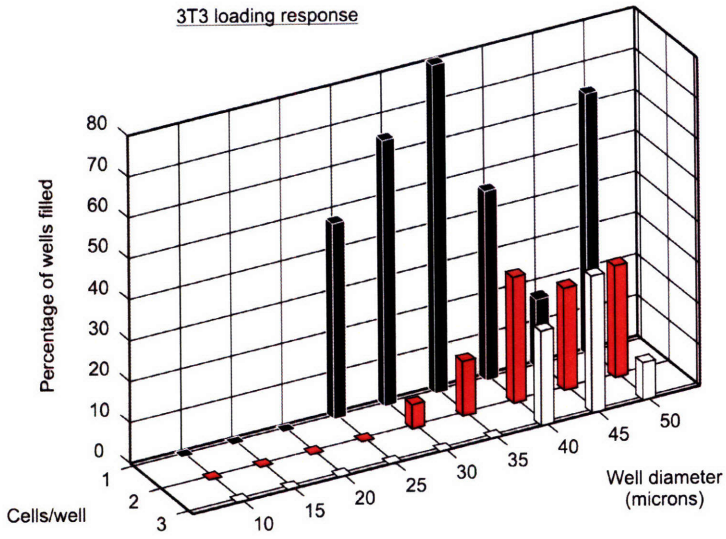

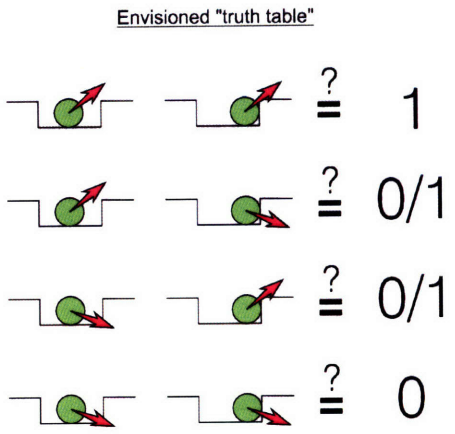

2D simulations

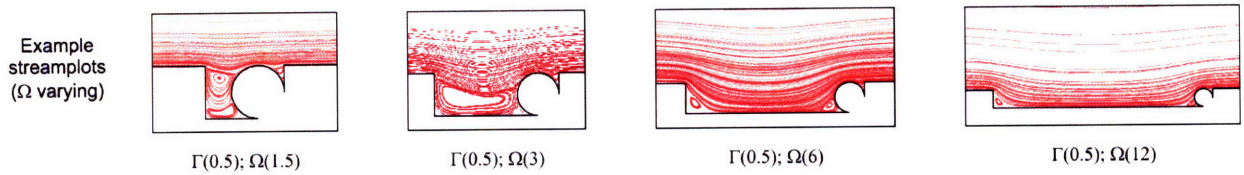

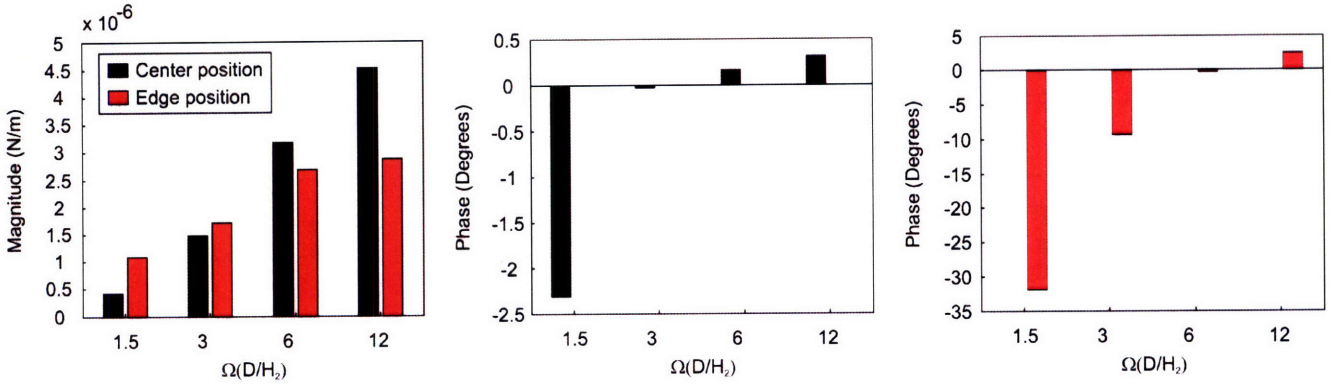

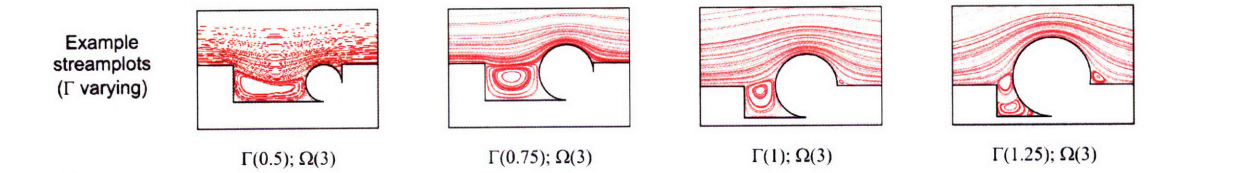

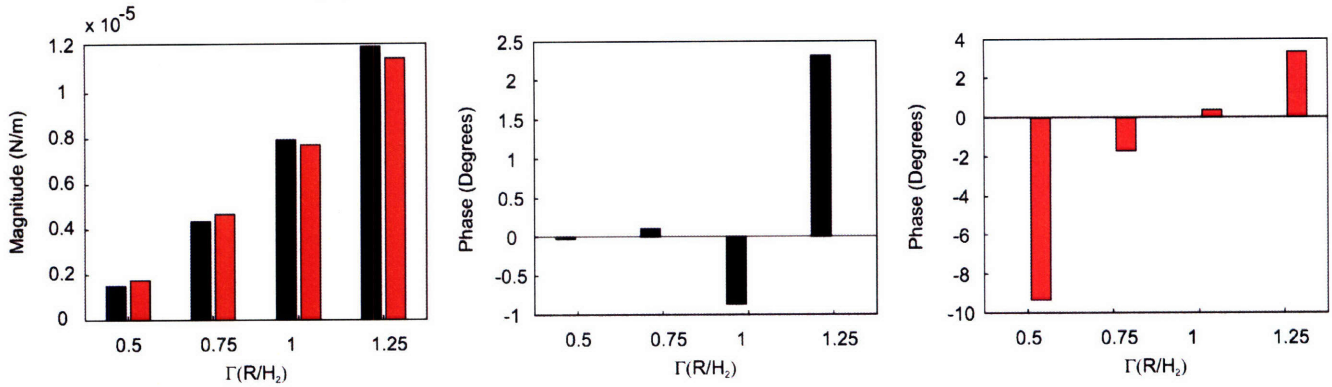

Appendix 2

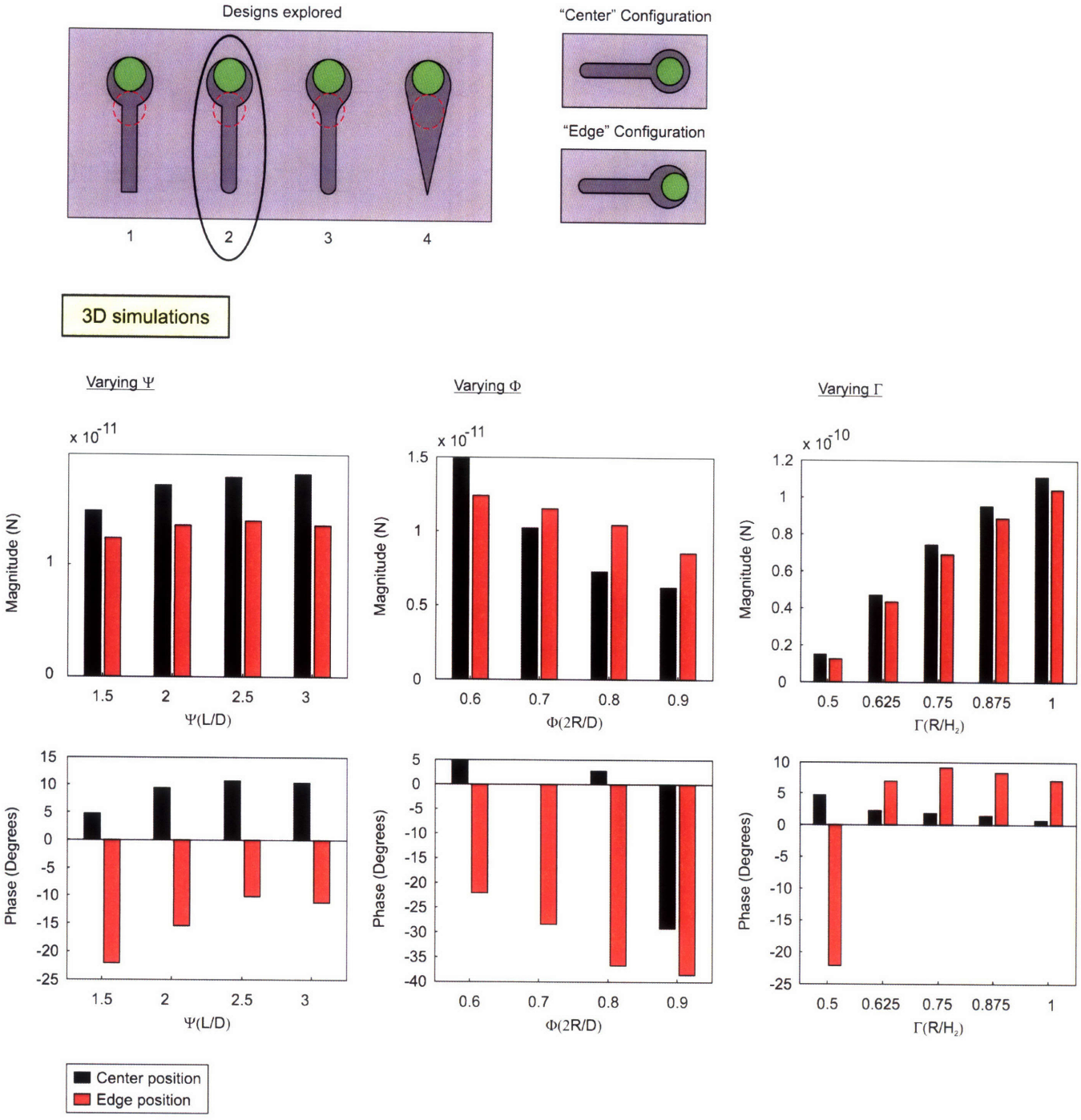
Designs explored
1
2
3
4
"Center" Configuration
"Edge" Configuration
3D simulations
Varying Ψ
Varying Φ
Varying Γ
x 10^-11
x 10^-11
x 10^-10
Magnitude (N)
Phase (Degrees)
Ψ(L/D)
Φ(2R/D)
Γ(R/H2)
Center position
Edge position

Chapter 3: Design considerations for scaled array formats

In the preceding chapter, we were left with a functional p-DEP-based "ring-dot" site-addressable array configuration. Though it yielded a series of useful results, its testing also suggested that efforts to scale toward large array formats could require added attention from a design and planning perspective. In this chapter, I will outline many of the simulation- and process-based efforts undertaken to enable transitions from a basic 16-site setup to designs presenting 400 individual on-chip cell trapping locations.

Shortcomings of the initial p-DEP design modeling work

While the p-DEP "ring-dot" architectures did enable the capture and addressable sorting of individual cells, during loading sequences I often observed incoming cells track around the periphery of the "rings" such that they bypassed the central "dots" (as detailed in Figure 13). Echoing the diagnostic efforts used to understand the non-specific trapping responses emergent from poor IMD etch processing, I too hoped that additional modeling might illuminate details of this unanticipated loading response.

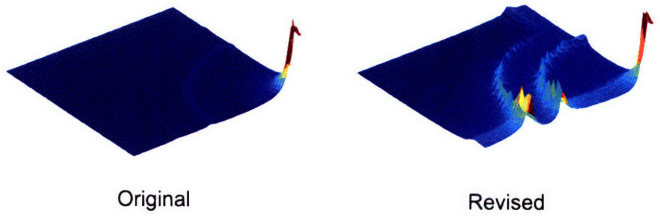

Figure 18: In my initial efforts to model the DEP electromechanics affiliated with "ring-dot" trap configurations, I only included considerations for ideal, isolated "ring" and "dot" structures (left) without including "parasitic" effects tied to the on-chip wiring layout (right). Here, I present 1/4 geometries displaying the square of the magnitude of the electric field ($|E|^2$) 1 μm above the traps.

As mentioned earlier, the initial simulations that led to the development of the "ring-dot" geometries examined a simple outer "ring" and central "dot" without considering details of their electrical connections to off-chip signaling. With this simplified trap configuration (see Figure 18) very little in the name of an electric field gradient existed along the periphery of its footprint. As such, there was no impetus for imagining that p-DEP forcing would dominate at any in-trap location other than the "dot". The major focus of the initial modeling work, then shifted to understanding relationships between the geometries of the "ring" and the "dot" and their subsequent impact upon trapping strength (detailed explicitly in my Masters thesis[124]).

Unfortunately, as experimental results accumulated, it became clear that trap holding strength was just one of several metrics that needed to be evaluated to render a reliable and functional design. By including the on-chip row and column interconnects, a notable distinction between the original modeling work and my revised designs emerged. As shown in Figure 18, this new expanded design, presented field gradients along both the outer "ring" and all edges of the row and column linkages. At locations where traces connected to the "ring" passed above wiring to the "dot" we witnessed especially notable effects. With this revised trap model, I began to image how incoming cells might fail to localize at the central "dot".

Attempts to simulate and remedy loading complications

With the electric field landscape mapped (using AutoCAD (Autodesk, Inc., San Rafael, CA) to generate the geometries and COMSOL to evaluate the electric field solution for a nominal 1V - 1MHz potential applied across the "ring" and the "dot" with an in-system conductivity set to 0.01 S/m), I further examined the original and revised traps using our developed DEP and Stokes flow

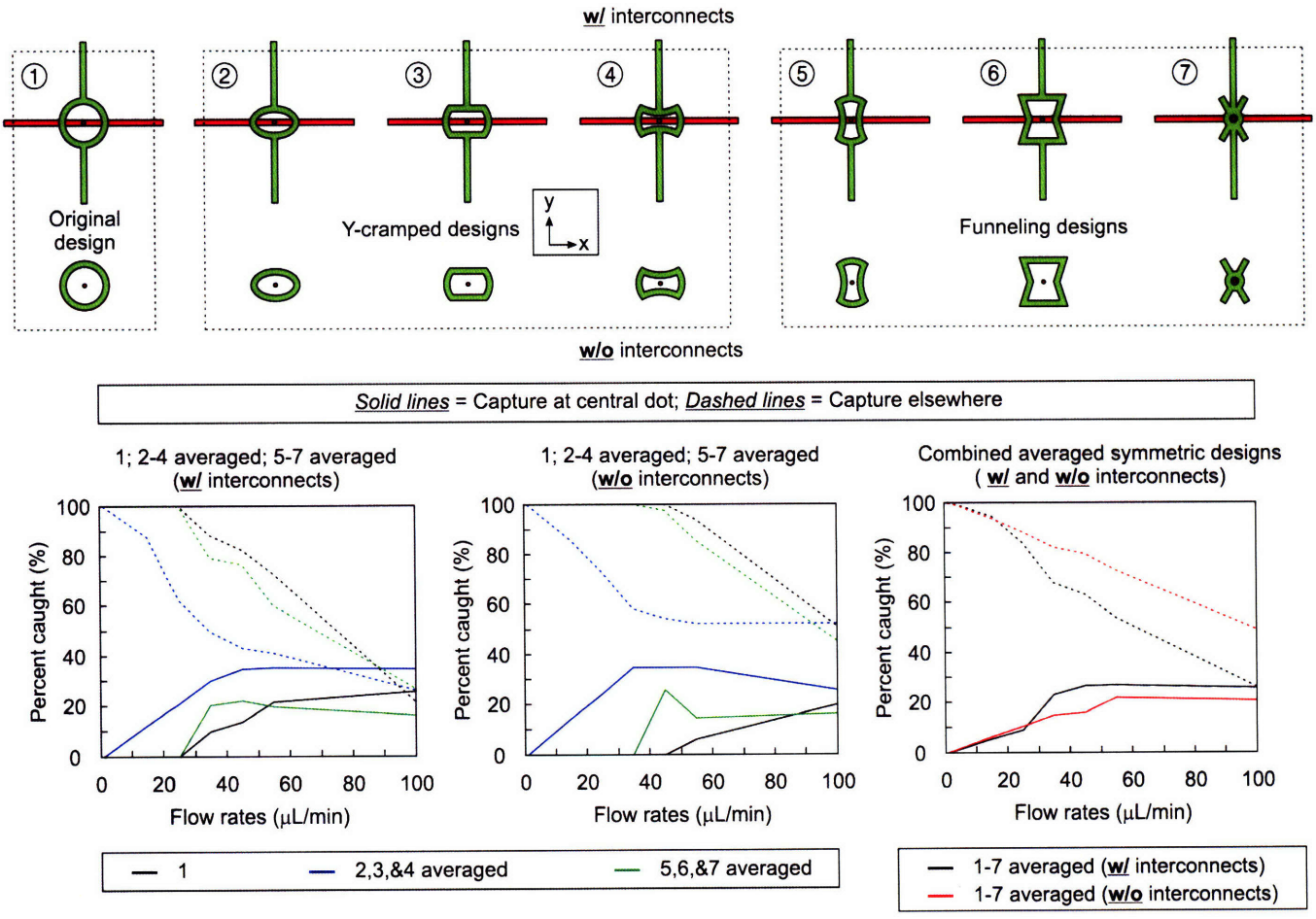

Figure 19: After witnessing empirical loading complications with the original p-DEP "ring-dot" trap geometries as mentioned in Chapter 2, I began exploring a collection of different designs to try and remedy the problem (top). In my efforts, I adopted two distinct approaches. On the one hand, I imagined that "cramping" the "ring" geometry in the y-dimension might enhance loading by allowing cells that progressed around the peripheral "ring" to pass more closely to the central "dot" where they could better "feel" its localizing DEP forces (see top center). Alternatively, I thought that I could possible improve loading by modifying the upstream edge of the outer "ring" such that it could "funnel" inwards toward the central trapping "dot" (see top right). I modeled examples both **w/** and **w/o** row and column connections by first solving the Laplace equation for each geometry. I then used our reported[5] DEP modeling software to position collections of cells in an equally spaced line upstream from the traps. For various applied flow rates in a modeled flow channel 250 μm in height and 4mm wide, I then swept the line of cells across the different trap types. To quantify differences in their responses, I measured what percentages of the initial starting number of incoming cells were trapped either at the "dot" or "elsewhere" in the trap geometry. I plot those results for various cases here (see bottom half of figure). As a general note, the sum of the percentage of cells arriving at the "dot" and "elsewhere" does not always sum to 100%, since cells may also completely bypass the trap and progress onward downstream.

force mapping code[5]. Through a series of simulations, I positioned a line of cells upstream from the traps and monitored loading dynamics by tracking the affiliate streamlines for a variety of flow rates. After evaluating the code by examining responses linked to changes in the number of DEP multipoles included and the degree to which I smoothed the COMSOL-delivered electric fields, I eventually witnessed the progression of incoming cells around the outer periphery of the "ring" structures. This behavior mimicked the responses seen empirically and surprisingly appeared in both the models that included considerations for the row- and column-based wiring connections as well as the models that did not.

After reproducing the experimental responses in a modeling environment, my next hope was that it might prove feasible to revise the baseline "ring-dot" geometry and thereby eliminate the unwanted "ring" electrode tracking effect. In Figure 19, I show a series of different trap designs that target two separate approaches for encouraging cell capture at the central "dot". In one case (designs 2-4), I explored various "y-cramped" layouts that I envisioned might reduce loading complication by shortening the distance that incoming cells (approaching from the x-direction) could be deflected away from the in-trap "dot". On the other hand (designs 5-7), I developed a set of "funneling" designs that I imagined might channel incoming particles toward the "dot". If cells were going to track the periphery of the "ring", why not use the ring to steer cells to locations where they were needed?

Again, using simulations that introduced a line (y-directed) of upstream cells, I began tracking the loading dynamics of each of the "y-cramped" and "funneling" designs subject to various flow rates. For these evaluations I assumed that the on-chip flow chamber exhibited a height of 250 μm and a cross-sectional width of 4mm. For each design and flow rate I tracked the percentage of cells (via streamline evaluation) that either localized to the "dot" or "elsewhere" in the trap geometry. I desired a response where for at least some portion of the flow rate spectrum, I could witness the dominance of trapping at the "dot" as compared to trapping "elsewhere" in a given geometry. I examined such loading patterns for trap geometries both with and without interconnects. In the bottom half of Figure 19, I present the averaged responses of both the "y-cramped" and "funneling" designs (with and without interconnects) and I compare their behaviors to my original "ring-dot" efforts. (For completeness, I further provide the individual non-averaged responses for each of the seven distinct trap designs in Appendix 3)

For both design revision subclasses, I did observe an enhancement of "dot"-based trapping compared to the original "ring-dot" geometries for at least some set of flow rates. Additionally, the "y-cramped" configurations seemed to outperform the "funneling" designs on the basis of higher "dot" capture and lower "elsewhere" capture at virtually all flow rates. When examining the averaged comparative performance of designs with and designs without interconnects their trapping mechanics matched more closely than anticipated. Though the capture "elsewhere" seemed to dominate for cases lacking interconnects, the "dot" capture percentages were practically identical for all flow rates.

Examining this entire data set holistically, it seemed bizarre to me that seemingly regardless of the geometry chosen, cell capture "elsewhere" in a footprint dominated dramatically over capture at the "dot". (Note: Summing the "dot" and "elsewhere" capture percentages does not always result in a total of 100%. This effect stems from the fact that some incoming cells may avoid

capture altogether and progress onward downstream.) I began to wonder whether or not the simple presence of a "ring", regardless of its shape, on the upstream side of the "dot" (whether modeled with or without interconnects) was somehow impeding the "dot" loading mechanics. To test such an effect, I considered the idea of breaking trap symmetry across the yz-plane such that I could entirely eliminate "ring" components on the upstream side. In Figure 20 I introduce a series of seven such designs. The first three (1A-3A) incorporate layouts that aimed to additionally capitalize upon the outperformance of "y-cramped" responses compared to "funneling" designs. The latter four (4A-7A) present broken symmetry versions of my original "ring-dot" setup.

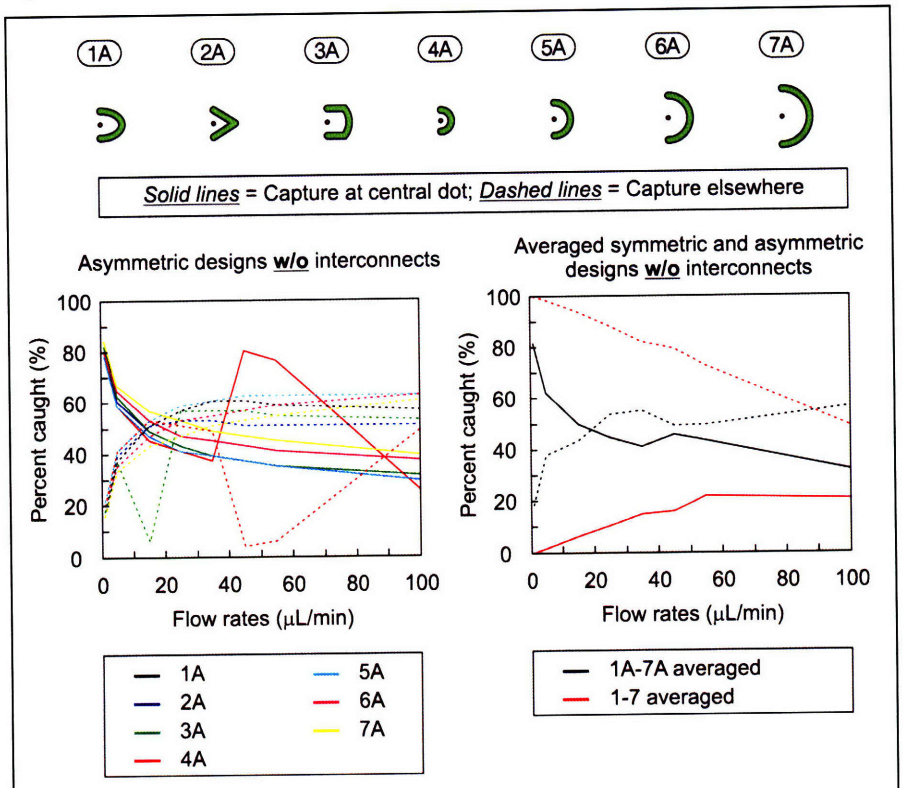

Figure 20: After carefully examining the responses of the "y-cramped" and "funneling" designs, both in plotted form and at a streamline level (not explicitly shown), it became clear that many of the contributions to the trapping "elsewhere" in a given geometry stemmed from the localization of cells along the front-side edges of all of the peripheral "rings". My curiosity then grew for understanding what sort of responses might occur if I fractured the design symmetry by eliminating front-side "ring" components in a variety of different footprints. Be expectation, such revisions, especially at slow flow rates, vastly improved the trapping percentages at the "dots" while minimizing capture "elsewhere". Essentially all broken symmetry designs tested presented nearly identical behaviors.

Again, in simulations, identical to those used when generating the data for Figure 19, I attempted to assess the behavioral mechanics of these new designs. As Figure 20 shows, this revised approach produced the desired dominance of "dot" capture over capture "elsewhere" (at least at the low end of the flow rate spectrum) and thus offered a response contrary what was observed with our original symmetric designs. (For a plot showing all individual symmetric and

asymmetric designs in non-averaged form please refer to Appendix 3.) Interestingly, almost all of the asymmetric designs presented similar behavioral results. For the sake of simplicity, based upon the marginal behavioral differences observed when comparing designs from Figure 19 that either lacked or accounted for on-chip interconnects, I elected to run broken symmetry simulations, as presented in Figure 20, only for cases that lacked row and column wiring. For ongoing efforts targeting "dot"-based capture in large format arrays, including trap geometries that did not position peripheral "ring"-type structures on the loading side of individual traps became a key concern.

A new approach to two-level metal processing

As an unexpected and greatly welcomed boon to the challenges faced in reliably etching the on-chip intermetal dielectric (as discussed more thoroughly in both Chapter 2 and my Masters work), the removal of a longstanding in-house (Microsystems Technology Laboratory - a.k.a. MTL) machine restriction enabled, for the first time, processing of CMOS-compatible[143, 144] metal-coated wafers in a production-quality plasma-based oxide etching tool. With this new freedom in hand, I could begin considerations for revising my approach to p-DEP "pixel" designs.

As I was originally restricted to using wet-etch BOE-style methods for patterning the IMD, I realized early on, that forming reliable vertically-oriented via-based connections between the two on-chip metal layers would surpass the realistic capabilities of our in-house wafer processing tool set. As a result, I structured the original "ring-dot" array geometries around topologies that only mandated electric-field-based connections between the bottom and top metal layers. In other words, I organized all electrical connections to the "dot" features using Metal 1 alone and all electrical connections to the "ring" features using Metal 2 alone. The electric-field-based connections spanning the two metal layers, in ideal implementations, arose only at on-chip locations where flux lines could bridge between the central etched "dot" and peripheral "ring".

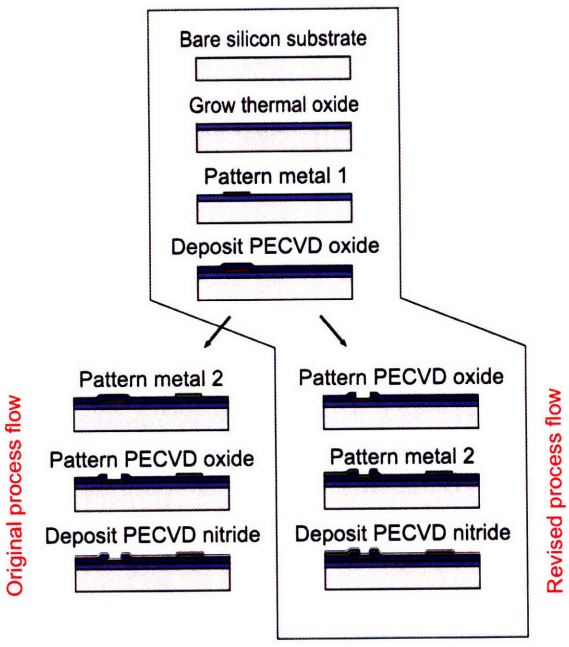

Figure 21: In the original micofabrication process sequence, due to limitations in available in-house tooling sets, I was forced to etch the PECVD oxide layer after patterning the Metal 2 layer. This limitation impacted my designs such that I could only establish electric field linkages between the two on-chip metal levels. As machine limitations changed, I revised my process to additionally enable direct vertically-connected via linkages between the two on-chip metal levels.

With the IMD etch sequence posing the most challenging fabrication demands, I was not confident in my original process design that I could readily deposit and pattern the Metal 2 level following a step that offered the potential to damage the on-wafer material stack. As such, I elected to pattern both my Metal 1 and

Metal 2 layers first and etch the intermetal PECVD oxide layer afterwards (see Figure 21 left branch). Obviously this decision impacted the permissible set of on-chip electrode designs as it would only prove feasible to etch portions of the IMD that were not covered by the Metal 2 layer.

All of these complications and design limitations were eliminated with the arrival of in-house tooling for reliable plasma-based oxide etching. As I show via cross-sectional schematic in Figure 21 (see right branch), I restructured my process flow to pattern each deposited on-chip material before piling on subsequent layers. With this revision, I could etch through the IMD to expose targeted portions of the Metal 1 layer and then deposit and pattern the Metal 2 layer to form vertically-directed via-based connections between the two on-chip conducting layers (see Fabrication Methods Appendix "2-level metal via-based process for either scaled p-DEP or electroactive weir designs" and the included etch and deposition recipes). This flexibility meant that there were enhanced capabilities for routing on-chip wiring and it would prove feasible to limit the total electrode footprint directly contacting the in-system liquid environment (i.e. anything routed on the Metal 1 layer would be separated from on-chip buffers by virtue of the overlying oxide). These two key benefits will become increasingly pertinent for discussions presented further along in this chapter.

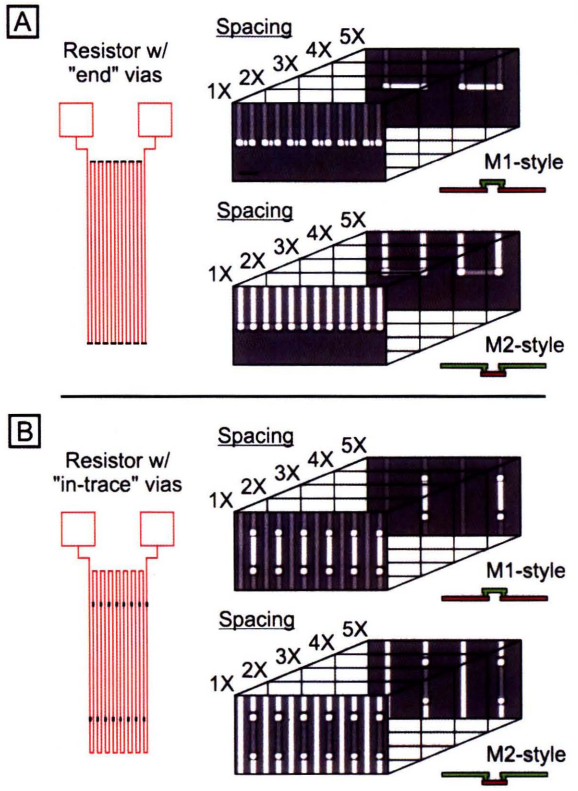

Figure 22: I designed and tested various collections of serpentine resistor elements to functionally evaluate the reliability of my revised via-based two-level metal process. I examined vias at the "ends" **(A)** of on-chip routing, dedicated "in-trace" **(B)** vias, and resistors with "large counts" of vias (not explicitly shown) to understand the resistive impact that vertical connections between the Metal 1 and 2 layers could present for electrode designs. For both the "end" vias and the "in-trace" vias, I examined numerous line spacings as well as distinct "M1-style" and "M2-style" routings. I provide the full set of data detailing the measured ΔR / via calibrations, as compared to control traces lacking vias, in Appendix 3 and Appendix 4. (Scale bar ≈30 μm.)

Functionally testing the new via-based two-level metal process

Before progressing from a process fabrication sequence to an elaborate collection of mask designs for revised and scaled p-DEP-based "pixel" arrays, I needed to obtain at least a basic understanding of the impact that on-chip via connections might impose. My biggest concern was that individual vias would enhance the electrical resistance along a given electrical trace and (if I included too many) threaten on-chip routing efforts to an extent that it would become impossible to deliver requisite DEP trapping potentials to individual "pixels".

To tackle this job I designed a simple series of masks that leveraged my new via-based process

to form on-chip serpentine resistor elements. As I partially demonstrate in Figure 22, I utilized three distinct footprint subclasses to explore limitations of the revised design approach. In one case, I positioned via connections at the "ends" of the traces; in another, I placed them "in-trace" at designated locations; and in the final subclass (not explicitly shown), I included "large counts" of vias (either 100, 200, 300, 400, or 500 in a given trace).

For both the "end" and "in-trace" via configurations, I included designs that explored the potential impact that spacings between switchbacks (1×-5×) in the traces might have on the reliability of individual via connections. I feared that if I packed the vias too tightly in a given on-chip area I might confront challenges for avoiding ill-formed connections between the two metal levels that could, in some applications, result in either shorts or unconnected open circuit breaks in the traces. Additionally, I pondered whether or not vias comprised of a predominant Metal 1 level trace interspersed with short vias on the Metal 2 level (labeled as M1-style vias) would perform any differently than vias comprised of a Metal 2 trace interspersed with short vias on the Metal 1 level (labeled as M2-style vias). Last, by examining the "large count" via designs, I hoped to provide a worst-case scenario where by utilizing far more vertical connections between the Metal 1 and Metal 2 layers than I ever anticipated using, I could search for the potential presence of an upper limit to the number of vias that one might safely include in an on-chip trace.

Because reliable vertical connections depend upon quality contacts between the two conductive layers, I examined two slight process variations for forming my on-chip vias. In one case, I simply deposited and etched the Metal 2 layer immediately following the IMD etch routine. In another, I included an additional step where, under vacuum, in the same machine (Endura - Applied Materials, Inc., Santa Clara, CA) used to deposit the second metal layer, I ran an argon preclean sequence (see Fabrication Methods Appendix - "Endura 'WAFER CLEAN'" for specifics) to remove any debris from the bottoms of the patterned IMD etch holes. Then without breaking vacuum, I proceeded to deposit the second on-chip layer of metal. I feared that since the plasma-based oxide etch sequence used oxygenated chemistries to cut away at the PECVD oxide, and the wafer would be transported through an oxygen rich atmosphere prior to being placed in the metal deposition tool, it might be likely that even if the etch progressed to the Metal 1 layer it would encourage growth of an aluminum oxide that could effectively serve as an insulator at the center of the via.

I examined four resistors of each type from separate chips and compared their resistances (as measured using a multimeter) to a comparable neighboring on-chip resistor of equal length that lacked vias. I then computed the ΔR / via for each resistor, assembled the averages and plotted them along with their standard deviations (as error bars). Appendix 3 shows the results from such comparisons for "end" and "in-trace" vias while Appendix 4 presents the results affiliated with "large count" resistors. Though there are some interesting trends (i.e. the M1-style vias in "end" and "in-trace" designs lacking a preclean step seem to display decreasing ΔR / via values for increased switchback spacings while the M2-style vias exhibit an opposing trend) the most notable behavior is the distinction between ΔR / via values for cases with and without the preclean sequence. With the preclean step included, the measured ΔR / via values suggested that on-chip vias presented insignificant changes in the overall resistance along a patterned trace. In cases examining "large count" conditions we had a better statistical sampling of vias (i.e. more

than the 16/resistor presented by the "end" and "in-trace" types) and regardless of whether I included 100 or 500 vias in an on-chip line, the ΔR / via values were on average all below 0.1 Ω. Without the preclean step, the via contributions were much more substantial as they presented changes in resistance that would have limited their functionality in most applications. For my purposes, these measured results meant that all of my future processing efforts would necessarily rely upon the use of a preclean sequence preceding the Metal 2 deposition that maintained vacuum conditions throughout. As an added caveat, I also found that including a thin (500 Å) layer of Titanium as a top coating layer during the Metal 1 deposition provided a nice etch stop that prevented unwanted damage to the underlying metal during the IMD etch sequence.

In my original process, I had to handle each chip individually to ensure proper IMD etching. As such, I was able to protect the on-chip wirebonds by covering them with hand-placed glass cover slips during the final silicon nitride deposition step. Lacking an in-process shadow mask (which would likely prove challenging to fabricate), my next concern was whether or not the final 250-Å-thick nitride deposition, necessary for avoiding unwanted cell/surface adhesion, would prevent or hinder effective chip-to-world wirebond connections. On the same chips containing the test resistors, I included a series of square bond-pads with differing sizes and spacings. I then took those chips and attempted to form wirebonds to off-chip printed circuit board (PCB) traces. As I highlight through a collection of images in Appendix 3, I successfully and reliably bonded to pads sized even as small as 100 μm on a side with 100 μm edge-to-edge spacings. Failure (such that one bond touched another in a way that would produce a short) occurred only when I attempted to bond to pads sized 100 μm on a side with 50 μm edge-to-edge spacings. For all future work I elected to use pads with at least 200 μm side lengths and 100 μm edge-to-edge spacings. These spacings, though not as tight as industry standards, did not present footprints that were expected to dramatically expand the overall die sizes even for arrays presenting 400 individual "pixels".

Aside from assessing the bonding potential for processing that included deposited nitride layers, I examined the electrical characteristics of such connections by using wirebonds to link to several on-chip resistors. Though not detailed here, the wirebond-based connections presented comparable resistances to those examined by directly probing the on-chip pads using a multimeter test kit. As had been supported in the work done for my Masters thesis, it proved regularly problematic to form bonds between on-chip aluminum pads and the standard tin- or chrome-plated traces found on PCBs sold by vendors specializing in rapid turnaround design-in/part-shipped foundries. To ensure proper bonding in a repeatable manner I was forced to use PCBs that presented gold traces. Though more costly, I will present a scheme later in this chapter that helped to manage such a demand quite effectively.

As a final validation for the new two-level process, I assessed the reliability of forming on-chip patterns of various sizes in the Metal 1, the IMD, and the Metal 2 layers. At the bottom of Appendix 3 I display arrays of 5 μm × 5 μm squares spaced with edge-to-edge distances of 5 μm as well as 10 μm × 10 μm squares with edge-to-edge spacings of 10 μm. It proved unreliable to pattern many of the smaller features using in-house methods (Heidelberg used for mask design) and, as a safeguard, I opted to continue using a nominal 10 μm minimum line width (had been used in initial designs) for all on-chip traces in on-going work.

N- and p-DEP forcing at discrete locations on a common platform

With a new via-based process available and validated, I began to consider the different types of flexibilities such manufacturing latitude might enable. Of key interest to me was the idea of using n-DEP forcing at certain on-chip locations and p-DEP forcing at others. Rather than proceed directly to mask designs attempting to incorporate such capabilities or move to simulations, I ran a basic functional test using to try and witness the two forcing regimes on a common surface. My efforts involved suspending a collection of CellTracker Green (Invitrogen, Corp., Carlsbad, CA) stained HL60s (cell concentrations ~ 1E5/mL; ATCC, Manassas, VA) in a buffer solution (deionized water base augmented with 10.25% w/v sucrose and 4% v/v phosphate buffered saline to render a net conductivity of 0.1 S/m - see green trace in Figure 23A) that I pipetted onto a chip presenting a series of interdigitated electrodes. These electrodes presented a series of neighboring traces driven at opposing polarities.

By monitoring the test device under a microscope, I applied voltages, delivered at either 100 kHz or 1 MHz to the on-chip electrodes. For the 100 kHz case I exerted n-DEP forces (shown by the dot in Figure 23A, highlighting the negative value on the plotted CM factor curve) on the in-system cells which caused them to localize to regions between oppositely polarized electrodes. When I switched the frequency of the applied signal to 1 MHz, I then moved to another portion of the CM factor curve (shown by the asterisk in Figure 23A) and exerted p-DEP forces that pulled cells toward on-chip electrode edges. In Figure 23B, I provide an indication of the shift in position the cells demonstrated when subjected to the two different forcing methods in my test setup. By observing a common field of view and indicating cell positions using red arrows the distinction becomes clear.

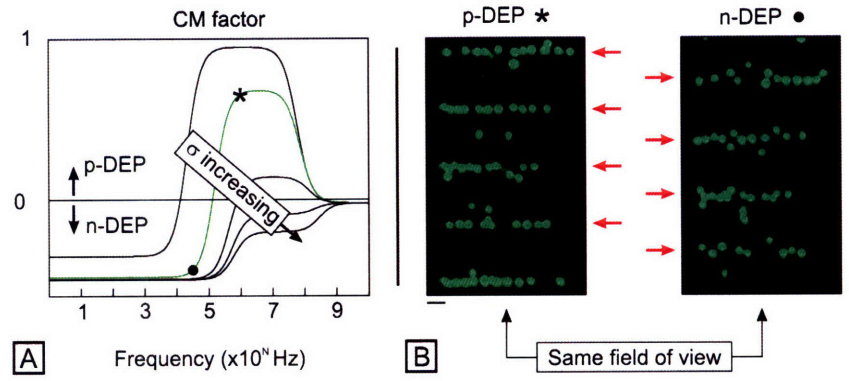

Figure 23: With the added flexibilities offered by a robust via-based two-level metal process, I began exploring the possibility of utilizing p-DEP forcing at certain on-chip locations and n-DEP forcing at others. Using CellTracker Green stained HL60 cell suspensions with "intermediate" buffer conductivities of 0.1 S/m, (see green trace in **(A)**) and a test chip presenting collections of interdigitated electrodes (IDEs) (each neighboring finger polarized with an opposing voltage), I demonstrated the effective switching between p- and n-DEP forcing regimes. I rendered this switching by alternately delivering either 1 MHz (see the asterisk in **(A)**) or 100 kHz (n-DEP as marked with the dot) frequencies to the on-chip electrodes. These two distinct frequencies forced cells to either the electrode edges (p-DEP) or to the regions between the electrodes (n-DEP). As the red arrows in **(B)** show, for a common field of view, I could either *pull* or *push* upon in-system cells to encourage localization to different on-chip domains. (Scale bar ≈25 μm.)

This confirmed ability to use electrode drive frequency as a means for assigning either *push* (n-DEP) or *pull* (p-DEP) forcing to designated on-chip electrodes opened the door to an incredible diversity of options for systems-level design. In the next several sections of this chapter I will explore this new latitude by outlining a technique for modeling

dual-frequency on-chip forcing and, in turn, leveraging it to develop two new on-chip system components.

On-chip IDE features for enhancing cell release capabilities

My initial motivation for exploring the possibility of delegating n-DEP forcing effects to certain on-chip features and p-DEP forcing effects to others, centered on the idea presented in Figure 24A. By moving to larger scale 400 site cell manipulation arrays, I imagined that releasing targeted cells positioned far from the array edges might prove challenging. I suspected that released cells might easily become recaptured further downstream in the array if they ever confronted an empty trap between the point of release and the outlet tubing. Traps in the same column would be activated at 1/4 strength and traps elsewhere in the array would be ON at full strength. To offset this potential I hoped to include a series of on-chip interdigitated electrodes (IDEs) that I could use to exert n-DEP forces upon released cells and thereby push targeted cells away from the devices substrate. Separated from the substrate they would ideally avoid witnessing the attraction effects of downstream p-DEP "dots". Higher velocity in-system flows would also tend to draw them off-chip more rapidly than if they rolled along the bottom of the array.

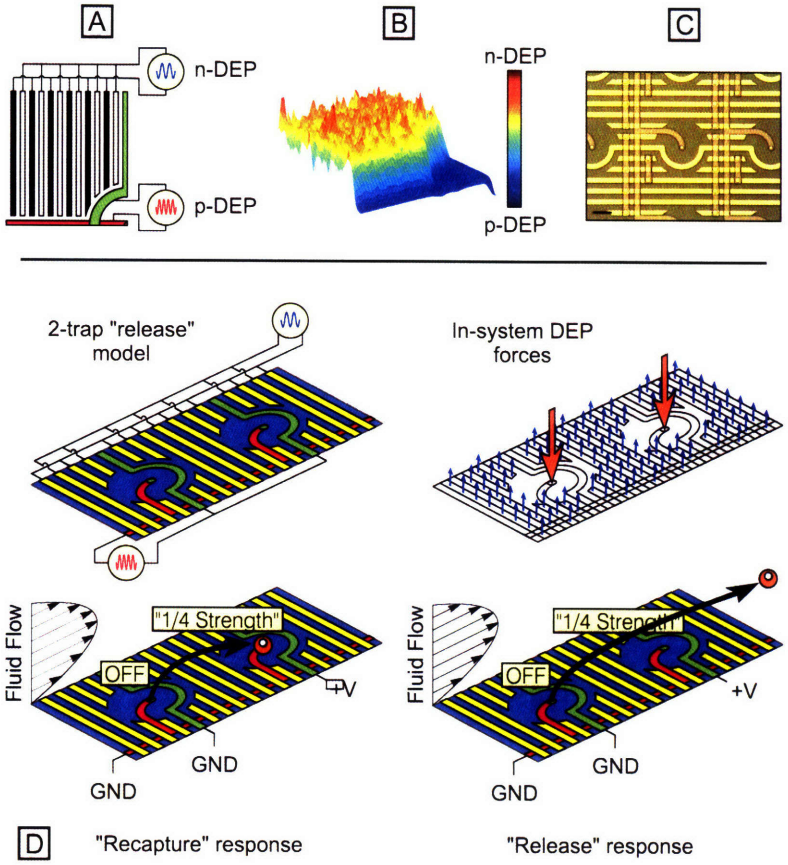

Figure 24: With the option of exerting both p- and n-DEP forces within a common microsystem environment experimentally validated (see Figure 22), I wanted to incorporate different on-chip structures for delivering distinct types of forcing. The original motivator was the idea for including a series of IDEs in close proximity to the "ring"- (or some variant) "dot" p-DEP trapping geometries **(A)**. Such IDEs could deliver n-DEP repulsion forces (see part **(D)**), to prevent the downstream "recapture" of released sorted cells. Such effects would ideally aid in sorting for large array footprints. Modeling such dual frequency effects (n-DEP repulsion and p-DEP trapping) demanded a protracted but novel simulation protocol (see Appendix 4) that provided valuable simulation results (**(B)** and Appendix 4) for assessing the operation of various IDE spacings and row/column electrode linkages. I eventually fabricated a test set of designs **(C)** and evaluated their performance (see the bottom of Appendix 4). (Scale bar in **(C)** ≈30 μm.)

An obvious concern for this type of design enhancement was a need for new modeling tools to evaluate various envisioned geometries. As I list in block diagram form in Appendix 4, I successfully revised and augmented our in-house DEP / Stokes flow

coding package[5] to enable such assessments.

The general approach used several key steps. First, I would draw 2D versions of the designs using AutoCAD (largely because of the affiliate ease of use versus the drawing environment provided by COMSOL). I would then export the designs as .dxf files. Using the COMSOL environment, I could then import the 2D electrode footprints and perform extrusions of key features to generate a 3D representation of any given design. Such representations would account for the on-chip flow chambers in addition to the on-chip wiring. With the 3D model in place, I would then save two copies of the COMSOL file. In one version I would set the p-DEP on-chip electrodes to a 1 V potential difference administered at 1 MHz and set the IDEs to a floating condition (no specified potential). In the other model, I would establish a 1 V potential drop (delivered at 100 kHz) across the n-DEP-actuated IDEs and allow the p-DEP cell trapping traces to float. For both models, I used on-chip buffer conductivities of 0.1 S/m (to match the case observed experimentally in Figure 23). I next solved the Laplace equation for each setup to determine the in-system electric fields. Via "fem" structure export, I then evaluated the on-chip multipolar DEP forces using our in-house solver[5] (streamforce.m). With the DEP forces available from both simulation runs (one where the n-DEP electrodes were operational and one where the p-DEP forces were in effect), I could then sum their independent contributions in a superposition-based effort and subsequently compute in-system streamlines to evaluate design behaviors.

As an example plot detailing the combined on-chip n- and p-DEP forcing, I show a resultant $|E|^2$ surface plot (see Figure 24B) for the 1/4 symmetry footprint shown in Figure 24A. The p-DEP "dot" geometries indeed tend to exert downward trapping forces while the surrounding IDEs tend to exert upward repulsion forces. Tuning the magnitude of such pushes and pulls could be directly modulated by varying the peak-to-peak voltage values of incoming control signals. The next step in system design then centered on investigations of geometries presenting two back-to-back traps (see Figure 24D). The idea behind such simulations involved painstaking evaluations of various design modifications (based upon both on-chip wiring as well as specific IDE spacings) that I hoped might enhance the potential for eliminating or reducing downstream cell recapture following targeted release.

To begin this work, I developed a series of control geometries (see top six model templates in Appendix 4) that considered the relative impact that on-chip IDEs offered compared to cases lacking them. Additionally, these models further examined the role played by our original centrally located, ±x oriented, Metal 1 level connections to on-chip "dots" (shown in purple in the top six model templates in Appendix 4). Using my dual frequency simulation routine, I then began to examine these "control" geometries by placing 20-μm-diameter cells at the "dot" positions in the frontmost trap, and then releasing them using row-column deactivation and a multitude of on-chip flow rates (channel height = 250 μm and channel width = 4 mm). I developed a map of the responses associated with the different designs (see bottom section of Appendix 4) by assigning blue boxes to conditions where cells failed to escape the front trap, white boxes to cases where cells became recaptured in the back trap, and red boxes to circumstances where cells progressed downstream for effective release. As I had hoped, using these control cases, I discovered that by incorporating on-chip IDEs (I had two different types labeled IDE-1 and IDE-2) I could, subject to various operating conditions, greatly reduce the

propensity for recapturing cells in the back trap. This behavior emerged visually in the response mappings by either a reduction in the size of or the elimination altogether of white boxes separating blue (remains in the front trap) and red (effectively released) sections. This dynamic indicated that the on-chip IDEs were indeed contributing to enhanced design performance.

Another interesting observation (which I do not present explicitly) was that for cases where I included both IDEs and centrally located, ±x oriented, Metal 1 linkages to the trapping "dots", I found that the locations where the peripheral "ring" crossed above the underlying interconnect trace seemed to present a p-DEP trapping response. In the response mappings this meant that though I would often see a switch from retention of a cell in the front trap to effective release, it was not uncommon that the underlying central traces could prescribe higher flow rates for cell removal from the front trap. The cells would release from the "dot" progress to the "ring" and then become trapped in place until a more sizeable flow rate could dislodge them. From that point on, the IDEs could prove functional for preventing capture in the downstream traps.

Such an effect meant that the manner by which I connected off-chip signals to the on-chip "dots" could directly impact design release behaviors. I consequentially elected to explore a variety of unique Metal 1 layer electrode routings in combination with my on-chip IDEs to try and further enhance the in-system release mechanics (see lower six designs presented in the "Two-trap" model templates section of Appendix 4). Metal 1 routing modifications 1-4 all presented cases where the in-trap "ring" crossed above the linkages to the "dot". In each of these designs I imagined that by offsetting that crossing from a centrally located configuration I might improve release behaviors. In the mod-5 electrode routing setup, I made even greater efforts to move the Metal 1 and Metal 2 crossing well away from regions internal to the "ring". Without explicitly providing the streamline responses for each of these test cases here, the mod-5 routing behaviors offered the most reliable and robust means for successfully releasing a cell from the front trap and preventing its subsequent recapture at points downstream. Via simulation-based evaluations it emerged that any crossing of the Metal 1 and Metal 2 levels owned the potential to produce a contaminating trapping response. As such, moving those locations well away from regions targeted for specific DEP forcing effects only served to enhance design performance.

In functional designs, I incorporated the mod-5 wiring pattern along with either the IDE-1 or IDE-2 designs (or slight variants). Figure 24C offers a simple visual of one of the actual fabricated devices. Using Ba/F3 mouse pro B cells[43] provided by Dr. Susan Lindquist's lab at the Whitehead Institute (details of the media formulation are offered in the Biological Methods Appendix "Standard cell culture medias" subsection - preperation of WeHi-3B conditioned media is discribed further elsewhere[145]), I demonstrated the desired IDE-based release mechanisms empirically. To perform this evaluation, I first suspended the Ba/F3 cells at densities of ~1E5/mL in deionized water-based buffers supplemented with 9.5% w/v sucrose, 2.5% Hepes taken from 1M stock, and 5% bovine calf serum (tabulated in the Biological Methods Appendix). I injected the cell suspensions onto the device surfaces using our standard approach and trapped cells at on-chip "dot" locations using 2V peak-to-peak potentials delivered at 7 MHz. With cells trapped in the device, I then actuated the IDEs using 4V peak-to-peak potentials administered at 200 kHz. Using a 5 μL/min flow rate (on-chip flow chamber cross-sectional dimensions: 250 μm in height by 4mm in width) and on-chip addressing, I deactivated targeted "pixels" and imaged the process using a 63x objective (LD Plan-NEOFLUOR, Zeiss).

The five step sequence at the bottom of Appendix 4 tracks a released cell progressing downstream away from the trapping "dot". As it encounters the IDEs, in frames 4 and 5, the cell rises above the substrate producing out of focus images. By taking a new fabrication capability through numerous simulation cycles, I thus developed an entirely new dual-frequency DEP-based format for handling cells in array-based layouts.

On-chip "V" structures for improved loading

After making the effort to incorporate n-DEP-actuated IDEs on a surface shared by p-DEP-actuated trapping "pixels", it only made sense to ponder what other types of on-chip n-DEP-activated entities might be included to further augment array performance in on-going work. Prior efforts by others[118, 146, 147] had used on-chip n-DEP repulsion structures to deflect particles away from their incident flow paths in a variety of focusing, sorting, and separation applications. I began exploring the feasibility for including similar "V"-shaped electrode footprints upstream of my device trapping arrays to increase the opportunities for loading all "pixel" locations.

As I provide in Figure 25, I successfully manufactured various collections of such "V" structures and demonstrated their propensity for separating disorganized grouping of incoming particles (here demonstrated with 27-μm-diameter polystyrene beads suspended in Type 1 - see Biological Methods Appendix "Low-conductivity buffers" - 0.1 S/m buffers at ~1E5/mL concentrations) into rank and file downstream columns. By locating these "V" geometries between the on-chip inlet port and the trapping array, I was successfully able to sweep particles directly over the p-DEP trap nexuses.

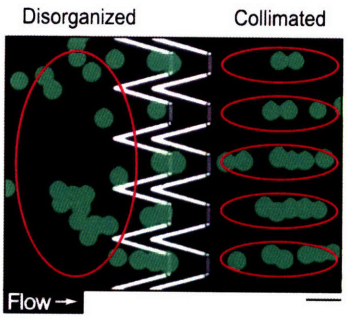

Figure 25: Beyond the on-chip IDE geometries, I incorporated a series of upstream "V" components that served to direct incoming cells into aligned downstream p-DEP traps. Such geometries leveraged n-DEP forcing to *push* disorganized groupings of cells into collimated traces. I offer several key performance-based evaluations of these designs in Appendix 5.

In a protocol matching much of the simulation work performed for both the dual-frequency-based assessments of IDE-reliant designs and the modeling used to evaluate the behaviors of the "y-cramped", "funneling", and asymmetric trap footprints, I used numerical methods to functionally test various implementations prior to manufacturing them. Using "V"s that presented angles ranging from 45° off the horizontal (y-axis in our case; direction perpendicular to on-chip fluid flow) to 75°, I first examined the flow rate dependent particle focusing power offered by "V"s that lacked aligned downstream "dots" (see first plot in Appendix 5). My investigation involved placing a line of cells upstream from a "V" (cells were initially resting on the substrate) and then sweeping that line across the substrate (flow chamber height = 250 μm; width = 4 mm; potential difference applied across the n-DEP "V" structures = 1 V delivered at 100 kHz). I defined a downstream 30-μm-wide centrally-located pocket and counted the percentages of upstream particles arriving therein. As a baseline for comparison, I also examined the percentages of cells arriving within the pocket in the case where no on-chip "V" existed. At virtually all examined flow rates, the presence of a "V" structure, regardless of type, enhanced the loading percentages. In this basic test, all of the "V" variations presented nearly identical behavioral responses.

To progress beyond this basic evaluation, I ran a more complex analysis by positioning a broken-symmetry "ring-dot" p-DEP trap downstream of the center portion of an upstream "V". I then quantified the percentage of incoming particles that were ultimately captured at the "dot" or "elsewhere" in the on-chip environment for a variety of on-chip flow conditions (p-DEP trap driven at 1 V delivered at 1 MHz; chamber dimensions match those for the preceding series of simulations). Again, when compared to the baseline case lacking an upstream "V" all designs exhibited higher capture percentages at the in-trap "dots" and comparable, if not reduced, capture percentages "elsewhere" (see second plot in Appendix 5). With these favorable results in hand, I implemented several designs incorporating on-chip "V" designs upstream of my array footprints.

Admittedly, like my trap design simulations, my "V" tests did not investigate conditions where incoming particles were delivered via streamlines elevated from the substrate. Though this may appear to be a strong limitation, it is typical that I perform in-device cell loading at flow rates small enough to enable particle settling. As such, in-system cells would nominally experience conditions closely matching those investigated using my modeling work.

Concerns pertaining to on-chip traces

Beyond the multitude of issues already considered for scaled array designs, I wanted to investigate the impact that lengthy on-chip traces might impose upon the voltages delivered to individual traps. Specifically, because I was using a single input to deliver voltages down an individual row of traps (or alternatively a single column), I wondered (in 20 × 20 implementations) whether or not traps positioned at the end of each row would experience so many dissipating resistive loads along their connecting paths that they would be compromised in their ability to effectively deliver DEP trapping forces.

Though I do not present all details here, using theory-based estimates for the in-fluid resistive losses tied to individual traps in a 20-trap row and their linking in-trace connections, I developed a circuit analog to model the potential present at all traps along the trace for a nominal input voltage of 1 V. Though the effective resistance associated with traps positioned at increasing distances from the input source mounted, the potential administered to the last trap in such a configuration (i.e. the 20^{th} trap) equaled $\approx$90% of drive potential subject to on-chip buffer conductivities of 0.1 S/m. This crude evaluation thus suggested that, for at least a 20 × 20 array footprint, lone connective paths linking traps along either a row or a column would effectively delivery adequate voltages to enable DEP trapping.

My final concern then centered on the possibility that sizeable parallel-connected electrode areas (as in alternate fingers on my in-system IDEs) in direct contact with on-chip buffers could present resistive drops that would in turn demand sizeable current delivery to maintain desired in-fluid voltage drops. To grapple with this notion, I developed a geometry (not explicitly detailed here) that presented a bank of six alternately polarized electrodes, each 10 μm in width and 100 μm in length (with 10 μm edge-to-edge spacings and driven at 1 V delivered at 100 kHz), to a 0.1 S/m buffer. I then used COMSOL to compute the averaged resistive heating (over time) taking place within such a configuration. Using this computed result, I could then develop the following relation:

$P_{avg} = \left(\frac{I^2 R}{2} \right)$	**Equation 27**

The only unknown here is the current variable, I, which I evaluated at ~0.120 mA. In other words, to maintain a unit voltage drop across such an electrode configuration, I would need to deliver ~0.120 mA of supply current. With this setup, I then had a gauge for understanding the impact that on-chip electrodes could own in assigning peripheral control circuit needs.

Modularity in system packaging design

As detailed originally in my Masters work[124], the basic premise I have leveraged for all device packaging designs has centered on the use of a chip-on-board approach. As the name implies, this type of packaging utilizes a printed circuit board as the backbone and support for individual die (see the lower portion of Appendix 5 - (A) = original 4 × 4 setup, (B) = scaled 20 × 20 setup). This technique not only provides a readymade structural underpinning for each device, it additionally enables effective on-chip fluid management and reliable electrical connections to off-chip control signaling.

To effectively establish on-chip flow environments I hand drill individual inlet and outlet holes through each chip. I then align those holes to a set of matching thru-board vias machined in the support PCB during its manufacture. Into those holes I press fit sections of PEEK (IDEX Health & Science Group, Oak Harbor, WA) tubing. The PEEK tubing then delivers or extracts fluid from the on-chip environment using linkages on the underside of each chip (chips mount onto the PCB using double-sided tape). To enclose the top-side fluid chamber on each device, I laser cut a polydimethylsiloxane (PDMS) (Bisco Silicones - Rogers Corporation, Rogers, CT) gasket that defines the chamber footprint and employ a glass coverslip to serve as the flow chamber ceiling. To bridge electrical ties from bond pads on the chip to off-chip peripherals, I typically use wirebonding. On-board traces then link into headers that interface with ribbon-cabling tied to various signal generators and off-chip switching units. Using high-performance epoxy (Henkel International, Inc., Düsseldorf, Germany) I seal the joints of this component stack and affix delicate parts in place.

In designing the chip-on-board packages used for my initial 4 × 4 proof-of-concept designs (see part A in the lower portion of Appendix 5), I developed an underlying aluminum base structure that proved functional for establishing strain reliefs for the connected PEEK tubing. Using a magnetic pad (Adhes-a-mag - Magnetic Specialty, LLC, Marietta, OH) on the underside of these base structures I could then stably mount each setup onto a custom machined steel microscope stage insert and minimize mechanical drift during assay-based imaging routines. When progressing from my original proof-of-concept designs to my scaled array formats, I looked for opportunities where I might escape a need for redesign. As such, I wanted to take advantage of the benefits offered by my original aluminum base structures without having to completely redesign my package.

This motivation led to a modular design approach. As highlighted using red text in Appendix 5, transitioning to a functional packaging setup for my scaled designs leveraged three key elements. First, I used a series of laser-cut acrylic adapter bars to connect my board-based die supports to

the underlying aluminum base. By taking half an hour to design and cut such components I avoided any need to redevelop a new scaled-up base geometry. Second, I parsed key functionalities of my original one-board approach into separate duties assigned to either an "adapter" PCB or a "packaging" PCB. Using this design scheme, the "packaging" PCB could embody a relatively small footprint to present gold traces for easing challenges associated with wirebonding. This board was processed using a high-resolution foundry (Advanced Circuits, Aurora, CO), and though it was more costly to manufacture, it reliably presented closely packed on-board pads. By using such a setup to simply bridge connections to larger headers, these boards only needed to be ~2" × 2". In volume format, the cost per board became reasonable. The underlying "adapter" boards presented larger layouts that served to route the connections from the "packaging" board to the proper pins on control system ribbon cabling.

By carefully planning the different chip varieties from the start, I was able to design a single "packaging" board to interface with any given die from my scaled-up-wafer process, regardless its on-chip array configuration. By additionally assigning specific functional duties to certain collections of on-chip bond-pads it was possible to map off-chip signaling to "packaging" board traces using only a small handful of "adapter" board designs. In many instances therefore, certain classes of chips could then operate using a common "adapter" board. With this design structure, if a chip became damaged during an assay, it was relatively easy to simply replace a chip and its affiliate packaging board by treating the adapter board and base support as a cradle unit. This benefit meant that it was relatively inexpensive (timewise) to get back to an operation state if disaster ever struck during device testing. Because the larger sized "adapter" boards simply bridged header connections to different portions of the device package, they could be made using inexpensive board houses (ExpressPCB, Santa Barbara, CA), low-resolution trace widths, and inexpensive materials (i.e. not gold). I have drawn the representations of my packaging scheme outlined in Appendix 5 to scale. As is noteworthy when comparing the design of my original setup to the scaled version, the overall chip footprint need to implement a 400 (20 × 20) site array was only marginally larger than the comparable 16 (4 × 4) site format (Scale bars = 1 mm). We therefore gain an incredible amount of new device functionality without requiring an associated and comparable growth in the device footprint (in both cases minimum on-chip line widths were 10 μm).

Peripheral control system design for on-chip DEP actuation

Though the total time involved in designing, building, and testing the peripheral support systems necessary for enabling targeted, switchable on-chip DEP actuation was substantial, I will only pay homage to it here, in brief. By avoiding a longwinded discussion on this somewhat tangential work, I hope to keep the reader focused on the core efforts embodying the academic developments central to my dissertation.

In general, each of my on-chip rows, columns, IDEs, and "V"s demanded the effective delivery of proper electrical signaling. It would be prohibitively expensive and inefficient to connect each component to its own off the shelf signal generator. Additionally, the output current delivered by such devices is typically too low to drive the electrical loads imposed by so many different on-chip features. To circumvent these challenges, I had to develop a control box that could use a pair of signal generators (one delivering an n-DEP actuation signal and the other providing p-DEP signaling) as inputs and then split, in some cases invert, buffer, and route those

signals to upwards of 80 different pin-based connections on the device "adapter" boards. Imbedded in this system for mapping signals to the chips, is a need for controllably switching which inputs are ON and which are OFF at any given time. Appendix 6 present a block diagram schematic that offers a high-level overview of the peripheral control system circuitry. I remotely engage with all aspects of this system using GPIB-based digital I/O signaling delivered by a MATLAB-run (The Mathworks, Natick, MA) graphical user interface (GUI) specifically catered to my system componentry. Using this GUI, I can additionally run the microscope stage to register the locations of individual "pixels" within cell trapping arrays and control the camera used to image my devices.

In Appendix 7, I present the wiring configuration and chip set involved in the unit cells comprising the key signal management portions of my peripheral control setup. Here, input signaling (from either Sig. gen. 1, 2 or 2-red.) connects into an AD8132 (Analog Devices, Inc., Norwood, MA) differential op amp. This chip generates a buffered and an inverted version of the signaling input and then sends it to an ADG333 (Analog Devices, Inc., Norwood, MA) digitally-controlled switching chip. This chip additionally receives four distinct digital inputs (Dig. IN_n - Dig. $IN_{(n+2)}$) that decide whether to direct the incoming buffered or inverted signals to the next stage in the unit cell. This switching block thus serves as the MATLAB-controlled element that decides which on-chip electrodes are turned ON or OFF. The signals directed to the array then pass through an AD8017 (Analog Devices, Inc., Norwood, MA) stage where additional current can be injected into the unit cell output. This is the stage where concerns related to the effective resistances of exposed electrode footprints came into play. I made sure that in organizing device designs the output power of this stage in the control circuitry was well matched to the load demands stemming from driven in-device elements. As AD8017 (Analog Devices, Inc., Norwood, MA) chips were originally developed as digital subscriber line (DSL) drivers, they are well-suited to handle this essential buffering task.

Appendix 7 also highlights the details of the pre-amp/buffer splitter stage mentioned in Appendix 6. The purpose of this stage is to enable the possibility for driving on-chip "V" structures at voltage ratings different from those needed to control the in-system IDE elements. It was my suspicion that the amount of DEP forcing needed to focusing cells upstream of the traps might not match the DEP forcing needed to aid in releasing target cells or prevent cell/substrate contact in non-trapping portions of arrays. By using a potentiometer coupled to an AD8017 op amp chip, I could port in a Sig. gen. 2 signal (the n-DEP frequency) and modulate gain values to produce a buffered version of that signal as well as a version presenting a truncated comparative amplitude (Sig. gen. 2-red.). I then piped one signal to the on-chip "V"s and another to the on-chip IDEs. This flexibility enabled straighforward tuning of the relative signaling seen by various on-chip n-DEP actuated elements.

In this chapter, we effectively examined experimental loading response challenges seen in our original "ring-dot" configuration from a modeling perspective to develop new footprints for cell capture. This work led to the elimination of upstream electrode components in the traps and enabled the placement of parasitic DEP trapping regions well away from central "dot" locations. Serving this effort we developed and validated a functional via-based fabrication process that ultimately enabled the incorporation of separate n-DEP- and p-DEP-actuated geometries on a common device surface. This flexibility serviced the design of on-chip "V" and IDE components

aimed to enhance loading and site-specific release operations, respectively. With matured packaging and signal routing capabilities we positioned our work to benefit novel biological assays and further validate modeling work from an empircal standpoint. I have attempted to highlight many of the details associated with transitioning from functional proof-of-concept cell manipulation arrays toward scaled version offering enhanced flexibility and reliability. Negligible concerns in front-end work can often present substantial complications in matured efforts. I hope that I have convinced the reader that making such design upgrades is anything but an issue of simply piecing together more of the same.

Appendix 3

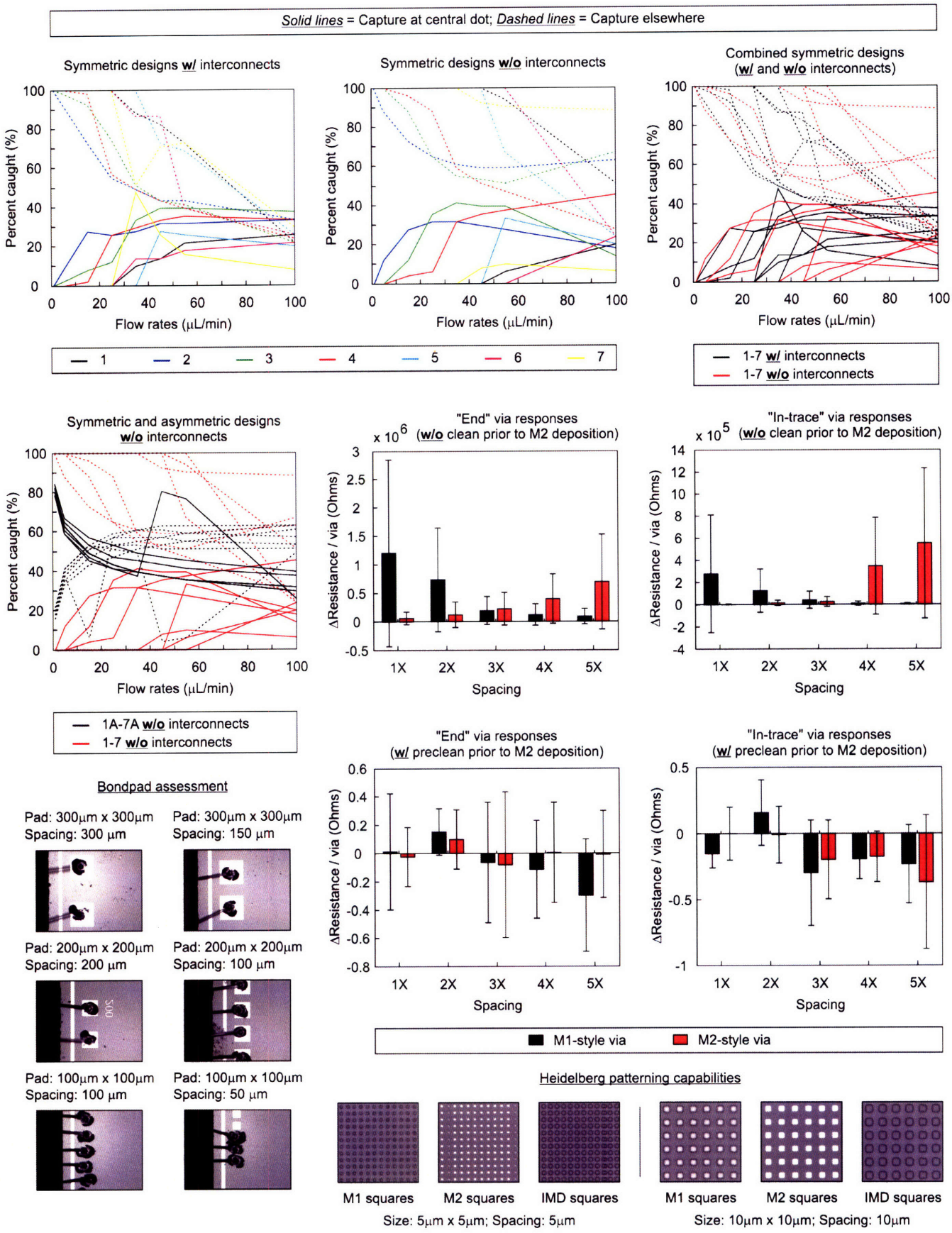
Solid lines = Capture at central dot; Dashed lines = Capture elsewhere
Symmetric designs w/ interconnects
Symmetric designs w/o interconnects
Combined symmetric designs (w/ and w/o interconnects)
Percent caught (%)
Flow rates (µL/min)
1
2
3
4
5
6
7
1-7 w/ interconnects
1-7 w/o interconnects
Symmetric and asymmetric designs w/o interconnects
1A-7A w/o interconnects
1-7 w/o interconnects
"End" via responses (w/o clean prior to M2 deposition)
"In-trace" via responses (w/o clean prior to M2 deposition)
ΔResistance / via (Ohms)
Spacing
"End" via responses (w/ preclean prior to M2 deposition)
"In-trace" via responses (w/ preclean prior to M2 deposition)
M1-style via
M2-style via
Bondpad assessment
Pad: 300µm x 300µm Spacing: 300 µm
Pad: 300µm x 300µm Spacing: 150 µm
Pad: 200µm x 200µm Spacing: 200 µm
Pad: 200µm x 200µm Spacing: 100 µm
Pad: 100µm x 100µm Spacing: 100 µm
Pad: 100µm x 100µm Spacing: 50 µm
Heidelberg patterning capabilities
M1 squares
M2 squares
IMD squares
Size: 5µm x 5µm; Spacing: 5µm
Size: 10µm x 10µm; Spacing: 10µm

Appendix 4

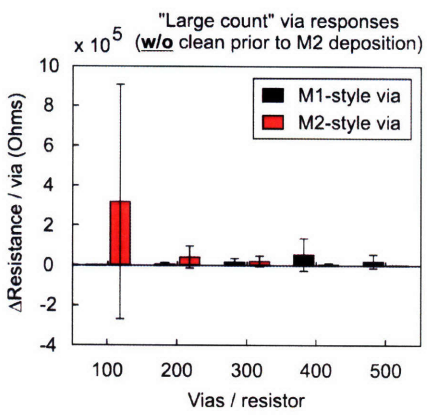

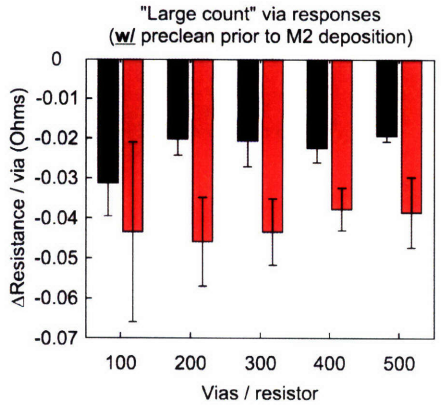

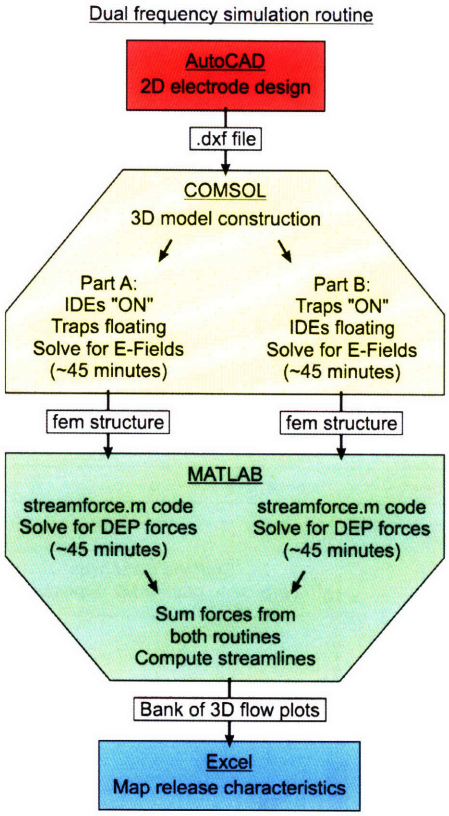

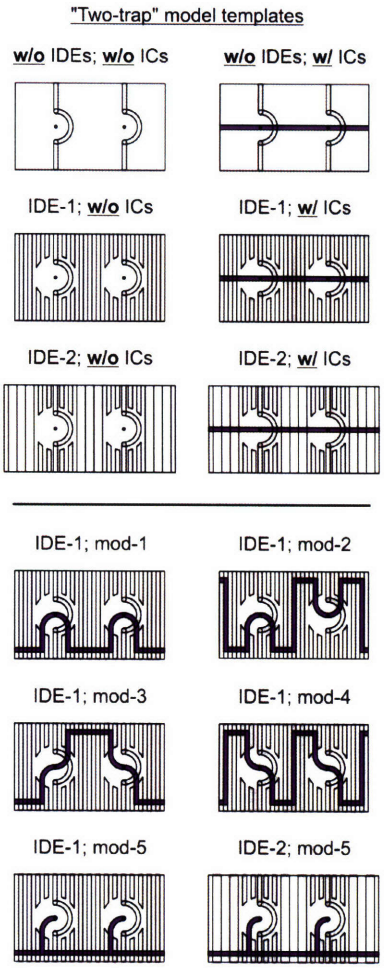

Tabulated "two-trap" responses

Retained in front trap | Recaptured in back trap | Effectively released

Flow rate (μm)	IDE@1V; Full "ON" traps @ 2V; "1/2 ON" traps @ 1V													
	1	5	10	15	20	25	35	45	55	65	75	85	95	100
w/o IDEs; **w/o** ICs														
w/o IDEs; **w/** ICs														
IDE-1; **w/o** ICs														
IDE-1; **w/** ICs														
IDE-2; **w/o** ICs														
IDE-2; **w/** ICs														
IDE-1; mod-1														
IDE-1; mod-2	X	X	X	X	X								X	
IDE-1; mod-3														
IDE-1; mod-4														
IDE-1; mod-5														
IDE-2; mod-5														

Flow rate (μm)	IDE@3V; Full "ON" traps @ 2V; "1/2 ON" traps @ 1V													
	1	5	10	15	20	25	35	45	55	65	75	85	95	100
w/o IDEs; **w/o** ICs														
w/o IDEs; **w/** ICs														
IDE-1; **w/o** ICs														
IDE-1; **w/** ICs														
IDE-2; **w/o** ICs														
IDE-2; **w/** ICs														
IDE-1; mod-1														
IDE-1; mod-2														
IDE-1; mod-3														
IDE-1; mod-4														
IDE-1; mod-5														
IDE-2; mod-5														

Experimentally observed IDE-based release

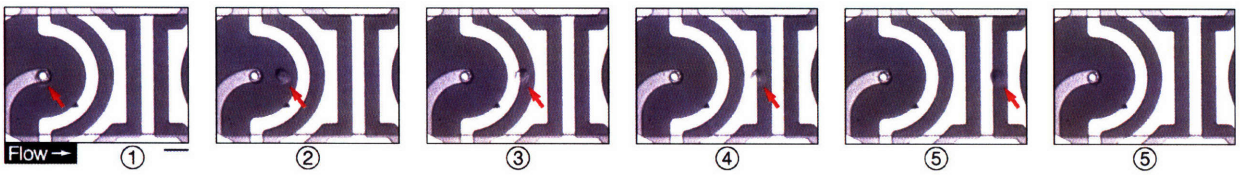

Appendix 5

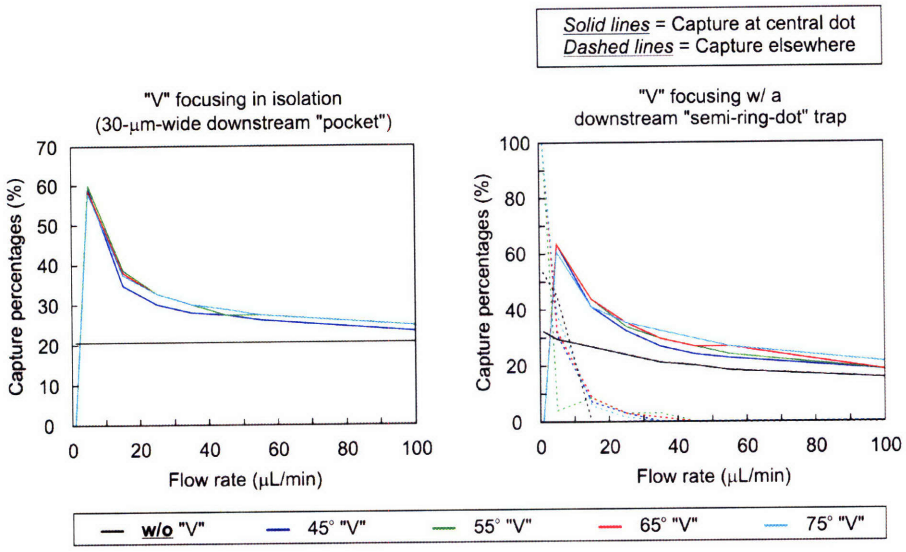

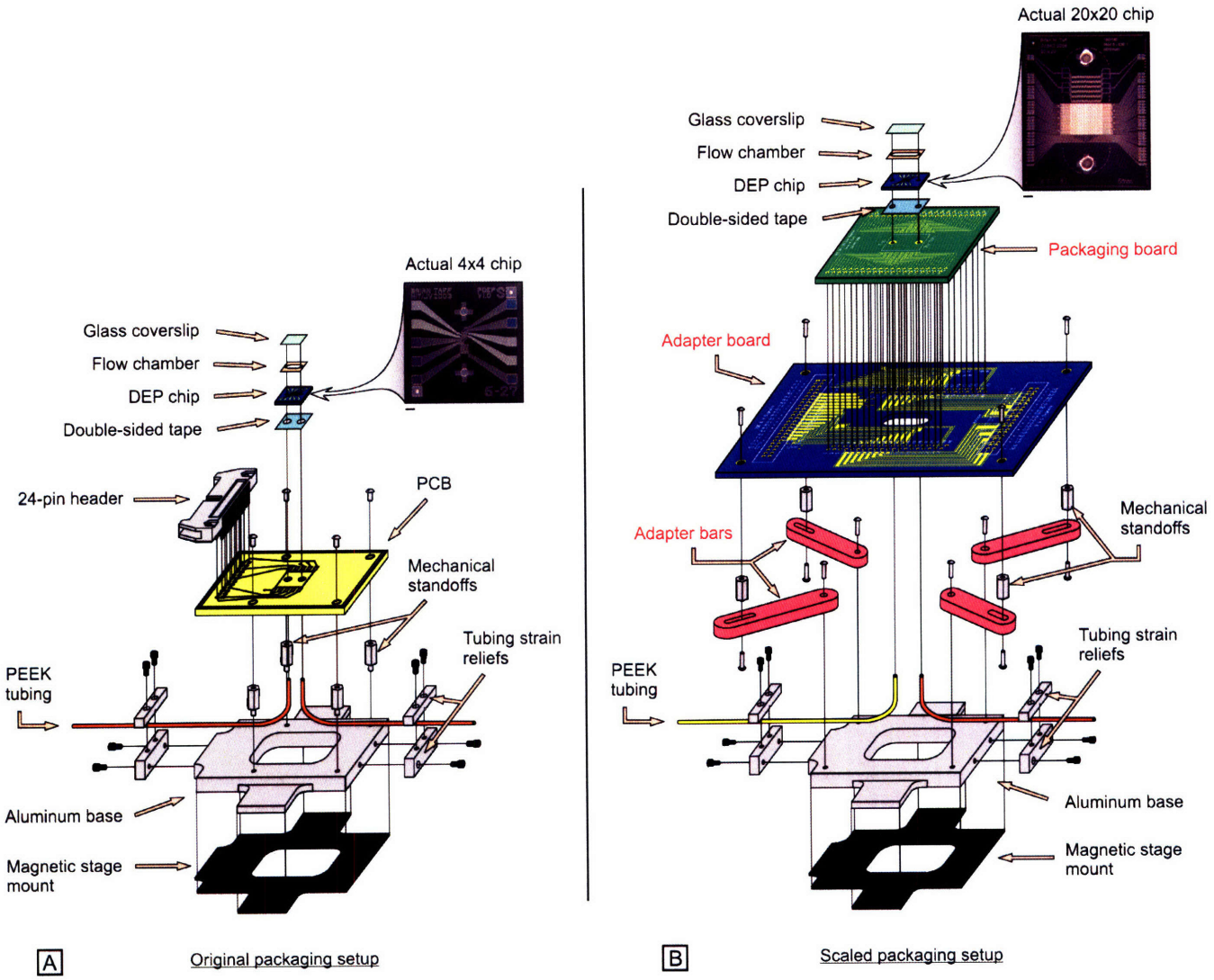

A Original packaging setup

B Scaled packaging setup

Appendix 6

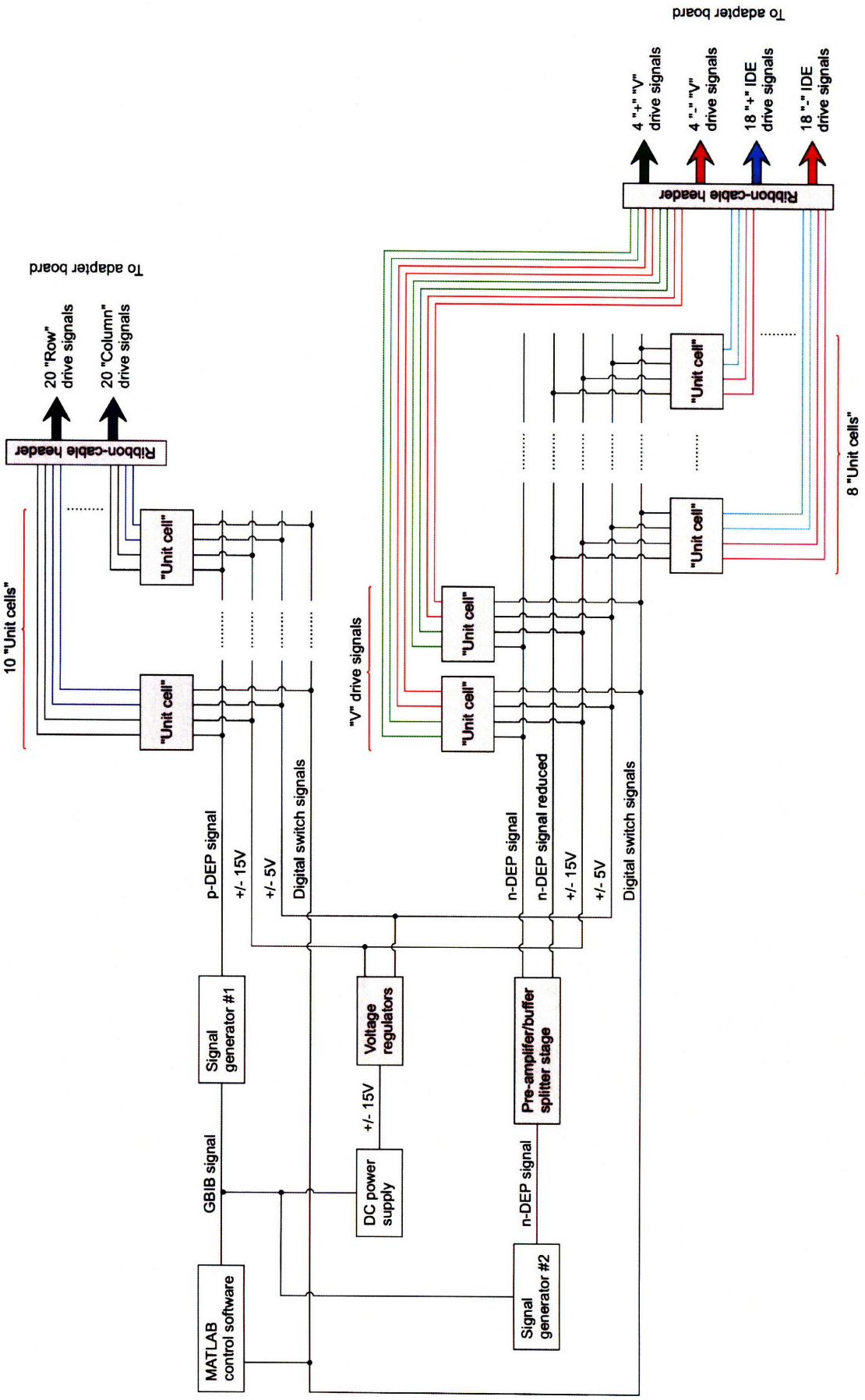
To adapter board
4 "+" "V" drive signals
4 "-" "V" drive signals
18 "+" IDE drive signals
18 "-" IDE drive signals
Ribbon-cable header
"Unit cell"
8 "Unit cells"
"V" drive signals
n-DEP signal
n-DEP signal reduced
+/- 15V
+/- 5V
Digital switch signals
To adapter board
20 "Row" drive signals
20 "Column" drive signals
Ribbon-cable header
"Unit cell"
10 "Unit cells"
p-DEP signal
+/- 15V
+/- 5V
Digital switch signals
Signal generator #1
Voltage regulators
+/- 15V
DC power supply
GBIB signal
MATLAB control software
Pre-amplifier/buffer splitter stage
n-DEP signal
Signal generator #2

Appendix 7

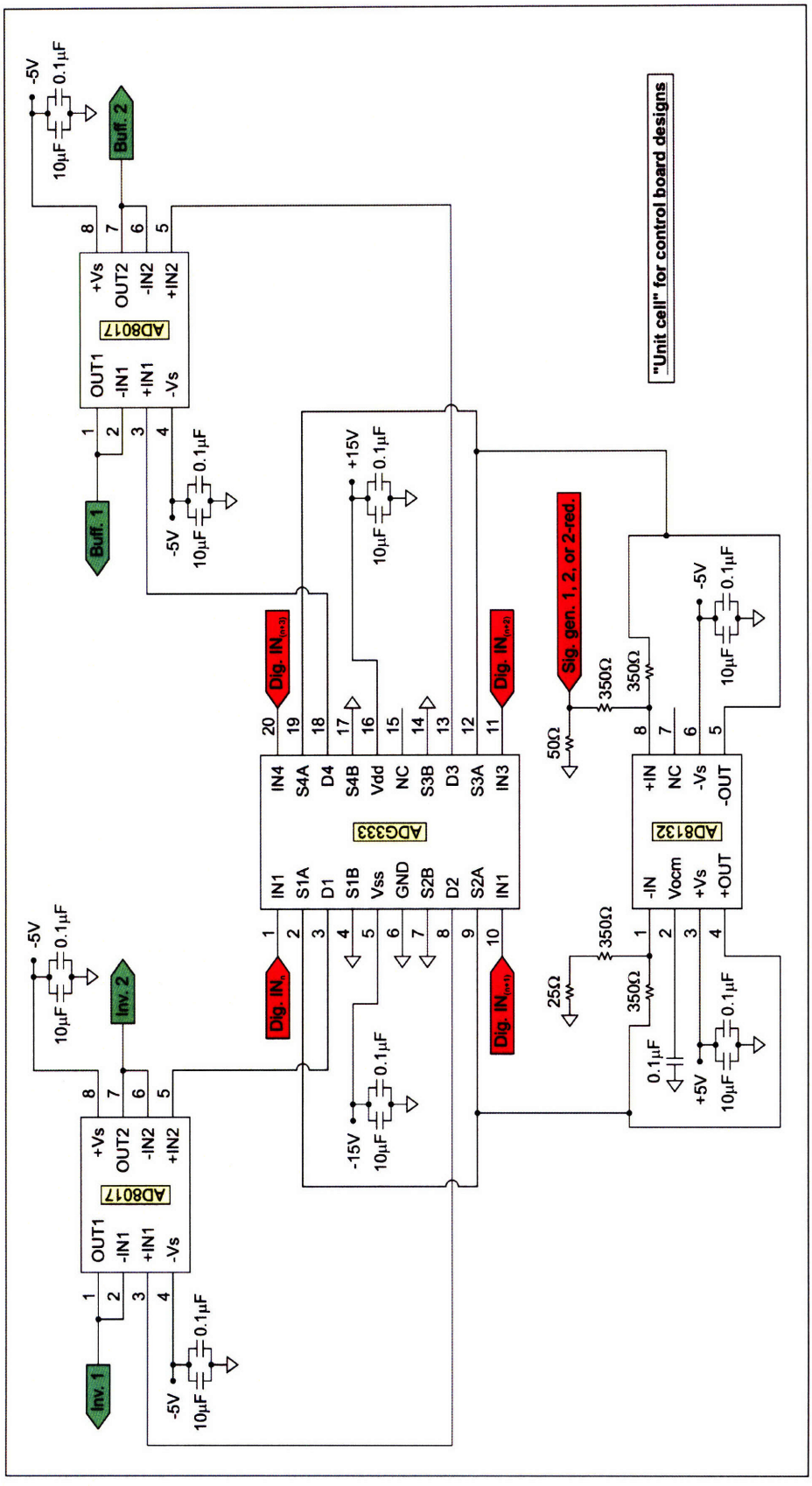
"Unit cell" for control board designs
AD8017
AD8132
ADG333
Inv. 1
Inv. 2
Buff. 1
Buff. 2
Dig. IN$_n$
Dig. IN$_{(n+1)}$
Dig. IN$_{(n+2)}$
Dig. IN$_{(n+3)}$
Sig. gen. 1, 2, or 2-red.
-5V
+15V
-15V
+5V
10µF
0.1µF
25Ω
50Ω
350Ω
0.1µF

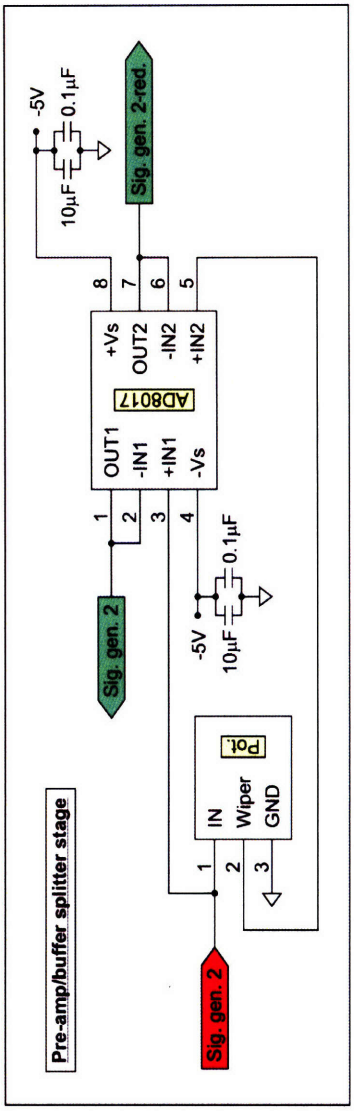
Pre-amp/buffer splitter stage
AD8017
Sig. gen. 2
Sig. gen. 2-red.
Pot.
IN
Wiper
GND
-5V
10µF
0.1µF

Chapter 4: An electroactive hydrodynamic weir approach

After due process in examining options for scaling my initial p-DEP-based forays to larger array formats, I began considerations for developing a complimentary n-DEP "pixel" design that could prove functional within the same system-level framework. As I had motivated in my efforts pertaining to well-reliant designs (see the latter portion of Chapter 2), n-DEP traps offered potential to expand manipulation capabilities to assays demanding on-chip culture media based environments. In this chapter, I will outline work, progressing from design through implementation and testing, that cultivates a revised approach to device-based cell handling.

An alternative perspective on device-based cell manipulations

In recent years, there have been a number of platforms proposed for on-chip cell manipulations that have capitalized upon in-flow hydrodynamic features to encourage the retention of individual cells at discrete locations within microfluidic environments. The first functional devices demonstrating such effects was offered by Wheeler et al.[23] and focused upon an application space surveying imaged biological responses stemming from rapidly switched drug treatments. As I recapitulate in adapted form in Figure 26A, this device retained cells by presenting an appropriately sized cup-like geometry. Initially drain channels in this cup would permit entering fluid flows to escape laterally via two opposing waste outlets. Once a single cell progressed into such a cup, it effectively blocked subsequent flows through the drain channels. With both drain channels blocked, subsequent impinging cells would deflect around the capture cup such that only one cell remained in place for on-chip survey.

Shortly thereafter, Di Carlo et al.[148](see Figure 26B) demonstrated an array-based implementation of this hydrodynamic means for cell handling. By positioning multiple copies of such weirs next to one another, he successfully trapped large collections of individual cells and then ran calcein uptake assays to probe cross-population membrane porosity.

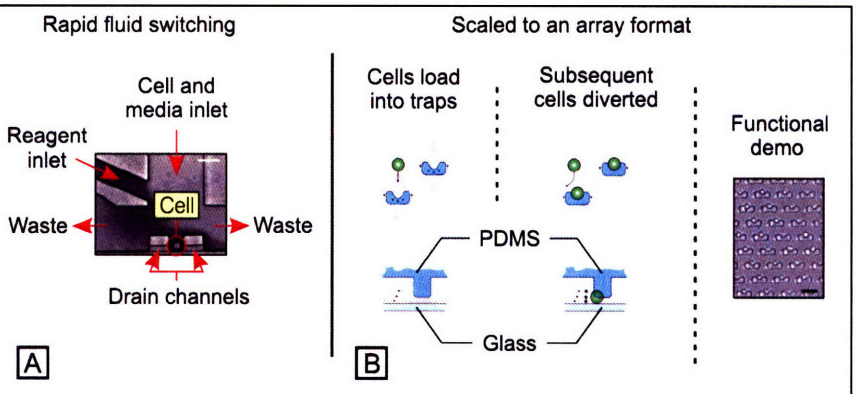

Figure 26: In prior efforts PDMS-based weir structures have been used to capture individual mammalian cells using a hydrodynamic damming effect. Designs have been demonstrated for applications where rapid switching between varied solution types presented functionalities beneficial for surveying the dynamics of various imaged responses **(A)**. Such advances have also been useful for establishing large arrays of on-chip cells **(B)**. All of these layouts have depended upon narrow in-system fluid gaps between a glass substrate and ceiling-affixed PDMS cell capture weirs. (Scale bars ≈ 50 μm)

Both of these efforts, despite their widespread acclaim within the microfluidic community, were built upon a sizeable history of prior dam-based retention architectures. Ages ago Native Americans even employed similar strategies for culling fish from flowing rivers, creeks, and streams. Using carefully placed

collections of reeds they could form weirs that permitted the passage of currents while channeling trout and other specimens into collections of reservoirs. Even at the microscale, in the past decade or more, various groups had used narrow on-chip geometries to retain biological samples in target locations[149-152]. The distinction between the efforts outlined above and other weir-based work is the dedicated focus toward stably capturing individual cells at very precisely positioned on-chip locations.

Perhaps ironically, in mid-2004, partially in the aftermath of experimental insights gained from tests with my original well-based n-DEP cell traps and partly motivated by a lab brainstorming session specifically focused on the development of novel cell manipulation strategies, I proposed exploring the feasibility of decoupling duties associated with on-chip cell capture and on-chip cell sorting. In other words, I wanted to assign the task of positioning cells in different substrate-indexed locations to one, or one set, of in-system components and conversely assign all sorting and manipulation responsibilities to another class of in-system parts. I knew that to constitutively activate on-chip electrodes, as would be necessary for DEP-based cell capture,

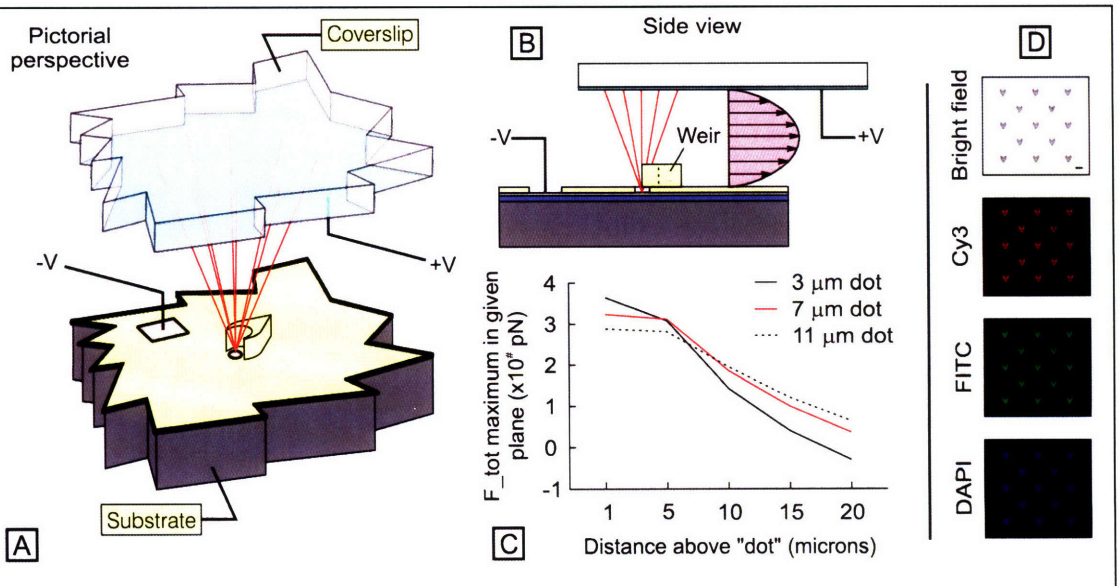

Figure 27: In an approach to on-chip cell manipulations developed concurrently with the works shown in Figure 26, I began testing an n-DEP-actuated weir system for enabling the selective retention of on-chip cells at target locations **(A)**. This design utilized substrate-affixed SU-8 weirs that presented large gaps between their top surfaces and the overhanging flow chamber ceiling. In these architectures I additionally positioned "dot" electrodes within the mouths of the capture crevice in the trapping weirs. I could polarize such "dots" by linking them to off-chip voltage sources and drive ITO conductive coatings on the fluid-side of the top coverslips using opposing voltages. As show by the red highlights an electric field would emerge to span the distance between the "dots" and the device coverslip. For assays using high-conductivity on-chip buffers, such field could create n-DEP forcing to unload cells from the weir capture faces. (The perspective view found in **(A)** highlights the geometry of an initial test design that patterns on-chip "dots" by simply covering a blanket film of aluminum with a thin perforated SU-8 layer.) For clarity, I provide a side view of this system setup in **(B)**. Using MATLAB-based simulations I modeled the maximum z-directed (normal to the device substrate) n-DEP forcing present throughout various planes located above "dots" of various sizes (on chip conductivity 1.5 S/m) **(C)**. A challenge affiliated with SU-8-based weir fabrication is the material's strong native autofluorescence response. Such effects could easily hinder observations of fluorescently-tagged proteins in neighboring cells **(D)**.

within a high-conductivity buffer would have the propensity for inducing unwanted Joule heating, electrohydrodynamic (EHD) flows, and additionally demand sizeable input currents to maintain proper in-buffer voltages. If I could therefore remove trapping duties from the suite of needs linked to in-system DEP actuation, I could potentially develop a viable scalable n-DEP-based "pixel" format for use in standard cell culture media.

In my then envisioned device architecture (as presented in Figure 27), I too imagined incorporating on-chip weir elements to serve as cell retention architectures. Beyond the functionalities offered by prior works[23, 148], my implementations would not only position cells at designated locations within a flow chamber, but they would also enable DEP actuated patterning and/or sorting of specific populations within the array. This heightened degree of flexibility could then serve to engender the precise organization of multiple cell populations, patterned as single cells, on a common substrate. As I mentioned in Chapter 1 and will further develop in Chapter 5, the ability to pattern cells as such meant that a functional version of an array incorporating such a novel "pixel" technology could adequately suit "endpoint" assays focused upon the divergent and/or overlapping responses of different cell types subjected to a common treatment.

The basic strategy for this setup incorporated substrate-affixed cell trapping weirs. My designs therefore, from the onset, contrasted the two techniques presented in Figure 26 which utilized patterned PDMS features mounted as stalactites (connected to an overriding PDMS slab that established the flow chamber ceiling) to establish narrow on-chip fluidic gaps. It was my conjecture that though a narrow fluid gap might enhance loading propensity, it was not necessary for producing a trapping response. With the weirs positioned on the floor of the flow chamber, I could align them to a series of on-chip electrodes which I hoped to use for delivering n-DEP repulsion forces. In my designs, I therefore needed a large gap between the top of the capture weirs and the in-chamber ceiling to enable repelled cells to vertically levitate and sweep out of the device. Such a setup could then essentially function as a revised version of the initial well-based designs, where here the electrodes rested beneath the cells to dislodge them from targeted array sites. Beyond an equivalent well-based geometry, this weir-based setup could additionally impose fewer confinement effects on retained cells after initial patterning efforts such that a more natural growth and migration dynamic could ensue. In other words, a surface peppered with weir-based cell traps was a closer mimic to a flat surface (such as within a tissue culture dish) than a well-laden surface.

Rather than attempt to assess the functionality of this new design using a two-level metal processing approach (both expensive and time consuming), I explored a simplified protocol for positioning polarized electrode "dots" beneath the capture regions of individual fabricated weirs (see Fabrication Methods Appendix "Initial SU-8 2002/2015-based process for electroactive weir designs). In the upper left of Appendix 8, I provide a breakdown of the actual layered stack of materials used to produce my initial test design. As shown, I first deposited a single 5000 Å thick blanket aluminum layer onto a thermally oxidized silicon wafer (thermal oxide grown under wet processing conditions to a thickness of 1.5 μm). I then used SU-8 2002 (MicroChem Corporation, Newton, MA) processing to establish a thin, 2-μm-thick, insulating layer covering all portions of the substrate except locations where "dot" features or probe taps were needed. With a second 20-μm-thick SU-8 layer (2015), I then formed the requisite on-chip weir

structures, registered in alignment with the on-chip "dots". (This portion of the process was largely inspired by work presented by Dr. Dirk Albrecht[153].) With the substrate portion of the device completed, I then used an indium-tin-oxide-coated (optically transparent, but electrically conductive; SPI Supplies Division of Structure Probe, Inc., West Chester, PA) coverslip to establish an in-system electrode along the flow-chamber ceiling. As is perhaps best seen in the side-view shown in Figure 27B (red highlights), I then assembled my devices such that, when oppositely polarized, the "dots" could form electric field linkages to the top ceiling-affiliated electrode. Using high-conductivity on-chip buffers, I then imagined that the strong field gradient surrounding the "dots" would institute n-DEP forcing effects that would repel nearby cells.

As an added attempt at clarification, I will point out that in all prior designs the on-chip "dots" served as sinks to which cells localized (via p-DEP forcing), and in this implementation the "dots" instead serve as sources that push cells away (via n-DEP forcing). In prior designs cells were simply moving up the field gradient and here they are moving down it (again, all consequences of the effective in-system CM factor values).

To try and understand what types of n-DEP forces might arise when using high-conductivity medias in this system setup, I examined a number of different "dot" sizes, ran the affiliate COMSOL and MATLAB codes, and surveyed the maximum z-directed (out of the substrate) forces in planes positioned at various distances from the substrate (see Figure 27B). The conclusion of my investigation was that, for a seemingly wide variety of different "dot" diameters, I could produce sizeable forces (tens to hundreds of pN) for a nominal "dot" to ceiling voltage difference of 1 V delivered at 100 kHz (flow chamber ceiling positioned 250 μm above the substrate).

In initial testing sequences with this design, largely run by my UROP (Theresa Guo), it proved possible to at least retain polystyrene beads of certain sizes against the capture faces of individual substrate-affixed weirs. Unfortunately, in part due to complications emerging from delamination of the thin SU-8 layer designated for patterning the "dot" geometries and perhaps due to inadequate "dot" formation, the desired DEP actuation proved to be an elusive response. Additionally, though not surprisingly, the autofluorescence response of the SU-8 material (see Figure 27D) offered an added complication for designs requiring the observation of fluorescently-tagged proteins located within neighboring cells. A dominating fluorescent signal from the weir itself could easily compromise the ability to observe more weakly-emitting responses from the in-cell constructs. In effect, it could unintentionally render the same sort of blinding effects experienced by deer gazing into the headlights of oncoming cars. Though I was confident I could overcome the on-chip DEP activation challenges faced in my initial designs, I was not initially certain how I might overcome the autofluorescence concerns endemic to SU-8-based weirs.

A new material for weir formation

Lacking a straightforward avenue for managing the SU-8 emission issues I shelved my dedicated push to investigate enhanced design implementations until I later discovered a photopatternable silicone (PPS) product manufactured by Dow Corning (Midland, MI). This material had originally been developed for flip-chip-based integrated circuit (IC) packages[154, 155] to enhance chip-to-chip contact reliability. When surveying literature regarding the product's material

properties, my colleague, Salil Desai, and I discovered that beyond its photopatterning capabilities, it was formulated to effectively mimic PDMS-based chemistries. We began to imagine that we might have an opportunity to combine key benefits once under the purview of either soft-lithography approaches alone (low autoflourescence and reliable bonding to oxided substrates) or SU-8 processing alone (high-aspect ratio, i.e. height:width, free-standing on-chip features). With this understanding in mind, we obtained a sample of the product and began testing its potential to service different project needs for my electroactive hydrodynamic weir designs[43].

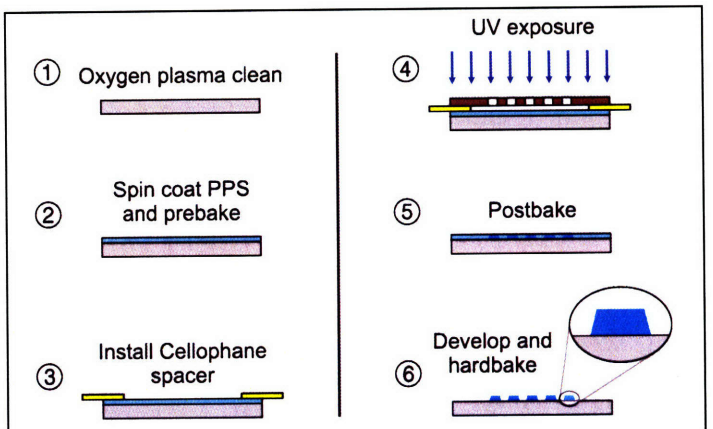

Figure 28: Here I provide the baseline sequence of steps needed for PPS processing. This photo-patternable silicone product produces on-chip free-standing features with minimized autofluorence characteristics. As the material is exceptionally "tacky" prior to curing, it is necessary to separate chrome masks from the spin-coated polymer (3&4). Such separation protects the film and the mask, but frustrates efforts to produce vertical sidewall profiles.

To process this material, we developed an in-house approach, partially adopted from the spec sheet recommendations and in part from discussions with one of the product's key developers, Herman Meynan[154] (detailed using cross sections in Figure 28). In brief, similar to SU-8-based efforts PPS demands spin-coating, UV exposure, and subsequent development and hardbake procedures. I offer the complete details of this process in the Fabrication Methods Appendix under the subheading "Original PPS weir fabrication process".

One of the challenges associated with its affiliate processing stems from the fact that uncured prebaked PPS films present remarkably tacky surfaces. Unlike other materials typically used in a microfabrication context, if uncured PPS ever directly contacts the patterning mask it can adhere with such strength that it will not only ruin the once-pristine PPS coating, but it will often additionally cause wafer and/or glass mask fracture during attempts to separate unintentionally bonded wafer/mask stacks. To offset this potential, through a bit of trial and error, we eventually decided to use hand-cut Cellophane rings around the perimeter of each wafer to slightly separate masks and uncured PPS films. Unfortunately, as one might expect, introducing this gap during the photopatterning stage, made imposed complications for producing on-chip features with vertical side walls. Obviously, in the context of weir fabrication, a vertical side wall would only serve to benefit cell retention capabilities. We hoped to avoid designs that could ramp cells up and over in-system weirs.

After refining the sequence outlined in Figure 28, we began efforts to evaluate key material performance metrics. As detailed in Figure 29 and the top middle of Appendix 8, our approach focused on sidewall profiles, resolution capabilities, fluorescence responses, and concerns pertinent to the material's biocompatibility. In comparison to SU-8 (2015; processed as detailed in the Fabrication Methods Appendix steps 11-19 of the "Initial SU-8 2002/2015-based process for electroactive weir designs"), PPS consistently presented a sidewall angle (measured with

respect to the chip surface, and internal to the PPS feature) of ≈76° (n=8), while equivalent SU-8 designs rendered reentrant angles measuring ≈94° (n=12). Certainly the SU-8 outperformed the PPS in this context for purposes of electroactive weir design, but at only 14° from vertical, I held hope that PPS might prove straight enough for functional designs.

From the perspective of resolution, we printed copies of a standard USAF 1951 test target to again render features in both PPS and SU-8 (films each nominally 20-μm-thick). As shown in Figure 29, and expected from the sidewall comparison, the PPS failed to match the patterning performance made possible when using SU-8 films. The ultimate resolution repeatedly enabled by PPS was ≈10 μm, while SU-8 catered to a resolution limit of ≈6 μm.

Interestingly, PPS features, in cured form, seemed to regularly adhere to the surface more reliably than comparable SU-8 structures[26]. In all cases, when we examined the smallest patterned PPS features, although they were ill-formed, they did remain fastened to the substrate. In contrast, many of the smallest SU-8 features (line width ≈5 μm) were entirely absent from the wafer. In subsequent mechanical probe tests, PPS structures stretched away from the substrate and even ripped prior to separation from the underlying wafer. Such a response comes in stark contrast to similar SU-8 features, which completely detached from the wafer when subjected to comparable probing forces.

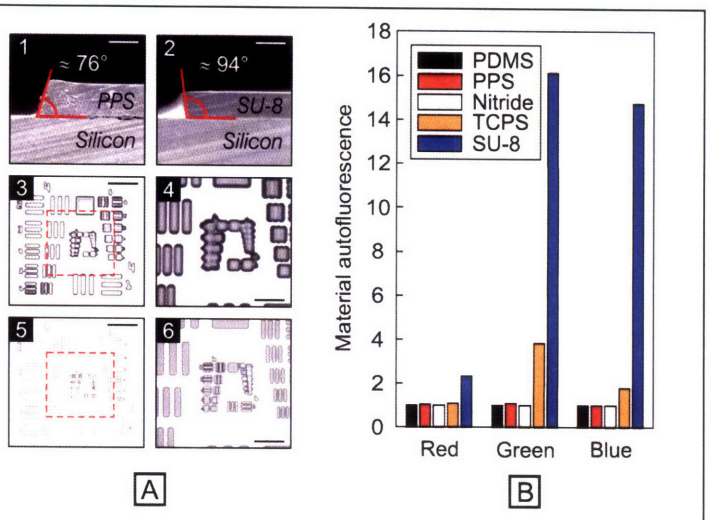

Figure 29: In 1&2 (Scale bars ≈25 μm) of **(A)** I present side-on SEMs displaying the sidewall profiles of PPS and SU-8 respectively. In 3&5 (Scale bars ≈50 μm), I provide a resolution test print of PPS and SU-8 with corresponding closeups in 4&6 (Scale bars ≈ 25 μm) (highlighted by the dashed red boxes). Using samples of both typical tissue culture surfaces as well as calibrated films of various types, I show comparative measured material autofluorescence values **(B)**. Here I normalize the autofluorecence levels associated with PDMS to values of 1 for each channel (red, green, and blue). For all channels, PPS demonstrates responses comparable to those endemic to PDMS and tissue culture polystyrene (TCPS).

We quantified the intrinsic fluorescence associated with various materials relevant to bioMEMS fabrication and tissue culture applications using the plot shown in Figure 29B. Here, we imaged silicon samples coated with PDMS (20 μm thick), PPS (20 μm thick), silicon nitride (250 Å thick - thickness commonly used in our in-house work), SU-8 (20 μm thick), and a separate tissue culture polystyrene dish (TCPS) (Nunclon Δ - Nalgene Nunc International, Rochester, NY) (all processing methods involve subcomponents of various sequences offered in the Fabrication Methods Appendix) using Cy3 (red), FITC (green), and DAPI (blue) filter sets (Chroma Technology, Rockingham, VT) at fixed exposure times (red = 750 ms; green = 3000 ms; blue = 150 ms). In acquiring these images we ensured that the camera's dynamic range was substantial enough to avoid pixel saturation. We then averaged the pixel-wise response from each image to produce an affiliate measure of the examined

fluorescence. By normalizing all of the values to the PDMS output of each channel we could then compare the relative responses for each material. Of significance, the PPS performed in a manner comparable to standard 10:1 PDMS and even presented responses that were less intense than TCPS for all channels. This low autofluorescence was somewhat surprising since many photopatternable polymers demand cationic activation of epoxy side chain groups and an associated cross-linking of shared aromatic hydrocarbon backbones[156]. Such aromatic constructs, with characteristically delocalized π-bond p-orbital overlap, permit a multitude of electron energy states that typically provide affiliated compounds with substantial, widely reported[157-163], native autofluorescence characteristics. SU-8 presented the highest fluorescence levels in this study, well above all materials examined, with a possible exception being made for imaging in red (~ 2× over PDMS).

To better understand these fluorescence behaviors in the context of applications demanding on-chip cell handling we grew HeLa cells (initial plating concentrations ~ 1E5/mL; ATCC, Manassas, VA) on each surface type for four days and then stained (see Biological Methods Appendix "Fixed-cell staining methods") with nuclear (hoechst; blue), and actin (phalloidin; red) specific fluorophores (see part A at the center top of Appendix 8; Scale bar $\approx$50 μm). (This HeLa line constitutively expressed a green whole-cell fluorescent reporter.) We chose exposure times for each channel such that we could produce high-contrast imaging on the largest possible subset of our examined surface types. Subject to these conditions, some of the SU-8 images saturated (green and blue channels) highlighting some of the challenges associated with imaging cells in microsystems reliant upon the polymer. To avoid falsely presenting the case, it *is* possible to optimize SU-8 exposure conditions (at least to some extent) for imaging cellular fluorescence (see part B at the center top of Appendix 8) but the autofluorescent behavior native to SU-8 fundamentally compromises the contrast enabled between the sample and the background, thus, as mentioned before, limiting the ability to perform sensitive fluorescence-based assays.

Coupled with this cell-based autofluorescence investigation, we examined, using the same staining techniques as mentioned prior, the material-specific morphologies present in both 3T3 and Hela cells after four days of on-surface growth. Though I do not present the data in explicit form here, for all surfaces, both cell lines exhibited morphologies closely matching those typically seen in standard tissue culture polystyrene dishes. Additionally, none of the tested materials altered the proliferation rates of either cell line over the span of the study.

As one final test, we attempted to pattern strips of PPS onto a wafer that displayed a series of interdigitated electrodes on its top surface. Not only did it prove feasible to align the PPS with ± ~1-2 μm x- and y-directed repeatability, we also discovered that development of the material left behind only negligible amounts of residue or in unintended portions of the wafer surface. We validated this effect by placing fluorescently-tagged cell suspensions onto the fabricated surface. We then activated the on-chip IDEs and witnessed DEP forcing effects upon the cells located above the electrodes and an acute lack of DEP forcing effects along portions of the wafer surface covered in patterned PPS strips. As I will discuss in more detail further along in this chapter, even small amounts of on-chip insulating residue own the potential to limit in-buffer forcing effects (especially when using cell culture media as we did in this round of functional testing).

With a clear cut, validated means in hand for manufacturing free-standing photopatterned biocompatible geometries that displayed minimal autofluorescence, PPS illuminated a new avenue for exploring electroactive weir "pixel" designs. In the following section I will discuss steps taken to deliver the first fully functional architecture of this type.

A functional n-DEP-actuated hydrodynamic trapping weir

Though I had hoped to avoid using advanced fabrication techniques to explore my envisioned electroactive hydrodynamic weir "pixel" designs, the challenges faced in attempting to offset complexities using the approach detailed in Figure 27 failed to provide a conclusive performance evaluation for on-chip n-DEP actuation. As such, I leveraged the expertise developed for the two-level metal processing work discussed in Chapter 3, to develop a series of test designs[37-39].

A unique aspect of the mask set associated with this next segment of my doctoral work, was the inclusion of two distinct chip classes that allowed me to stop fabricating after either the Metal 1 level was patterned or after the Metal 2 level was finished and still produce wafers with fully functional chips. In other words, if I wanted to invest only a short amount of time in substrate fabrication, I could remove a wafer from the manufacturing process after etching the Metal 1 layer, and at least some fraction of the total number of die on the wafer would present collections of electrodes that, when properly packaged, would deliver the correct voltages to all essential on-chip locations. Additionally, if I needed to test chips on the wafer that would otherwise be nonfunctional without the presence of a second metal layer, I was careful enough to organize my mask set such that I could protect the subset of chips not dependent upon such extended attention. While such efforts may not sound overtly sophisticated, they actually demanded the inclusion of on-chip vias in specific locations and redundant trace patterning (i.e. routing patterns originally made in the Metal 1 layer would be repeated again in the Metal 2 layer) to avoid inadvertently burying electrodes beneath the deposited intermetal dielectric. If I had been intending to always push wafers through the Metal 2 patterning step, the overall wafer organization would have been simplified, but it would have arrived at the expense of demanding more extensive processing for each and every device.

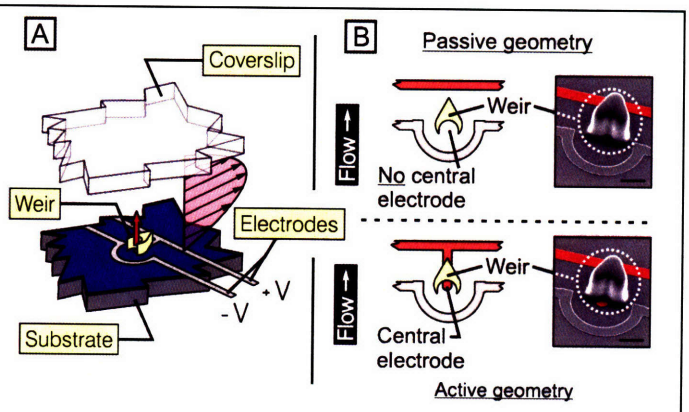

Figure 30: In revised designs, I successfully fabricated electroactive hydrodynamic weirs using basics from the two-level metal process developed in the work from Chapter 3 coupled with successive PPS patterning efforts as outlined in Figure 28 **(A)**. For functional tests, I used combinations of *passive* and *active* geometries that either lacked or leveraged a central actuation electrode **(B)**. In addition to top-down schematics **(B)** offers pictorial SEMs of each of these "pixel" types.

Beyond parsing my overarching process flow to enable stop points after either the Metal 1 or Metal 2 patterning sequences, I organized my entire chip set such that I could effectively package my devices in a way that would meld with the full suite of scaled peripheral design componentry discussed in Chapter 3. Here, I once again used the duty-based bondpad segmentation originally developed for my 20 × 20 designs to link on-chip

electrode elements to off-chip signaling. This added planning produced a chip set that required no new "packaging" or "adapter" boards beyond those that had originally been manufactured for prior scaled efforts. I was also able to simply reassign MATLAB-controlled digital I/O signaling using a few lines of added coding on the backend of my software interface and, in short order, I had a complete set of functional chips available for testing. Two key factors with different time sensitivity played into this chip set organization. On the one hand, I needed rapid turnaround to evaluate my designs prior to the MicroTAS 2007 abstract deadline but alternatively I also wanted to hedge my bets that I could produce a functional device that might later prove useful for more involved biological assays. As a result, stopping fabricating after Metal 1 processing gave me a decent set of test chips. For enhanced work that was less time sensitive, I could progress through the Metal 2 sequence and eventually have production-style devices in hand for performing more advanced assays.

In Figure 30, I present the first functional implementation of an electroactive weir. Using patterned on-chip aluminum traces and subsequently-aligned PPS weirs, I fabricated a "pixel" design that offered the potential to surpass all assay-based capabilities demonstrated by prior passive single-cell trapping weirs and could use n-DEP forcing (see red arrow in Figure 30A) in ways that would both minimize in-buffer heating and current demands when compared to all prior works employing such means to both trap and sort cells[106, 114, 164, 165]. In my initial test configurations, which simply sought to evaluate the feasibility of using this new manipulation approach, I employed two different "pixel" types, one I termed *passive*, and the other I termed *active* (see Figure 30B). In my *passive* footprints, I intentionally avoided patterning electrodes beneath the capture cups of the cell trapping weirs. Alternatively, the *active* designs presented centralized 10-μm-wide electrodes that, when partially covered by the PPS weir, functioned as "dot" electrodes that could initiate electric field line linkages to a surrounding peripheral half-"ring" electrode. Again, in both the *passive* and the *active* designs on-chip flows would load the weirs. The *active* weirs would simply have an added n-DEP-based means for unloading their affiliate capture faces. Later in this chapter, I will discuss functional results obtained and assays run using this new device configuration.

Mechanical properties of patterned on-chip weirs

In all of my prior developed microsystems platforms, a key endpoint step in almost any cell-based assay has involved a brief sonication bath routine. In such sequences I turn ON an ultrasonic transducer to bombard my devices with various pressure waves, while I hold the system packaging submerged in a water-filled tank. The incident pressure waves cause small vibrations along the surface of the chips that prove effective in releasing stubbornly adhered biomaterial within the on-chip flow chamber. In many ways, such procedures offer a reset functionality that cleans and unfouls the chip either readying it for a subsequent round of experimentation or leaving it in a safe condition prior to storing it for later use.

As I noted earlier in this chapter, PPS seemed to render a stronger adherent bond to underlying substrates than SU-8. In initial tests with SU-8 based weirs, sonication cleans at the end of a set of experiments proved somewhat disastrous. Though they were useful for removing in-chamber debris, they also regularly separated the weirs from the substrate. Without weirs there was then no way to trap cells and the device was effectively ruined. I was then curious to investigate

whether or not such effects were common for PPS-based weirs, and if so, whether or not there might be some way of circumventing such a complication through altered weir designs.

Using a high-resolution in-house-processed glass mask (Heidelberg USA, Inc., Kennesaw, GA) I developed a series of distinct weir test geometries. As shown and labeled at the upper right of Appendix 8, when progressing from design type 1 through 4, the weir footprints provided larger and larger footprints. It was my suspicion that if I could increase the contact area between individual weirs and the underlying substrate, I could potentially offer designs that might not become damaged during sonication bath exposure.

Though I only tested this effect one time across eight different chips (one of type 1, 2, 3, and 4 both with and without a central slit as shown in the key found at the center of Appendix 8), I did gather some support for the idea that larger weir footprints (at least when fabricated in PPS) indeed tended to promote enhanced substrate adhesion. The plots located mid-page in Appendix 8 provide some interesting insight. First, as sonication exposure time increased, all weir types eventually began to detach from the substrates. Second, the weir designs that lacked a central slit almost always outperformed the comparable slit-based geometries. As one might speculate, the presence of a central slit effectively reduces the total amount of x- and y-linked polymer in contact with the substrate. As a result, a slit in even the largest footprints essentially creates two adjacent smaller foot-print designs which logically would tend to release more easily.

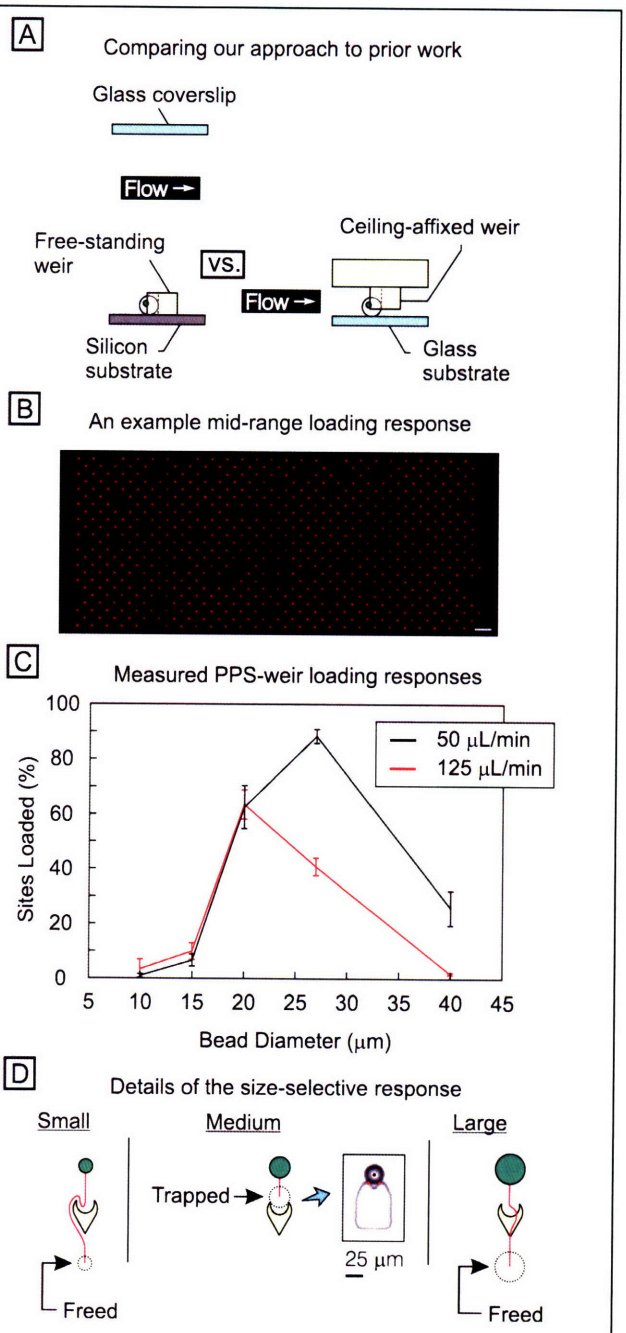

Figure 31: In side-view form, I compare my efforts (left) to competing designs offered by other groups in the field (right) **(A)**. Despite the large-gap features present in my designs, array-based bead capture proves feasible (Scale bar ≈100 μm; bead diameter ≈27 μm) **(B)**. For differing flow rates (flow chamber height ≈250 μm; width ≈4mm) my PPS weirs demonstrate an interesting size-selective response where capture is preferred for specific bead sizes **(C)**. The typical rejection means for small beads (10-15 μm) is to wrap laterally around the trap, while the typical unloading avenue for large beads (40 μm) is to rotate up and over the weir **(D)**.

Though this set of response curves was not terribly encouraging, I should note that in retrospect my evaluation protocol was a rather aggressive routine. In general, 15 seconds (the first data point recorded) of sonication exposure extends well beyond the time spans typically used in most such cleaning efforts. In cursory subsequent examinations I discovered that a short 1-2 second sonication burst, especially with the larger footprint designs, was adequate for resetting devices without tearing PPS weirs away from the device substrate. In the protocols outlined in the following section, I found that I could clean my devices in such a manner multiple times without inducing undesired chip damage.

To be certain, the size of the individual weirs can eventually impact the maximum number of trap sites one might wish to pack into a given amount of exposed surface area. Carefully balancing between a need to render implementations capable of surviving sonication cleans and a converse need to position as many traps within an array as possible is a realizable objective.

Passive loading responses of substrate-affixed weirs

As discussed prior, the basic configuration for my weir designs demanded on-chip free-standing substrate-attached geometries that contrasted the traditional ceiling-mounted approach. To better outline this difference in stark terms, I present side-view perspectives of my designs and those offered by others[23, 148] in Figure 31A. Again, my implementation uses a large gap between the top of the individual weirs and the ceiling enabling the vertical repulsion of unloaded cells. Prior works have always instead leveraged a narrow gap separating weirs from the on-chip substrate.

Though I had some empirical support for the presence of effective trapping responses in my implemented architectures, I wanted to investigate the behavior more rigorously before progressing to assays with electroactive weirs. To approach this end, I used an experimental protocol outlined in the bottom left hand corner of Appendix 8. I would first assemble a chip that lacked on-chip electrodes and presented over 600 instances of a given weir design (step1). Based upon my initial sonication testing, I decided to use the largest configuration weir designs (a.k.a. type 4) for all of my loading tests. (If I was going to use a chip multiple times I wanted to give it the best possible chances of surviving.) I would then saturate the on-chip environment with beads of a designated size (step 2; typically using concentrations in the 1E7/mL range or higher) and finally, use syringe-pump-driven flow, to flush the chamber at a prescribed rate (all on-chip chamber heights $\approx$250; all widths $\approx$4 mm) for designated amounts of time. At the end of such routines, I would then count the number of beads retained in the traps and record loading percentages for different flow rate and bead size pairings. I performed 4 runs for each flow rate and bead size condition and then, as shown in Figure 31C, plotted the average responses (error bars indicative of standard deviations seen across the individual runs).

As shown in Figure 31B, certain assay conditions (27-μm-diameter beads at 50 μL/min) produced high-percentage loading efficiencies, echoing the behaviors seen in ceiling-mounted approaches. Such experimental evidence showed, for the first time, that the presence of a narrow on-chip fluid gap was NOT essential for enabling single-particle retention in array-based formats. Of additional interest, my PPS weir loading study uncovered a size-selective response where particles falling within a specific range of diameters routinely offered higher cross-array loading percentages than particles sized either smaller or larger. Figure 31D provides a

mechanistic explanation for the size-selective behavior that emerged in the loading response curves of Figure 31C.

Smaller particles (i.e. 10-15 μm) would often enter the capture cups and then follow streamlines that encouraged the impinging particles to progress laterally around the sides of individual weirs where they were subsequently caught by passing flow and swept off-chip. Such unloading effects were not always immediate as it was often the case that small particles could hold in place for 10s of seconds at the center of the capture cup before initiating a migration out of the trap. Oversized particles (i.e. 40 μm) would instead, hold momentarily within the capture cups and then by means of a torquing effect rotate up and over the in-system weirs. It is my suspicion that, in such cases, the center of gravity associated with the loaded particles is elevated above some critical height that makes it energetically more favorable for particles to unload over the top of the weir than by meandering around the side. Appropriately sized beads (i.e. ~20-30 μm) seemed to remain in place and regularly appeared to contact the weir structures at two discrete locations (highlighted using red dots in Figure 31D). I am curious to know whether or not this two-point-contact mode of loading ensures the stable retention of particles within a trapping weir. To date, efforts to shed added light on this effect from a model-based approach have been inconclusive. Further along in this chapter I will detail some of the modeling work that has been done to analyze my weir geometries and in Chapter 6 I will point to on-going progress in this domain.

As one final note on the loading response curves developed for Figure 31, each trace represents the single-bead loading characteristic. To avoid unnecessary detail, I chose not to include data reflecting the multi-bead loading characteristics observed for each case (in other words, traces for the number of on-chip weirs retaining two or more beads within their capture cups). Regardless of flow rate and/or bead size, across all examined conditions multi-bead loading produced only single-digit retention percentages. This dynamic supports the notion that once an individual weir loads with a single-bead, a crowding effect arises such that additional beads are not encouraged to localize to the filled trapping sites.

Functional demonstrations with my electroactive weir geometries

To encapsulate the significance tied to the first functional validation of my electroactive weir designs, I present its two key operation modes and an affiliated patterning result in Figure 32. As rendered in a stepwise sequence at the top of Figure 32A, my first demonstration with this new "pixel" type examined an ejection response behavior. Here, based upon the sizing work done when exploring the effects monitored in Figure 31, I chose to initially load on-chip weir locations with reliably-captured 27-μm-diameter polystyrene beads delivered in a PBS buffer (frame 1). With both *passive* (highlighted by the blue arrow) and *active* (designated with the red arrow) weirs filled, I then turned ON the in-system n-DEP actuating electrodes. The *active* sites, which presented "dot" electrode mimics beneath the loaded beads, successfully exerted levitation forces upon the initially loaded beads. This forcing effect, as hoped, caused the trapped beads to rise above the weir capture cups. These rising beads then became caught in the overriding fluid flow such that they were eventually drawn downstream and out of the device. Alternatively all of the *passive* sites, which lacked the critical central electrodes, retained their initially loaded cells. In this sequence I therefore effectively demonstrated the differential behaviors of both *passive* and *active* designs.

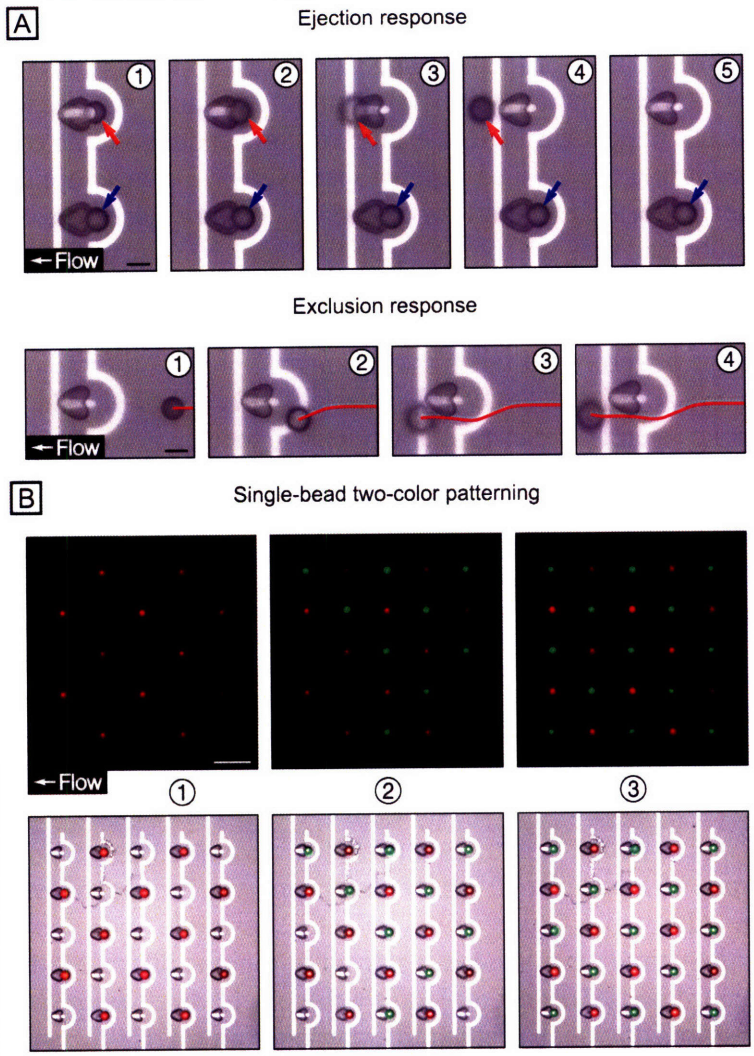

Figure 32: In **(A)** (Both scale bars ≈30 μm), I highlight the two distinct actuation modes enabled by my electroactive hydrodynamic weir "pixel" implementations. At top, the ejection response can unload initially-filled sites by exerting n-DEP pushing forces that encourage held particles to levitate away from the weir capture crevices. As these particles rise, they become caught by overriding fluid flow and eventually progress off-chip. Alternatively (bottom portion of **(A)**), it is possible to prevent weir site loading altogether using exclusion response dynamics. Here, we activate the on-chip electrodes prior to introducing particle-laced fluids onto the chip. As particles impinge on the traps, they deflect away from the capture crevices eluding viable retention. In a functional demonstration with beads, I use the ejection response technique to first fill only the passive on-chip sites (first frames in **(B)**). I then deactivate all of the electrodes and slowly backfill the remaining sites with a different bead population (green). This effort produces a dual population interleaved collection of patterned beads. (Top series of images in (B) show fluorescence channels only; Bottom series merged with brightfield; Scale bar ≈100 μm)

As a second strategy for enabling on-chip particle manipulations, the lower portion of Figure 32A details elements of an exclusion response dynamic. In this manner of device operation, I successfully prevented weir loading altogether. Here, prior to injecting particle-laced solutions into the on-chip fluid environment, I activate all on-chip electrodes. As particles approach the weir-based traps, they experience n-DEP repulsion effects that prohibit them from localizing to individual capture cups. As a result, the beads never fill the activated sites.

Regardless of which operational mode one chooses to use, an interesting aspect of this "pixel" design implementation is that all particles remaining loaded within a trapping array nominally witness no n-DEP forcing. For on-chip "endpoint" assays, this effect means that issues and concerns related to induced transmembrane potentials or Joule heating become largely irrelevant. In many ways, this key component of device operation, when coupled with the fact that on-chip operations prove feasible in standard high-conductivity cell culture media, allays many of the fears that skeptical users might have once directed toward prior efforts developed as a part of my doctoral work. With a demonstrated functional configuration of this type, I have provided a means for

overcoming a great number of long-standing complications for cell-based work leveraging DEP-actuated microsystems.

In Figure 32B, I offer the first known means for positioning separate subpopulations of individual micron-scale particles in organized patterns on a common surface, where the technique enabling such functionality is not dependent upon the field of view endemic to an off-chip microscope. I make this caveat regarding the imaged field of view simply because optical tweezing-based strategies[25] have demonstrated the potential for organizing particles as such, but depend upon the ability to view the objects that are being manipulated. This dependence emerges because lasers necessary for enabling on-chip forcing must be ported in through the microscope objective. To the contrary, in scaled implementations of my "pixel" designs, it is feasible to imagine forming large areas of patterned particles that span well beyond the regions specific to any imaged field within the array. All that is needed is the presence of a weir and an affiliate set of electrodes. Such on-device elements can prove active, whether or not someone elects to view them while they are in operation.

I outline the routine used to form the interleaved checkerboard pattern of green and red beads (shown in Figure 32B), using a sequence of images. I first loaded all on-chip locations with red fluorescent 27-μm-diameter polystyrene beads. I then (as labeled "1") used the on-chip ejection response to unload all of the *active* sites. After swapping the input bead suspension to one containing green fluorescent 27-μm-diameter polystyrene beads I then turned all of my system electrodes OFF and began backfilling the empty *active* sites. After some time, all of the on-chip weir locations loaded to produce the desired interleaved checkerboard pattern of green and red beads.

As I detail in the lower right hand corner of Appendix 8, while performing the functional tests presented in Figure 32, I noticed an admittedly unintended, but still desirable, behavioral mechanism affiliated with my devices. Any time when a bead localized to regions internal to the outer peripheral semi-"ring" electrode and I subsequently turned ON the electrodes, I witnessed an interesting reset effect. All beads positioned as such seemed to experience an n-DEP focusing force that encouraged bead migration toward the central capture region in the weir. My n-DEP modeling efforts had originally focused upon the dominant "dot" emergent forcing effects within such "pixels". Again, here, a full system model might have provided the added insight necessary to predict effects linked to the less substantial DEP forcing effects emergent from the peripheral semi-"dot" electrodes. In *active* design footprints it proved possible to tune the applied activating voltage to either focus beads into the capture cup or to repel them vertically out of the traps. This type of on-chip reset potential meant that if there was ever a case where I stopped on-chip flows and then inadvertently jostled the chip, the stage, or the attached fluidics to an extent that caused particles to partially unseat from the capture faces, I could simply turn the electrodes back to an ON setting and reload the on-chip weirs. (To clarify, it is not necessary to maintain an on-chip flow to retain particles in the weirs once they have loaded.) Again this sort of functionality surpasses that seen in any prior weir-based efforts.

On might ask whether or not it could prove possible to engineer a ceiling-mounted weir for the purposes of enabling the types of functionality present in my implemented designs. Because there is no physical path to permit the vertical displacement of held cells in a ceiling-mounted

implementation, it is not possible to couple such an approach with on-chip electrodes such that an ejection response could enable cells to cascade over and out of on-chip weirs. It is however conceivable to imagine eliciting an exclusion response dynamic, where nearby electrodes prevent site loading from the onset. Two challenges arise in such a context. First, for proper operation each weir would demand effective alignment with an affiliate set of electrodes. Unfortunately, since ceiling-mounted weirs are produced separately from the substrate, there would be a need for aligning weirs and electrodes as a key step in the device packaging process. In general, far fewer tools exist for enabling such alignment efforts when compared to the types of in-cleanroom capabilities associated with PPS-based processing. Second, the narrow gaps needed for ceiling-mounted weir trapping, can easily create on-chip regions where the forcing effects induced by hydrodynamic flows readily dominate over the forcing delivered by DEP actuation. (Note: I make the preceding statement based upon my own personal experience with narrow-gapped geometries used in another context. I will discuss such details more specifically in Chapter 6.) If, as I suspect, this condition were to arise, even for a ceiling-mounted design that was well aligned with in-system electrodes, the DEP repulsion effects could do very little to prevent site loading. In the end, such an effect would mean that great pains had been taken to try and add a level of functionality to an originally passive weir that would not in fact provide the desired response.

The impact of on-chip insulating films

Though I have mentioned details pertaining to on-chip insulating films in relation to work presented while investigating the non-specific trapping responses stemming from ill-formed on-chip "dots" (see Chapter 2) and as a validation for the low residue patterning potential of PPS (earlier in this chapter), such concerns become especially relevant in contexts where high-conductivity on-chip buffers are the norm (as is the case for my electroactive weir geometries). To transition from a platform functional for bead-based assays, I thus needed to understand the impact that on-chip nitride layers (seemingly key for preventing cell adhesion) would present for producing designated in-buffer voltage drops. In all of my p-DEP based efforts, I had used a 250-Å-thick nitride to passivate the surface of my wafer. I was suspicious that a film with this thickness could easily limit my capacity for exerting on-chip DEP forces.

To examine the case in generalized terms, let us take the bank of interdigitated electrodes and the associated lumped-element model presented at the top of Appendix 9 as our starting point. In this context the IDEs represent a generic set of electrodes that we might want to place onto a given device. We can examine and model the impedances spanning adjacent electrodes using a linear network of resistors and capacitors.

Essential to this model are three key impedance blocks (highlighted in red) that characterize individual electrode pairs. Each impedance block consists of a resistor-capacitor pair connected in parallel. Z_{INS} (assembled from R_{INS} and C_{INS} components - left unlabeled in the impedance block for clarity) models insulating films that might cover the top surface of our IDE-based device. On the other hand, Z_{MEDIA} (comprised of unlabeled R_{MEDIA} and C_{MEDIA} components) models electrical characteristics of the on-chip liquid.

For effective operation our devices must minimize the voltage drop arising across any on-chip insulating films. This fractional voltage drop, which I have alluded to at points prior in this dissertation, is best described by the following transfer function:

$$H(i\omega)=\frac{V_{OUT}}{V_{IN}}=\frac{1}{\frac{2R_{INS}}{R_{MEDIA}}\left(\frac{1+i\omega R_{MEDIA}C_{MEDIA}}{1+i\omega R_{INS}C_{INS}}\right)+1}$$ **Equation 28**

Here, V_{OUT} represents the in-media voltage drop resulting from the input voltage, V_{IN}. We can model the resistances and capacitances in this equation as:

$$R_{INS}=\frac{t_{INS}}{\sigma_{INS}wl} \qquad C_{INS}=\frac{\varepsilon_{INS}\varepsilon_0 wl}{t_{INS}}$$
$$R_{MEDIA}=\frac{t_{MEDIA}}{\sigma_{MEDIA}h_{MEDIA}l} \qquad C_{MEDIA}=\frac{\varepsilon_{MEDIA}\varepsilon_0 h_{MEDIA}l}{t_{MEDIA}}$$ **Equation 29**

In these expressions, t_x is the layer-specific thickness, σ_x is the material-specific electrical conductivity, w is the electrode width, l is the electrode length, ε_x is the material-specific relative electrical permittivity, ε_0 is the permittivity of free space, and h_{MEDIA} represents the media height used to characterize the resistive and capacitive paths passing between the electrodes, through the media.

In this setup, the time constants (RC) reduce to the expected forms shown here:

$$R_{MEDIA}C_{MEDIA}=\frac{\varepsilon_{MEDIA}\varepsilon_0}{\sigma_{MEDIA}} \qquad R_{INS}C_{INS}=\frac{\varepsilon_{INS}\varepsilon_0}{\sigma_{INS}}$$ **Equation 30**

The resistance ratio $\frac{R_{INS}}{R_{MEDIA}}$ evaluates to:

$$\frac{R_{INS}}{R_{MEDIA}}=\frac{\sigma_{MEDIA}t_{INS}}{\sigma_{INS}w}\cdot\frac{h_{MEDIA}}{t_{MEDIA}}$$ **Equation 31**

To determine a value for the ratio $\frac{h_{MEDIA}}{t_{MEDIA}}$, I used COMSOL to solve Laplace's equation between an electrode pair positioned in an ohmic medium subject to the limiting case where no on-chip insulating films exist. Applying a 1 V potential across the electrodes and numerically evaluating the resulting current, provides:

$$\frac{h_{MEDIA}}{t_{MEDIA}}\approx 0.5\ [\text{S/m}]$$ **Equation 32**

This value permits computation of the system transfer function $H(i\omega)$. Though not explicitly developed here, the form of $H(i\omega)$ is largely independent of the specific electrode geometry, thereby offer a result useful for a variety of on-chip electrode implementations.

Figure 33 provides a Bode plot of the transfer function's (Equation 28) magnitude response for a set media conductivity of 1.5 S/m and a range of insulator thicknesses (for this specific case I assumed the on-chip insulator was silicon nitride). Ideally, in the typical DEP frequency operation band (100 kHz - 100 MHz) one would like a magnitude response of 0 dB. In the case of the 1.5 S/m media, even 10 nanometers of a residual on-chip insulator would begin to undesirably mask on-chip voltages at frequencies below 10 MHz.

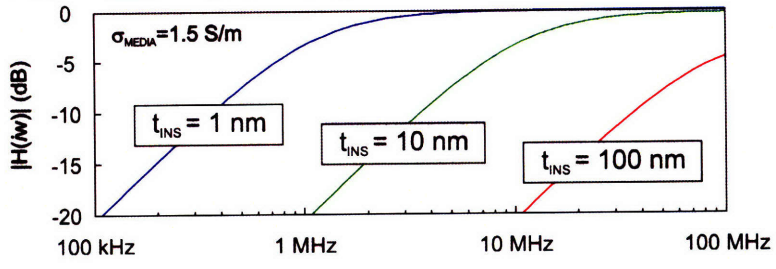

Figure 33: Using a model first mentioned in Chapter 2 and further developed here, I provide a response plot showing the impact that on-chip insulating films can have upon the ability to produce in-buffer voltage drops. In a plot of the transfer function magnitude (detailed in Equation 28 and at the top of Appendix 9) insulating films even 10 nm thick can cause notable reductions in the magnitude of administered signals. This response affects permissible deposited nitride coatings as well as residual on-chip PPS "scum".

This result has a serious implication for attempting to passivate device surfaces using deposited insulating nitride layers. It means that if I want to enable effective on-chip n-DEP forcing in a nitride-coated device, I need to deposit blanket films that are only a few nanometers in thickness. Since fabrication tools typically exhibit notable variability in their effective deposition rates over time, I explored efforts to calibrate our in-house RIE-CVD tool (Surface Technology Systems, PLC, Newport, UK) by running a series of PECVD nitride sequences over the course of several days. By depositing these calibrated films onto silicon samples that I partially front-side protected by overlaid masking, I produced a collection of chips presenting various nitride step heights. Using an atomic force microscope (Dennis Freeman's lab - Research Laboratory of Electronics), I then measured each step to develop a feel for my ability to reliably reproduce specific deposited thicknesses. With some work, I determined that plasma exposures of ~14 seconds using the LFSiN [Need to check my notes.] recipe could regularly produce deposited films with thicknesses of ~3 nm (see the upper right of Appendix 9 for an example measured film; x-y relevant scale bar ≈ 20 μm). With such thin depositions incorporated in the process, small absolute variations in rendered thicknesses offered the potential to substantially impact performance. It was my hope that this calibrated deposition could generate on-chip films that would not truncate in-system DEP forcing effects and would simultaneously prevent undesired cell adhesion.

Advanced functional demonstrations

Beyond the success of my electroactive weirs in the context of on-chip bead-based manipulations, I hoped to pursue equivalent cell-based operations. In my first attempt, I decided to avoid the complexities associated with managing two distinct cell populations by focusing upon efforts to organize interleaved collections of beads and cells. As highlighted in Figure 34A, I was successful in producing at least small checkerboard-style patterns of red beads and CellTracker Green stained K-562s (see Biological Methods Appendix for culture specifics, ATCC, Manassas, VA).

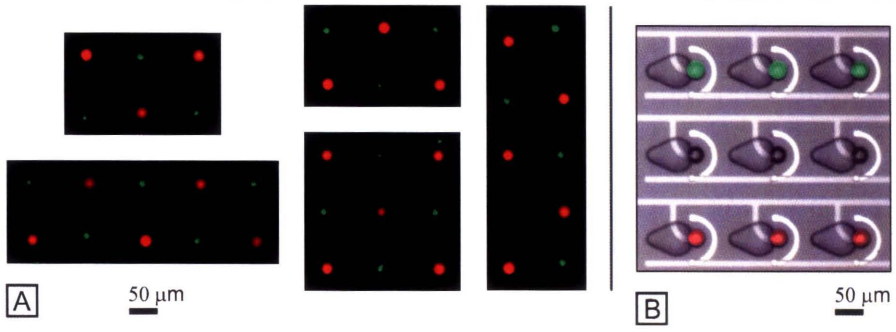

Figure 34: In advanced efforts, I have successfully formed small patterns of interspersed beads (red) and CellTracker Green stained K-562 cells **(A)**. Additionally, using a column-connected device, I have organized multiple individual green-fluorescent, non-fluorescent, and red-fluorescent beads in side-by-side orientations.

Just as I had done in Figure 32B, I first load beads at the on-chip *passive* site locations. I subsequently then deactivated the n-DEP forcing electrodes and attempted to backfill all remaining sites. As is notable in all of the presented images, non-specific adhesion of cells in locations other than the weir capture cups was not a complicating factor. Additionally, despite having an on-chip ~3-nm-thick nitride film DEP forcing proved feasible. Unfortunately, I was not able to replicate the fully loaded 5 × 5 checkerboard matrix that I had initially presented using green and red beads. For reasons which will become clearer in the next section of this chapter, as well as in ongoing discussions in Chapters 5 and 6, the on-chip weirs simply struggled to reliably retain individual loaded cells. As a result, the footprints presented here were ultimately the most sophisticated cell-based loading patterns that I could successfully produce.

Knowing that the weir designs were quite effective for capturing 27-μm-diameter beads, I explored added device functionalities by processing a series of chips through the Metal 2 level (using the dual-stop-point mask set discussed prior) to render a column-wise connected "pixel" array. With this design and some slight reprogramming of my peripheral support software, I successfully organized three distinct bead populations (green fluorescent, non-fluorescent, and red fluorescent) into a series of neighboring columns (see Figure 34B). Though this demonstration utilizes non-biological polystyrene particles, as I will discuss in on-going visions outlined in Chapter 6, even bead patterning of this type offers the potential to expand analytical tool sets serving a variety of research purposes.

Probing weir loading responses using small particles

Despite all of the work I had put forth to try and avoid incorporating SU-8-based weirs in my "pixel" designs, I began weighing considerations for reexamining its use. As noted in the comparative work performed when validating on-chip PPS capabilities, SU-8 regularly offered superior print resolution and straighter sidewall profiles. I therefore imagined it might prove possible to use the material for manufacturing on-chip weirs with sharper features that could enhance the replication of design geometries present in the original chrome mask. If I could better replicate the crisp features present in the masks I imagined that I might enhance the capability for individual weirs to retain smaller and smaller particles. As mammalian cells typically embody diameters localized to the 10-15 μm range, the loading characteristics from Figure 31 suggested that cells were simply below the capture threshold enabled by my PPS weirs. By running my devices using sharper SU-8 weirs and slower on-chip flow rates I hoped to expand my flexibility for capturing and stably retaining individual cells.

To redesign my "pixels" in such a fashion meant that the benefits associated with the low autofluorescence of PPS would necessarily be shelved. I imagined that for a proof-of-concept demonstration, I might still have some window of flexibility (by adjusting camera settings carefully) if I examined red channel fluorophores alone. As reported in the material diagnostics of Figure 29B, for imaging at longer wavelengths the material's less dominant emission response (as compared to green and blue channels) presented a diminished likelihood for competing with in-cell signals of interest. As per discussions with Dr. Peter Sorger, I imagined it might additionally prove possible to one day bypass emission concerns altogether by transitioning to matured implementations of some of the more recently developed in-cell constructs reliant upon infrared portions of the spectrum.

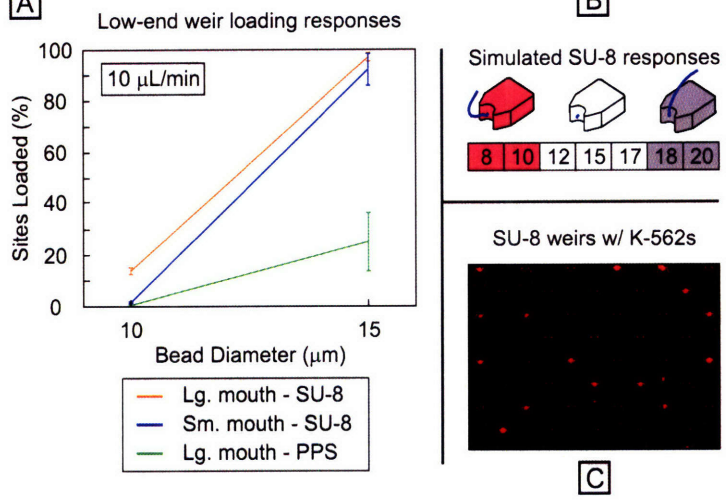

Figure 35: By forgoing the autofluorescence benefits of PPS and instead manufacturing weirs using SU-8, we see an interesting and new loading dynamic for smaller bead sizes **(A)**. Regardless of the material used to form the weir, it proves virtually impossible to retain high percentages of the 10-μm-diameter beads. Additionally, for 15-μm-diameter beads SU-8 weirs outperform PPS weirs on the basis of retention percentages. Using modeling efforts developed elsewhere[1] and tested by our collaborators in Dr. Karen Willcox's group we are beginning to reconcile such loading dynamics from a simulation-based standpoint **(B)**. (Numbers in (B) indicate the bead diameter.) In my attempts to load cells into weir arrays, I have struggled to obtain high loading percentages. The modeling and experimentation with small bead sizes have shed some light upon this challenge and may eventually offer a path to overcoming it.

In a manner identical to the protocols used when gathering data for the response plot in Figure 31C, I manufactured and tested a comparable set of devices that presented 600+ non-active (no on-chip electrodes) SU-8 weirs (again 20 μm in height). (See Fabrication Methods Appendix steps 11-19 in the "Initial SU-8 2002/2015-based process for

electroactive weir design" subsection.) Using a flow rate of 10 μL/min (flow chamber height ≈ 250 μm; width ≈4 mm) which attempted to mimic cell-based assay conditions and bias the chip toward maximum loading percentages, I examined responses using multiple (n=3) separate runs with 10-μm-diameter and 15-μm-diameter polystyrene beads (averages plotted; standard deviations across runs used for error bars). Beyond examining the typical "large mouth" weir designs that I had tested in all prior effort with PPS, I additionally surveyed responses for "small mouth" SU-8 weir designs. Such designs occupy identical footprints to those shown at the upper right of Appendix 8 (all "large mouth" designs) but instead of forming the capture crevices with an 11 μm radius, they use 6 μm radii. As shown in Figure 35A, both SU-8 weir types ("large mouth" and "small mouth"), demonstrate a switchlike dynamic when transitioning between loading assays run with 10-μm-diameter beads and assays run using 15-μm-diameter beads. In the case of 10-μm-diameter beads, only scant percentages of the incoming bead populations remain captured in the on-chip SU-8 weirs. In stark contrast, sequences run using 15-μm-diameter beads display nearly perfect responses with loading percentages well into the high 90s. Such an effect highlights the presence of a very sharp lower limit to bead-based capture. SU-8 weirs furthermore outperformed comparable PPS designs (green trace in Figure 35A) by offering an approximately 5-fold increase in the retention percentages enabled for 15-μm-diameter beads.

The response dynamics of the SU-8 weirs seemed to provide preliminary support for the idea that sharper designs owned the potential to enhance device performance in the context of cell-based assays. To position this latest set of results side-by-side with the curves presented in Figure 31C, I provide a combined loading response plot in Appendix 9 that maintains the color scheme adopted in the two originally separate figures. Additionally, I offer brightfield images indicative of example SU-8 weir loadings seen when using 15-μm-diameter beads (I include examinations of both "large mouth" and "small mouth" geometries). The overlap of various response curves in cases where we attempt to load small diameter beads suggests that individual weir designs have an inherent, geometry dependent, lower limit for capture. In other words, even the smallest flow rates can dislodge particles sized below a certain range. On the other hand, for more sizeable particles, retention becomes more directly dependent upon the on-chip flow rates used when running an assay. The slower the flow, the more likely it will be for an individual site to retain an initially loaded particle. I did not explore the responses of larger bead sizes at the 10 μL/min flow rate for two reasons. First, each data point is fairly costly to obtain from the standpoint of experimentation time. Second, I was most concerned with attempting to use my devices to capture cells. Since I was unlikely to find lines surpassing a 10-15-μm-diameter size range, my focus was mainly on efforts to expand the potential to capture smaller particles and it thus became less important to track behaviors associated with larger particle sizes.

Coupled with my experimentation efforts, collaborators from Dr. Karen Willcox's lab began working with a collection of code originally developed as a part of Dr. Carlos Pinto Coelho's doctoral thesis[1] to try echoing in-lab behaviors in a simulation-based context. In brief, this coding strategy examined in-flow dynamics by utilizing an accelerated boundary-element solver that incorporated semi-implicit time integration schemes and a specialized Green's function for handling arbitrary substrate configurations. The setup thus leveraged the linearity of Stokesian flow to provide a simulation package that calculated hydrodynamic effects within a matter of hours compared to prior efforts requiring days or weeks of computation time.

Here, I outline the basic overview of this approach using a more mathematically grounded effort. Given the Green's function, $\overline{\overline{G}}$, mapping a source point force, $\overline{f}$ (located at position $\overline{x}_s$), to the velocity of any target point, $\overline{x}_t$, we can develop a boundary integral equation for the forces on the surfaces of objects in on-chip flow using the following relation:

$\int_{S_{all}} \overline{\overline{G}}(\overline{x}_t, \overline{x}_s)\overline{f}(\overline{x}_s)\,dS = -8\pi\mu\overline{v}(\overline{x}_t)$	**Equation 33**

By means not presented here, it is possible to simplify this integration step using a substrate Green's function. After eliminating translation invariant portions of the relation using a modified projection scheme, it is then possible to use a precorrected fast Fourier transform (pFFT) technique to accelerate calculations related to the interactions between source and target terms in this integral. A velocity implicit time integration technique then provides the update terms needed to track dynamics within a time variant flow.

Using this coding strategy, we began testing SU-8 weirs for different functional responses (flow rate set to 10 μL/min). For completeness, in Appendix 9, I outline the stepwise sequence used to develop simulated models of the actual fabricated SU-8 weirs. (First, we imaged the designs using 10× objectives on an upright microscope (step 1). Next, we thresholded the image to create a binary mapping of black and white pixels (step 2). We then thinned the binary mapping to a single-pixel-wide representation and double-checked it with the imaged weir (step3). Using discrete points around the single-pixel-wide trace, we developed a spline fit for the design and again double-checked it with the original imaged weir (step 4). We then extruded the geometry (step 5) and meshed it (step 6) to render a modeled incarnation of our designs.) With an adequate representation in hand, we ran a series of simulations that initially positioned individual rigid particles at the center of the capture cups (in contact with the weir) and then turned ON in-chamber flow. As shown in Figure 35B, for small diameter particles (8-10 μm) we witnessed a lateral rejection response where particles dislodged from the sides of the traps (shaded in red). For mid-range particles (12-17 μm) we saw a stable retention effect (colored white). Larger particles (18-20 μm) unloaded by vertically rotating up and over the weirs. Though I do not have exact experimental matches for the larger bead sizes the small- and mid-range particle responses matched my empirical efforts. In on-going work, outlined in Chapter 6, I will detail further efforts to leverage these coding techniques for investigating possible added system design latitude.

To further explore on-chip loading using cells, I stained a population of K-562s (chosen because they are non-adherent and exhibit larger diameters than many other cell types) using our standard CellTracker Orange protocols and then attempted to load a 600+ site SU-8 weir device. As I present in Figure 35C, though it did provide an avenue for enabling single-cell capture, this effort still fell short of offering the high-percentage loading responses needed for many of the assays that had originally motivated my work. In Chapter 5, I will discuss in more extended fashion, many of the experiments that surveyed these cell-based loading responses.

Complementing my SU-8-based assays, I must pay tribute to a series of processing improvements jointly developed by my colleague Salil Desai and me. In an attempt to tighten the resolution capabilities offered by PPS, we sought ways to eliminate the Cellophane ring that produced a physical separation between the spin-coated films and the chrome-plated glass masks. As shown at the bottom left of Appendix 9 (highlighted via red numerals), we developed in-house techniques for both spin-coating our masks with a teflon-like polymer (much thinner than the Cellophane) and including a descum plasma etch at the end of the process. We coated our masks using a water-soluble barrier coat BC 7.5 (Shin-Etsu MicroSi, Inc., Phoenix, AZ) product originally developed for contrast-enhanced resist applications. (See Fabrication Methods Appendix "Enhanced PPS weir fabrication process" for complete details.) This coating enabled direct mask/substrate contact during UV exposure steps without forming an intractable bond. The plasma etch, utilizing (1:1) SF_6:O_2 chemistries, anisotropically trimmed the sidewalls of patterned on-chip features to produce much sharper detail. As I present in tabulated form at the bottom right of Appendix 9, these processing enhancements (which also included expanding UV exposure times well beyond recommendations from the manufacturer - upwards of 1500 mJ/cm^2, specifically 150 seconds at the 10 mW/cm^2 output rating of EV1) did improve print resolution, but they still typically fell short of that offered by comparable 2015 SU-8 patterning.

In this chapter, I have detailed the development of an electroactive hydrodynamic particle manipulation topology. Contrasting other, exclusively passive, weir-based manipulation platforms we have thus offered new capabilities for organizing multiple particle populations on a shared surface. Serving this end we developed large-gap free-standing weir implementations that could enable alignment with underlying electrodes. In "ejection" and "exclusion" operations with active devices we examined key functionalities that presented unique single-bead and single-cell patterning effects. Via empirical means we furthermore uncovered a size-selective loading effect in passive devices that we have since partially recapitulated in collaborative model-based efforts. Last, by exploring efforts to form our substrate-affixed weirs using photopatternable silicones we transfered a new material set to the biological microsystems community.

As the reader will likely recognize by now, the grand diversity of challenges and engineering demands explored in this chapter have made the path from design ideation to functional validation a significant trek for my electroactive weirs. Despite these roadblocks and obstacles it is somewhat amazing that, in the end, the only limitation for developing a functional array-based technology for single-cell applications centers on resolution-related concerns. As enhanced polymer patterning techniques may someday overcome such complications, it is reassuring to imagine that this work has cleared large portions of the remaining path to functional implemented designs. My efforts using beads and, in part, using cells, have thus outlined an avenue for approaching a wide variety of novel of on-chip assays.

Appendix 8

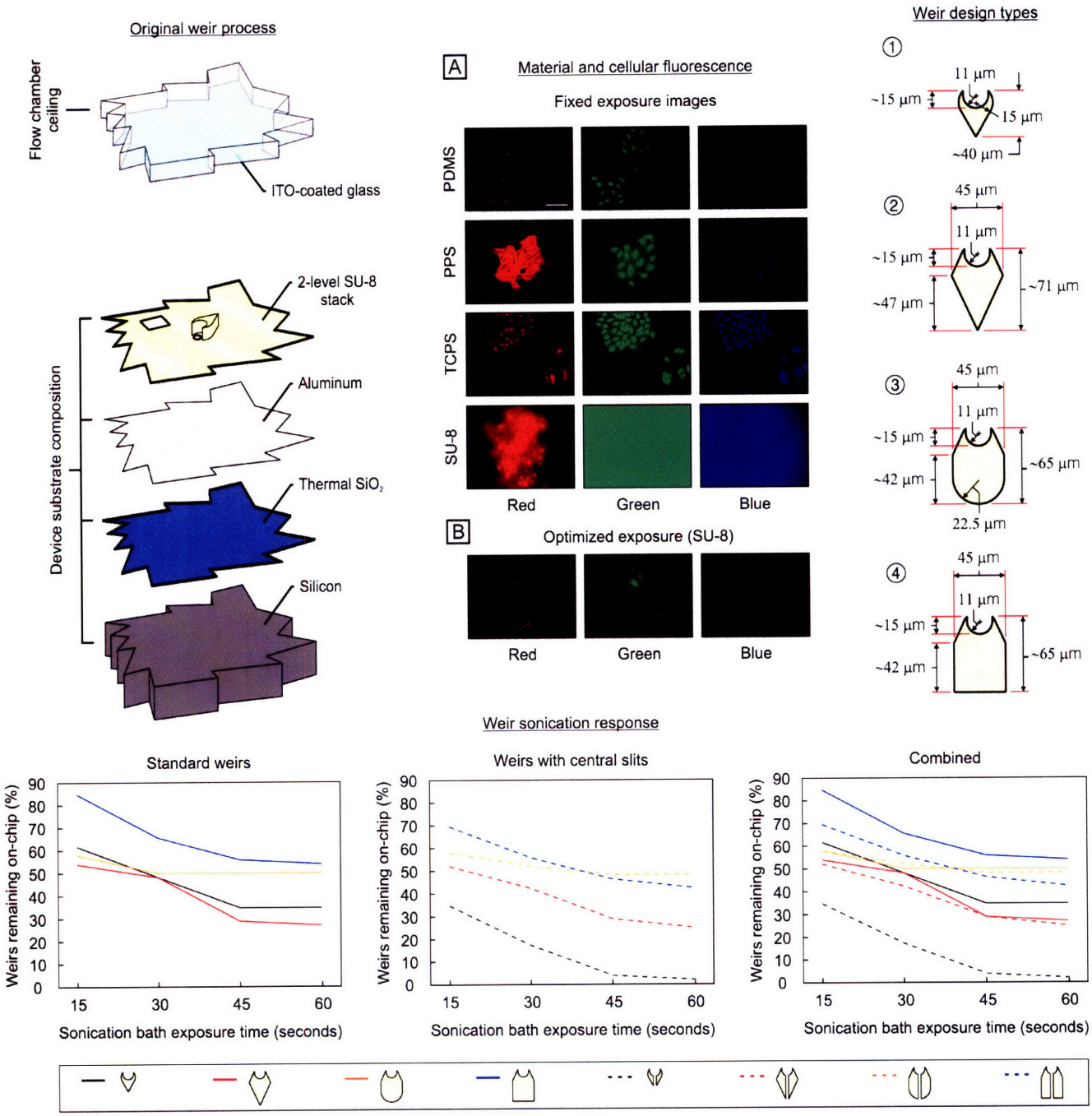
Original weir process
Flow chamber ceiling
ITO-coated glass
2-level SU-8 stack
Aluminum
Thermal SiO2
Silicon
Device substrate composition
A
Material and cellular fluorescence
Fixed exposure images
PDMS
PPS
TCPS
SU-8
Red
Green
Blue
B
Optimized exposure (SU-8)
Red
Green
Blue
Weir design types
11 µm
~15 µm
15 µm
~40 µm
45 µm
11 µm
~15 µm
~47 µm
~71 µm
45 µm
11 µm
~15 µm
~42 µm
~65 µm
22.5 µm
45 µm
11 µm
~15 µm
~42 µm
~65 µm
Weir sonication response
Standard weirs
Weirs with central slits
Combined
Weirs remaining on-chip (%)
Sonication bath exposure time (seconds)
Weir loading response assay sequence steps
Flow
45 µm
Device "reset" capabilities
Magnitude tunable via voltage application
Active geometry
Passive geometry

Appendix 9

On-chip deposited insulator modeling

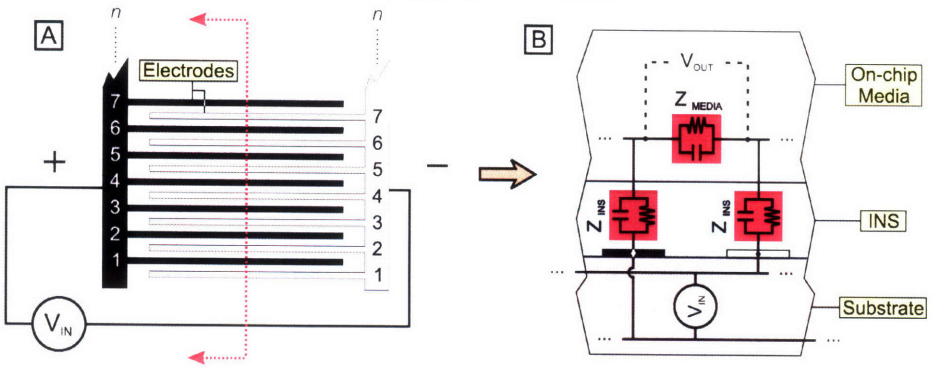

AFM-calibrated nitride deposition

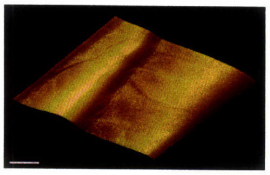

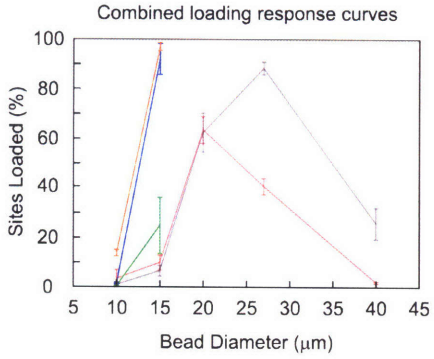

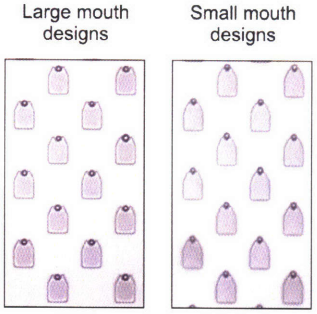

Example 15μm bead loadings

Stepwise sequence used to form SU-8 weir models

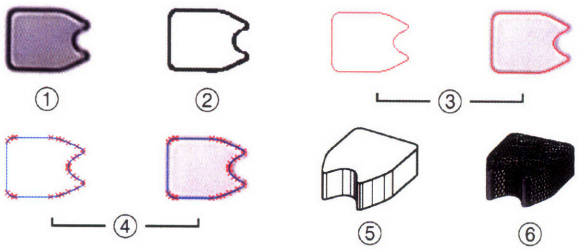

PPS weir fabrication process enhancements

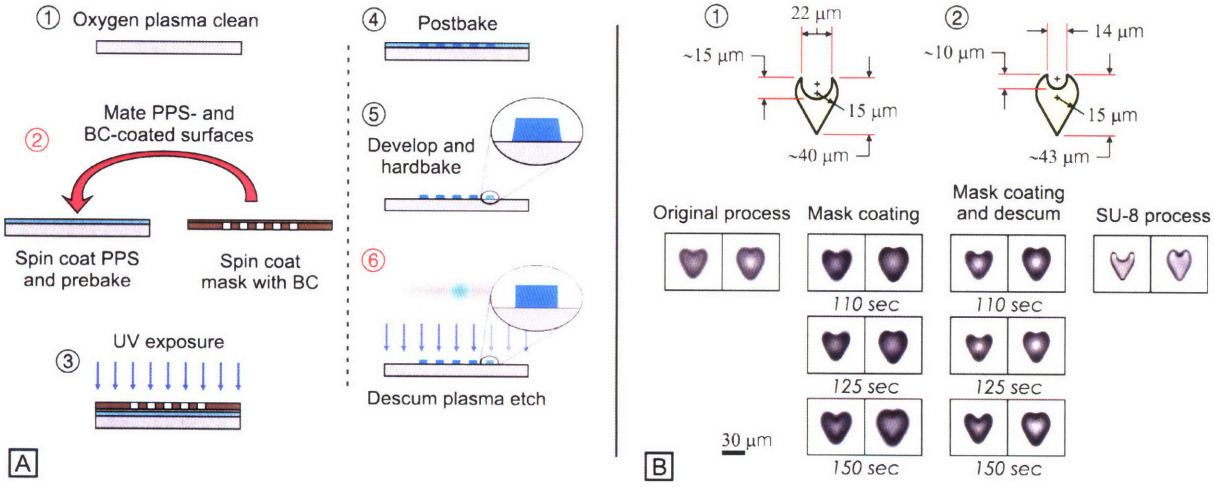

Chapter 5: Pushing toward on-chip biological assays

Until now much of the work presented in my dissertation has centered on the sizeable abundance of technological details endemic to device design and system development. In many cases such challenges have demand attention to an extent that has challenged transitioning toward on-chip biologically-focused assay. In this chapter, I outline a variety of key experimental engagements that strive to delineate the application space best served by my developed single-cell array-based platforms. A desire to exhibit new investigative flexibilities and analytic techniques surpassing what is readily available using alternative approaches, serves as a dominant driver in this effort.

Cell sorting as a prime motivator

As mentioned in Chapter 1, one of the initial drivers for my doctoral work centered on the development of novel single-cell manipulation technologies that could combine some of the traditionally non-overlapping capabilities native to fluorescence-activated cell sorting (FACS) and automated microscopy. By targeting image-cued cell sorting, I hoped to demonstrate a new analytical capability. This project motivator served as a key step in developing the row/column site addressability developed in Chapter 2. As I envisioned applications where only a small number of mutant (or divergently behaving) cells might need sorting from a larger background population, I did not consider the inherently sequential nature of my row/column release architecture a limiting factor.

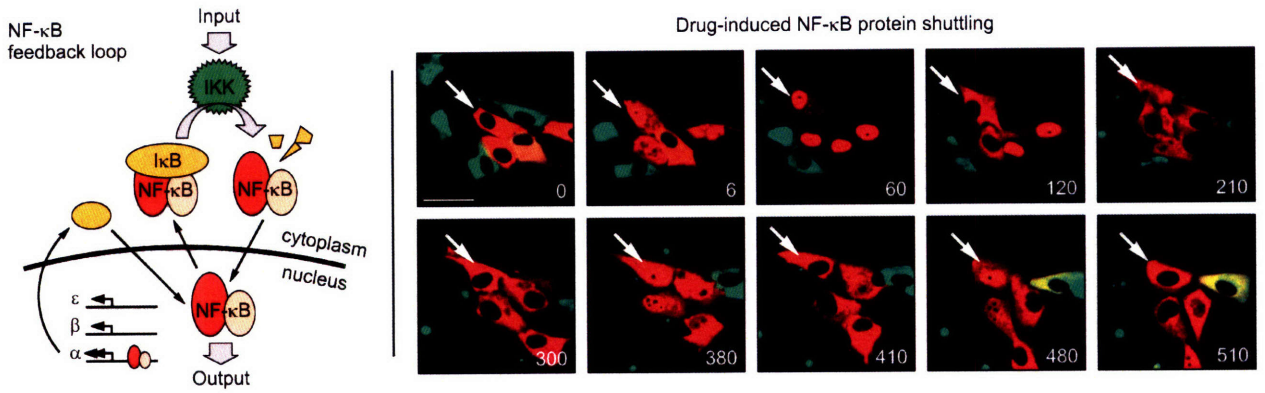

Figure 36: At left I outline a key feedback loop affiliated with the NF-κB signaling module (adapted from Hoffmann et al.[4]). When stimulated with TNF-α, an activation sequence degrades internal IκB proteins that in turn expose a nuclear localization element on the NF-κB proteins. NF-κB then shuttles into the cell nuclei, where it then transcribes α, β, and ε isoforms of IκB. As IκB is produced, it locates free NF-κB proteins in the nucleus. Upon binding, the IκB/NF-κB complex then exports to the cytoplasm to start the cycle over again. At right Nelson et al.[7], have tracked this shuttling response in plated cell cultures (NF-κB indicated in red). The dynamics of such a response are highly regulated by the relative concentrations of the unique IκB isoforms. In some cases damped responses occur, in others steady oscillations result, and in others still, shuttling seems to halt following a single translocation event. Attempts to track such dynamics and manipulate distinct subpopulations framed many of my efforts to develop cell handling arrays. (Scale bar ≈50 μm)

In surveying the literature and through numerous conversations with collaborators, biological phenomena affiliated with both the NF-κB signaling loop and drug-induced apoptotic responses appeared well suited for the sorting-centric objectives established in the early stages of my work. As depicted in Figure 36A, the NF-κB signaling module[4], which typically motivates "pro-survival" cell responses, exhibits an interesting translocation dynamic. When external stimuli, generally manifested as receptor-bound ligands like TNF-α, interact with a cell, a cascade of activation events takes place such that IKK proteins within the cell encourage the degradation of IκB proteins. In their unperturbed state, the IκB proteins normally remain bound in protein complexes with NF-κB. Upon IκB degradation, NF-κB becomes free within the cell cytoplasm and its native nuclear localization sequence (NLS) is no longer sheltered. Upon NLS exposure, NF-κB proteins translocate to the cell nucleus. Inside the nucleus, they then upregulate various genes. This upregulation, results in the transcription of the α, β, and ϵ isoforms of the IκB protein. In unbound forms, these IκB also present native NLS sequences which encourage their migration to the nucleus. Within the nucleus free IκB and NF- κB proteins bind to one another, reforming their original complex. In this condition the proteins then expose nuclear export sequences (NES) which cause them to shuttle back to the cytoplasm. This step completes the cycling loop which can repeat in accordance with cell input stimulus levels and in-cell protein concentrations. Using electromobility shift assays (EMSA)[4] as well as automated microscopy efforts using fluorescently-tagged NF-κB proteins[7], various groups have observed this shuttling dynamic (see Figure 36B).

The oscillations associated with NF-κB shuttling are tightly regulated by the in-cell IκB protein isoforms. In many cases the β and ϵ isoforms motivate damping responses. By artificially introducing cells into a mixed population where the function of the β and ϵ isoforms is silenced (using siRNA techniques), by or attempting to simply track cross-population response heterogeneity in unaltered cultures, this in-cell dynamic offered an interesting image-cued biological phenomenon to target with my array-based platforms. As I highlight explicitly at the top of Appendix 10, I imagined using the sorting capabilities of my developed microsystems to locate and cull differentially responding cell groups. I envisioned then porting such sorted populations off-chip and subsequently expanding and restimulating them in dish-based environments. The ultimate aim was to then investigate the potential heritability of different response traits.

Programmed cell death studies[2, 6, 11, 56, 58, 62, 166, 167] (otherwise known as apoptosis), further seemed to suit the unique sorting flexibilities built into many of my single-cell handling arrays. To understand their relevance to my work, it is instructional to briefly examine a few basics of apoptotic signaling. In Figure 37A, I present an adapted figure from Hengartner[2] that outlines several key players in receptor-activated cell death decision processes. Of note are the two distinct, but coupled, signaling paths that result in apoptotic responses. Following stimulation via TRAIL (TNF-related apoptosis-inducing ligand) or an variety of other ligands, a cascade of events occur that cause Caspase-8 proteins to slowly begin degrading in-cell components (known as apoptotic substrates) that ultimately motivate orchestrated cell destruction responses. This "direct" route to programmed cell death is generally considered a slow-response path as Caspase-8 proteins are themselves somewhat ineffective in degrading apoptotic substrates. Alternatively, a "side-chain" avenue involving the mitochondria tends to play a more dominant role. Along this route truncated Bid proteins localize to the mitochondria where they eventually puncture holes in

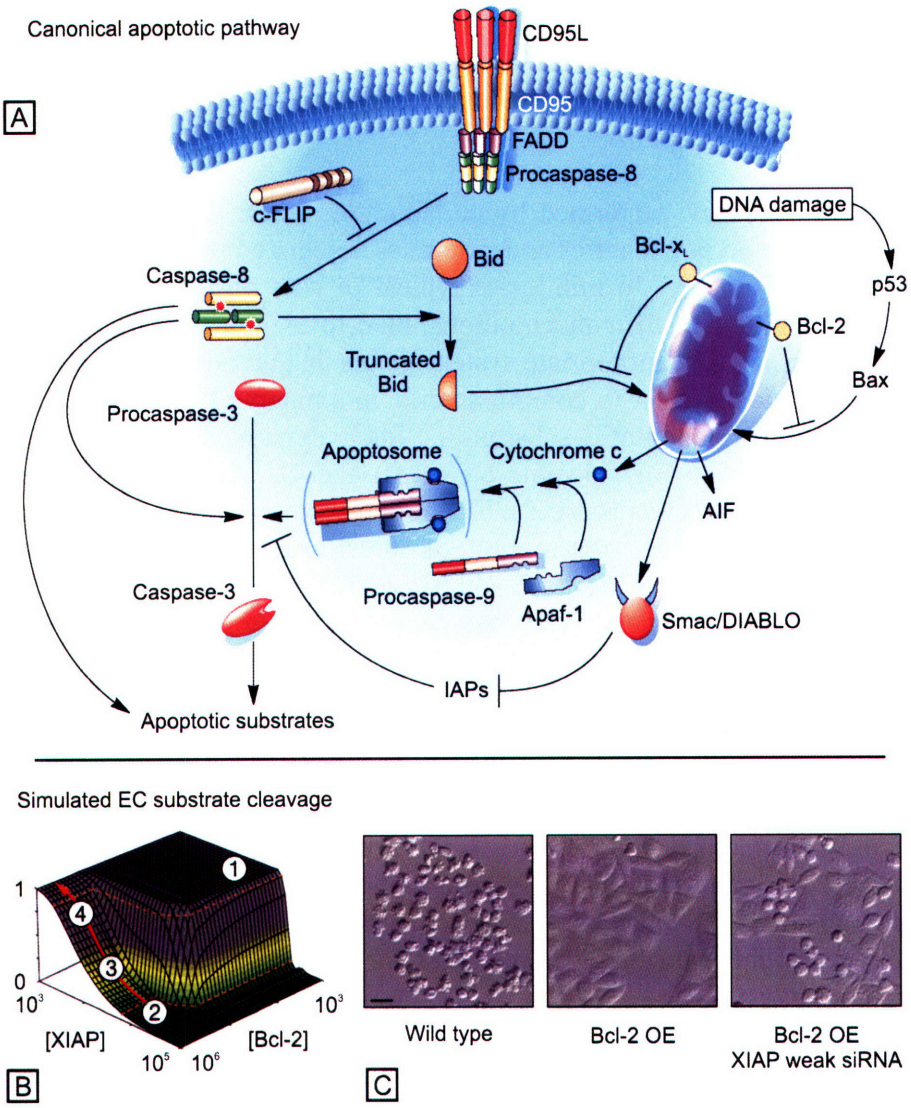

Figure 37: In the canonical apoptotic pathway **(A)** (adapted from Hengartner[2]), two main receptor-activated signaling avenues operate to encourage cells to "commit suicide". In the "direct" path, Caspase-8 proteins can cleave various apoptotic substrates ultimately leading to the compartmentalized destruction of the cell. The dominant "side-chain" pathway alternatively recruits collections of proteins to the mitochondrial membrane that perforate the organelle and release Cytochrome C and Smac/DIABLO. Such proteins, once free in the cytoplasm then release a flood of Caspase-3 activity which ultimately leads to cell death. In systems biology efforts put forth by Dr. Peter Sorger's lab[6], functional models have helped to illuminate key nuances of the cell decision processes associated with programmed cell death. In **(B),** we see a simulated landscape depicting the cleavage of apoptotic substrates. When stimulated by TRAIL, most wild-type cells effectively cleave thes substrates (labeled 1 and depicted in **(C)**) resulting in apoptotic death. In case where Bcl- constructs are overexpressed, elect not to "commit suicide" and their apoptotic substrates remain intact (labeled 2 and depicted in **(C)**). For other conditions such as Bcl-2 overexpression and weak XIAP siRNA activity, we witness an odd intermediate decision where cells partially cleave their substrates to exist in a "half dead" state. Understanding this fate of such cells from an experimental context motivated much of my work. (Note: Both (B) and (C) adapted from Albeck[6] et al. Scale bar in (C) ≈30 μm.)

the affiliate membranes. The perforated mitochondria then release sizeable concentrations of

Cytochrome C and Smac/DIABLO proteins into the cell cytoplasm. These free proteins operate to assemble apoptosome structures and to deactivate the break-like dynamics of in-cell IAP (inhibitor of apoptosis proteins) proteins. With inactive IAPs and functional apoptosomes, cells release a flood of Caspase-3 proteins that effectively cleave apoptotic substrates and ultimately induce programmed cell death responses.

In significant investigative work performed by collaborators in Dr. Peter Sorger's lab[6], model-based efforts have illuminated key features and dynamics associated with this apoptotic signaling network (see Figure 37B and C). In mimics of typical *in vivo* responses, wildtype cell lines, when exposed to appropriate TRAIL concentrations, tend to exhibit snap-action dynamics. To better explain, when cells witness appropriate system inputs that amount to a prescription for cell death, individual cells typically elect to commit suicide in a manner that ensures both rapid and complete cleavage of in-cell apoptotic substrates. Such dynamics correspond to the items labeled "1" in Figure 37B (high EC substrate cleavage) and C. As seen in the wild type cell image, virtually all such treated cells present a blebbed morphology. This snap-action response is largely motivated by the sudden perforation of in-cell mitochondria and the subsequent flooding of the cytoplasm with Cytochrome C and Smac/DIABLO proteins. In altered cell lines (representative of certain cancer types), it is often common that Bcl proteins are overexpressed. In such cases the "side-chain" signaling network for apoptosis becomes compromised as both Bid and Bax proteins can not perforate the mitochondrial membrane. As seen in Figure 37B (labeled "2") and C, cells with overexpressed Bcl-2 proteins fail to cleave internal apoptotic substrates and present attached viable morphologies. An interesting case occurs when we overexpress Bcl-2 constructs and simultaneously weakly downregulate IAP functionality using siRNA. In this condition (labeled "3" in Figure 37B), cells do not exhibit the same sort of snap-action response where all apoptotic substrates cleave in a rapid manner. In fact, it is common that the apoptotic substrates only become partially degraded. As a result, cells seem to have trouble lack direction in choosing downstream fates. They appear to exist in what might be termed a half-dead state.

The eventual fate of such cells is largely unknown. They also seemed to present a grand diversity of morphologies and in-culture heterogeneities. Analyzing such odd behaviors thus seemed well suited to the types of sorting assays I had originally hoped to perform. I imagined that I might collect different subpopulations of half-dead cells such that I could attempt to understand and monitor their growth and proliferation capabilities. If I could expand any sorted groups, it might shed new light on cancer mechanics.

It is often the case that after nominally successful chemo- and radiation-based therapies, cancers reemerge to cause problems for patients at later points in time. The mechanisms behind this response are largely speculative at present, but it is considered likely that various cancer treatments actually damage cells in ways that initiate disease recursion. The Bcl-2 overexpressing cells with weak IAP downregulation may be a type that is representative of the damaged cells potentially arising from cancer treatments. Using a sorting-based approach, I thus imagined testing the growth dynamics of half-dead cells to provide new insight.

To enable such investigations, a number of techniques proved available. As in-house technologies, the Sorger lab already had plasmid constructs for engineering cells lines to enable

fluorescent tracking of Smac dynamics and FRET-based monitoring of caspase activity. Coupled with monitored morphology characteristics, I had several avenues for making categorical cell classifications that I could ultimately use to make sorting decisions. For completeness, I included images (courtesy of Dr. John Albeck) of these three imaging capabilities at the bottom of Appendix 10.

Initial surveys of cell health in low-conductivity buffers

My initial forays in the context of sorting-based biological assays occurred concurrently with the development of my 20 × 20 p-DEP semi-"ring-dot" array platforms. As such, I imagined all assays would necessarily take place in buffers presenting conductivities of 0.1 S/m. Two dominant concerns prevailed for me at that time. I was curious to understand the induced transmembrane potentials occurring in this new category of on-chip buffers (conductivity used in 4 × 4 experiments was 0.01 S/m) and I wanted to further test the biological impact associated with cell exposure to such medias. (I assumed brief exposures would only be necessary since the cells would only remain in such environments during imaging and sorting routines.)

To examine transmembrane effects, I used the model detailed in Chapter 1 to examine the effective response at various locations above my in-system trapping "dots". In Figure 38A, I plot the results. For the 0.01 S/m case (again, reflective of my 4 × 4 experiments), the entire response curve is well below the cautionary 100 mV limit recommended by prior works in the field[113, 168, 169]. There, it seemed safe to assume that induced potentials would be small. Such conditions were not the case for 0.1 S/m buffers. Approaching the substrate, the recorded value rapidly increased well above the 100 mV rating. The model used to develop such curves was however, likely to overpredict the severity of on-chip conditions. Such an effect stemmed from an implicit assumption in the development of the model maintaining that the entire cell should be surrounded by a uniform field of a given

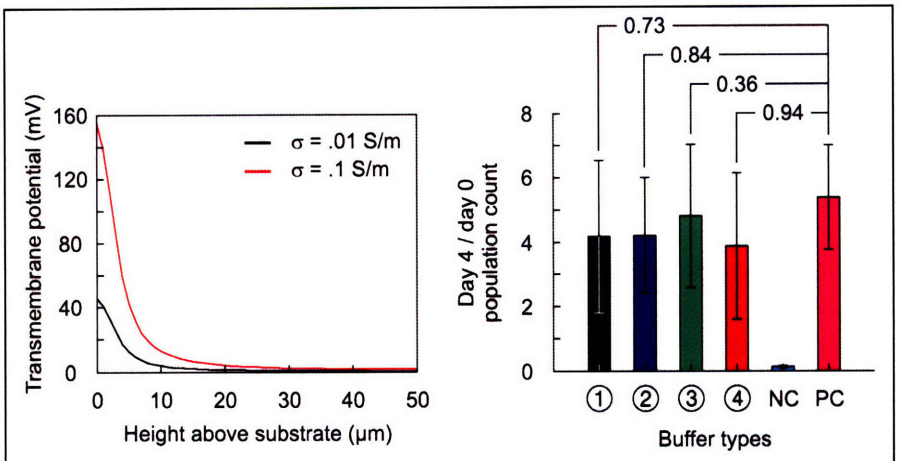

Figure 38: My attempts to use modeling to understand the impact of induced transmembrane potentials provided only limited insight for cases run in higher conductivity buffers (left). It was challenging to confidently state whether or not the ~160mV ratings listed at locations just above the "dots" in my p-DEP designs were a true reflection of the voltage drops across cell membranes. This complication stemmed from the fact that the formulation used to model such effects carried the assumption that the field present at such locations would be uniform across the cell. In reality, such a severe condition was not the case. At right, I examine the day 4 proliferation rates of HL-60 populations that have been subjected to 3 hour "baths" in one of four low-conductivity buffer types (see text for details related to buffer content) (n=3). As validated using Welch's T test, none of the four buffer types significantly impacts the growth dynamics of this line when compared to the positive control (PC) grown in standard media. For cases where cells were left in a low-conductivity buffer for four days (NC) cells failed to proliferate and most died.

magnitude. In reality the fields present in the on-chip environment created anything but uniform field conditions surrounding the cell and the sharp in-system gradients made it challenging to interpret the modeled results as anything but overestimates. Additionally the x-axis in the plot created a bit of a paradox. Though it examines values for distances above the substrate that become diminishingly small, a cell (which is referenced in the model by its center point) can only exist as close as one cell radii above the surface. The modeling therefore proved to be an inconclusive investigative tool and I elected to pass duties for further analyzing field-based cell health to Salil Desai (his doctoral studies center upon such work)[41, 170].

To evaluate the effects of low-conductivity buffers on cell proliferation rates (see Figure 38B), I treated HL-60s with one of the four following media types (also listed for convenience in the Biological Methods Appendix "Low-conductivity buffers"):

Buffer type 1	Buffer type 2	Buffer type 3	Buffer type 4
9.5 g sucrose / 100 mL	9.5 g sucrose / 100 mL	9.5 g sucrose / 100 mL	9.5 g sucrose / 100 mL
2.5 mL 1M Hepes / 100 mL	2.5 mL 1M Hepes / 100 mL	2.5 mL 1M Hepes / 100 mL	2.5 mL 1M Hepes / 100 mL
4 mL PBS	5 mL BCS	3.5 mL Isoton	undoped

I exposed HL-60s to such buffers (~1E5 cells/mL) for spans of three hours using our standard cell passaging techniques and then resuspended the cells in their standard media. After four days of growth, I then counted the cell populations and plotted growth rates normalized to their initial (day 0) seeding populations to examine proliferation responses. Using Welch's T-test, in comparison to positive control (PC) populations grown only in standard HL-60 media, three hour exposures to any of the four buffer types did not alter growth dynamics in significant ways. In contrast, negative controls (NC) left in buffer type 4 over the course of the four day time span failed to proliferate and demonstrated widespread death.

This coarse evaluation of low-conductivity buffers provided encouraging support for sorting assays. As long as I could image and sort populations in short order, substantial flexibility existed for enabling viable cell separation. As a general note on the buffers used in this study, they were each carefully modified and calibrated to present nominal ratings of 300 mOsm, 7.35 pH, and 0.1 S/m (excepting buffer 4 which displayed a lower conductivity and 275 mOsm). The doping via phosphate-buffered saline (PBS), bovine calf serum (BCS), or Isoton (Beckman Coulter, Fullerton, CA) was used to elevate the conductivity to the proper value for on-chip assays.

Transfection of non-adherent cell lines

Though a wide range of in-cell fluorescent constructs were readily available for serving assay relevant to NF-κB shuttling dynamics and apoptotic signaling, none were established in stable non-adherent cell lines. All of my successful sorting demonstrations (see Chapter 2) had however leveraged non-adherent lines to offset unwanted surface binding effects in non-trapping portions of my devices. As such, through collaborative efforts with Dr. John Albeck, I began exploring options for engineering HL-60s cell lines that could serve our targeted biological assays.

Using FuGENE-6 (Roche, Basel, Switzerland) and eventually even Amaxa-based (Amaxa, Inc., Gaithersburg, MD) transfection techniques we struggled to successfully incorporate desired

fluorescent protein constructs in our HL-60 lines. For each of the transfection attempts, we used plasmids that were designed to promote Geneticin resistant responses to cells that effectively incorporated the target samples of peripheral DNA. Though we had calibrated a Geneticin dose curve for HL-60s (see upper left of Appendix 11), in all selections run at 0.4 mg/mL we witnessed widespread in-dish death and after two weeks in selection media failed to recover sizeable cell populations of any kind.

After numerous frustrated attempts, I began to wonder if there wasn't some sort of diffusible signaling component associated with the responses we were observing. I was curious to know whether or not some critical in-dish cell density needed to exist to effectively promote proliferation responses. As I present in Figure 39A, I ran a ten-day time course (approximately the times necessary for Geneticin selections) surveying the behaviors of different cell seedings on growth dynamics (imaged daily). Using a developed cell-counting routine I tracked proliferation effects and, across three separate runs, I witnessed an interesting bifurcation response. HL-60s seeded with initial in-dish densities below 1E4 cells/mL failed to expand and over time began to die off. Cells seeded above this limit, rendered a distinct survival and growth response.

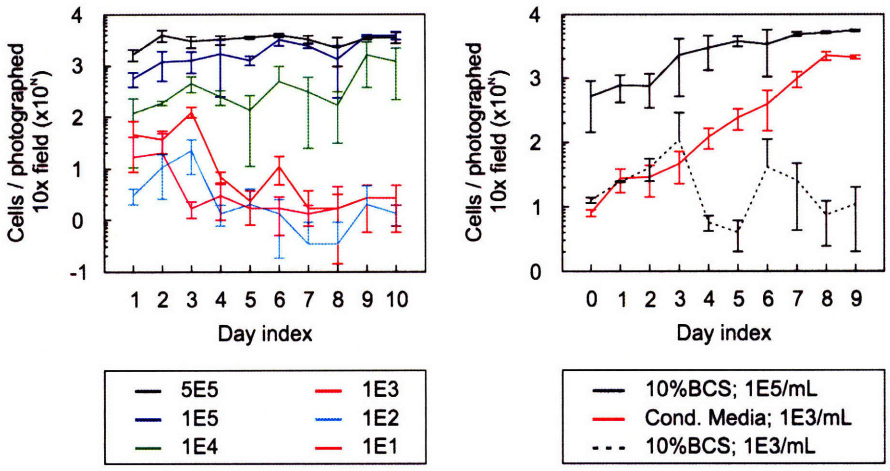

Figure 39: During attempts to transfect HL-60 cells with various plasmid types, Geneticin selection seemed to kill off all cells in a given culture. After observing such an effect several times, I was curious to know whether or not HL-60s might demand certain minimal in-dish densities to successfully proliferate. At left, I show the results from several (n=3) experimental runs where I tracked the daily in-dish cell counts (done automatically using a cell/imaged field counting program) across multiple days and multiple cell/mL starting densities (cells fed every three days). In these results cells with initial in-dish densities < 1E4 cells/mL failed to proliferate effectively. At right, I then attempted to "rescue" the proliferation response for low-density platings by incubating cultures with densities below the 1E4 cells/mL threshold using conditioned media. As desired (red trace) conditioned media provided adequate conditions for proliferation. Any further attempts at transfection would take such an effect into account.

This result carried strong implications for our transfection efforts. If selections were strong enough to reduce in-dish densities below a critical limit, then there would likely be a dearth of essential nutrients needed to enable effective recovery of the cells that had successfully incorporated target plasmids. Assuming that this effect was a paracrine dynamic caused by secreted factors from neighboring cells, I ran an assay to attempt rescuing the proliferation behavior for a series of cells who's starting in-dish density fell below the 1E4 cells/mL cutoff. In three separate runs, I successfully used conditioned media (taken from dishes seeded at 5E5

cells/mL that had been left to incubate for 24 hours) to recover the desired proliferation effect. Such a result suggested an added avenue might exist to enable HL-60 transfection.

Since performing this investigation, I have discovered a number of sources lamenting the challenges associated with HL-60 transfection[171, 172]. Despite our frustrations, it was somewhat comforting to know that we were in good company. Dr. John Albeck and I eventually began looking to other possible non-adherent lines, but halted our efforts on the basis of results I will present in the following section.

Complications to preclude sorting-focused assays

Though I had encountered and remedied a variety of sizeable technical challenges in developing my 400-site sorting-focused platforms, during device testing, a subsequent round of complications emerged. As I highlight in Figure 40A, capturing large groups of single cells was relatively straightforward using our standard sample loop injection procedures. With both HL-60 and BA/F3 lines, my UROP, Hari Singal, and I regularly recorded single-cell cross-array trapping percentages approaching 70% (i.e. number of sites filled with one and only one cell divided by 400). The hindrance arrived when we attempted to release targeted cells located within the array. Though I had made efforts to calibrate the 3-nm-thick nitride deposition in my fabrication sequence, it proved largely inadequate for preventing captured cells from affixing to the device substrate after trapping. Effective sorting using row/column deactivation unfortunately proved to be an elusive response for my array-based platforms. To add thickness to the deposited nitride film might have offset this unwanted binding effect but it would bring associated compromises to the in-system DEP mechanics. It seemed unclear to me that there was an operational window where I could leverage both n- and p-DEP forcing (both essential for high loading percentages) while at the same time enabling effective targeted site release.

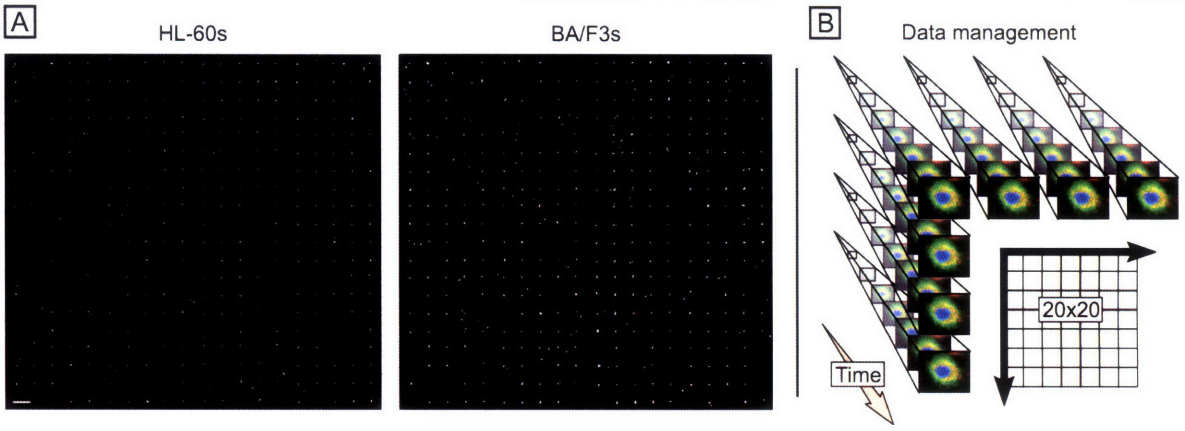

Figure 40: Using my revised 20 × 20 p-DEP chips my UROP, Hari Singal, and I successfully demonstrated widespread cell loading effects in array-based formats. In **(A)** (Scale bar ≈100 μm) I highlight this result using both HL-60 and BA/F3 cell lines. It proved regularly feasible to load my 400-site design such that over 60% of all "pixels" filled with single-cells. A complication for work depending upon the analysis of imaged dynamics within such cell groupings is the acute need for effective data management and image processing power. The diagram in **(B)** attempts to highlight the abundance of information that must be stored and examined in "real time" for the types of sorting assays initially envisioned as a target application of my work.

Beyond release complications, while surveying even whole-cell fluorescently-stained lines I began encountering several data management and storage complications. First, I had coded all of peripheral software using MATLAB GUI-based development tools. Though this approach offered an excellent avenue for quickly (3-5 weeks) designing a functional control interface, it is well known that MATLAB operational efficiencies become taxed as coding complexity grows. Its interpreted, programming structure, means that coding that fails to leverage compiled (and consequently, fast) subroutines internal to the language can ultimately limit run-time capabilities, For systems needing to manage information in real time, this limitation can present sizeable complications.

In a non-optimized system, surveying an entire 400-site array using magnifications powerful enough to enable single-cell imaging could impact the types of information that one might gather. If the inefficiencies of the coding mean that it requires sizeable cycle times to image all array sites, in some contexts, grouping recordings from a single pass through the array under a shared time stamp heading (i.e. t_0) could potentially present a strained approximation. Rapid intracellular dynamics occurring within the cells might additionally pose challenges for effective monitoring. It is often possible to overcome data acquisition cycle times concerns by imaging multiple cells in individual recorded images. Additionally, for many of the commonly surveyed biological pathways, the kinetics associated with intracellular protein dynamics occur on the 10s of minutes to hours time scale, which would not necessisarily impose unmanageable hindrances. By understanding some of these details of the data acquisition process, one can make better choices for pairing candidate assays with in-hand technologies and furthermore appreciate ways that optimization efforts might provide notable gains.

To illustrate yet another aspect of this data management challenge, I provide an example data set in Figure 40B. Since the target application space for my project centered upon the idea of tracking dynamics within cell populations and then making decisions regarding which cells to sort, I needed an effective means for not only recording single-cell data from multiple locations across the chip at many points in time, but also the processing power to analyze dynamics within those data stacks subject to the 3 hour time frames established by the studies outlined in Figure 38B. In other words, I needed to have a means for rapidly determining which cells out of the total held population were displaying protein shuttling oscillations, morphologies, or translocation events of a specific type. Though several platforms exist that enable the automated recognition of specific imaged phenotypes[74, 173], incorporating such capabilities into my control software setup added a level of complexity that I was not entirely ready to approach.

Transitioning to on-chip endpoint "full stream" analyses

With a full understanding of the hard realities involved in approaching sorting-focused assays, I took some time to refocus my efforts and, as discussed in general terms in Chapter 1, began considering opportunities in the domain of on-chip endpoint assays. As I highlight in specific terms using Figure 41, I attempted to frame details of the NF-κB signaling module in a revised context involving "full stream" assays. Rather than trying to analyze cells positioned in arrays and then make image-cued sorting decisions, I opted to try and simply position cells with my arrays and use imaged readouts as the endpoint collected data. This would mean that I would still need to maintain viable cells within my devices but that I would not need to be as concerned with how on-chip manipulations would impact subsequent efforts to record data. Also, if cells

remained affixed in place on the device substrate it would not necessarily be a problem. This expanded capability meant that I could potentially move toward using adherent lines in various device types.

As a brief reminder, in these "full stream" assays, I wanted to track effects from a new perspective that could monitor imposed drug stimuli (i.e. pulsed, ramped, or maintained exposure), in-cell protein dynamics, and downstream outputs. For the NF-κB pathway, the drug stimuli would amount to different TNF-α concentrations; the intracellular dynamics would center on the shuttling of NF-κB proteins between the cytoplasm and the nucleus; and the downstream response would focus upon quantified measurements of IL-8 secretions. The specifics of this assay, arrived with the key benefit of framing my project within the overarching mission the MIT-affiliated Cell Decision Process (CDP) Center. As a member of this collective of researchers, I found myself well positioned within a community of multidisciplinary thinkers who could provide valuable advice and help tune the relevance of my work within a systems biology context.

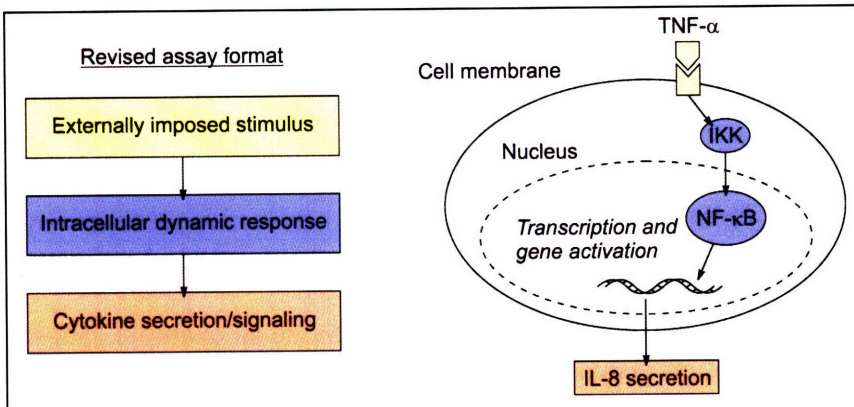

Figure 41: After facing several substantial challenges related to sorting based studies, I began examining a revised assay format focused upon "full stream" cell analysis. In this approach (left) I hoped to monitor cell responses from the drug stimuli, to the internal signaling dynamics, and subsequently track secretion responses. Using the the NF-κB pathway as a target system, I began efforts to study the relationship between TNF-α-induced receptor activation, NF-κB shuttling mechanics, and the eventual secretion of the inflammatory cytokine IL-8.

In general terms, TNF-α is a ligand that can elicit a diversity of responses in different biological systems. In some settings it acts as a pro-death signal and in others it appears to function as a pro-life stimulus. As the CDP center works to analyze pathways from the perspective of inputs that drive eventual cell fates, using TNF-α to probe the nominally pro-life NF-κB signaling cascade while monitoring the activated secretion of an inflammatory cytokine, presented an interesting survey space that could adequately advertise novel functionalities of my cell-handling arrays. From this stance I was opting to try and connect, from input to output, potential relationships in a series of system components that had never been studied in single assays as a continual chain of events. While I was originally excited about studying the shuttling mechanics of NF-κB proteins as a cue for sorting, here they could serve as a new avenue for understanding related IL-8 behaviors. (Note: NF-κB activates many genes when it translocates to the nucleus. Though the upregulation of IκB production was the focus in the original feedback dynamic, here we are more interested in the activation of genes that control IL-8 secretions.)

To transition to this revised investigation format, several technological components came into play. At the time, I had in hand a large collection of row/column-connected semi-"ring-dot" arrays that I had produced in my drive to develop a large-scale single-cell sorting array (described in Chapter 3). Unfortunately, as noted above, since the targeted sorting effects proved challenging to elicit, I was then left with the task of attempting "full stream" assays using devices originally adapted to another purpose.

A major driver for these new investigations centered on positioning multiple distinct cell types on a common surface. Through this added flexibility, I hoped to demonstrate capabilities surpassing those made available using either standard cell culture techniques or alternative microsystems platforms. Monitoring a "full stream" response across numerous cell types and testing for cell-pattern-dependent responses would clearly set my work apart from competing approaches. To utilize my 20 × 20 row/column-connected devices for such efforts would have demanded routines such as the one illustrated at the upper right of Appendix 11. First, I would need to load all sites in the array with cells of a specific type (colored in red in the Appendix). Then, using row-column addressing, I would need to selectively remove targeted cells

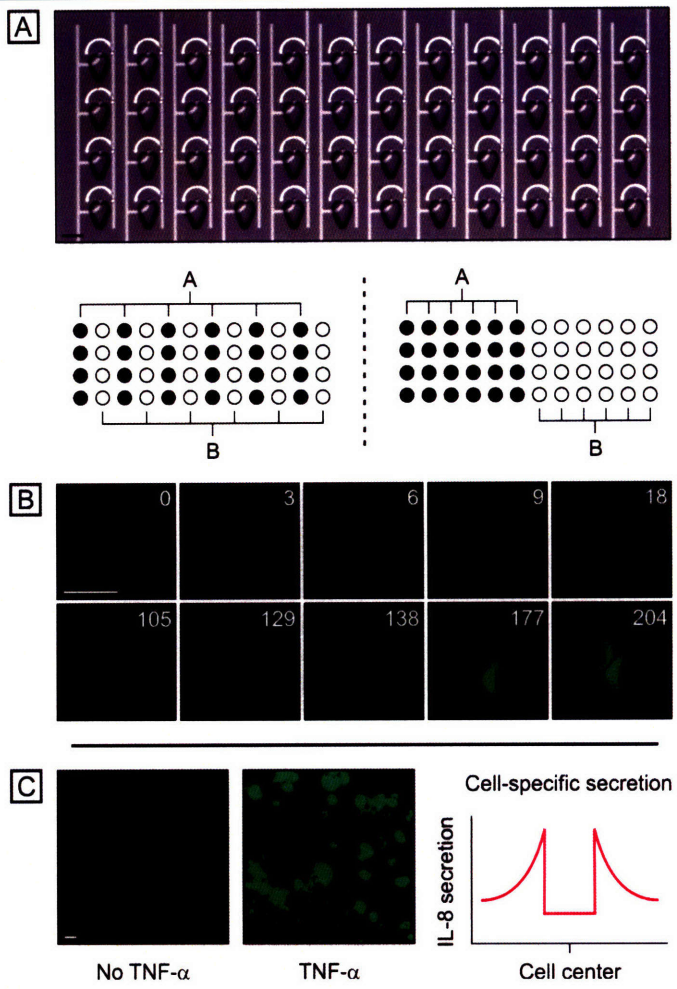

Figure 42: Using a series of column-wise connected array devices (upper part of **(A)**), I hoped to investigate possible differences in the cascade of events outlined in Figure 41. Suspecting that diffusible factors played a roll in various kinetics, I imagined organizing distinct cell populations (with unique siRNA pretreatments) in two different configurations try eliciting differential behaviors (lower portion of **(B)**). In **(B)** I present a set of HT-29 cells displaying GFP-tagged NF-κB proteins. In a dish-based live-cell microscopy environment, Dr. John Albeck and I validated the presence of subcellular translocation mechanics in our hands using direct stimulation with TNF-α (Numbers indicate minutes after TNF-a introduction. Scale bar ≈15 μm.). With help from Dr. Suzanne Gaudet and Dr. Mingsheng Zhang, I likewise began employing ELISPOT detection methods (see Appendix 11 for added details) to monitor IL-8 secretions from HT-29s in dish-based setups **(C)** (the "downstream" component in our "full stream assays") (Scale bar ≈15 μm). In conditions lacking a TNF-α stimulus, very little IL-8 secretion occurred. In such dish-based environments, the cell-specific secretions proved challenging to delineate since there had been no cell patterning at the onset of the assay. Using my array-based systems, I hoped to decipher such effects through precise cell placement and the collection of measured data similar to what is shown at the far right in **(C)**.

from the originally captured grouping. I could then backfill the unloaded sites with a second population (colored green in the Appendix). By repeating such routines I could eventually load up an entire array with patterned groupings of different cells (shown in step 5 in Appendix 11). Unfortunately, such an effort would have demanded reliable row/column release mechanics and thus the 400-site arrays developed in Chapter 3 would not suffice.

As I show in Figure 42A, when designing the dual-stop mask set mentioned in Chapter 4, I solved this system-level experimental need by including a series of chips enabling column-wise DEP activation in 4 × 12 arrays. By linking distinct control lines to each of the columns in such arrays I could selectively load different portions of the chip with different cell lines and avoid struggling with row/column techniques that are ill-suited for such purposes. By using a 48-site array, I also could bypass some of the data management complexities affiliated with more sizeable array formats. Each of the device footprints presented in Figure 42A furthermore offered avenues for functioning via two distinct operational modes. On the one hand, assuming that the on-chip weirs could effectively capture cells, I could use standard cell-culture medias and hydrodynamic capture mechanics to organize multi-cell patterns. Alternatively, if I encountered challenges with weir-based on-chip cell retention, I could avoid PPS (or SU-8) processing steps altogether and use the device for a semi-"ring-dot" p-DEP-based capture. I hoped that this added flexibility to adapt a common chip type to operations in any buffer condition would grant key latitudes for obtaining "full stream" data.

My focus for "full stream" assays centered on positioning cells of two different types in configurations outlined in the lower portion of Figure 42A. One line would exhibit an unfettered wild type cell with fluorescently-tagged NF-κB proteins. The other would be developed by taking portions of the original wild type population and subjecting such cells to siRNA treatments[12, 13] that could shut down the functionalities of IκB β and ϵ isoforms (should undamp NF-κB shuttling dynamics allowing continual translocations between the cytoplasm and nucleus). Using the two patterns (...ABAB... and ...AABB...), I imagined that paracrine signaling factors from the different cell lines might interact in ways that could render unique IL-8 secretion responses. In other words, I thought it might be possible to see a more uniform effect in the IL-8 secretion responses tied to ...ABAB... patterns as the local microenvironment of each cell (regardless of type) would largely be the same. On the other hand, I imagined that the IL-8 secretions stemming from ...AABB... cell patterning might show a graded differential effect. In such cases cells close to the AB border might behave similar to cells in the ...ABAB... setup and cells well-removed from such locations might show cell-line-specific responses.

To approach this type of survey, I began working with live-cell in-dish adherent HT-29 (ATCC, Manassas, VA) cell lines (culture specifics outlined in the Biological Methods Appendix). A gift from Dr. Peter Sorger's lab, these lines presented NF-κB-GFP fusion proteins for tracking translocation dynamics. Over time, with the help of Dr. John Albeck, I too successfully replicated the protein shuttling oscillations reported elsewhere (see Figure 42B). To track IL-8 secretions, I worked with Dr. Suzanne Gaudet and Dr. Mingsheng Zhang to gain experience using Enzyme-linked immunosorbent spot (ELISPOT) detection protocols. I highlight the basics of such assays as well as my envisioned method for incorporating them within the overarching "full stream" analyses in Appendix 11 (see "Key steps in ELISPOT "full stream" analyses").

In brief, ELISPOT methods leverage the coordinated kinetics of separate in-culture "capture" and "detection" antibodies. The "capture" antibodies are initially plated on the inner surfaces of a target culture vessel. Cells are then seeded onto such surfaces and allowed to attach. After a drug stimulus (in our case TNF-α), cells can respond by secreting a variety of diffusible factors (in our case we are interested in IL-8 secretions). Such factors then bind to the "capture" antibodies in a highly specific fashion. To detect this binding effect, a second primary antibody (the "detection" antibody) is needed. This "detection" antibody is fluorescently tagged or else biotinilated and also binds (with a specificity matching that of the "capture" antibody) to the secreted factors of interest. Using fluorescence microscopy, tracking the secretion levels of various cytokines becomes feasible either directly or via Alexa-linked streptavidin treatments.

As I show in Figure 42C, using plates specifically designed for ELISPOT assays, I had no trouble producing a differential response between populations of HT-29s treated with TNF-α and others lacking such a system input in runs with the ELISPOT routine outlined in the Biological Methods Appendix ("ELISPOT protocol - human IL-8 development module"). With the ability to position cells in the array-based configurations shown in Figure 42A, I hoped to help elucidate details related to cell-specific secretions (see Figure 42C right). As the unorganized dish-based ELISPOT test assays show, lacking cell patterning, it is challenging, if not impossible to match secretion profiles to individual cells within the culture. Responses tend to overlap as cells clump together along on the plated surface.

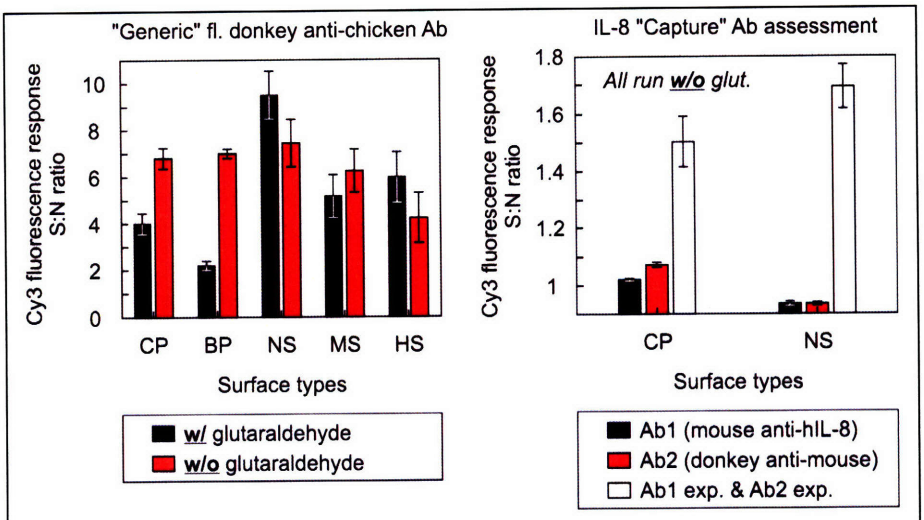

Figure 43: After battling with complications in transferring ELISPOT detection methods to the silicon nitride surface chemistries presented within my devices, I became suspicious that the "capture" antibody was failing to bind to the chips in reliable or effective ways. As such, I attempted to simplify the "sandwich"-style approach and investigate the adhesion of any "generic" fluorescently-tagged antibody to nitride surfaces. As shown at left in the signal:noise (noise ratings measured using comparable surfaces - not exposed to antibodies) plot, using clear and black plates (CP and BP) as well as nitride surfaces with no siliane (NS), mid-level silane (MS), and high-level silane (HS) treatments, all surface types seemed to provide adequate S:N values either with or without a glutaraldehyde surface pretreatment step (n=3 for all data points. Averaged values presented along with their standard deviations - error bars.) This response looked promising and seemed to support the idea that gluteraldehyde pretreatments did little to enhance performance. Addtionally, silane surface treatments, if anything, only seemed to degrade the responses. (See Appendix 11 for actual imaged surfaces.) At right, I then tested the propensity for the in-assay mouse anti-hIL-8 antibody to adhere to nitride surfaces. I used a secondary fluorescent antibody (donkey anti-mouse) as the system readout. For both clear plate (CP) and non-silanized nitride (NS) surfaces that lacked pretreats with gluteraldehyde, I regularly produced sizeable S:N values. Unfortunately, such metrics were somewhat misleading as they stemmed from patchiness in the cross-image responses. (See Appendix 11 lower right.)

The next step involved transferring such a detection scheme to the silicon-nitride-coated surfaces used in my array-based chips. As I highlight in Appendix 11 ("Full IL-8 ELISPOT assay - Initial attempts on nitride-coated surfaces"), this technology transfer proved to be somewhat confounding. Though I could use either standard plate reader dishes with black sidewalls (black plate or BP) or the dishes specifically developed for ELISPOT detection (clear plate or CP), on silicon samples coated with 250-Å-thick nitride layers using our standard LF-SiN process, it proved challenging to observe differences between stimulated and untreated populations (see the lack of green signaling in the "Nitride on Si; TNF-α" case). I observed this effect across three separate assay sequences of this type.

After struggling in my efforts to exhibit ELISPOT responses using full IL-8 detection assays on nitride surfaces, I began working to enumerate possible failure modes. My prime suspicion was that the nitride surfaces were not presenting favorable conditions to enable proper and stable adhesion of the "capture" antibody. To try examining this effect I began work with a "generic" fluorescently-tagged antibody. This "generic" antibody was a donkey anti-chicken (PeproTech, Inc., Rocky Hill, NJ) type that simply offered a means for understanding whether or not any primary antibody would properly adhere to chip-like surfaces. After a single deposition step matching the protocols used for depositing the capture antibody in the full IL-8 development module, I could use microscopy techniques to examine surface adhesion properties.

As I show at left in Figure 43, using this fluorescently-tagged "generic" antibody, I successfully produced sizeable signal:noise ratings (noise levels measured for each case by imaging equivalent surfaces lacking any antibody exposure) for depositions on clear plates (again CP), black plates (BP), and nitride-coated chips with no silane (NS), vapor-deposited silanes[24] (mid-level, designated MS; 24 hour exposure in a desicator to tridecafluoro-1,1,2,2-tetrahydrooctyl-1-trichlorosilane), or dip-deposited silanes[129] (high-level, designated HS; 10 second submersion in a 5% dimethyl dichlorosilane in dichlorobenzene) (n=3). (I offer the actual raw values recorded for each surface type in Appendix 11 along with sample images of the distinction in signaling levels seen on clear plates versus nitrides.) For each surface type, I likewise examined the use of glutaraldehyde treatments[174] (applied to surfaces at 1% concentrations for one hour at room temperature, following antibody deposition). Such treatments along with the silanes were expected to potentially enhance the adhesion response between the antibodies and the surfaces. Across three separate assays of this type, the glutaraldehyde and silane treatments seemed to do very little to improve binding effects.

With these promising results in hand, I ran a subsequent series (n=3) of tests using my assay specific non-fluorescent IL-8 "capture" antibody again following the same deposition protocols (see Figure 43 right). In these experiments, I examined only clear plates and unsilanized nitride surfaces. I also elected not to include glutaraldehyde treatments. For both surfaces, I witnessed sizeable signal:noise responses only for the case where the capture antibody (R&D Systems, Minneapolis, MN) (Ab1 - mouse anti-hIL-8 Cat. No.: MAB208) and a secondary fluorescent antibody (R&D Systems, Minneapolis, MN) (Ab2 - donkey anti-mouse Cat. No.: AF-208-NA; designed to attach to the constant portion of the heavy chain element in the capture antibody) were applied in sequence. This effect suggested that for both surface types, the IL-8 "capture" antibody was successfully adhering and there were furthermore minimal off-target binding events occurring when using the secondary fluorescent antibody. Unfortunately this signal-to-

noise-based assessment was a bit misleading. While it appeared (numerically at least) to be a viable response, upon examining the images used to generate the signaling readout, it became clear that scattered locations across the images presented saturated pixel groupings (see Appendix 11 - IL-8 raw values also included). These patchy saturated regions contributed to a net elevated average pixel fluorescence level for our surfaces. As opposed to the preceding work with "generic" antibodies, the assay specific setup failed to produce the uniform cross-surface antibody coatings desired. This response presented a bit of a problem for using ELISPOT techniques in my devices, as it suggested that the "capture" antibody was in fact struggling to adhere properly. Without a capture antibody in place, IL-8 detection would prove challenging.

Much appreciated commentary from my doctoral committee helped me to realize that incorporating such detection means as a part of my "full stream" assays was somewhat superfluous. As I aimed to directly regulate responses by organizing cells into two distinct configurations (...ABAB... and ...AABB...), I had an effective means for modulating in-chamber paracrine signaling effects (i.e. responses linked to cell secretions). As such, the impact of this regulation was something that I could potentially observe by simply monitoring differences in the internal shuttling mechanics of the NF-κB proteins. Though I would not directly observe IL-8 by forgoing on-chip ELISPOT strategies, I would have an avenue for monitoring secretion responses implicitly. Furthermore, after added committee-based discussion and a continued dialogue with Dr. Suzanne Gaudet, it became clear that simply demonstrating a differential response among distinct lines in different patterning configurations (...ABAB... and ...AABB...) did not have to mandate the complexities of siRNA-based methods. Rather than sticking with the NF-κB module and attempting to knockdown activity specific to various IκB isoforms, it made more sense to look for distinctions in cell-pattern-specific apoptotic responses using either wildtype HeLa cells or Bcl-2 overexpressing HeLa lines. In this case the two different cell types were already available as engineered lines in the Sorger lab, and so all that would be required from a biological pretreatment perspective would be cell line maintenance and injection into devices at the appropriate times. Here the response could amount to a morphology-based metric where apoptotic cells blebbed and surviving cells remained attached and spread out. Additionally, little work had been done to evaluate regulated paracrine signaling in the context of apoptosis. This revised stance offered the potential to shed new light upon some of the cascaded dynamics occasionally observed during in-dish TRAIL-stimulated apoptosis assays. Such dynamics often amounted to a wave-like progression of cell suicide from one portion of the culture to another. We were curious to know if regulating the spacing between such wildtype and Bcl-2 overexpressing HeLa lines might alter this response or at least offer an approach for new types of investigative studies.

Troubles with weir-based cell handling

Though I mentioned complications associated with weir-based cell-manipulations in Chapter 4, here I will discuss some of the key experiments related to my eventual decision to abandon such techniques in pursuing more advanced biological assays. After struggling to load cells in PPS weirs I reexamined the higher-resolution patterning capabilities offered by SU-8 chemistries and temporarily ignored complications associated with autofluorescence responses.

As I show in my first test (see upper left of Appendix 12), using 20-μm-high SU-8 weirs patterned (no electrodes; over 600 weirs per chip; used standard SU-8 2015 protocols outlined in

the Fabrication Methods Appendix) on nitride-coated silicon surfaces (subjected to bovine serum albumin (BSA) pretreatments - 1 hour exposure to a 1% solution in PBS) I did witness K-562 cell capture (used K-562s because they were the largest cells I could find and thus offered the best chance for demonstrating a loading response). Unfortunately, even with these sharper SU-8 features and larger cells, I only could only produce minimal loading percentages. I attempted to capture higher numbers by injecting subsequent boluses of cells (labeled "runs") into the device chamber. After only two runs of this type, cells clumped within the array to an undesirable extent. Additionally (see sequence at the top right of Appendix 12), though the typical unloading response stemmed from lateral cell rejection around the sides of individual weirs, I did notice, in many cases, cells rotating over the tops of weirs to escape.

To try remedying the non-specific surface binding and the vertical unloading responses, I fabricated another series of chips. These devices presented taller (30-μm-high) weirs (again on nitride-coated silicon; SU-8 2015 spread speed reduced to 1300 rpm) and surfaces pretreated with Pluronic F127 chemistries (1 hour soak in a 1%w/v solution in PBS; BASF, Florham Park, NJ). As the SU-8 film needed to be thicker to render such capture structures, the mask was necessarily further separated from the wafer substrate during processing. As an undesired effect, these new weirs replicated mask features less effectively, leading to a more rounded set of printed features. These taller weirs captured very few cells. Additionally, the Pluronic-based surface treatments seemed to do little to offset device fouling.

As a last ditch effort, I carefully reexamined 20-μm-tall weirs using Pluronic F127 surface coatings. Though I was able to eliminate the non-specific binding observed in earlier assays (though I am not fully certain why), even after four cell injections, where I saturated the chip surfaces with K-562s, the cross-array loading densities proved to be incredibly low. As highlighted in the Appendix (using red outlines), this response was the best I could produce using weir-based designs. Not unexpectedly, subsequent tests using enhanced process PPS weirs (mask coating and descum) left much to be desired.

Cell attachment and growth in packaged devices

With weir-based strategies unsuited for the on-chip endpoint assays targeted in my work, I transitioned back to using p-DEP-based platforms alone. My first concern then centered on determining whether or not HeLa cells (the type I aimed to use in more advanced biological assays) could attached in the low-conductivity buffers (0.1 S/m) necessary for their operation. I knew that they could survive for at least three hours in such media types, but other cell responses were unknown. It was my hope that I could use p-DEP patterning to position cells in target locations, allow them to attach to the in-chip substrate, and then displace the in-chamber media with standard cell culture media. In this manner of operation, the low-conductivity buffer would only then be used for patterning and attachment protocols.

In Appendix 12 ("A need to swap media after loading - Will HeLas attach in LC buffers?"), I detail my first experiment examining attachment responses. Using a 20 × 20 array-based device and standard device-specific cell handling techiques, I patterned cells to on-chip "dot" locations and used a heat gun to maintain the on-stage setup at 37°C. After six hours, cells in the chip environment had not attached. In control cases run in an incubator, cells on surfaces suspended in low conductivity buffers all failed to attach in this time span, while Helas in standard medias

did at-least begin to attach. I worried that exposures to low conductivity buffers for more substantial periods might impact cell physiology to an undesired extent. With even a six hour time course I was doubling the buffer exposure time known not to impact proliferation dynamics (as established by the initial studies from Figure 38.)

I decided to step back for a moment and perform a bit of a sanity check. I wanted to make certain that I could produce a cell attachment response within my devices by replacing my low-conductivity buffers with standard culture media. As I show at the bottom of Appendix 12 ("Will HeLas attach/live on-chip in standard culture media?"), after injecting HeLas into my devices (no voltages applied this time) and leaving them on-stage at 37°C (again via heat gun) for 24 hour periods, I observed widespread cell death. Comparable nitride surfaces when left in an incubator instead showed substantial attachment and growth. This effect was somewhat surprising and led me to believe that the heat gun temperature management was perhaps failing to maintain a 37°C on-chip environment.

As I had run all of these attachment-style assays using HeLas, I began to wonder if my chosen line was more finicky about attaching than other cell types. As I provide at the top of Appendix 13 ("In-dish attachment - varying cell types") I ran a simple in-dish study to try and probe for such effects. Using HeLas, HT-29s, and 3T3s (cell concentrations ~1E5/mL), I examined attachment responses in both low-conductivity buffers and standard culture medias at 3 hour, 6 hour, and 24 hour time points. For all cell types surveyed, over the course of 24 hours, low-conductivity buffer exposure decreased in-dish cell counts and eventually promoted widespread death responses. No attachment behaviors appeared for any of the lines. Alternatively, the controls run in standard medias, promoted the anticipated attachment responses. 3T3s began attaching after only 3 hours, HeLas started doing so around 6 hours, and by the end of the time course all cell types had fully anchored themselves to their culture substrates.

This set of results did not bode well for my hope of using p-DEP-based strategies to investigate more advanced on-chip endpoint assays. Though I had reported in Figure 40 challenges associated with cells readily affixing to the on-chip "dots", I found myself struggling to reproduce such a response in this stage of my work.

Despite its potential irrelevance, I wanted to try and uncover added insight regarding some of the possible reasons why I was seeing widespread cell death in my devices even when using standard cell culture medias. Again, my main suspicion was that heat gun temperature management was a poor means for maintaining a 37°C on-chip environment. I elected to try porting cells into my devices (using standard media and no on-chip voltages) and then placing the entire packaging setup into a cell culture incubator (7.5% CO_2). As shown mid-page in Appendix 13, after 24 hours, cells plated in such a fashion failed to survive. Comparable controls run on nitride-coated silicon samples and culture dishes enabled the desired attachment and growth response. This result seemed to suggest that something native to the device packaging was hindering cell viability.

I, in turn, packaged two new devices using nitride-coated chips that lacked electrodes. I exposed one of the devices to a vacuum plasma (2 minute run time in a plasma cleaner; Harrick Scientific Products, Inc., Pleasantville, NY) prior to installing the on-chip microfluidic enclosure. The

other I left untreated. (At times I had used plasma runs of this type when packaging and I wondered if the treatments run on my prior tested devices had somehow altered their in-device surface chemistries.) Using standard cell culture media and an incubated environment, I again witnessed cell death within my packaged devices. Comparable runs on unpackaged nitride chips (blanks) enable viable responses. Across all cases, the plasma treatments seemed to have no impact.

I then began to suspect that the enclosed nature of my packaging setup might be the cause. I envisioned it limiting essential gas exchange dynamics. My first attempts to address this concern leveraged both equilibrated media (left in an incubator for 2 hours) and CO_2-independent media. Placing newly packaged nitride chips in an incubator and subjecting in-device cells to these new media conditions still failed to promote viability responses (see upper portion of Appendix 14).

My next thought was that if it was a gas-exchange-related matter, I might successfully alter on-chip kinetics if I could replace the top coverslip with a more gas-permeable material. As I detail in the cross sections found in Appendix 14, I thus attempted to rescue a survival phenotype by taking one of my original packaged nitride chips and replacing its in-system flow chamber ceiling with a 4mm thick slab of PDMS. After placing this modified device into an incubated environment and running a 24-hour time course with standard culture media, I finally witnessed an in-chamber viability response. Echoing the controls, HeLas attached in my devices and presented health elongated morphologies. This rescued response seemed to support the notion that coverslip-based packaging was hindering critical gas-exchange dynamics.

Not fully satisfied with this result, I wanted to also examine additional material-related effects. I traced the path from flow inlet to outlet on all packaged devices and assembled a list of every material that could potentially contact in-device fluidics. I then focused upon items I imagined might harbor the capacity for inducing on-chip cell death. Using a series of coverwell-based (Molecular Probes, Eugene, OR) assays (HeLas loaded via pipette at 1E5/mL concentrations into 350 µL coverwells and left in 37°C incubated environments for 24 hour time spans), I discovered (see Figure 44) that the high-performance epoxy (Part No.: 99393, Loctite Corp., Rocky Hill, CT) used to encapsulate and seal all of my devices, when left in contact with growing cultures, decimated cell populations. Other, in-system materials seemed to present no net negative effects on growth dynamics.

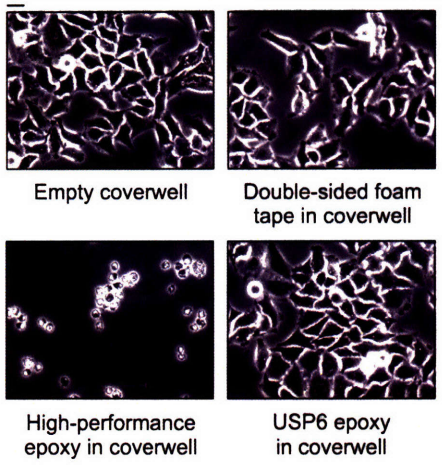

Figure 44: After struggling to maintain viable HeLa cultures in the on-chip environments, I began testing the toxicity of various in-system materials. Unfortunately (lower left), the high-performance epoxy used to seal my devices promoted cell death. An alternative USP6 epoxy (Part No.: 354, Epoxy Technology, Billerica, MA) offered a potential substitute. (Scale bar ≈20 µm)

With this material-related effect in play, one might wonder how replacing the coverslip with a PDMS slab in prior efforts rescued the survival response, when high-performance epoxy was still used to seal the modified chamber type. I suspect that the high-performance epoxy sealing never actually

contacted in-system fluids after the PDMS slab-based flow-chamber ceiling was installed. In working with prior devices reliant upon coverslip tops, I occasionally witnessed in-chamber fluids seeping underneath the gasket layer used to define the on-chip flow chamber. It is my suspicion that the rigidity of the coverslip (which was always bonded to the flow chamber gasket) was the prime cause of such effects. A stiff flow chamber top could easily pull the gasket away from the device substrate if debris was present on the chip surface at the time that the device was assembled. This separation from the substrate would then leave a direct path for in-system fluidics to contact the high-performance epoxy. On the other hand, the PDMS slab-based lid was much more flexible. It could therefore bend to allow the on-chip flow chamber to establish a functional seal preventing direct contact between fluids and the cell caustic epoxy.

To reexamine gas-exchange-related concerns one last time, I assembled two new devices (see Figure 45). Here I hoped to produce results that were unclouded by materials-related concerns. In one case I packaged a nitride chip using a coverslip top in another I used a PDMS slab-based top. For both devices I then used liquid PDMS sealing (known to be inert in cell culture contexts). As shown by the results in Figure 45, for cases incubated using cell culture media, I

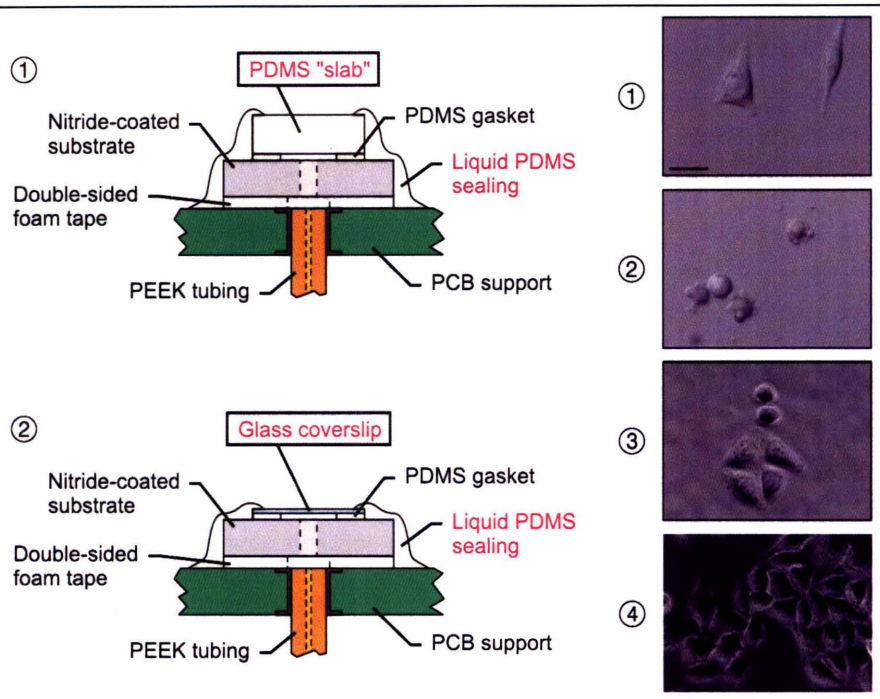

Figure 45: Beyond the material toxicity complications, viability concerns arose from apparent limitations pertaining to in-system gas-exchange. To evaluate this behavior I packaged two nitride-coated blank (no electrodes) chips using, in one case, a PDMS "slab"-based device flow chamber ceiling (labeled 1) and, in another, a standard glass coverslip-based chamber ceiling (labeled 2). Using PDMS liquid sealing (instead of high-performance epoxy) and standard high-conductivity culture media, I then seeded their chip-surfaces with HeLa cells and placed each packaged device into a cell-culture incubator for a 24-hour time span. In the device that presented a PDMS "slab"-based lid, cells attached and survived (see 1 at right). In the device encapsulated using a coverslip-based lid, cells did not survive (see 2 at right). For comparison, I used two added positive control conditions. In one case I ported cells through upstream fluidics and then "dumped" them into a plate (labeled 3 at right) and in another I simply plated cells in a standard Nuncalon delta dish (labeled 4 at right). In both of these control cases I also used standard cell culture media and 24-hour in-incubator treatments. Both control cases enabled cell survival. (Scale bar ≈20 μm)

again replicated the responses seen in my original attempt to modify the device flow-chamber ceiling using a more gas-permeable top. Coupled with my materials result, my work had uncovered two critical components to enabling on-chip viability in my devices. All future designs needed to avoid incorporating high-performance epoxies and they needed to make considerations for effective gas-exchange.

Refocusing for on-chip mitosis assays

After progressing through an experimental trajectory that presented a number of design challenges confounding progress toward more advanced biological assays, I began to reassess the key functionalities enabled by my device platforms. From a cell handling perspective, the forcing effects enabled by my developed p-DEP-based platforms offered a robust means for stabily holding single, isolated, non-adherent cells in designated on-chip locations. By means of software-controlled off-chip signalling, I could additionally modulate such holding forces dynamically over the course of live-cell imaging routines. This functionality, though less technologically involved than the sorting and on-chip organizational efforts that had motivated key components in many of my designs, still set much of my work apart from other approaches to cell handling. I thus began efforts to exploit this capability for novel biologically-relevant purposes.

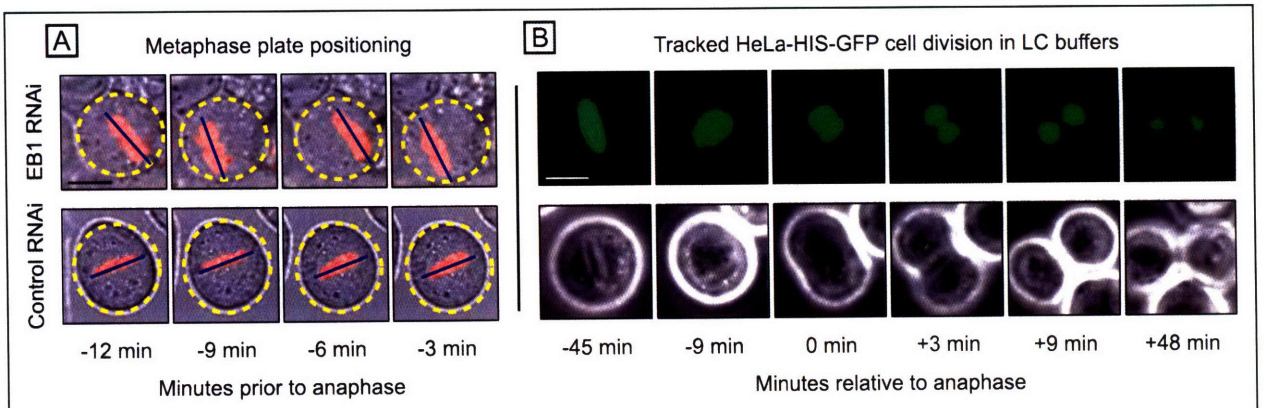

Figure 46: In work presented by Dr. Viji Draviam[3] **(A)**, an apparent tumbling effect has been seen in the mitotic plate for cells depleted of EB1 functionality. Unfortunately without having an in-dish method to "pin" the cell membrane in place, assays run in standard plated cultures fail to eliminate the possibility that the entire cell itself is tumbling instead of the mitotic plate alone (cells become non-adherent when they progress through mitosis). To test for the feasibility of examining such effects in low-conductivity buffers (within arrays reliant upon p-DEP cell "pinning" at in-system "dot" locations) , I ran assays subject to such conditions in microcoverwell environments **(B)**. Supporting the non-acute effects of such buffers, I did witness cell division in HeLa lines (used GFP-histone tags). Though this sequence crops images of a consistent size, Appendix 14 shows a fixed image field that highlights the in-well drift associated with these cells over the span of the assay. Again, such an effect makes the case for using DEP to "pin" cells in place and cultivate a better understanding of distinctions in membrane and mitotic plate dynamics. (Scale bars ≈10 μm)

One specific application that presented a need for stably holding non-adherent cells at dedicated on-chip locations related to work published in 2006 by Dr. Viji Draviam[3]. In her studies of mitotic division, she had observed an interesting tumbling effect in cells depleted of EB1 activity (see left in Figure 46). As such cells approached anaphase, the internal mitotic spindle proteins appeared to detach from cell membrane contact points to enable free rotation and translation of

the aligned chromsomes. Using an engineered HeLa line displaying GFP-tagged histones, she could directly monitor such effects using live-cell imaging techniques. In discussions with Dr. Suzanne Gaudet and Dr. Viji Draviam, a common question often directed at this work centered on challenges in understanding the extent that possible cell membrane motions might be contributing to the observed dynamics. As a nominally adherent HeLa cell progresses toward a division event, it temporarily becomes non-adherent such that it can separate from the substrate and parse into two new daughter cells. During this progression it is conceivable that in-dish convection components could exert hydrodynamic forces upon such non-adhered HeLas which could in turn motivate whole-cell rotation and/or translation events. Rather than attempting to engineer pixilated in-membrane fluorescent constructs, Dr. Draviam and I imagined leveraging p-DEP-based cell trapping to decouple concerns related to possible relative motions between the mitotic spindle and the surrounding cell. With halted in-system fluid flows we anticipated that on-chip dielectrophoretic trapping forces would dominate over any electrorotation effects that might arise, since the fields surrounding individual on-chip array sites lacked rotational components. In this context, it seemed challenging to imagine an induced torquing condtion that could stem from a phase lag between in-cell charge moments and the trapping fields.

Before we could progress with work in this revised application space, I needed to understand whether or not it would be feasible for cells to progress through division events while being suspended in the low-conductivity buffers needed for p-DEP-based forcing. To prime collections of HeLa-HIS-GFP cells for this study, I treated populations (cells plated one day prior in 150 mm dishes at seeding densities of 5E5 cells/mL using standard passaging techniques - densities were Coulter counter calibrated - Z2 Beckman Coulter, Fullerton, CA) to a 2 hour long MG-132 (Calbiochem, La Jolla, CA) drug treatment (administered at 1:1000 dilutions in standard cell culture media from original 10 mM stocks in dimethylsulphoxide (DMSO)) that halted cultures in metaphase. After shaking these primed cells out of their dish-based environments, I ran three rinse routines (with standard HeLa cell culture media) before resuspending them in low-conductivity buffers (Type 2 - BCS doped - as listed in the "Low-conductivity buffers" subsection in the Biological Methods Appendix). I then injected these low-conductivity cell suspensions into micro coverwell chambers and began imaging their dynamics using live-cell protocols (inverted scope; on-stage temperature set to 37°C; on-stage CO_2 concentration set to 5%). As I highlight on the right in Figure 46, I successfully recorded cell division subject to these low-conductivity conditions.

Such a result proved to be a milestone. While I had confirmed that short exposures to low-conductivity buffers did not impact long-term proliferation mechanics, this was the first time that I had observed a natural cell process in these non-native environments. During this in-buffer division study, I came to fully appreciate the need for preventing cell translation and rotation within an on-chip environment. Though I had no fluidic connections linked to the micro coverwells used in this work, cells regularly migrated throughout the imaging field over the course of the experiments. The images shown on the right in Figure 46 follow a specific cell division event by cropping a consistently sized frame around a translating and rotating set of cells. To better understand this dynamic, the sequence of frames located at the bottom of Appendix 14 present the same division event from the perspective of a non-moving reference frame. It is easily seen that over the course of the experiment our dividing cells move from the

lower left hand corner of the image field to the upper right hand corner. Using p-DEP forcing we would have a potentially useful means for offsetting such effects.

Knowing that division was possible in low-conductivity buffers, I then began efforts to examine such effects in a functional chip-based setting. Despite understanding that high-performance epoxy and on-chip coverslips promoted in-system death responses, I had not had the time to repackage a new p-DEP-based device lacking such components. It was certain that these material- and gas-exchange-related matters affected viability over the course of a 24 hour time period, but it was not known if such concerns mattered for the two hour windows needed to run on-chip mitosis studies. I decided to take the chance and investigate potential leeway by injecting low-conductivity suspensions of metaphase-halted cells into a device packaged with the caustic epoxy and coverslip enclosures. As I present at the very bottom of Appendix 14, I discovered that the on-chip incubation promoted apoptotic morphologies within the two hour time frames. Apparently, either in isolation or combination, epoxy and coverslip components created acutely detrimental conditions that motivated cells to commit suicide rather than progress through division. In some ways, this was an interesting effect, as it seemed to suggest that though the cells were primed for division, they still had capacity for deciding upon their eventual response fates.

To simply try assessing the capacity for observing on-chip division, I ran a follow-up experiment using a blank silicon nitride chip (no electrodes) packaged with a PDMS slab-based lid and liquid PDMS sealing. As I show in Figure 47, I successfully observed progression through mitosis using this on-stage setup. This result was my first demonstration of the functional viability of heat gun methods for maintaining 37°C on-chip environments. For at least the two hour window used to run this assay, it proved feasible to keep cells alive without having to resort to moving my packaging setup to a standard tissue culture incubator. As such, live-cell imaging strategies remained feasible.

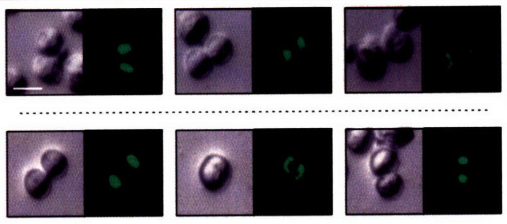

Figure 47: At the top I present both brightfield and FITC images of cells demonstrating on-chip division in low-conductivity buffers. Such a response offers support for the adequacy of heat-gun-based methods for maintaining 37°C on-chip microenvironments. As controls, at the bottom, I present on-chip division for the case where I have seeded a device surface and then placed the chip packaging into an incubator. (Scale bar ≈10 μm)

Unfortunately, due to the substantial overhead needed to sort through the complexities of transitioning to more advanced bio-assays, I have not yet had ample opportunities to perform further assays focused upon mitosis under the condition of on-chip p-DEP-based cell trapping. I believe that it will only be a matter of time, before I can attempt to validate this targeted device flexibility and potentially offer a new avenue for surveying cell function.

In this chapter, I explored a variety of options for utilizing my developed cell handling platforms for more advanced biologal assay purposes. Much of this work involved surveys of cell viability in on-chip environments. Compatibilities with low-conductivity buffers, density-dependent inplications for transfection efforts, device surface/antibody binding effects, toxicities affiliated with device packaging materials, and even gas-exchange matters, all served to impact the

flexibilities of this engagement. My investigative trajectory motivated a transition from sort-focused assays to on-chip "endpoint" approaches and I ultimately provided a novel outlay for continued investigations related to mitotic cell division processes. Though obstacles arose throughout the design, fabrication, and testing portions of my doctoral studies, by careful strategizing and a willingness to reconsider available options, I believe that my work has offered new and valued insight to the biological microsystems field. I hope that it has paved some small portion of the path that pairs engineering capabilities with cell biology investigational needs.

Appendix 10

Envisioned chip-based assay format for exploring NF-κB shuttling dynamics

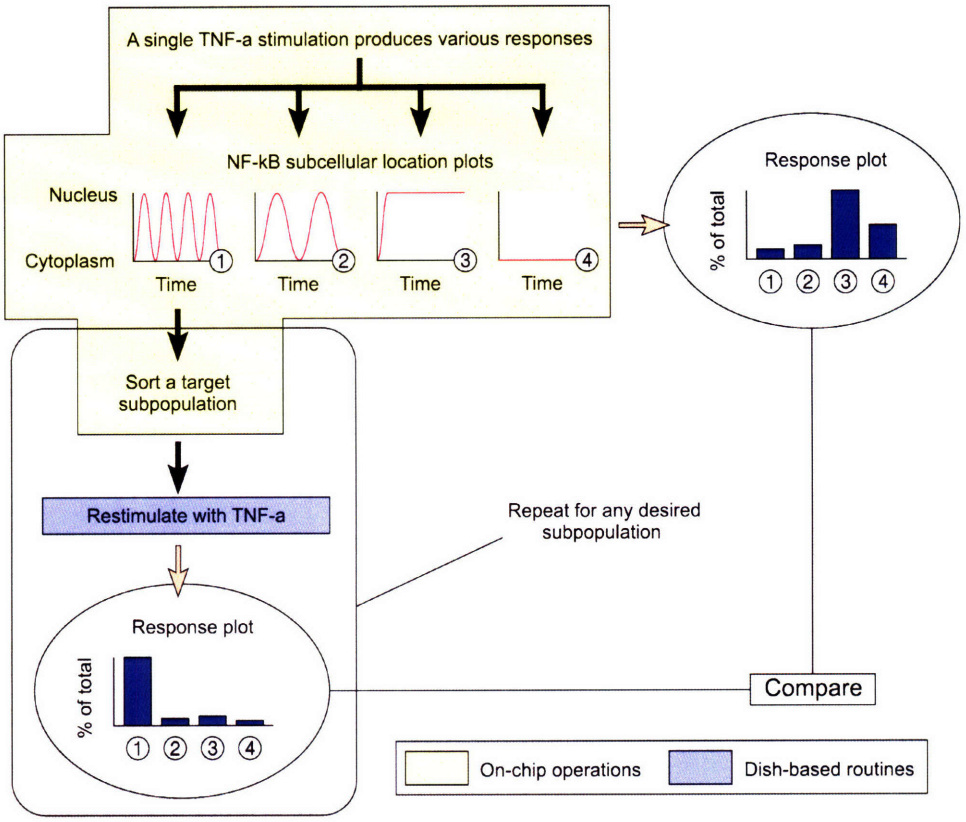

Available in-cell "tools" for studying apoptosis

Smac-reporter for tracking mitochondrial membrane status

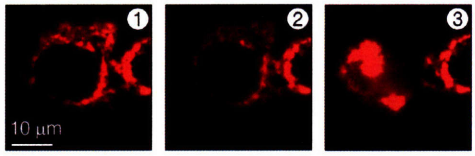

FRET-reporter to monitor caspase activation within individual cells

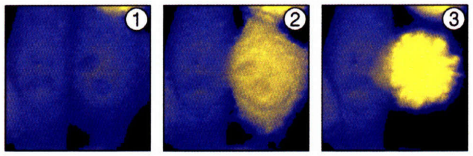

Whole-cell morphology as a marker for apoptotic status

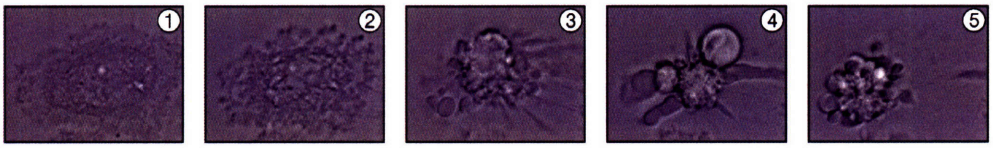

Appendix 11

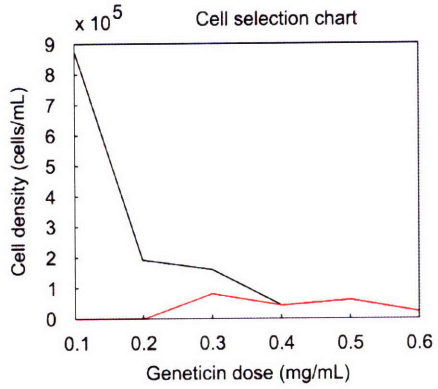
x 10^5
Cell selection chart
Cell density (cells/mL)
9
8
7
6
5
4
3
2
1
0
0.1
0.2
0.3
0.4
0.5
0.6
Geneticin dose (mg/mL)

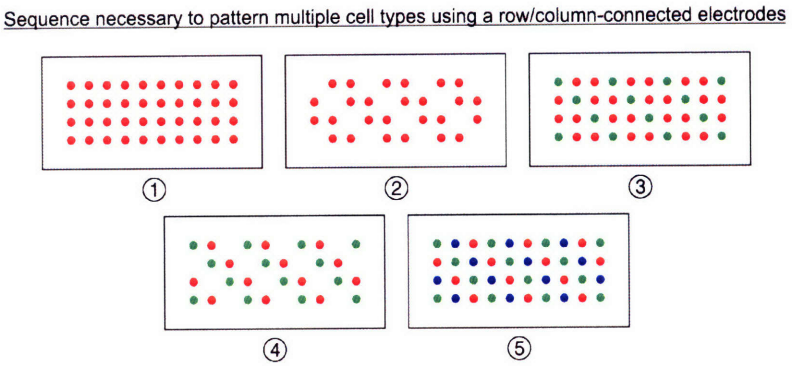
Sequence necessary to pattern multiple cell types using a row/column-connected electrodes
①
②
③
④
⑤

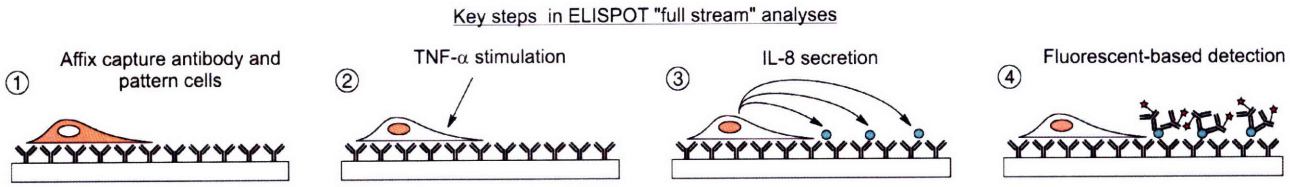
Key steps in ELISPOT "full stream" analyses
①
Affix capture antibody and pattern cells
②
TNF-α stimulation
③
IL-8 secretion
④
Fluorescent-based detection

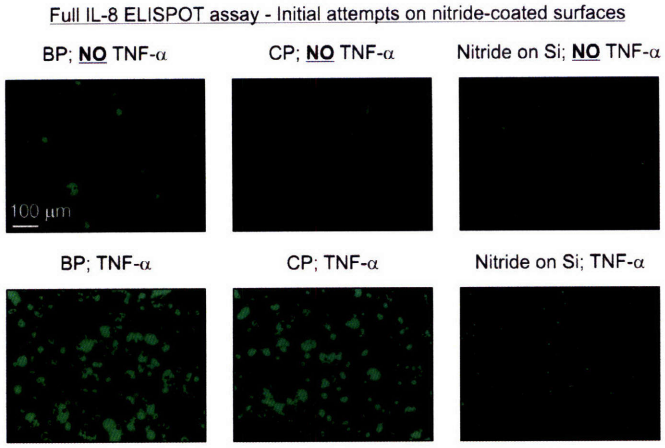
Full IL-8 ELISPOT assay - Initial attempts on nitride-coated surfaces
BP; NO TNF-α
CP; NO TNF-α
Nitride on Si; NO TNF-α
100 μm
BP; TNF-α
CP; TNF-α
Nitride on Si; TNF-α

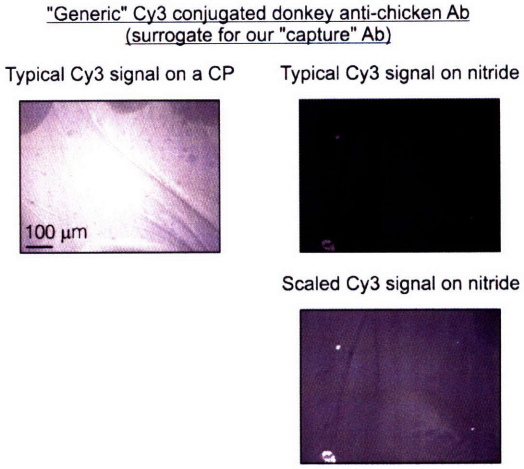
"Generic" Cy3 conjugated donkey anti-chicken Ab
(surrogate for our "capture" Ab)
Typical Cy3 signal on a CP
Typical Cy3 signal on nitride
100 μm
Scaled Cy3 signal on nitride

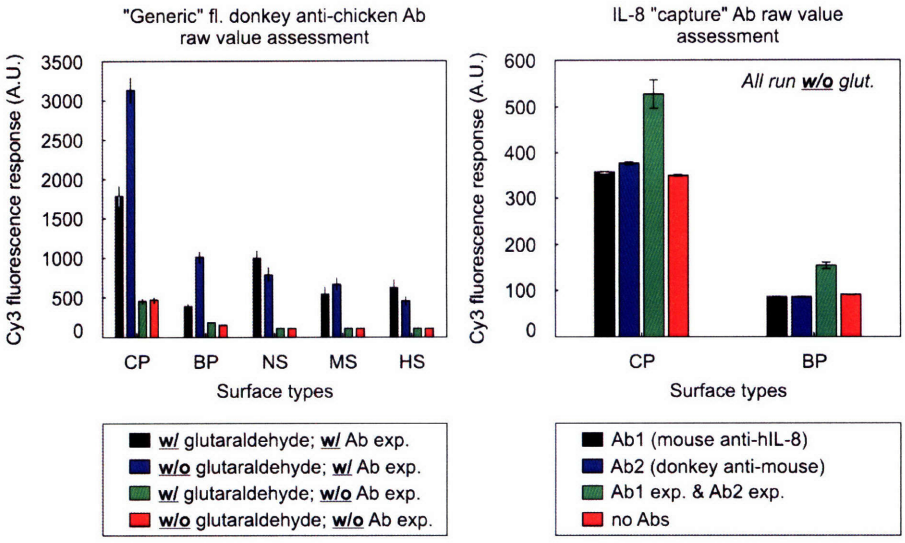
"Generic" fl. donkey anti-chicken Ab
raw value assessment
Cy3 fluorescence response (A.U.)
3500
3000
2500
2000
1500
1000
500
0
CP
BP
NS
MS
HS
Surface types
w/ glutaraldehyde; w/ Ab exp.
w/o glutaraldehyde; w/ Ab exp.
w/ glutaraldehyde; w/o Ab exp.
w/o glutaraldehyde; w/o Ab exp.

IL-8 "capture" Ab raw value
assessment
All run w/o glut.
Cy3 fluorescence response (A.U.)
600
500
400
300
200
100
0
CP
BP
Surface types
Ab1 (mouse anti-hIL-8)
Ab2 (donkey anti-mouse)
Ab1 exp. & Ab2 exp.
no Abs

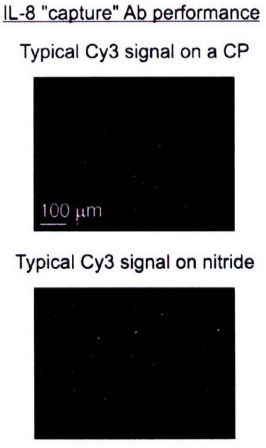
IL-8 "capture" Ab performance
Typical Cy3 signal on a CP
100 μm
Typical Cy3 signal on nitride

Appendix 12

SU-8 weirs (20 μm) **w/** nitride surface and BSA coating
(Fouling commonplace)

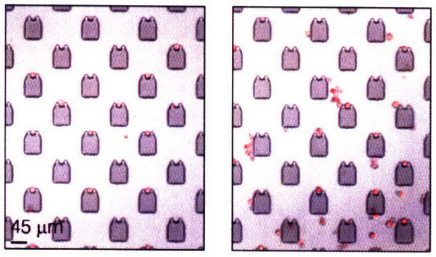

Run 1 Run 2

K-562s often "pop" vertically over SU-8 weirs (20 μm)

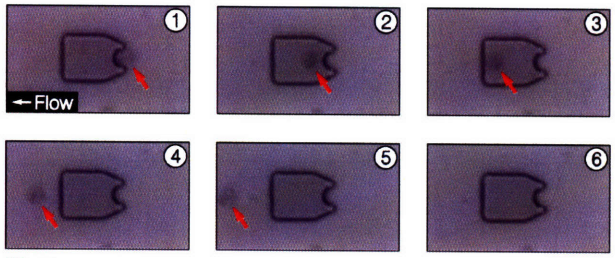

15 μm

SU-8 weirs (30 μm) **w/** nitride surface and Pluronic F127

Few cells trapped; poor print resolution

SU-8 weirs (20 μm) **w/** nitride and Pluronic F127
(Some cells trapped; much less fouling)

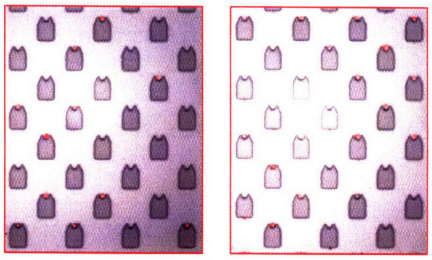

Run 1 Run 4

PPS weirs (20 μm; mask coating + descum) **w/** nitride and Pluronic F127 *(Poor performance)*

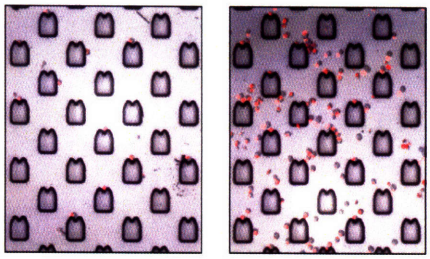

Run 1 Run 4

A need to swap media after loading - Will HeLas attach in LC buffers?

All images recorded 6 hours after cell seeding

20x20 chip, patterned initially w/ electrodes, LC buffer, on stage w/ heat gun

Nitride blank, LC buffer, in incubator

Nitride blank, std. media, in incubator

Nuncalon delta, LC buffer, in incubator

Nuncalon delta, std. media, in incubator

Will HeLas attach/live on-chip in standard culture media?

20x20 chip, no on-chip voltages, std. media, on stage w/ heat gun

Nitride blank, std. media, in incubator

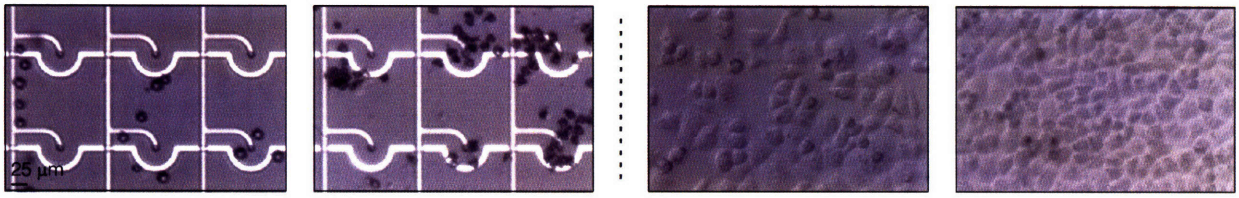

12 hours 24 hours 12 hours 24 hours

Appendix 13

In-dish attachment - varying cell types

All assays run on Nuncalon delta TCPS

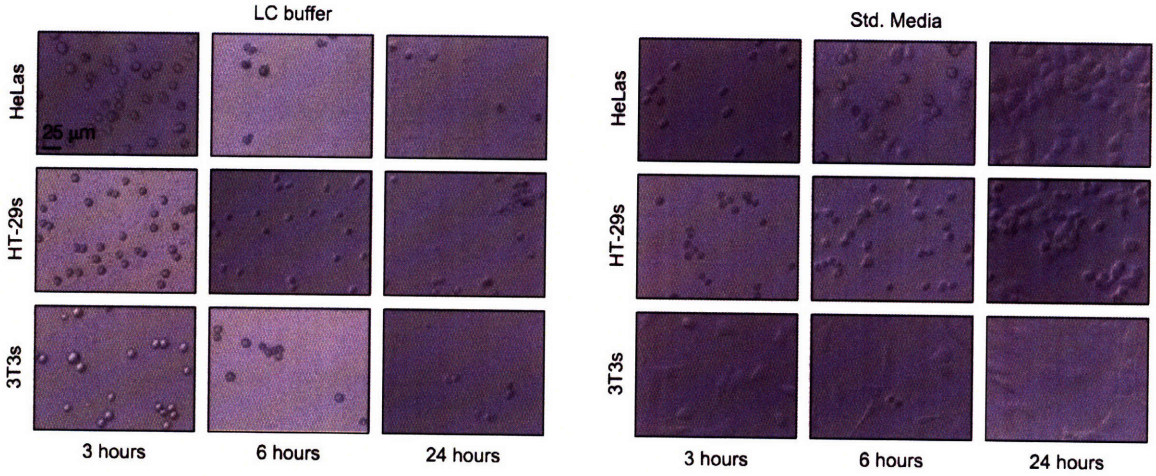

Will HeLas attach/grow in my devices if I place the in an incubator and use standard media?

All images recorded 24 hours after cell seeding

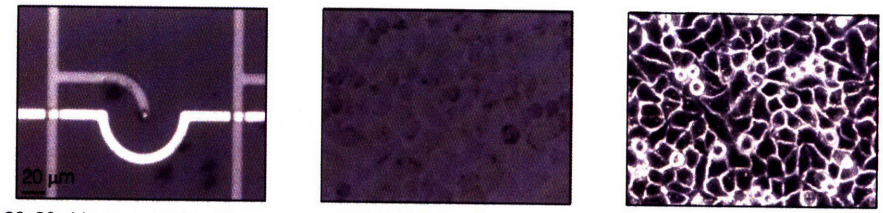

20x20 chip, no on-chip voltages, std. media, in incubator

Nitride blank, std. media, in incubator

Nuncalon delta, std. media, in incubator

First solid clue that something native to the device was hindering cell attachment/growth

Will HeLas attach/grow on packaged nitride surfaces lacking electrodes (placed in an incubator; using standard media)?

All images recorded 24 hours after cell seeding

Packaged nitride blank (exposed to 1 min vacuum plasma), std.media, in incubator

Packaged nitride blank, std.media, in incubator

Nitride blank (exposed to 1 min vacuum plasma), std. media, in incubator

Nitride blank, std. media, in incubator

Nuncalon delta, std. media, in incubator

Appendix 14

Will equilibrated or CO_2-independent medias enable in-device attachment/growth (devices, again, placed in an incubator)?

All images recorded 24 hours after cell seeding

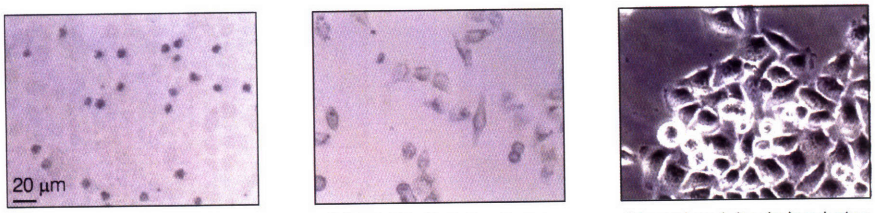

Packaged nitride blank, in incubator

Nitride blank, in incubator

Nuncalon delta, in incubator

Despite several assays including ones with Hepes buffers - cells still do not survive in the devices

Can we "rescue" the survival phenotype by modifying our device flow chamber to enable enhanced gas exchange?

All images recorded 24 hours after cell seeding

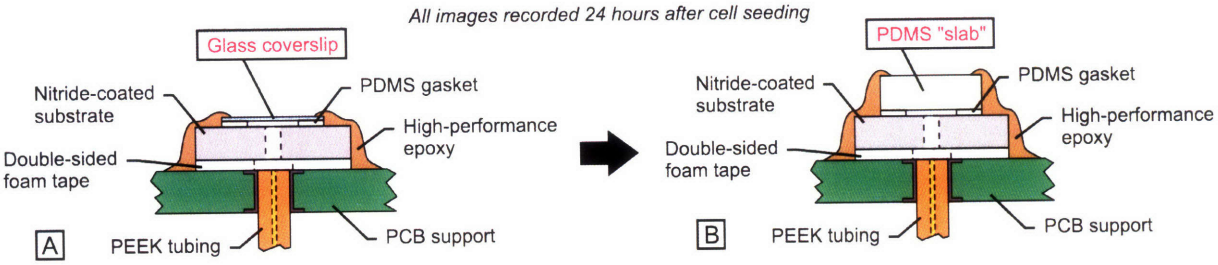

Packaged nitride blank (fixed PDMS "slab" flow chamber), std. media, in incubator

Nitride blank, std. media, in incubator

Nuncalon delta, std. media, in incubator

Potentially wide-sweeping packaging implications

Tracked HeLa-HIS-GFP cell division in LC buffers - notable cell movement within the coverwell

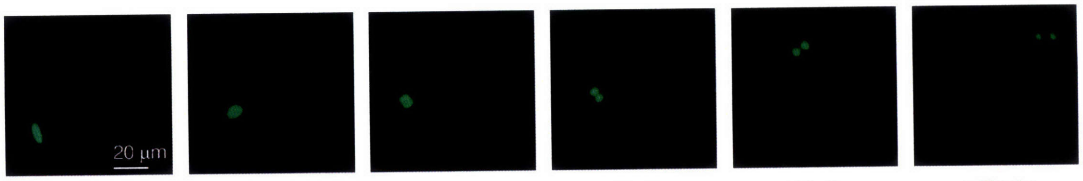

-45 min | -9 min | 0 min | +3 min | +9 min | +48 min

Minutes relative to anaphase

Packaged nitride blank (high-performance epoxy and coverslip), LC buffer, in incubator

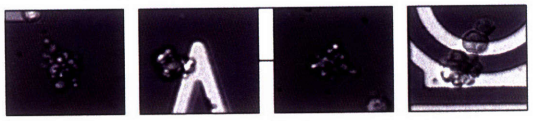

15 µm

Apoptosis = default response

Chapter 6: Conclusions, contributions, and future plans

Throughout the preceding five chapters, I have presented a multifaceted collection of microsystems-based platforms and commensurate testing initiatives dedicated to the service of single-cell biological assays. Here, I will attempt to add perspective to these developments and outline, in concrete terms, many of the contributions I have made as a part of this work. Supplementing an overarching summation, I will also discuss a variety of tangential efforts, and speculative investigational plans that, subject to matured refinement, could offer new roadmaps for on-going research.

Key proof-of-concept developments

At the onset of my graduate studies, a fascination with the development of system-level complexities for enabling novel image-cued cell sorting played a pivotal role. Though this motivation changed in time, it led me to focus upon a number of strategies for designing, building, and testing activated cell-trapping "pixels" structured within larger array-formatted topologies. Following this cognitive trajectory, helped me to establish a sizeable body of work and an associated knowledge base that has impacted the direction of my work ever since and has had widespread implications at least within our local lab community and within the broader biologically-focused microsystems field.

This proof-of-concept work led to two distinct cell trapping architectures. The first[40, 124] leveraged a central "dot" and a peripheral "ring" geometry to generate localized electric field non-uniformities and affiliated positive dielectrophretic forcing to "pin" individual cells at prescribed on-chip locations. In developing this geometry I revised and leveraged in-house modeling efforts, which we have since disseminated via free-ware distribution, to characterize holding responses, induced transmembrane voltage effects, and even in-system temperature rises[5] prior to device fabrication. This "ring-dot" topology offered the first scaleable DEP-based approach to single-cell trapping that leveraged planar electrodes wedded to the device substrate alone.

These designs effectively coordinated with a new method for enabling in-array site addressing. Using a strategy that did not require on-chip transistor elements, I implemented a novel row/column-based electrode routing scheme to enable the targeted deactivation of any site within the "pixel" array. When compared to conventional methods that dedicated two linkages (one nominally positive and one nominally negative) to any on-chip "pixel" and scaled as $2n$ (where n equals the number of "pixels" in the array), I could form arrays where interconnect demands grew only as $2\sqrt{n}$.

With my proof-of-concept 4 × 4 p-DEP "ring-dot" architectures, I then demonstrated, for the first time, transistor-independent row/column-based particle sorting first with silver-coated polystyrene beads, and subsequently with CellTracker Green stained HL-60 cells. This work laid the foundation for future efforts targeting sorting on the basis of any imaged cue.

To test the initial proof-of-concept designs, I additionally developed a unique chip-on-board (COB) packaging format. With this setup, I could easily position my devices onto an upright microscope stage and stably hold them in place for essentially drift free imaging of on-chip cell handling routines. This format not only established a template for all future implementations explored in my doctoral work but also became an adopted standard employed in well over half of all microsystems-based designs emerging from our lab.

Scaled design contributions

In progressed scaled designs I merged, side-by-side, discrete on-chip components for exerting n-DEP forces with other on-chip components design to exclusively exert p-DEP forces. To enable functional designs with this new approach, I developed a superposition-based means for simulating the forcing effects tied to components driven at different activating frequencies and I further assessed a multitude of design implementations in quantitative ways via in-system flow stream analyses.

Feeding into this emphasis on simulation-based design evaluations, I realized from initial lab tests that cell-trap holding strength was but one component in a broader suite needed for developing platforms from a system-level perspective. Beyond an ability to simply hold one cell at each on-chip "pixel" location, there were also concerns related to both loading and release operations. Managing each of these system-level design challenges led to an enhanced understanding of on-chip DEP forcing characteristics and the development of several novel progressions beyond the initial "ring-dot" implementations.

To better manage loading behaviors and attempt to drive cells toward the designated "dot" trapping regions, I borrowed techniques from other DEP-based cell handling effort to implement on-chip "V" structures capable of channeling disorganized cell suspensions into collimated traces. By aligning these cell traces with downstream in-trap "dots" I modeled, fabricated and, on at least a rudimentary level, tested a new method for enhancing array-wide loading efficiencies.

Coupled with this effort, I redesigned the original "ring-dot" geometries to present a modified semi-"ring-dot" topology. This new "pixel" footprint eliminated the presence of a peripheral activating ring on the upstream sides of each trap offsetting a loading complication seen during tests with the original designs. Rather than impinging upon a trap, meandering around the peripheral ring, and failing to localize to the central "dots", in these new designs, any cells approaching a "pixel" within a prescribed region of influence would trap in the desired fashion.

Beyond just a simple elimination of upstream "ring" components, I further came to appreciate that any on-chip locations where electrodes of opposing polarity crossed produced parasitic in-system DEP forcing effects. With this simulation-based understanding, I then structured my array-based row and column routings so that any electrode crossings would take place in areas not collinear with flow paths sweeping over "dot" trapping centers.

To tackle demands associated with enhanced unloading dynamics, I further developed efforts for incorporating on-chip interdigitated electrode structures. I positioned these IDEs in the fill spaces between "pixel" trapping locations to enable z-directed (out of the substrate) n-DEP

forcing responses. By incorporating such geometries, I then progressed through a series of dual-frequency-based simulations to evaluate the potential for levitating targeted released cells above the trapping envelope presented by empty down-stream "1/4 strength" p-DEP "dots". In this manner, I developed a unique algorithm for testing envisioned device functionalities and, after fabricating a series of such devices, I successfully, at least in small-scale form, demonstrated the desired in-array n-DEP-levitation-enhanced release behavior.

These scaled efforts have provided the first microsystems-based initiative to incorporate frequency-modulated n-DEP (at the IDEs and the "V"s) and p-DEP (at the semi-"ring-dot" cell traps) forcing for single-cell handling in a single integrated platform. Though some of the anticipated functions of these scaled designs have been challenging to realize in consistent and reliable ways, they have enabled large-scale single-cell trapping responses (on the order of 70% across 400-site arrays) and it is probably safe to speculate that this undertaking has produced the world's most complex DEP-based system for handling array-organized groupings of single cells.

As a springboard for this scaled design work, I developed and validated a via-based two-level metal process. Again, stemming from the success of my original 16-site array designs, the functional incentives promised by such a process helped pressure the PTC to revise their in-house machine compatibility charts. With these new tooling capabilities and my subsequent demonstration efforts, others within the MTL community have since adopted some of the aspects of my process to serve their own on-chip electrical connection needs

Building upon the packaging developed for my proof-of-concept forays, with scaled designs I introduced a novel modular organizational strategy[176]. This effort split electrode management between a generalized "packaging" PCB and a separate "adapter" board. Using careful planning, I successfully implemented schemes for grouping bond pad functionalities such that a small number of distinct "adapter" boards could correctly route signaling for a multitude of different chips. This parsed modular approach offered a new flexibility for easily replacing damaged chips and their "packaging" boards to minimize down time on days dedicated to experimentation. An additional benefit centered on the reuse of the original aluminum mounting plates developed for my 16-site designs. To my knowledge, no other microsystems-based initiative has structured design efforts around such an elaborate set of packaging capabilities. As there are no restrictions on the specifics of such modular implementations, this new way of approaching system-level design could prove beneficial across a range of different technology bases.

Electroactive weir offerings to the microsystems community

After facing limitations associated with undesired cell/surface adhesion, my project focus began to transition toward efforts to organize multiple distinct cell subpopulations on a shared substrate. If I could not overcome conditions that promoted binding, why not use them to my advantage to target on-chip "endpoint" analyses decoupled from a need to sort and subsequently collect specific cell subpopulations? Experimental efforts had also shed light upon the challenges associated with managing large data sets. The storage and computational processing power needed to investigate even 400-site arrays quickly outpaced the capacities readily available in our lab.

By developing and testing a novel electroactive weir "pixel" design, I made strides to service this new "full stream" assay format. These new electroactive weirs presented an entirely new strategy for cell-handling and provided new ways to consider tracking cell input stimuli, internal signaling, and eventual cell decision processes. While prior efforts had used passive ceiling-mounted designs, separating weirs from opposing substrates by narrow fluid gaps, my designs adopted a unique substrate-affixed topology that presented large gaps between weir tops and the microfluidic ceiling enclosures while enabling weir alignment with on-chip activation electrodes. These aligned electrodes could then exert targeted n-DEP forcing effects to modulate weir loading and particle retention mechanics.

To calibrate native loading behaviors (no electrode activation involved) of my substrate-affixed designs, I ran a series of assays that probed retention effects using a variety of polystyrene beads with differing diameters. In doing so, I empirically demonstrated, for the first time, the capability for large-gap geometries to enable high-percentage single-bead trapping behaviors and I uncovered interesting size-selective response that was dominated by a flow-rate dependence for oversized beads and by weir topologies for undersized beads.

As part of my testing, in active designs I demonstrated the capacity for these integrated devices to use on-chip n-DEP forcing to selectively repel electrically-polarizable particles from weir capture faces via "ejection"- and "exclusion"-based operational modes. I, in turn, used these strategies to produce several examples of unique on-chip patterning, including a checkerboard footprint of interlaced red and green fluorescent particles, structuring of three distinct bead populations in separate single-bead columns, and small-scale arrays of interlaced beads and cells.

In the development work needed to fabricate bioassay-compatible weir geometries, my colleague, Salil Desai, and I became the first to use commercially-available Dow Corning photopatternable silicone products in a biological microsystems context[43]. Through a number of iterations and careful diagnostic routines we modified processing parameters to increase the print resolution enabled by this unique polymer ("Enhanced PPS weir fabrication process" in the Fabrication Methods Appendix). Though the minimal line widths approached in this work did not surpass those endemic to SU-8 2015 patterning, we did manage to effectively reduce PPS sidewall angles via both mask-coating and anisotropic etch sequences. While the material's low autofluorescence (which we calibrated in comparison to other commonly used cell-culture substrates) was an initial motivator, in steps taken to further validate it for our purposes, we began what may become an on-going assessment of the material's biocompability.

By managing capture necessities via hydrodynamic means and sorting and patterning needs using DEP, I presented and validated the world's lowest-power/"pixel" array-based electroactive platform for targeting in-media single-cell-manipulation. I thus developed a fundamentally new template technology for cell handling and have eliminated essentially all non-weir-print-resolution-related barriers for progressing toward more advanced on-chip bioassays.

Concrete biological assay benefits

Though I faced a number of technical challenges in my efforts to produce more advanced biological results with my cell-handling platforms, accompanying the pursuit, I learned a great deal. From a packaging perspective and cell imaging stance, I demonstrated the possibility of

using my developed technologies to maintain viable cells for extended periods of time outside of incubated environments. In my work, I came to appreciate cytotoxicity effects pertaining to in-house sealing epoxies and even gas-exchange-related consequences associated with on-chip coverslip-based fluidic enclosures.

Though admittedly preliminary in form, I presented compelling arguments for using non-traditional low-conductivity buffers while surveying cell function. Subject to short term exposures, such buffers imparted no significant effects on long-term cell proliferation dynamics. I additionally proved that it was possible for cells to progress through mitotic cell division in these solution types even when placed in on-chip environments. As a partial offshoot of this work, I experimentally demonstrated that halting cells in metaphase and then releasing drug-induced stops still left opportunities for cells to shift their endpoint fates to apoptotic responses. These assays and their results have readied my work for making notable contributions to our biological understanding of key cell behaviors. I anticipate that on-going efforts may soon begin to more adequately highlight the investigative potential offered by my work. Stably holding cells in place during division events would provide a new way to distinguish spindle dynamics from those associated with whole-cell translation and/or rotation mechanics.

Ongoing efforts to assess scaled design performance metrics

As I highlight in Figure 48, preliminary empirical efforts have validated the enhanced functionality of these model-motivated changes. Using a series of video sequences aligned and stacked using post-processing methods, my UROP, Hari Singhal, and I used particle image velocimetry techniques[175] to develop traces reflecting the distinct (silver-coated bead based) loading responses of my original "ring-dot" and my newer semi-"ring-dot" p-DEP-activated "pixels".

In the "ring-dot" geometries we again observed enhanced trapping at the outer "ring" and complications for capture at the central "dot". Alternatively, the semi-"ring-dot" approach appeared to capture any particles entering the trap aligned with minimal y-directed offsets from the central "dot". Though this depiction qualitatively demonstrates an enhanced design, in on-

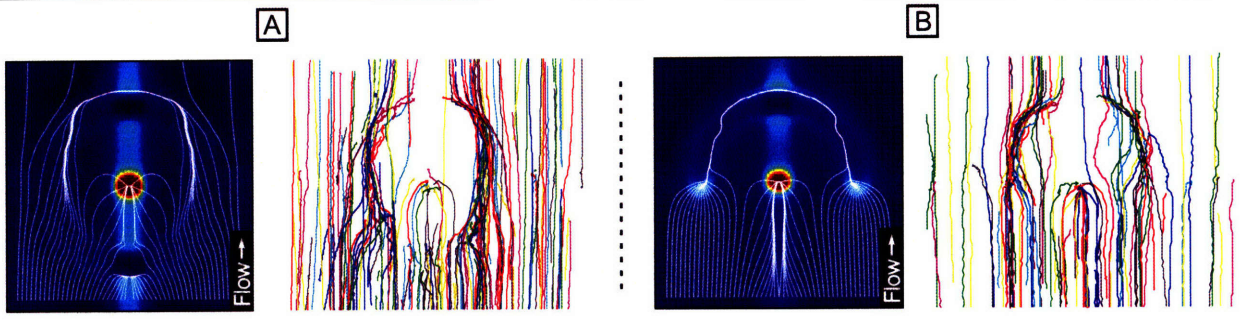

Figure 48: To compare distinctions in the loading behaviors of the "ring-dot" **(A)** and semi-"ring-dot" **(B)** footprints, we used video sequences to track the trajectories of silver-coated polystyrene beads sweeping over activated traps. Using particle image velocimetry we could assemble traces that we could then compare to the initial loading response modeling work. Though we certainly have observed a qualitative match between our modeling and experiments, in future work it will be important to begin examining specific empirically-gathered trajectories and making an effort to replicate them within a modeling environment.

going work it will prove instrumental to revisit our model and, rather than using a uniformly-spaced line of upstream particles, employ the imaged starting locations as test conditions. Ideally, we would then recreate, in a simulation-based context, the actual traces observed during experimental evaluations. This type of exploration would validate our in-house system modeling software tools beyond any extent made possible by prior design efforts.

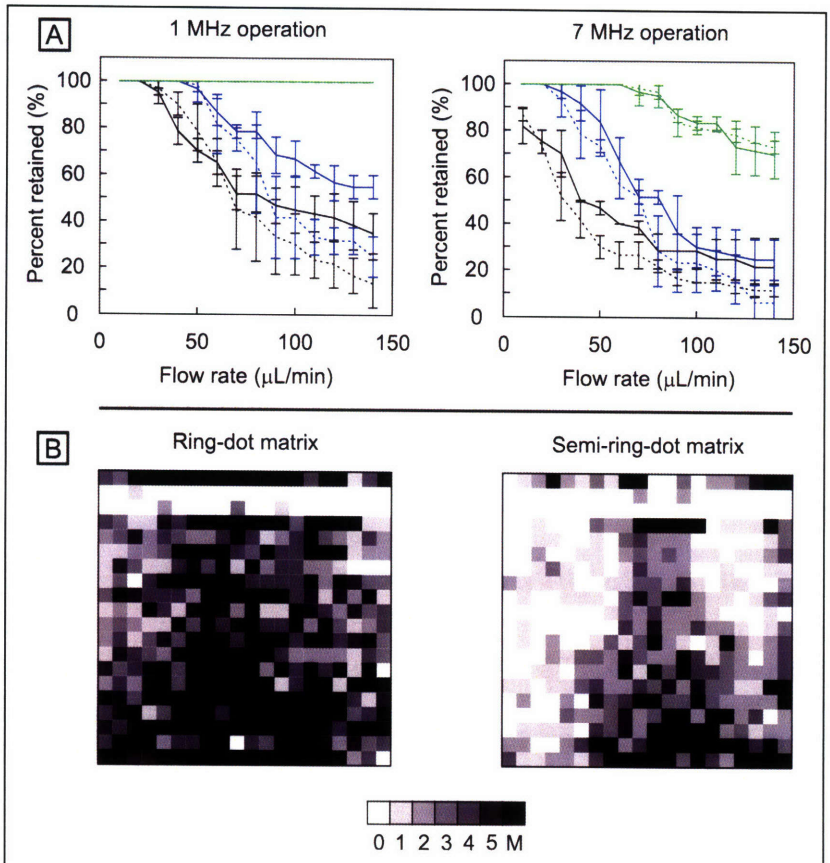

Figure 49: Across separate trials (n=3), I examined the holding characteristics **(A)** of both semi-"ring-dot" (solid traces) and "ring-dot" (dashed traces) trap architectures. For each trial, I loaded 20 on-chip traps in single-bead fashion using silver-coated polystyrene test particles (20 μm in diameter). I then ramped in-chamber flows across a range of rates and recorded the number of beads remaining in the 20-trap set at pauses between rate changes. I ran these studies at two different frequencies (1 MHz and 7 MHz) for a range of different activation voltages (left: black = 750 mV, blue = 1 V, green = 2 V; right: black = 1 V, blue = 2 V, green = 3 V) and computed the associated retention percentages. Despite the geometric differences of the two trap designs, I observed comparable holding mechanics supporting model-based studies suggesting such an effect. As is seen in both plots, there is not a sharp "drop off" where particles transition from holding to release. This effect underscores the "sticking" problems that made targeted release in large arrays challenging. In **(B)**, I show a somewhat qualitative comparison of the consistent and distinct whole-array loading efficiencies seen when using 400-site designs reliant upon either "ring-dot" or semi-"ring-dot" traps. Each pixel is shaded according to the number of silver-coated beads present within a corresponding trap. It is readily apparent that the semi-"ring-dot" arrays provide enhanced single-bead loading responses.

At present I am still in the process of ongoing testing efforts to measure functional differences and similarities between my original "ring-dot"-based designs and my new semi-"ring-dot" configurations. In Figure 49, I provide several interesting results. Across numerous runs, Hari Singhal and I first examined the holding characteristics of these two distinct array types. We performed such surveys by initially loading 20 on-chip sites in single-bead fashion using silver-coated polystyrene beads and our standard injection protocols (bead concentrations typically ~1E5/mL). We would then apply a designated p-DEP trapping voltage and run on-chip flows for one minute spans at prescribed flow rates. We would then halt the flows, count the beads remaining in the original 20-site collection of traps, and transition to a new higher flow rate. In confirmation of preliminary modeling efforts, both designs performed nearly identically. This response suggested that, as desired, reducing the size of the trapping "ring" area did not

serve to compromise the retention mechanics associated with individual "pixels". Additionally, for all traces tracking these mechanics, we did not observe responses detailing a sudden transition from a fully loaded array condition to an entirely unloaded state. I suspect this slow progression of beads out of the activated arrays stems from the undesired adhesion of beads at "dot" locations. Adhesion forces can easily outpace flow-induced drag forces and if there are non-uniformities in such an effect across the array, then it would make sense that certain beads would release subject to differing flow rates. As noted in Chapter 5, it was this adhesion behavior that ultimately led to a shift in focus toward on-chip "endpoint" style assays.

Beyond the loading effects observed from a trap-level perspective (see Figure 48), Figure 49 also provides an examination of array-wide loading characteristics. In the example maps shown, we routinely observed that "ring-dot"-reliant arrays tended to cluster unwanted beads at locations along the peripheral "ring" electrode. Across such arrays we therefore tended to produce low single-bead loading percentages. In stark contrast, out experiments with semi-"ring-dot" designs showed a preference for holding beads at the designated "dot" locations. To date, we have only run a limited number of assays comparing loading characteristics from this vantage point. To enhance the reliability of such surveys we need to perform additional calibrations that ensure each array type witnesses an equivalent quantity of in-coming beads. Without solidifying this dimension of our investigations it is possible to imagine that we have unintentionally biased the outcome of this preliminary work in ways that falsely confirm our conviction that the new design enhancements have improved array loading responses.

Though we had imagined that silver-coated polystyrene beads would prove beneficial in offsetting any potential to bind to in-device surfaces, it became clear that they presented an enhanced potential to cluster together at targeted trapping locations as compared to cells. In effect, by localizing to on-chip "dot" locations their conductive properties served to physically enlarge the on-chip electrodes. The beads could then provide new in-system tethers for subsequently trapping additional incoming particles. These particle-trap and particle-particle interactions then served to compromise the overall loading potentials enabled for any given "pixel" footprint. What we had envisioned as an ideal test particle thus arrived with complexities reflected in array-wide loading efficiencies that, in many ways, made beads ironically more challenging to handle than cells.

My colleague, Salil Desai, has developed a variety of stress-reporter cell lines[41, 170] for assessing the impact of various on-chip handling effects at a transcriptional level. Coupled with his efforts, one might additionally envision utilizing thermal imaging techniques, as suggested in Figure 50, to further probe details of the in-system microenvironment. Such investigations would offer yet another feedback for evaluating front-

Figure 50: Using thermal imaging techniques it might prove useful to monitor in-device temperature profiles. Pairing such analyses with stress-reporter cell line investigations, would offer a more comprehensive overview of the on-chip microenvironment.

end design strategies and validating our model-based understanding of electrode-driven Joule-heating responses.

The future of weir-relevant modeling engagements

In my attempt to further characterize these passive loading dynamics I developed a strong collaboration with members of Dr. Karen Willcox's research group. Through this interaction, one of her graduate students, Boon Hooi Ooi, refined elements of code originally developed by Dr. Carlos Pinto Coelho[1] to examine simulated stabilities relevant to a variety of different weir architectures. By centering rigid spheres in the capture cups of various implementations and then monitoring unloading and retention behaviors for different on-chip flow rates, we made several gains in attempting to replicate experimentally-observed behaviors. As I described in Chapter 4, for SU-8-based weirs, in simulated form, we assembled stability charts reproducing both the lateral unloading and stable holding behaviors. Though I only showed there the output for a 10 μL/min flow rate, at the top of Figure 51 I highlight some of the more comprehensive mappings (red = lateral unloading, white = stable trapping, grey = vertical unloading) that led to my originally presented result.

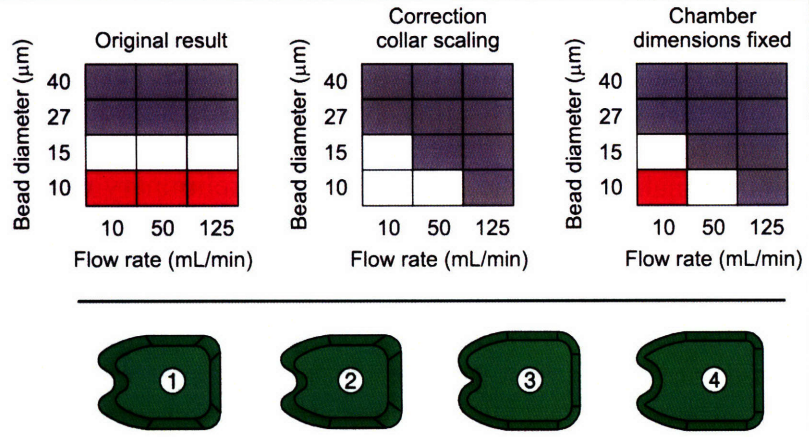

Figure 51: At top, I present several different loading maps tied to our attempts to model SU-8 weir behaviors using the code developed[1] by Dr. Carlos Pinto Coelho (red = laterally unloaded, white = stably captured, grey = vertically unloaded). Small variations related to the pixel:length values used to develop meshed versions of the weirs have been seen to dramatically change the observed responses ("Original result" versus "Correction collar scaling"). Additionally changes in the on-chip flow chamber dimensions have presented a strong capacity for modifying the results (rightmost plot). With such sensitivity, it has been somewhat difficult to transition from model validation to optimization efforts that might lead to the development of weirs with enhanced capture capacities. At bottom, I display some of our attempts to build models of similar PPS geometries with sloped sidewall profiles (top down images). Though we have photographs of the footprints and measurements of the sidewall angles, developing "representative" incarnations has proven challenging. Attempts to match PPS weir behaviors to measured responses, should help to further solidify our confidence in design-focused efforts.

By examining behaviors across a number of different flow rates and bead sizes we gained an appreciation for some of the sensitivities present in the modeled environment. Originally (upper left in Figure 51) we had used an improper pixel:length value for generating our meshed weirs from scope-based images of our SU-8 weirs. When we included an additional scaling factor resulting from a correction collar in the optical path to the camera we observed a rather stark change in the on-chip loading responses (center top in Figure 51). We were somewhat surprised by this sensitivity and wondered why we were no longer observing lateral unloading for the smaller-sized beads. After carefully reexamining the code, we discovered that improper values had been used to describe the cross-sectional areas of on-chip flows. With this correction in hand, we finally had a series of simulated results (shown in Chapter 4) that matched

experimental studies (see upper right in Figure 51 - a refined version of the first column in this map was shown in the data offered in Chapter 4).

To further assess and validate this coding, we are currently working to match PPS-based weir simulations to recorded experimental results. As I highlight in the lower half of Figure 51, the presence of a sizeable sidewall angle in weirs made of this material has made development of representative models challenging. Despite a variety of different strategies (1-4) for pairing images of such geometries with measured sidewall profiles, it is unclear which design best matches the actual fabricated PPS weirs. As our response plots have been notably sensitive to small changes made across various simulation runs (top of Figure 51) it will likely prove important to properly manage this effect. Ultimately, we would like to use such simulation efforts to run a series of follow-on design optimization routines. Through this type of effort we hope that we will someday better understand the impact that weir sizing and patterning resolution plays in determining loading mechanics. It may then prove possible to develop design revisions within a simulation environment that could render effective single-cell capture across sizeable arrays of such weirs. We could then possibly build and test such structures to produce a new series of electroactive weirs with enhanced functionalities relevant to cell-based biological assays.

Beyond these protracted simulations for investigating passive weir loading behaviors, it may prove possible to adopt alternative simplified options for gaining key insights. At present, I am uncertain how one might approach such an effort, but in speculative terms Figure 52 provides several basics of this envisioned design assessment protocol. One might imagine developing a simple "energy landscape" representation to describe weir-covered in-device substrates. This type of representation would necessarily include some way of characterizing the "potential" for retention at various locations across the chip surface. It is conceivable to then picture localized

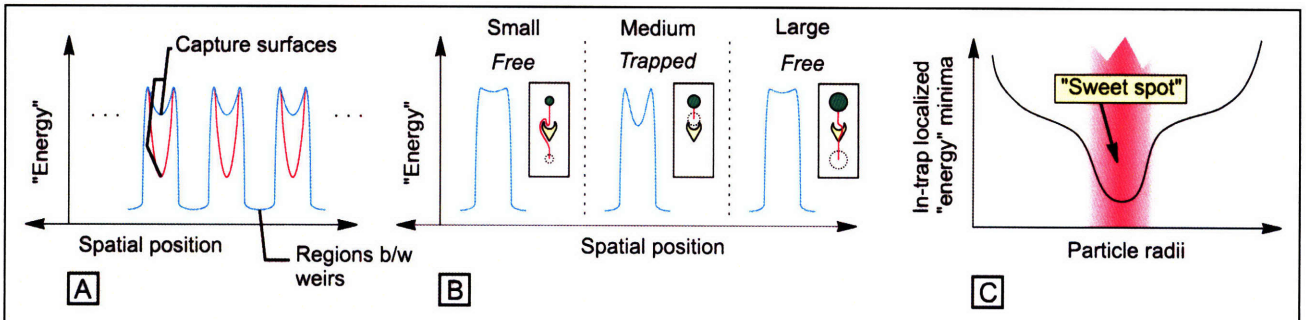

Figure 52: Beyond simulation efforts that employ Green's function solutions to the Stokes equation, it may prove possible to develop reduced-order models that offer analytical insight regarding weir function. One could imagine using "energy" landscapes as a means to describe capture propensity **(A)**. How to approach such efforts is unclear, but with such a mapping it might prove possible to directly compare the functionalities of my substrate-affixed designs (envision blue trace in (A)) to the ceiling-mounted strategies (envisioned red trace in (A)) used by others [cite]. I imagine that it would prove to be the case that the stability of narrow-gap ceiling-mounted weirs outpaces offerings from large-gap substrate-affixed designs (i.e. lower "energy" minima at the weir capture surfaces). Such efforts might further offer a new perspective on the "energy" dynamics associated with different weir/particle size-dependent interactions **(B)**. If we were to examine such interactions by then plotting the in-weir (along the capture surface) "energy" minimas as a function of impinging particle radii, it might be possible to replicate observed size-selectivity responses in a novel context **(C)**. This type of modeling work would ideally offer rapid insight without a demand for hours of simulation time.

"energy" minima at weir capture surfaces (see Figure 52A) with magnitudes that would depend upon flow rates, weir sizing, and impinging particle diameters (see Figure 52B). By using such mappings, it might then perhaps prove possible to reduce the complexity of such designs to a handful of adjustable parameters that could easily be changed and functionally assessed. Such efforts might shed new light upon distinctions between large-gap and small-gap implementations (see Figure 52A) while also rendering an alternative means for understanding size-selective responses (see Figure 52C). This approach would likely never serve design optimization to the extent made possible by more elaborate Green's function-based simulations, but it might prove instrumental for basic analytical purposes.

This approach, along with others inspired partially by this work (which I will discuss later in this chapter), offers a field-of-view independent means for cell handling. Any on-chip location with active weirs in place can enable manipulations, even if the overarching array footprint is too large for observation at any one point in time. Additionally, the ability to pattern multiple distinct single-particle populations presents flexibilities surpassing those offered by alternative activated-surface-chemistry-based strategies. Such efforts have successfully enabled single-cell capture at discrete on-chip locations and the subsequent backfilling of all remaining on-chip areas with cells of a second type, but they offer few avenues for localizing the second cell type to targeted regions and even fewer for managing cells of a third type. Moreover, unlike well-based configurations, weir-reliant designs present minimal confinement for patterned cells. In assays requiring long-term culture following an initial patterning effort, cells can grow upon a surface that permits proliferation and migration in all directions excepting regions occupied by the weir.

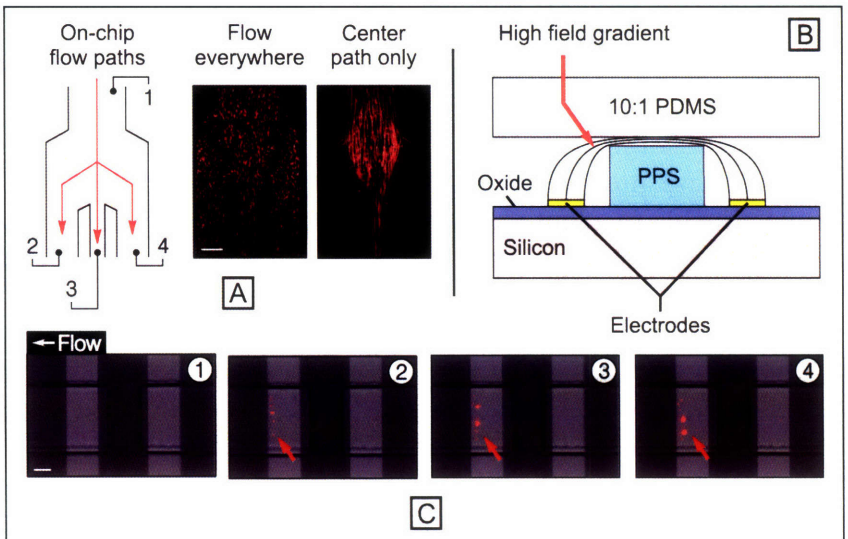

Figure 53: In prior iDEP-based (insulator DEP) efforts **(A)** (scale bar ≈ 100 μm), "z-cramped" regions (grey regions highlighted in the diagram shown in (A) - shorter ceiling-to-substrate distances than in other portions of the chip) in on-chip flow channels have enabled DEP forcing within electroosmotically-driven microfluidic systems. By applying voltages that span the chip (inlet at "1" and outlets at "2", "3", and "4") it is possible use these DEP-forcing to focus biomaterial to toward designated flow outlets (see the rightmost picture in (A)). With this known dynamic, my colleague, Michael Vahey, and I attempted to build a concentrator **(B)** that could leverage similar field-line-confined forcing to investigate PPS-based device fabrication capabilities (device basics shown in side view). As shown in **(C)**, we used one such device to collect 2-μm-diameter polystyrene beads from passing in-system flows. (Scale bar ≈100 μm).

PPS-related manufacturing opportunities

The ability to align and pattern PDMS-like free-standing features on substrates led my colleage, Michael Vahey, and I to explore several other tangential PPS-dependent device designs. As I

show in Figure 53, we were inspired to try developing a new form of on-chip cell concentrator. In a number of prior iDEP-based[177, 178] (insulator DEP) applications narrow in-chamber constrictions (see grey bars in schematic of Figure 53A) had often been used to squeeze electric fields in prescribed ways within electro-osmotic flows. These squeezed fields, in turn, were often used to exert n-DEP forcing from the resulting gradient. As shown in Figure 53A (right two images), by applying the correct balance of voltages across the device inlet and outlets (shown as 1-4 in Figure 53A) one could focus incoming biomaterial to various designated outlets. As I show in the side view of Figure 53B, I hoped to adopt a similar field confining strategy that used on-chip electrodes and PPS barriers to establish on-chip DEP forces capable of collecting cells from passing fluid flows.

As I show in the time lapse sequence of Figure 53C, Mike and I successfully fabricated one such device (using standard PPS processing and an added SU-8 2005 master-molding protocol to form the PDMS device ceiling) and then used it to concentrate masses of 2-μm-diameter red-fluorescent polystyrene beads. In contrast to i-DEP-based efforts which use electro-osmotic on-chip flows, we used a syringe-pump to flush our particle-laced suspensions across the device. Though we had expected to witness particle collections on the upstream side of our PPS barrier, we observed beads collecting instead on the downstream portion of the channel. We had neglected to consider that the coupled dynamic associated with on-chip electro-osmotic flows and DEP forcing prescribes a different set of conditions compared to syringe-pump-driven flows. In our environment it proved exceptionally challenging to create environments where the upstream drag forces did not dominate over the in-system DEP forces. As a result, we demonstrated a functional concentrator, but it operated in a manner different from expectation. Though we never tested the device with cells, one could imagine using such a setup to collect them from passing flows without having to 1.) resort to STS-based (Surface Technology Systems) silicon substrate etching as part of the processing sequence (as had been done for prior i-DEP efforts[177]) or 2.) face concerns related to imagining complications stemming from the use of alternative autofluorescent polymer chemistries.

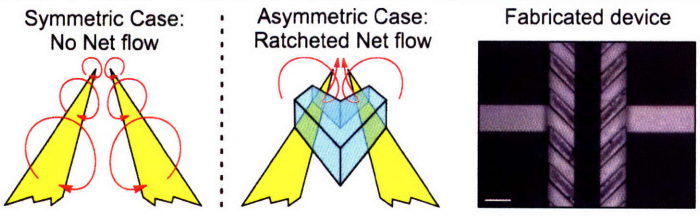

Figure 54: In another demonstration of PPS-based device development, Michael Vahey and I developed a pump inspired by prior works. Using adjacent oppositely-polarized electrodes it is feasible to induce electrohydrodynamic flows. Normally such flows circulate with no net contributions along the length of such electrodes (left). By patterning PPS chevron-style features on top of such electrodes it proves feasible to "ratchet" the flow along the electrodes to produce a pumping effect (middle). Though the flows were weak and visualization particles tended to settle along the substrate, we successfully fabricated and demonstrated one such topology (right). (Scale bare ≈50 μm)

Another spin off from the PPS-based studies in my dissertation, centered on attempts to develop a new type of on-chip fluid pump. Much of this initiative was inspired by work done by Dr. Martin Bazant[179, 180] and Dr. Armand Ajdari[181, 182] whose theoretical and, in some cases, experimental publications had outlined conceptual approaches for incorporating in-device geometric asymmetries to impart electrokinetic fluid flow. As I show at left in Figure 54, within microsystems contexts, it is widely known that two oppositely-polarized electrodes can create on-chip circulating electro-

hydrodynamic flows. These on-chip flows do not however offer a means for rendering net motion along the lengths of the electrodes. To change this dynamic, we developed designs that positioned chevron-style PPS features directly above these on-chip traces (see schematic at the center of Figure 54). Prior designs[181] had used in-chamber ceiling-affixed geometries to service this effect and we speculatively imagined (based upon other efforts[180, 182]) that patterning such features along the substrate might offer avenues for enhancing net ratcheted flow rates. As shown at the right in Figure 54, we did fabricate and test one such device using processing familiar to the device highlighed in Figure 53. Though depicting the movies as stills proved challenging due to tracer particle settling within the device, we did in fact witness weak net flows along the length of the electrodes. More modeling would certainly be required to enhance such a design to a point where it might prove practical for use as a functional component within microfluidic systems.

I can not say if either one of these tangential forays holds promise in its own right for further development, but either or both may help pave paths for other PPS-based applications that would be useful to the biological microsystems field. Since these studies, others within our group have begun incorporating PPS-processing as a new means for device flow-chamber packaging. Rather than laser-cutting a gasket or using soft lithography techniques, they have elected to pattern on-chip PPS gaskets as an in-fab protocol and then plasma bond glass slides and/or coverslips to form the top-side fluidic enclosures. This new approach has made it readily feasible to modulate the height of on-chip flow-chambers (by modulating PPS spin-coating speeds) and realize low-aspect-ratio channels (very wide, but not very tall) without facing concerns related to bulging or collapse during assays (due to the presence of non-pliable in-system floors and ceilings). I personally believe that the development work, Salil, Mike, and I have made with this material has outlaid benefits that others could someday leverage. The extent to which PPS could become part of the biological microsystems vernacular is something time will necessarily dictate.

Stencil-delineated electroactive patterning as a new approach

Partly as a consequence of the innovations offered by my doctoral work, my colleague, Somponnat Sampattavanich, and I brainstormed to develop yet another approach to cell patterning. For several years, Somponnat had refined techniques (originally presented by Albert Folch's lab at the University of Washington[96]) employing thin (~50 μm) PDMS stencils to organize stem cell colonies on various culture surfaces. This patterning technology which allows collections of seeded cells to contact and attach to underlying substrates at locations where "holes" exist in the stencils, has proven instrumental for investigating both signaling and proximity-related fusion dynamics for organized colonies. One complication of such work centers on the idea of tracking individual cells within the colonies as cultures proliferate *in vitro*. Observing such effects is challenging, as it is difficult to discern cell boundaries within fused colonies. To add capabilities to Somponnat's approach, we, in turn, developed a new stencil-delineated electroactive patterning (S-DEP) method[42, 183].

As I show in Figure 55, the premise of this strategy leverages the aligned placement of PDMS stencils (formed via SU-8-based master molding of thin PDMS membranes) onto substrates that present various IDE electrodes (processed through the first metal level in the scaled via-based fabrication process). By overlaying the stencil and then turning ON the substrate-affixed

electrodes, it is possible to seed cells such that they settle into the stencil wells and then cluster, via n-DEP forcing, into aligned strips (see steps "1" and "2" in Figure 55). After allowing this initial population of cells to attach, we can then seed the PDMS/substrate stacks with a second cell type (while leaving all in-system electrodes OFF - see step "3"). Following another attachment routine, we can finally remove the stencils to leave in place isolated tissue-like constructs (TLCs) with unique internal cell patterns (step "4").

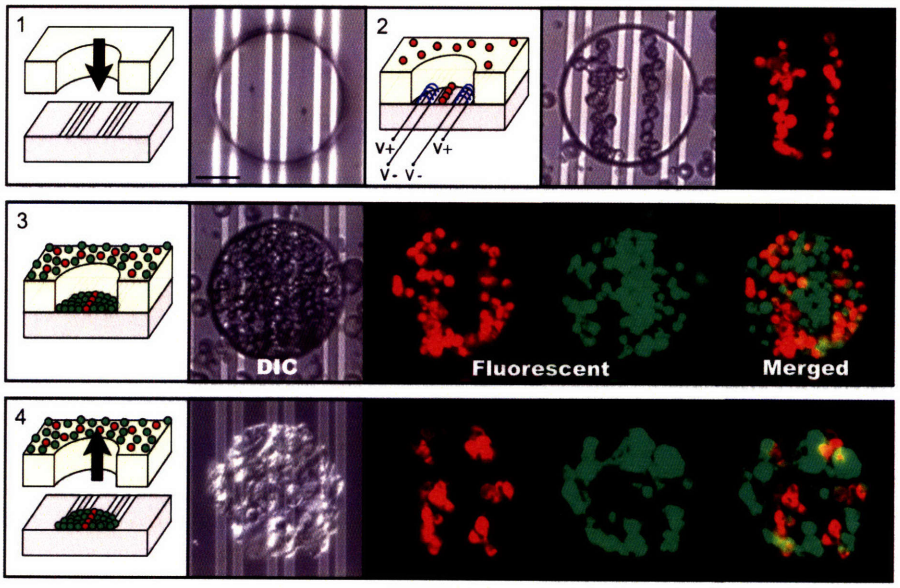

Figure 55: Using combined stencil- and n-DEP-based methods, my colleague, Somponnat Sampattavanich, and I developed a novel stencil-delineated electroactive patterning (S-DEP) platform for enabling cell manipulations. Here we could position a PDMS stencil onto an electrode-covered substrate (1), apply on-chip voltages (2), and deposit cells that would localize to in-well strips (again 2). After deactivating the electrodes and waiting for cell attachment, we could then load a second cell type that would localize to other regions within the stencil-delineated well (3). Following another round of cell attachment, we could then remove the stencil (4) to produce isolated tissue-like constructs with internal cell patterns. This technology offers a new means for tracking cell movement within tissue mimics and provides unique flexibilities for probing cell-cell interactions. (Scale bar ≈40 μm)

To date, we have demonstrated this approach using stained A431 (culture specifics offered in the Biological Methods Appendix, ATCC, Manassas, VA) cells (courtesy of Dr. Peter Sorger's lab) as a test line. We have additionally tracked the dynamics of cell movement within TLCs over multi-day time spans (see Appendix 15). Understanding such effects in the context of more advanced stem-cell-related efforts could shed new light upon matters relevant for cross-colony communication. We could additionally imagine clustering different cell types with varied levels of differentiation to examine details pertinent to colony fate mapping in chimeric cell assemblies. As was the case with other technologies developed in my dissertation, the ability to pattern cells within larger isolated TLCs offers flexibilities for cell handling that surpass designs reliant upon electroactive-[184, 185], mechanical-[96, 186], or surface-chemistry-based[187, 188] strategies alone. As Somponnat plans to continue work with this new technology, it will be interesting to observe the outcome of further studies.

Flexibilities for bead-based assays

Though we are currently limited in our electroactive weir-based cell handling capabilities by print resolution concerns affiliated with polymer patterning, in principle, I have demonstrated a new format for conducting novel "full stream" assays in the event that new weir fabrication flexibilities one day emerge. Adopting a more holistic perspective, my electroactive weir-based platforms have provided new opportunities for effectively handling 20-30-μm-diameter beads. As I show in Figure 56, I believe that even this functionality could prove worthwhile for developing new analytical tools.

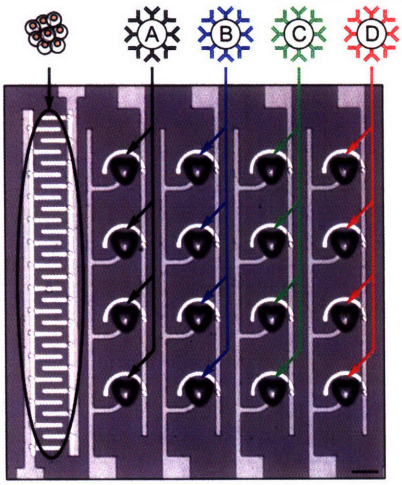

Figure 56: As the weir-based designs are well-suited for capturing mid-sized (27-μm-diameter) beads, it seems sensible to develop a series of bead-based analytical assays. One could imagine coating different bead populations with different antibodies ("A", "B", "C", "D", etc.), organizing them into on-chip columns and then capturing cells at nearby IDE electrode banks. Using "overdriven" voltage stimuli one could then lyse the cells and use the on-chip beads to detect various proteins. (Scale bar ≈50 μm)

If one were to functionalize separate bead populations using antibodies (as one example) it might be possible to selectively pattern them in targeted on-chip locations. With these functionalized beads in position, we could then use on-chip IDE banks, in close proximity to the weirs, to capture collections of cells targeted for analysis. With the same input lines used to gather cells at in-system IDEs, we could introduce higher amplitude signaling to lyse held populations. By exceeding critical induced transmembrane potentials we would rupture the cells and their lysates would disperse via diffusion-based mechanisms. As the contents progressed across the chip, they could then interact with the antibody-coated bead populations. By either sorting the beads out of the device or by holding them in place we could use additional fluorescently-tagged antibodies to test for the presence of various proteins within our cell lysates. In effect, we could develop a Bio-Plex (Luminex Corp., Austin, TX) style approach to conducting western-blot-based analyses that could additionally leverage on-chip spatial organization as an orthogonal surveying tool.

In this chapter, I have outlined many of the key contributions offered by my work. From proof-of-concept forays, to scaled designs, and more advanced biological assays, many components of my doctoral efforts have opened opportunities for continued explorations that could be serviced by the engagements of others. As is the case for most scientific endeavors, attempts to solve a specified problem regularly lead to additional sets of investigative curiosities. The work I present offers no exception to this effect and it will be be interesting to witness continued progress related to variants of the contributions I have offered in the biological microsystems domain.

Appendix 15

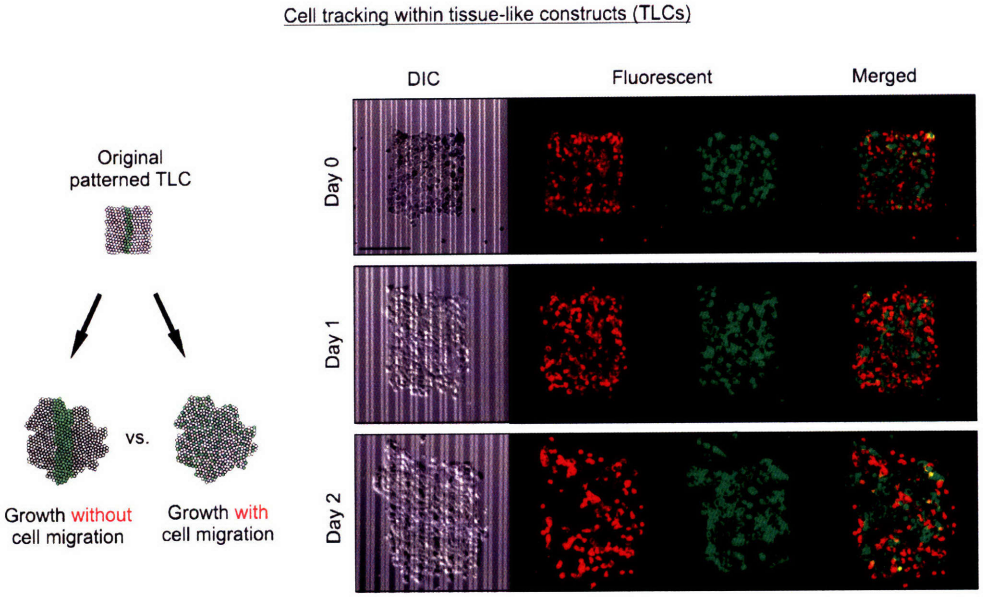
Cell tracking within tissue-like constructs (TLCs)
DIC
Fluorescent
Merged
Day 0
Day 1
Day 2
Original patterned TLC
vs.
Growth without cell migration
Growth with cell migration

Biological Methods Appendix

Standard cell culture medias

Suspension lines:

BA/F3	HL-60	K-562
RPMI	RPMI	RPMI
10% FBS	10%BCS	10% FBS
10% WeHi-3B conditioned media	1% L-glutamine	1% L-glutamine
2% L-glutamine	1% Pen/Strep	1% Pen/Strep
1% Pen/Strep		

Adherent lines:

3T3	HT-29	HeLa	A-431
DMEM	McCoy's 5A Medium	DMEM	DMEM
10% BCS	10% FBS	10% FBS	10% FBS
2% L-glutamine	1% L-glutamine	2% L-glutamine	2% L-glutamine
1% Pen/Strep	1% Pen/Strep	1% Pen/Strep	1% Pen/Strep

For all listings:
L-glutamine taken from 200 mM stock
Pen/Strep taken from 10000 U/mL penicillin G sodium and 10000 µg/mL streptomycin sulfate stocks

Low-conductivity buffers

0.01 S/m type - used in initial 4 × 4 p-DEP-based operations = 10.25% w/v sucrose/deionized water

0.1 S/m type - used in scaled 20 × 20 dual-frequency cell manipulation platforms

Type 1	Type 2	Type 3	Type 4
Deionized water	Deionized water	Deionized water	Deionized water
9.5% w/v sucrose	9.5% w/v sucrose	9.5% w/v sucrose	9.5% w/v sucrose
2.5% Hepes	2.5% Hepes	2.5% Hepes	2.5% Hepes
4% PBS	5% BCS	3.5% Isoton	

Passaging techniques

Suspension lines:

1) Warm media in bath for ~30 minutes
2) Wipe down bottle with EtOH and place in hood along with a new dish and a Falcon tube
3) Remove cells from incubator
4) Triturate culture and transfer to Falcon tube at desired split ratio

5) Run Falcon tube in centrifuge for 5 minutes at 1000 rpm
6) Return to hood and aspirate supernatant from Falcon tube
7) Place fresh media into the Falcon tube and triturate vigorously
8) Aliquot cells into new dish
9) Return to incubator

Adherent lines

1) Warm media and trypsin in bath for ~30 minutes
2) Wipe down media and trypsin bottles with EtOH and place in hood along with a new dish and a bottle of PBS
3) Remove cells from incubator
4) Carefully aspirate old media from side of dish
5) Add PBS to the dish and allow it to sit for ~30 seconds.
6) Aspirate the in-dish PBS
7) Add trypsin-EDTA to cells
   Common volumes: 10-cm dish, 1.5 mL
   20-cm dish, 3 mL
8) Incubate at 37°C for 5 minutes
9) Add media to quench the trypsin
   Common volumes: 10-cm dish, 4.6 mL
   20-cm dish, 9 mL
10) Triturate vigorously in dish to break up cell clumps
11) Prepare a new dish with media
12) Aliquot cells from old dish to new dish at desired split ratio
13) Return to incubator

CellTracker staining procedures

Preparing the reagent:

1) Let dye warm to room temperature
2) Dissolve lyophilized product in hiqh-quality DMSO to a final [] of 10 mM
3) Dilute this stock solution to working concentrations between 0.5-25 μM in serum-free media (most often we use 5 μM)
4) Warm working solution to 37°C

Staining process (suspension lines):

1) Allow cells to reach desired in-dish density (typically around 1E6/mL for most lines)
2) Warm the working solution in a water bath for ~30 minutes
3) Remove cells from incubator
4) Transfer cells to a Falcon tube
5) Spin down the cell suspension in a centrifuge for 5 minutes at 1000 rpm
6) Aspirate the supernatant and add working solution to the Falcon tube. Place cells into a new dish and incubate at 37°C for 15-45 minutes (most often use 45 minutes)

7) While cells are being exposed to the working solution warm serum-containing media in a water bath
8) Remove cells from incubator, transfer suspension to a Falcon tube, and spin down in centrifuge for 5 minutes at 1000 rpm
9) Aspirate the working solution and add serum-containing media to the Falcon tube.
10) Triturate vigorously and incubate for another 30 minutes

Staining process (adherent lines):

1) Allow cells to reach desired confluence in dish
2) Warm the working solution in a water bath for ~30 minutes
3) Remove cells from incubator
4) Aspirate media from dish
5) Add working solution to dish and incubate at 37°C for 15-45 minutes (most often use 45 minutes)
6) While cells are being exposed to the working solution warm serum-containing media in a water bath
7) Remove cells from incubator and aspirate the working solution from the dish
8) Add serum containing media to the dish and incubate for another 30 minutes

Sample loop injection procedure

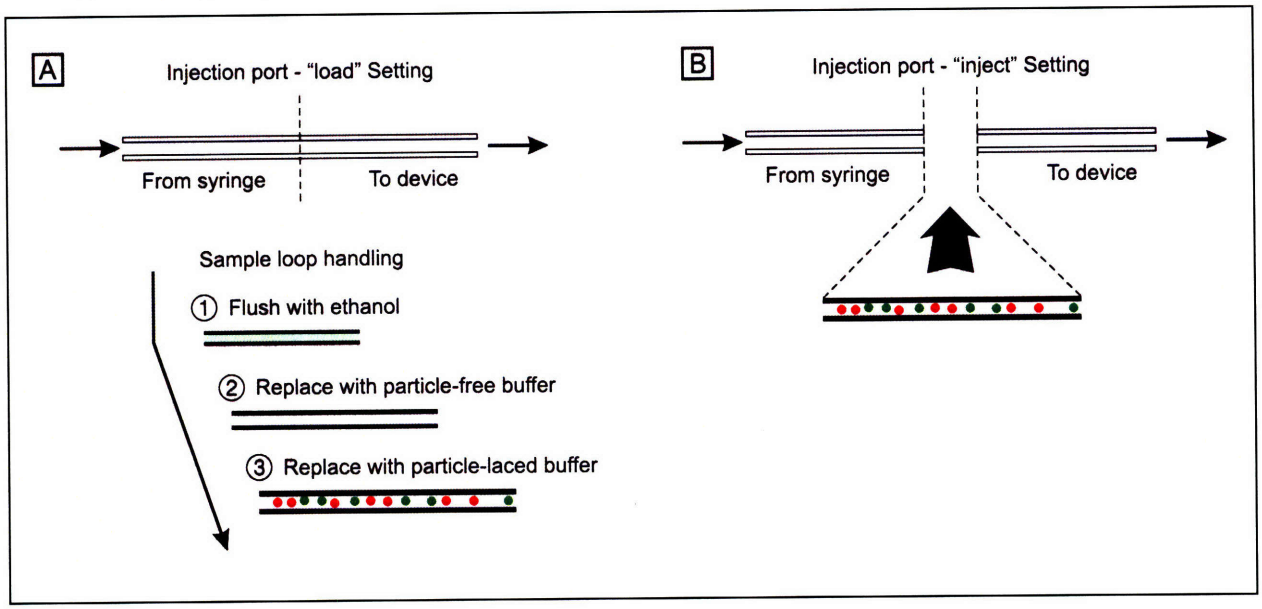

When porting particles onto my devices I typically use cell or bead densities ranging between 6E4 and 1E6 /mL. In cell-based work I rinse cell suspensions 1-3 × in the on-chip working buffer prior to injections. The procedure outlined here has been instrumental for enabling the introduction of particle suspensions without simultaneously creating bubbles in on-chip flow chamber environments:

Critical supplies needed:
Off-chip 6-port injection valve - Upchurch Scientific
50 μL glass syringe

Routine:

1) Inject a particle bolus into the device's flow chamber using a 50 μL glass syringe and an off-chip 6-port injection valve with a 15-50 μL sample loop. As shown in the Figure above, perform this injection using a 4-part procedure - 1.) with the injection valve set to the "load" setting, flush the loop with ethanol, 2.) replace the ethanol with particle-free buffer, 3.) replace the particle-free buffer with particle-laced buffer, and 4.) turn the injection valve to the "inject" setting (shown in B).
2) With the suspension in line, start the syringe pump to flush the particles over the active surfaces in our devices - it is typically best to set injection rates to 100 μL/min until cells or beads arrive in the device fluid chamber. Once a sizeable population is on-chip, we then advise halting the syringe pump, flushing the connections to the sample loop on the injection port with ethanol, and then returning the valving to the "load" setting. This process reduces the management of non-essential particles while avoiding the introduction of bubbles.
3) By observing the on-chip environment using microscopy we can track loading responses. We restart the syringe pump flow at a reduced rate of 5-20 μL/min for a majority of cell and bead handling assays.

Fixed-cell staining methods

Used rhodamine phalloidin (Molecular Probes Catalog # R415) for actin staining
Used hoechst 33258 (Molecular Probes Catalog # H3569) for nuclear staining
Functional only for adherent lines

Reagents needed:
Methanol
PBS
Methanol-free formaldehyde
Triton X-100
BSA

Working solutions:
rhodamine phalloidin - dilute 5 μL methanolic stock into 200 μL PBS for each cell set needing staining, add 1% BSA to the staining solution to avoid nonspecific background staining
hoechst - dilute at 1:100 ratio in PBS from original stock solution

Procedure:

1) Wash cells twice with prewarmed PBS
2) Fix the sample in 3.7% formaldehyde solution (in PBS) for 10 minutes at room temperature
3) Wash two more times with PBS
4) Perform an extraction with 0.1% Triton X-100 (in PBS) for 3 to 5 minutes
5) Wash two or more times with PBS
6) Place staining solution(s) on the cells for 20 minutes at room temperature - keep samples inside a covered container to avoid evaporation during this process
7) Wash two more times with PBS
8) Air dry and mount using Fluoromount G

ELISPOT protocol - human IL-8 development module

R&D Systems Catalog Number: SEL208

Antibodies included:
Human IL-8 Capture Antibody Concentrate (Part # 840678)
- lyophilized goat anti-human IL-8 polyclonal antibody

Human IL-8 Detection Antibody Concentrate (Part # 840679)
- lyophilized biotinylated goat anti-human IL-8 polyclonal antibody

Agents needed:
PBS - (137 mM NaCl, 2.7 mM KCl, 8.1 mM Na_2HPO_4, 1.5 mM KH_2PO_4, pH 7.2 -7.4, 0.2 μm filtered)
Wash buffer - (0.05% Tween 20 in PBS)
Blocking buffer - (1% BSA, 5% Sucrose in PBS)
Reagent Diluent - (1% BSA in PBS, pH 7.2 - 7.4, 0.2 μm filtered)

Assays typically run in 96-well PVDF-bottom Immunospot plates or flat-bottom polystyrene Immulon ELISA plates.

1) Calculate the total volume of Capture Antibody needed and dilute to the working concentration using PBS (generally use 1:60 dilutions).
2) Immediately add 100 μL of the diluted Capture Antibody per well. Cover the plate with the lid and incubate overnight at 2-8°C.
3) Aspirate Capture Antibody from each well and wash 3 times with Wash Buffer or PBS (350 μL/well). After the final wash, remove any remaining liquid by inverting the plate and plotting it against a clean paper towel.
4) Block membranes by adding 200 μL of Blocking Buffer to each well. Incubate for 2 hours at room temperature.
5) Aspirate Blocking buffer. Rinse with the same media in which the cells designated for this assay will be cultured. Do not discard the culture media until cells are ready to be plated.
6) Aspirate culture media from the plate and immediately fill appropriate wells with 100 μL of culture media containing human IL-8 secreting cells. It is here that we add TNF-α at concentrations of 10 ng/mL to cell populations that we wish to stimulate. Incubate at 37°C in a 5% CO_2 incubator. (We typically incubate for at least 4 hours.).
7) Wash the plate 4 times with Wash Buffer.
8) Calculate the total volume of Detection Antibody needed and dilute to the working concentration using Reagent Diluent. (Again we typically use 1:60 dilutions).
9) Add 100 μL of the diluted Detection Antibody per well. Cover the plate with the lid and incubate overnight at 2-8°C.
10) Aspirate the Detection Antibody and wash as described in step 3). By replacing the given detection antibody with a fluorescently-tagged version we can perform direct analysis of the IL-8 secretion responses. Alternatively the remaining steps are needed for color development.
11) Flush the detection surfaces with the Wash Buffer 3 times.
12) Coat Alexa 488 linked streptavidin (1:500 dilution from a 1 mg/mL stock) onto each surface and wait for 30 minutes.
13) Flush the surfaces with Wash Buffer 3 times and then image the samples using fluorescence microscopy.

Fabrication Methods Appendix

Original 2-level metal non-via-based process for wafers presenting p- and n-DEP designs

Substrate: 150 mm diameter silicon wafers

1) Run RCA clean (*rcaICL* [ICL])
2) Grow wet thermal oxide - 1.5 microns thick (*5D-FieldOx* [ICL] or *5C-ThickOx* [ICL])
3) Clean wafers (*premetal-piranha* [ICL])
4) Sputter deposit 5000 Å Aluminum (*endura* [ICL] - "Al 5000 A")
5) Spin on standard positive photoresist – 1 micron thick (*coater6 – track1*[ICL] - "T1HMDS")
6) Expose photoresist - mask aligner (*EV1 – green chuck* [TRL] - hard contact)
7) Develop photoresist (*coater6 – track2* [ICL] - "DEV6")
8) Descum to remove photoresist from areas where not desired (*asherTRL - green side* [TRL] - "5 minutes)
9) Plasma etch Aluminum – include dump rinse step (*rainbow* [ICL] - "11032005")
10) Strip photoresist (*asher-ICL* [ICL] - "4 minutes")
11) Deposit blanket film of PECVD SiO_2 - 1.5 microns thick (*concept1* [ICL] - "1.5 um Oxide")
12) Sputter deposit 5000 Å Aluminum (*endura* [ICL] - "Al 5000 A")
13) Spin on standard positive photoresist – 1 micron thick (*coater6 – track 1* [ICL] - "T1HMDS")
14) Expose photoresist - mask aligner (*EV-1 – green chuck* [TRL] - hard contact)
15) Develop photoresist (*coater6 – track2* [ICL] - "DEV6")
16) Descum to remove photoresist from areas where not desired (*asherTRL - green side* [TRL] - "5 minutes")
17) Plasma etch aluminum –include dump rinse step (*rainbow* [ICL] - "11032005")
18) Strip photoresist (*asher-ICL* [ICL] - "4 minutes")
19) Spin on standard positive photoresist – 1 micron thick (*coater6 – track1* [ICL] - "T1HMDS")
20) Expose photoresist - mask aligner (*EV-1 – green chuck* [TRL] - hard contact)
21) Develop photoresist (*coater6 – track2* [ICL] - "DEV6")
22) Descum to remove photoresist from areas where not desired (*asherTRL - green side* [TRL] - "5 minutes")
23) Wet etch PECVD oxide in Transene's Silox Vapox III – exposes the underlying metal layer - timed (*acid-hood* [TRL])
24) Strip photoresist (*asher-ICL* [ICL] - "4 minutes")
25) Spin on standard positive photoresist – 2.7 microns thick (*coater6 – track1* [ICL] - "TAFFC")
26) Expose photoresist - mask aligner (*EV-1 – green chuck* [TRL] - hard contact)
27) Develop photoresist (coater6 – track2 [ICL] - "TAFFD")
28) Descum to remove photoresist from areas where not desired (*asherTRL - green side* [TRL] - "5 minutes)
29) Dry etch thermal oxide (*AME5000* [ICL] - "Oxide Pegasus")
30) Silicon deep trench etch – 20 micron depth etch (*sts2* [TRL] - "STSHAL-A")
31) Strip photoresist (*asher-ICL* [ICL] - "4 minutes")
32) Spin on thick AZ9260 – protects front-side of wafer for die saw operations (*coater-green chuck* [TRL])
33) Bake-harden photoresist layer (*pre-bake – green cassette* [TRL])
34) Cut wafer into individual die (*diesaw* [ICL])

Items enclosed in [] *shown in list above indicate the locations of specific machines.*

Functional 2-level metal non-via-based process for p-DEP trap fabrication

Substrate: 150 mm diameter silicon wafers

1) Run RCA clean (*rcaICL* [ICL])
2) Grow wet thermal oxide - 1.5 microns thick (*5D-FieldOx* [ICL] or *5C-ThickOx* [ICL])
3) Clean wafers (*premetal-piranha* [ICL])
4) Sputter deposit 5000 Å Aluminum (*endura* [ICL] - "Al 5000 A")
5) Spin on standard positive photoresist – 1 micron thick (*coater6 – track1* [ICL] - "T1HMDS")
6) Expose photoresist - mask aligner (*EV1 – green chuck* [TRL] - hard contact)
7) Develop photoresist (*coater6 – track2* [ICL] - "DEV6")
8) Descum to remove photoresist from areas where not desired (*asherTRL - green side* [TRL] - "5 minutes)
9) Plasma etch Aluminum – include dump rinse step (*rainbow* [ICL] - "11032005")
10) Strip photoresist (*asher-ICL* [ICL] - "4 minutes")
11) Deposit blanket film of PECVD SiO_2 -1.5 microns thick (*concept1* [ICL] - "1.5 um Oxide")
12) Sputter deposit 5000 Å Aluminum (*endura* [ICL] - "Al 5000 A")
13) Spin on standard positive photoresist – 1 micron thick (*coater6 – track 1* [ICL] - "T1HMDS")
14) Expose photoresist - mask aligner (*EV-1 – green chuck* [TRL] - hard contact)
15) Develop photoresist (*coater6 – track2* [ICL] - "DEV6")
16) Descum to remove photoresist from areas where not desired (*asherTRL - green side* [TRL] - "5 minutes)
17) Plasma etch Aluminum – include dump rinse step (*rainbow* [ICL] - "11032005")
18) Strip photoresist (*asher-ICL* [ICL] - "4 minutes")
19) Spin on thick AZ9260 photoresist – 4 microns thick (*coater – green chuck* [TRL])
20) Expose photoresist - mask aligner (*EV-1 – green chuck* [TRL] - hard contact)
21) Develop photoresist (*coater - green chuck* [TRL])
22) Descum to remove photoresist from areas where not desired (*asherTRL - green side* [TRL] - "5 minutes)
23) Protect front side of wafer using blue diesaw tape
24) Cut wafer into individual die (*diesaw* [ICL])
25) Plasma etch PECVD oxide on individual die - cut through the bulk of the oxide (*Plasmatherm* [EML] - "84 minutes; 40 sscm HC23; 5 sscm O_2")
26) Perform final wet etch of PECVD oxide on individual die using Transene's Silox Vapox III – exposes the underlying metal layer (*acid-hood-EML* [EML] - "4.5 minutes")
27) Remove photoresist from individual die using acetone (*photo-hood-EML* [EML])
28) Deposit blanket film of PECVD silicon nitride on individual die - 25 nm thick - cover bondpads using hand-placed glass coverslips (*Plasmatherm* [EML] - "PPSSF6")

Items enclosed in [] *shown in list above indicate the locations of specific machines.*

2-level metal via-based process for either scaled p-DEP or electroactive weir designs

Substrate: 150 mm diameter silicon wafers

1) Run RCA clean (*rcaICL* [ICL])
2) Grow wet thermal oxide – 1.5 microns thick (*5D-FieldOx* [ICL] or *5C-ThickOx* [ICL])
3) Clean wafers (*premetal-piranha* [ICL])
4) Sputter deposit 5000 Å Aluminum & 500 Å Titanium – Ti provides protects Al layer during via etching in Step 16) (*endura* [ICL] - "Z-PZ-Brian Al-Ti")
5) Spin on standard positive photoresist – 1 micron thick (*coater6 – track 1* [ICL] - "T1HMDS")
6) Expose photoresist - mask aligner (*EV1 – green chuck* [TRL] - hard contact)
7) Develop photoresist (*coater6 – track2* [ICL] - "DEV6")
8) Descum to remove photoresist from areas where not desired (*asherTRL – green side* [TRL] - "5 minutes)
9) Plasma etch Aluminum/Titanium stack – include dump rinse step (*rainbow* [ICL] - "11032005")
10) Strip photoresist (*asher-ICL* [ICL] - "4 minutes")
11) Deposit blanket film of PECVD SiO_2 – 1.5 microns thick (*concept1* [ICL] - "1.5 um Oxide")
12) Spin on standard positive photoresist – 1 micron thick (*coater6 – track 1* [ICL] - "T1HMDS")
13) Expose photoresist - mask aligner (*EV1 – green chuck* [TRL] - hard contact)
14) Develop photoresist (*coater6 – track2* [ICL] - "DEV6")
15) Descum to remove photoresist from areas where not desired (*asherTRL – green side* [TRL] - "5 minutes)
16) Plasma etch PECVD SiO_2 to open vias exposing the underlying metal layer (*Centura –chamberB* [ICL] - "TAFF-OX")
17) Strip photoresist (*asher-ICL* [ICL] - "4 minutes")
18) Sputter deposit 5000 Å Aluminum – will want to run a clean step in the Endura recipe to ensure effective electrical contact b/w M1 and M2 levels (*endura* [ICL] - "X Al 5KA W-PCLN")
19) Spin on standard positive photoresist – 1 micron thick (*coater6 – track1* [ICL] - "T1HMDS")
20) Expose photoresist - mask aligner (*EV1 – green chuck* [TRL] - hard contact)
21) Develop photoresist (*coater6 – track2* [ICL] - "DEV6")
22) Descum to remove photoresist from areas where not desired (*asherTRL – green side* [TRL] - "5 minutes)
23) Plasma etch Aluminum – include dump rinse step (*rainbow* [ICL] - "11032005")
24) Strip photoresist (*asher-ICL* [ICL] - "4 minutes")
26) Deposit blanket film of PECVD silicon nitride – 25 nm thick for scaled p-DEP designs or 3 nm thick for n-DEP actuated weir topologies (*STS-CVD* [TRL] - "LF-SiN")
28) Spin on standard positive photoresist – protects front-side of wafer for die saw operations (*coater-red chuck* [TRL])
29) Bake-harden photoresist layer (*pre-bake – red cassette* [TRL])
30) Cut wafer into individual die (*diesaw* [ICL])

Items enclosed in [] *shown in list above indicate the locations of specific machines.*

Initial SU-8 2002/2015-based process for electroactive weir designs

Substrate: 150 mm diameter silicon wafers

1) Run RCA clean (*rcaICL* [ICL])
2) Grow wet thermal oxide - 1.5 microns thick (*5D-FieldOx* [ICL] or *5C-ThickOx* [ICL])
3) Clean wafers (*premetal-piranha* [ICL])
4) Sputter deposit 5000 Å Aluminum (*endura* [ICL] - "Al 5000 A")
5) Perform dehydration bake (*hotplate300* [TRL] - "200°C for 25 minutes")
6) Coat the wafer with SU-8 2002 - targets a 2 micron thick layer (*SU8spinner* [TRL] - "500 rpm for 10 seconds; 3000 rpm for 30 seconds")
7) Perform prebake (*hotplate2* [TRL] - "95°C for 1 minute")
8) Expose via mask aligner (*EV1 - purple chuck* [TRL] - "80 mJ/cm^2 a.k.a. 8 seconds")
9) Perform postbake (*hotplate2* [TRL] - "95°C for 2 minutes")
10) Develop in PM Acetate (*SU8spinner* [TRL] - "2 minutes")
11) Coat the wafer with SU-8 2015 - targets a 20 micron thick layer (*SU8spinner* [TRL] - "500 rpm for 10 seconds; 2100 rpm for 30 seconds")
12) Perform prebake (*hotplate2* [TRL] - "65°C for 1 minute, ramp to 95°C and hold for 1 minute")
13) Expose via mask aligner (*EV1 - purple chuck* [TRL] - "150 mJ/cm^2 a.k.a. 15 seconds")
14) Perform postbake (*hotplate2* [TRL] - "65°C for 1 minute, ramp to 95°C and hold for 2 minutes")
15) Develop in PM Acetate (*SU8spinner* [TRL] - "6 minutes")
16) Cure the wafer (*hotplate2* [TRL] - "150°C for 30 minutes")
17) Spin on standard positive photoresist – protects front-side of wafer for die saw operations (*coater-red chuck* [TRL])
18) Bake-harden photoresist layer (*pre-bake – red cassette* [TRL])
19) Cut wafer into individual die (*diesaw* [ICL])

Items enclosed in [] *shown in list above indicate the locations of specific machines.*

Original PPS weir fabrication process

Compatible with either prepatterned or non-patterned silicon substrates

1) Ash the substrate (*asherTRL - green side* [TRL] - "5 minutes")
2) Coat the wafer with PPS - targets a 20 micron thick layer (*SU8spinner* [TRL] - "500 rpm for 10 seconds; 2100 rpm for 30 seconds")
3) Perform prebake (*hotplate2* [TRL] - "120°C for 2 minutes")
4) Install cellophane spacer around the perimeter of the wafer
5) Expose via mask aligner (*EV1 - purple chuck* [TRL] - "1100 mJ/cm^2 a.k.a. 110 seconds")
6) Remove cellophane spacer
7) Perform postbake (*hotplate2* [TRL] - "150°C for 3 minutes")
8) Develop in mesitylene (*SU8spinner* [TRL] - "6 minutes")
9) Cure the wafer (*hotplate2* [TRL] - "150°C for 2 hours")
10) Ash the substrate (*asherTRL - red side* [TRL] - "2 minutes")
11) Spin on thick AZ9260 – protects front-side of wafer for die saw operations (*coater-red chuck* [TRL])
18) Bake-harden photoresist layer (*pre-bake – red cassette* [TRL])
19) Cut wafer into individual die (*diesaw* [ICL])

Items enclosed in [] *shown in list above indicate the locations of specific machines.*

Enhanced PPS weir fabrication process

Compatible with either prepatterned or non-patterned silicon substrates

Mask processing:

1) Fully coat the front side of the mask with BC 7.5 (SU8spinner [TRL] - "500 rpm for 5 seconds; 1000 rpm for 30 seconds")
2) Repeat step 1) two additional times
3) Allow the mask to air dry and then load it into EV1

Wafer processing:

1) Ash the substrate (*asherTRL - green side* [TRL] - "5 minutes")
2) Coat the wafer with PPS - targets a 20 micron thick layer (*SU8spinner* [TRL] - "500 rpm for 10 seconds; 2100 rpm for 30 seconds")
3) Perform prebake (*hotplate2* [TRL] - "120°C for 2 minutes")
4) Expose via mask aligner (*EV1 - purple chuck* [TRL] - "1100 mJ/cm^2 a.k.a. 110 seconds")
5) Perform postbake (*hotplate2* [TRL] - "150°C for 3 minutes")
6) Develop in mesitylene (*SU8spinner* [TRL] - "6 minutes")
7) Cure the wafer (*hotplate2* [TRL] - "150°C for 2 hours")
8 Perform plasma descum process to trim sloped sidewalls (plasmaquest [TRL] - "PPSSF6")
8) Ash the substrate (*asherTRL - red side* [TRL] - "2 minutes")
9) Spin on thick AZ9260 – protects front-side of wafer for die saw operations (*coater-red chuck* [TRL])
10) Bake-harden photoresist layer (*pre-bake – red cassette* [TRL])
11) Cut wafer into individual die (*diesaw* [ICL])

Cleanup:

1) Rinse the mask in deionized water to remove the BC 7.5 (photo-wet [TRL])

Items enclosed in [] *shown in list above indicate the locations of specific machines.*

Photopatterning recipes

Coater6 "T1HMDS"

Stage 1	Stage 2	Stage 3	Stage 4	Stage 5
130°C	130°C	95°C	500 rpm	3000 rpm
30 seconds	60 seconds	60 seconds	8 seconds	30 seconds

Coater6 "TAFFC"

Stage 1	Stage 2	Stage 3	Stage 4	Stage 5
130°C	130°C	95°C	500 rpm	700 rpm
30 seconds	60 seconds	60 seconds	8 seconds	30 seconds

Coater6 "DEV6"

Stage 1	Stage 2	Stage 3	Stage 4	Stage 5
115°C	130°C	25°C	400 rpm	3500 rpm
60 seconds	60 seconds	60 seconds	25 seconds	30 seconds

Coater6 "TAFFD"

Stage 1	Stage 2	Stage 3	Stage 4	Stage 5
115°C	130°C	25°C	400 rpm	3500 rpm
60 seconds	60 seconds	60 seconds	42 seconds	30 seconds

EV1 "Recipe 1" is user modifiable - typically use hard contact and separations of 30-40 microns. Exposure times calibrated via spec sheets in TRL. For 1 micron thick standard positive resists exposure settings of 2.5 seconds have generally proven adequate.

Etching recipes

Rainbow "1103205"

Step. No.	1	2	3	4	5	6
Pressure mount	13 mTorr	13 mTorr	13 mTorr	10 mTorr	20 mTorr	0 mTorr
RF top	0 W	0 W	375 W	375 W	0 W	0 W
RF bottom	0 W	0 W	120 W	120 W	0 W	0 W
Gap	3 cm	3 cm	3 cm	3 cm	6 cm	6 cm
BCl_3	40 scc	40 scc	40 scc	40 scc	0 scc	0 scc
Cl_2	60 scc	60 scc	60 scc	40 scc	0 scc	0 scc
He clamp	0 scc	10 scc	10 scc	10 scc	0 scc	0 scc
N_2	0 scc	0 scc	0 scc	5 scc	0 scc	0 scc
Ar	0 scc	0 scc	0 scc	0 scc	120 scc	0 scc

AME5000 "Oxide Pegasus"

Step 1	Step 2	Step 3	Step 4	Step 5
Stabilization	Descum	Stabilization	Etch	Stabilization
20 seconds	20 seconds	30 seconds	180 seconds	150 seconds
200 mTorr	200 mTorr	200 mTorr	200 mTorr	200 mTorr
O_2 10 scc	O_2 10 scc	CF_4 8 scc	CF_4 8 scc	CF_4 8 scc
		CHF_4 6 scc	CHF_4 6 scc	CHF_4 6 scc
RF 0 W	RF 100 W	RF 0 W	RF 350 W	RF 0 W
50 Gauss	50 Gauss	50 Gauss	50 Gauss	50 Gauss

STS2 "STSHAL-A"

Base pressure	5 mTorr
Platen power	10 W
Generator power	600 W
Gases	C_4F_8 80 scc
	SF_6 40 ssc
Plasma run time	55 minutes

Plasmaquest "PPSSF6"

Gases	SF_6:O_2 (1:1)
Total gas flow rate	200 scc
Pressure	100 mTorr
Source power	400 W
Bias power	50 W
Plasma run time	20 minutes

Centura "TAFF1.5" called by "TAFFOX"

Step No.	1	2
Step name	Etch	Strip
Pressure	3 mTorr	15 mTorr
Source power	2400 W	2400 W
Bias power	1000 W	0 W
Gas flow	C_2F_6 scc 25	O_2 scc 95
Time	126 seconds	3 minutes
TV position	100% open	30% open

Chamber used	B
Roof temperature	240°C
Wall temperature	210°C
Cathode temperature	10°C
Backside He cooling	15 mTorr

Deposition recipes

Concept 1 "1.5 um Oxide"

A1 N_2	1.5
B1 N_2	0
A2 SiH_4	0.3
B2 N_2O	9.5
HF power	1.10 kW
LF power	0 kW
Pressure	2.4 T
Temperature	400°C
Time	34.6 seconds
Deposition rate	5250 Å / minute
Precoat	60 seconds
PreA delay	0.5 seconds
PostA delay	0.5 seconds
Temp soak	10 seconds

Endura sequences details:
The sequence "Al 5000 A" calls the recipe "Al 5000 A" alone.
The sequence "Z-PZ-Brian Al-Ti" calls the recipe "Al 5000 A" followed by a subsequent run with "TI 500A".
The sequence "X Al 5KA W-CLN" calls the recipe "WAFER CLEAN" followed by a subsequent run with "Al 5000 A".

The recipe specifics are shown below:

Endura "Al 5000 A"

Step No.	1	2	3	4
Step name	Gas Stabilization	Strike	Deposition	Purge
Step end control	By Time	By Time	By Time	By Time
Max. step time	10 seconds	3 seconds	25 seconds	75 seconds
Gate	Full	Full	Full	Full
Wafer gas pressure	5000 mTorr	5000 mTorr	5000 mTorr	0 mTorr
DC power	0 W	750 W	9000 W	0 W
DC power ramp rate	0 W/second	750 W/second	4500 W/second	0 W/second
Pressure servo gas	AR-1: 45 scc	AR-1: 45 scc	AR-1: 45 scc	N/A
Gas names and flows	ARH-1:14 scc	ARH-1:14 scc	ARH-1:14 scc	N/A

Endura "TI 500A"

Step No.	1	2	3	4
Step name	Gas Stabilization	Strike	Deposition	Pumpdown
Step end control	By Time	By Time	By Time	By Time
Max. step time	10 seconds	3 seconds	5 seconds	5 seconds
Gate	Full	Full	Full	Full
Wafer gas pressure	3000 mTorr	3000 mTorr	3000 mTorr	0 mTorr
DC power	0 W	500 W	3000 W	0 W
DC power ramp rate	0 W/second	500 W/second	3000 W/second	0 W/second
Gas names and flows	ARH-4:14 scc AR-4: 50 scc	ARH-4:14 scc AR-4: 50 scc	ARH-4:14 scc AR-4: 35 scc	N/A

Endura "WAFER CLEAN"

Step No.	1	2	3	4	5
Step name	Fill	Strike	Etch	Discharge	Purge
Step end control	By Time	By Time	By Time	By Time	By Time
Max. step time	10 seconds	3 seconds	20 seconds	1 second	3 seconds
Wafer gas pressure	0 mTorr	0 mTorr	0 mTorr	0 mTorr	0 mTorr
RF power	0 W	100 W	125 W	1 W	0 W
RF second power	0 W	150 W	300 W	100 W	0 W
Gas names and flows	AR-C: 20 scc	AR-C: 5 scc	AR-C: 5 scc	AR-C: 5 scc	AR-C: 5 scc

STS-CVD "LF-SiN"

Process pressure	550 mTorr
Platen temperature	300°C
Showerhead temperature	250°C
N_2	1960 scc
SiH_4	40 scc
NH_3	20 scc
Low frequency RF	60 W at 380kHz
Match (Load/Tune)	15/80 W
Run time	~14 seconds for 3 nm or ~55 for 25 nm

References:

1. Pinto Coelho, C. Efficient tools for the design and simulation of microelectromechanical and microfluidic systems. Massachusetts Institute of Technology, Cambridge, MA, 2007.
2. Hengartner, M. O., The biochemistry of apoptosis. *Nature* **2000,** 407, (6805), 770-6.
3. Draviam, V. M.; Shapiro, I.; Aldridge, B.; Sorger, P. K., Misorientation and reduced stretching of aligned sister kinetochores promote chromosome missegregation in EB1- or APC-depleted cells. *Embo J* **2006,** 25, (12), 2814-27.
4. Hoffmann, A.; Levchenko, A.; Scott, M. L.; Baltimore, D., The IkappaB-NF-kappaB signaling module: temporal control and selective gene activation. *Science* **2002,** 298, (5596), 1241-5.
5. Rosenthal, A.; Taff, B. M.; Voldman, J., Quantitative modeling of dielectrophoretic traps. *Lab on a Chip* **2006,** 6, (4), 508-15.
6. Albeck, J. G.; Burke, J. M.; Aldridge, B. B.; Zhang, M.; Lauffenburger, D. A.; Sorger, P. K., Quantitative analysis of pathways controlling extrinsic apoptosis in single cells. *Mol Cell* **2008,** 30, (1), 11-25.
7. Nelson, D. E.; Ihekwaba, A. E.; Elliott, M.; Johnson, J. R.; Gibney, C. A.; Foreman, B. E.; Nelson, G.; See, V.; Horton, C. A.; Spiller, D. G.; Edwards, S. W.; McDowell, H. P.; Unitt, J. F.; Sullivan, E.; Grimley, R.; Benson, N.; Broomhead, D.; Kell, D. B.; White, M. R., Oscillations in NF-kappaB signaling control the dynamics of gene expression. *Science* **2004,** 306, (5696), 704-8.
8. Serrano, M.; Hannon, G. J.; Beach, D., A new regulatory motif in cell-cycle control causing specific inhibition of cyclin D/CDK4. *Nature* **1993,** 366, (6456), 704-7.
9. Ip, Y. T.; Davis, R. J., Signal transduction by the c-Jun N-terminal kinase (JNK)--from inflammation to development. *Curr Opin Cell Biol* **1998,** 10, (2), 205-19.
10. Shibasaki, F.; Kondo, E.; Akagi, T.; McKeon, F., Suppression of signalling through transcription factor NF-AT by interactions between calcineurin and Bcl-2. *Nature* **1997,** 386, (6626), 728-31.
11. Green, D. R.; Reed, J. C., Mitochondria and Apoptosis. *Science* **1998,** 281, (5381), 1309-1312.
12. Juliano, R. L.; Dixit, V. R.; Kang, H.; Kim, T. Y.; Miyamoto, Y.; Xu, D., Epigenetic manipulation of gene expression: a toolkit for cell biologists. *J Cell Biol* **2005,** 169, (6), 847-57.
13. Moffat, J.; Sabatini, D. M., Building mammalian signalling pathways with RNAi screens. *Nat Rev Mol Cell Biol* **2006,** 7, (3), 177-87.
14. Burdon, R. H., Heat-Shock and the Heat-Shock Proteins. *Biochemical Journal* **1986,** 240, (2), 313-324.
15. Subjeck, J. R.; Shyy, T. T., Stress protein systems of mammalian cells. *Am J Physiol* **1986,** 250, (1 Pt 1), C1-17.
16. Emmert-Buck, M. R.; Bonner, R. F.; Smith, P. D.; Chuaqui, R. F.; Zhuang, Z.; Goldstein, S. R.; Weiss, R. A.; Liotta, L. A., Laser capture microdissection. *Science* **1996,** 274, (5289), 998-1001.
17. Taylor, L. C.; Walt, D. R., Application of high-density optical microwell arrays in a live-cell biosensing system. *Analytical Biochemistry* **2000,** 278, (2), 132-142.
18. Rettig, J. R.; Folch, A., Large-scale single-cell trapping and imaging using microwell arrays. *Anal Chem* **2005,** 77, (17), 5628-34.
19. Huang, Y.; Ewalt, K. L.; Tirado, M.; Haigis, R.; Forster, A.; Ackley, D.; Heller, M. J.; O'Connell, J. P.; Krihak, M., Electric manipulation of bioparticles and macromolecules on microfabricated electrodes. *Analytical Chemistry* **2001,** 73, (7), 1549-1559.
20. Love, J. C.; Ronan, J. L.; Grotenbreg, G. M.; Van Der Veen, A. G.; Ploegh, H. L., A microengraving method for rapid selection of single cells producing antigen-specific antibodies. *Nature Biotechnology* **2006,** 24, (6), 703-707.
21. Burg, T. P.; Godin, M.; Knudsen, S. M.; Shen, W.; Carlson, G.; Foster, J. S.; Babcock, K.; Manalis, S. R., Weighing of biomolecules, single cells and single nanoparticles in fluid. *Nature* **2007,** 446, (7139), 1066-9.
22. Thery, M.; Jimenez-Dalmaroni, A.; Racine, V.; Bornens, M.; Julicher, F., Experimental and theoretical study of mitotic spindle orientation. *Nature* **2007,** 447, (7143), 493-6.
23. Wheeler, A. R.; Throndset, W. R.; Whelan, R. J.; Leach, A. M.; Zare, R. N.; Liao, Y. H.; Farrell, K.; Manger, I. D.; Daridon, A., Microfluidic device for single-cell analysis. *Anal Chem* **2003,** 75, (14), 3581-6.
24. Gray, D. S.; Tan, J. L.; Voldman, J.; Chen, C. S., Dielectrophoretic registration of living cells to a microelectrode array. *Biosensors & Bioelectronics* **2004,** 19, (7), 771-780.
25. Akselrod, G. M.; Timp, W.; Mirsaidov, U.; Zhao, Q.; Li, C.; Timp, R.; Timp, K.; Matsudaira, P.; Timp, G., Laser-guided assembly of heterotypic three-dimensional living cell microarrays. *Biophysical Journal* **2006,** 91, (9), 3465-73.

26. Salazar, G. T. a.; Wang, Y.; Young, G.; Bachman, M.; Sims, C. E.; Li, G. P.; Allbritton, N. L., Micropallet arrays for the separation of single, adherent cells. *Analytical Chemistry* **2007,** 79, (2), 682-687.
27. Nelson, C. M.; Chen, C. S., Cell-cell signaling by direct contact increases cell proliferation via a PI3K-dependent signal. *FEBS Lett* **2002,** 514, (2-3), 238-42.
28. Rosenthal, A.; Macdonald, A.; Voldman, J., Cell patterning chip for controlling the stem cell microenvironment. *Biomaterials* **2007,** 28, (21), 3208-16.
29. Cookson, S.; Ostroff, N.; Pang, W. L.; Volfson, D.; Hasty, J., Monitoring dynamics of single-cell gene expression over multiple cell cycles. *Mol Syst Biol* **2005,** 1, 2005 0024.
30. Rosenfeld, N.; Young, J. W.; Alon, U.; Swain, P. S.; Elowitz, M. B., Gene regulation at the single-cell level. *Science* **2005,** 307, (5717), 1962-5.
31. Volfson, D.; Marciniak, J.; Blake, W. J.; Ostroff, N.; Tsimring, L. S.; Hasty, J., Origins of extrinsic variability in eukaryotic gene expression. *Nature* **2006,** 439, (7078), 861-4.
32. Colman-Lerner, A.; Gordon, A.; Serra, E.; Chin, T.; Resnekov, O.; Endy, D.; Pesce, C. G.; Brent, R., Regulated cell-to-cell variation in a cell-fate decision system. *Nature* **2005,** 437, (7059), 699-706.
33. Geva-Zatorsky, N.; Rosenfeld, N.; Itzkovitz, S.; Milo, R.; Sigal, A.; Dekel, E.; Yarnitzky, T.; Liron, Y.; Polak, P.; Lahav, G.; Alon, U., Oscillations and variability in the p53 system. *Mol Syst Biol* **2006,** 2, 2006 0033.
34. Shin, S.; Sun, Y.; Liu, Y.; Khaner, H.; Svant, S.; Cai, J.; Xu, Q. X.; Davidson, B. P.; Stice, S. L.; Smith, A. K.; Goldman, S. A.; Reubinoff, B. E.; Zhan, M.; Rao, M. S.; Chesnut, J. D., Whole genome analysis of human neural stem cells derived from embryonic stem cells and stem and progenitor cells isolated from fetal tissue. *Stem Cells* **2007,** 25, (5), 1298-306.
35. Hague, A.; Paraskeva, C., Apoptosis and disease: a matter of cell fate. *Cell Death Differ* **2004,** 11, (12), 1366-72.
36. Jordan, C. T.; Guzman, M. L.; Noble, M., Mechanisms of Disease: Cancer Stem Cells. *New England Journal of Medicine* **2006,** 355, (12), 1253-1261.
37. Taff, B. M.; Desai, S. P.; Voldman, J. In *Dielectrophoretically switchable microfluidic weir structures for exclusion-based single-cell manipulation*, Micro Total Analysis Systems 2007: Eleventh International Conference on Miniaturized Systems for Chemistry and Life Sciences, Paris, France, October 7-11, 2007, 2007; Viovy, J.-L.; Tabeling, P.; Descroix, S.; Malaquin, L., Eds. The Chemical and Biological Microsystems Society: Paris, France, 2007; pp 8-10.
38. Taff, B. M.; Desai, S. P.; Voldman, J. In *Electromechanically Active Hydrodynamic Arrays for Single-Cell Manipulation*, Biomedical Engineering Society Annual Fall Meeting, Los Angeles, CA, 2007; Los Angeles, CA, 2007.
39. Taff, B. M.; Ooi, B.-H.; Desai, S. P.; Willcox, K. E.; Voldman, J., Electroactive Hydrodynamic Weirs for Micro-particle Manipulation and Patterning. *Applied Physics Letters* **2008,** In preparation.
40. Taff, B. M.; Voldman, J., A scalable addressable positive-dielectrophoretic cell-sorting array. *Analytical Chemistry* **2005,** 77, (24), 7976-7983.
41. Desai, S. P.; Voldman, J. In *Measuring the Impact of Dielectrophoresis on Cell Physiology Using a High-Content Screening Platform*, Micro Total Analysis Systems 2008, San Diego, CA, October 12-16, 2008; San Diego, CA, 2008.
42. Sampattavanich, S.; Taff, B. M.; Desai, S. P.; Voldman, J. In *Organizing Complex Multicellular Constructs Using Stencil-Delineated Electroactive Patterning (S-DEP)*, Micro Total Analysis Systems, San Diego, CA, 2008; San Diego, CA, 2008.
43. Desai, S. P.; Taff, B. M.; Voldman, J., A photopatternable silicone for biological applications. *Langmuir* **2008,** 24, (2), 575-581.
44. Zhu, J.; McKeon, F., Nucleocytoplasmic shuttling and the control of NF-AT signaling. *Cell Mol Life Sci* **2000,** 57, (3), 411-20.
45. Volk, S. W.; Radu, A.; Zhang, L.; Liechty, K. W., Stromal progenitor cell therapy corrects the wound-healing defect in the ischemic rabbit ear model of chronic wound repair. *Wound Repair Regen* **2007,** 15, (5), 736-47.
46. Basu, S.; Gerchman, Y.; Collins, C. H.; Arnold, F. H.; Weiss, R., A synthetic multicellular system for programmed pattern formation. *Nature* **2005,** 434, (7037), 1130-4.
47. Suel, G. M.; Garcia-Ojalvo, J.; Liberman, L. M.; Elowitz, M. B., An excitable gene regulatory circuit induces transient cellular differentiation. *Nature* **2006,** 440, (7083), 545-50.
48. Acar, M.; Becskei, A.; van Oudenaarden, A., Enhancement of cellular memory by reducing stochastic transitions. *Nature* **2005,** 435, (7039), 228-32.
49. Austin, D. W.; Allen, M. S.; McCollum, J. M.; Dar, R. D.; Wilgus, J. R.; Sayler, G. S.; Samatova, N. F.; Cox, C. D.; Simpson, M. L., Gene network shaping of inherent noise spectra. *Nature* **2006,** 439, (7076), 608-11.

50. Newman, J. R.; Ghaemmaghami, S.; Ihmels, J.; Breslow, D. K.; Noble, M.; DeRisi, J. L.; Weissman, J. S., Single-cell proteomic analysis of S. cerevisiae reveals the architecture of biological noise. *Nature* **2006,** 441, (7095), 840-6.
51. Pedraza, J. M.; van Oudenaarden, A., Noise propagation in gene networks. *Science* **2005,** 307, (5717), 1965-9.
52. Rao, C. V.; Wolf, D. M.; Arkin, A. P., Control, exploitation and tolerance of intracellular noise. *Nature* **2002,** 420, (6912), 231-7.
53. Bar-Even, A.; Paulsson, J.; Maheshri, N.; Carmi, M.; O'Shea, E.; Pilpel, Y.; Barkai, N., Noise in protein expression scales with natural protein abundance. *Nat Genet* **2006,** 38, (6), 636-43.
54. Cai, L.; Friedman, N.; Xie, X. S., Stochastic protein expression in individual cells at the single molecule level. *Nature* **2006,** 440, (7082), 358-62.
55. Vucic, D.; Franklin, M. C.; Wallweber, H. J.; Das, K.; Eckelman, B. P.; Shin, H.; Elliott, L. O.; Kadkhodayan, S.; Deshayes, K.; Salvesen, G. S.; Fairbrother, W. J., Engineering ML-IAP to produce an extraordinarily potent caspase 9 inhibitor: implications for Smac-dependent anti-apoptotic activity of ML-IAP. *Biochem J* **2005,** 385, (Pt 1), 11-20.
56. Verhagen, A. M.; Ekert, P. G.; Pakusch, M.; Silke, J.; Connolly, L. M.; Reid, G. E.; Moritz, R. L.; Simpson, R. J.; Vaux, D. L., Identification of DIABLO, a mammalian protein that promotes apoptosis by binding to and antagonizing IAP proteins. *Cell* **2000,** 102, (1), 43-53.
57. Valero, A.; Merino, F.; Wolbers, F.; Luttge, R.; Vermes, I.; Andersson, H.; van den Berg, A., Apoptotic cell death dynamics of HL60 cells studied using a microfluidic cell trap device. *Lab on a Chip* **2005,** 5, (1), 49-55.
58. Kominsky, D. J.; Bickel, R. J.; Tyler, K. L., Reovirus-induced apoptosis requires mitochondrial release of Smac/DIABLO and involves reduction of cellular inhibitor of apoptosis protein levels. *J Virol* **2002,** 76, (22), 11414-24.
59. Adrain, C.; Creagh, E. M.; Martin, S. J., Apoptosis-associated release of Smac/DIABLO from mitochondria requires active caspases and is blocked by Bcl-2. *Embo J* **2001,** 20, (23), 6627-36.
60. Loeffler, M.; Kroemer, G., The mitochondrion in cell death control: certainties and incognita. *Exp Cell Res* **2000,** 256, (1), 19-26.
61. Du, C.; Fang, M.; Li, Y.; Li, L.; Wang, X., Smac, a mitochondrial protein that promotes cytochrome c-dependent caspase activation by eliminating IAP inhibition. *Cell* **2000,** 102, (1), 33-42.
62. Borner, C.; Monney, L., Apoptosis without caspases: an inefficient molecular guillotine? *Cell Death Differ* **1999,** 6, (6), 497-507.
63. Li Jeon, N.; Baskaran, H.; Dertinger, S. K.; Whitesides, G. M.; Van de Water, L.; Toner, M., Neutrophil chemotaxis in linear and complex gradients of interleukin-8 formed in a microfabricated device. *Nat Biotechnol* **2002,** 20, (8), 826-30.
64. Lodish, H., Berk, A., Matsudaira, P., Kaiser, C. A., Krieger, M., Scott, M. P., Zipursky, S. L., and Darnell, J., *Molecular Cell Biology*. 5 ed.; W. H. Freeman and Co.: New York, 2004.
65. Davey, R. E.; Zandstra, P. W., Spatial organization of embryonic stem cell responsiveness to autocrine gp130 ligands reveals an autoregulatory stem cell niche. *Stem Cells* **2006,** 24, (11), 2538-48.
66. Gibson, M. C.; Patel, A. B.; Nagpal, R.; Perrimon, N., The emergence of geometric order in proliferating metazoan epithelia. *Nature* **2006,** 442, (7106), 1038-41.
67. Lucchetta, E. M.; Lee, J. H.; Fu, L. A.; Patel, N. H.; Ismagilov, R. F., Dynamics of Drosophila embryonic patterning network perturbed in space and time using microfluidics. *Nature* **2005,** 434, (7037), 1134-8.
68. Nelson, C. M.; Vanduijn, M. M.; Inman, J. L.; Fletcher, D. A.; Bissell, M. J., Tissue geometry determines sites of mammary branching morphogenesis in organotypic cultures. *Science* **2006,** 314, (5797), 298-300.
69. Hui, E. E.; Bhatia, S. N., Micromechanical control of cell-cell interactions. *Proc Natl Acad Sci U S A* **2007,** 104, (14), 5722-6.
70. Takahashi, K.; Tanabe, K.; Ohnuki, M.; Narita, M.; Ichisaka, T.; Tomoda, K.; Yamanaka, S., Induction of pluripotent stem cells from adult human fibroblasts by defined factors. *Cell* **2007,** 131, (5), 861-72.
71. Ilkhanizadeh, S.; Teixeira, A. I.; Hermanson, O., Inkjet printing of macromolecules on hydrogels to steer neural stem cell differentiation. *Biomaterials* **2007,** 28, (27), 3936-43.
72. Janes, K. A.; Kelly, J. R.; Gaudet, S.; Albeck, J. G.; Sorger, P. K.; Lauffenburger, D. A., Cue-signal-response analysis of TNF-induced apoptosis by partial least squares regression of dynamic multivariate data. *J Comput Biol* **2004,** 11, (4), 544-61.
73. Janes, K. A.; Gaudet, S.; Albeck, J. G.; Nielsen, U. B.; Lauffenburger, D. A.; Sorger, P. K., The response of human epithelial cells to TNF involves an inducible autocrine cascade. *Cell* **2006,** 124, (6), 1225-39.

74. Carpenter, A. E.; Jones, T. R.; Lamprecht, M. R.; Clarke, C.; Kang, I. H.; Friman, O.; Guertin, D. A.; Chang, J. H.; Lindquist, R. A.; Moffat, J.; Golland, P.; Sabatini, D. M., CellProfiler: image analysis software for identifying and quantifying cell phenotypes. *Genome Biol* **2006,** 7, (10), R100.
75. Ha, T.; Ting, A. Y.; Liang, J.; Caldwell, W. B.; Deniz, A. A.; Chemla, D. S.; Schultz, P. G.; Weiss, S., Single-molecule fluorescence spectroscopy of enzyme conformational dynamics and cleavage mechanism. *Proc Natl Acad Sci U S A* **1999,** 96, (3), 893-8.
76. Zhang, J.; Campbell, R. E.; Ting, A. Y.; Tsien, R. Y., Creating new fluorescent probes for cell biology. *Nat Rev Mol Cell Biol* **2002,** 3, (12), 906-18.
77. Senturia, S. D., *Microsystem Design*. Kluwer Academic Publishers: Boston, 2001.
78. Kovacs, G. T. A., *Micromachined Transducers Sourcebook*. WCB McGraw-Hill: Boston, 1998.
79. Nam, Y.; Chang, J. C.; Wheeler, B. C.; Brewer, G. J., Gold-coated microelectrode array with thiol linked self-assembled monolayers for engineering neuronal cultures. *IEEE Transactions on Biomedical Engineering* **2004,** 51, (1), 158-65.
80. Suzuki, I.; Sugio, Y.; Jimbo, Y.; Yasuda, K., Stepwise pattern modification of neuronal network in photo-thermally-etched agarose architecture on multi-electrode array chip for individual-cell-based electrophysiological measurement. *Lab on a Chip* **2005,** 5, (3), 241-7.
81. Folch, A., Toner, M., Microengineering of Cellular Interactions. In *Annual Review of Biomedical Engineering*, 2000; Vol. 2, pp 227-256.
82. Barron, J. A., Wu, P., Ladouceur, H. D., and Ringeisen, B. R., Biological Laser Printing: A Novel Technique for Creating Heterogeneous 3-dimensional Cell Patterns. *Biomedical Microdevices* **2004,** 6, (2), 139-147.
83. Bhatia, S. N. B., U. J.; Yarmush, M. L.; Toner, M.;, Microfabrication of Hepatocyte/Fibroblast Co-cultures: Role of Homotypic Cell Interactions. *Biotechnol. Prog.* **1998,** 14, (3), 378-387.
84. McFadden, P., Broadband biodetection: Holmes on a chip. *Science* **2002,** 297, (5589), 2075-2076.
85. Pancrazio, J. J.; Whelan, J. P.; Borkholder, D. A.; Ma, W.; Stenger, D. A., Development and application of cell-based biosensors. *Annals of Biomedical Engineering* **1999,** 27, (6), 697-711.
86. Kovacs, G. T. A., Electronic sensors with living cellular components. *Proceedings of the IEEE* **2003,** 91, (6), 915-29.
87. Chen, P.; Xu, B.; Tokranova, N.; Feng, X.; Castracane, J.; Gillis, K. D., Amperometric detection of quantal catecholamine secretion from individual cells on micromachined silicon chips. *Analytical Chemistry* **2003,** 75, (3), 518-524.
88. Isik, S.; Berdondini, L.; Oni, J.; Blochl, A.; Koudelka-Hep, M.; Schuhmann, W., Cell-compatible array of three-dimensional tip electrodes for the detection of nitric oxide release. *Biosensors & Bioelectronics* **2005,** 20, (8), 1566-72.
89. Tan, J. L., Tien, J., Pirone, D. N., Gray, D. S., Bhadriraju, K., Chen, C. S., Cells lying on a bed of microneedles: An approach to isolate mechanical force. *PNAS* **2002,** 100, (4), 1484-1489.
90. Shawgo, R. S.; Grayson, A. C. R.; Li, Y. W.; Cima, M. J., BioMEMS for drug delivery. *Current Opinion in Solid State & Materials Science* **2002,** 6, (4), 329-334.
91. Peterman, M. C.; Mehenti, N. Z.; Bilbao, K. V.; Lee, C. J.; Leng, T.; Noolandi, J.; Bent, S. F.; Blumenkranz, M. S.; Fishman, H. A., The Artificial Synapse Chip: a flexible retinal interface based on directed retinal cell growth and neurotransmitter stimulation. *Artif Organs* **2003,** 27, (11), 975-85.
92. Ziauddin, J.; Sabatini, D. M., Microarrays of cells expressing defined cDNAs. *Nature* **2001,** 411, (6833), 107-110.
93. McKnight, T. E.; Melechko, A. V.; Hesnley, D. K.; Mann, D. G. J.; Griffin, G. D.; Simpson, M. L., Tracking gene expression after DNA delivery using spatially indexed nanofiber arrays. *Nano Letters* **2004,** 4, (7), 1213-19.
94. Walt, D. R., Imaging optical sensor arrays. *Current Opinion in Chemical Biology* **2002,** 6, 689-695.
95. Ostuni, E.; Chen, C. S.; Ingber, D. E.; Whitesides, G. M., Selective deposition of proteins and cells in arrays of microwells. *Langmuir* **2001,** 17, (9), 2828-2834.
96. Folch, A.; Jo, B.-H.; Hurtado, B.-H.; Beebe, D. J.; Hurtado, O.; Toner, M., Microfabricated elastomeric stencils for micropatterning cell cultures. *Journal of Biomedical Materials Research* **2000,** 52, (2), 346-353.
97. Chin, V. I.; Taupin, P.; Sanga, S.; Scheel, J.; Gage, F. H.; Bhatia, S. N., Microfabricated platform for studying stem cell fates. *Biotechnology and Bioengineering* **2004,** 88, (3), 399-415.
98. Kapur, R., Giuliano, K. A., Campana, M., Adams, T., Olson, K., Jung, D., Mrksich, M., Vasudevan, C., and Taylor, D. L., Streamlining the Drug Discovery Process by Integrating Miniaturization, High Throughput Screening, High Content Screening, and Automation on the CellChip System. *Biomedical Microdevices* **1999,** 2, (2), 99-109.

99. Hung, P. J.; Lee, P. J.; Sabounchi, P.; Lin, R.; Lee, L. P., Continuous perfusion microfluidic cell culture array for high-throughput cell-based assays. *Biotechnology and Bioengineering* **2005,** 89, (1), 1-8.
100. Takayama, S., Ostuni, E., LeDuc, P., Naruse, K., Ingber, D., Whitesides, G., Selective Chemical Treatment of Cellular Microdomains Using Multiple Laminar Streams. *Chemistry & Biology* **2003,** 10, 123-130.
101. Thompson, D. M.; King, K. R.; Wieder, K. J.; Toner, M.; Yarmush, M. L.; Jayaraman, A., Dynamic gene expression profiling using a microfabricated living cell array. *Analytical Chemistry* **2004,** 76, (14), 4098-4103.
102. Jiang, X.; Ferrigno, R.; Mrksich, M.; Whitesides, G. M., Electrochemical desorption of self-assembled monolayers noninvasively releases patterned cells from geometrical confinements. *Journal of the American Chemical Society* **2003,** 125, (9), 2366-2367.
103. Hayward, R. C.; Saville, D. A.; Aksay, I. A., Electrophoretic assembly of colloidal crystals with optically tunable micropatterns. *Nature* **2000,** 404, (6773), 56-9.
104. Rosenthal, A.; Voldman, J., Dielectrophoretic Traps for Single-Particle Patterning. *Biophys. J.* **2005,** 88, (3), 2193-2205.
105. Heller, M. J., Forster, A. H., and Tu, E., Active microelectronic chip devices which utilize controlled electrophoretic fields for multiplex DNA hybridization and other genomic applications. *Electrophoresis* **2000,** 21, 157-164.
106. Voldman, J.; Toner, M.; Gray, M. L.; Schmidt, M. A., A Microfabrication-Based Dynamic Array Cytometer. *Analytical Chemistry* **2002,** 74, (16), 3984-3990.
107. Sato, K.; Kawamura, Y.; Tanaka, S.; Uchida, K.; Kohida, H., Individual and mass operation of biological cells using micromechanical silicon devices. *Sensors & Actuators A-Physical* **1990,** A21-A23, 948-53.
108. Khine, M., Lau, A., Ionescu-Zanetti, C., Seo, J., and Lee, L. P., A Single Cell Electroporation Chip. *Lab on a Chip* **2005,** 5, (1), 38-43.
109. Huang, Y.; Rubinsky, B., Flow-through micro-electroporation chip for high efficiency single-cell genetic manipulation. *Sensors and Actuators a-Physical* **2003,** 104, (3), 205-212.
110. Braff, R. A.; Gerhardt, A. L.; Schmidt, M. A.; Gray, M. L.; Toner, M. In *A microbubble-powered bioparticle actuator*, Solid-State Sensor and Actuator Workshop, Hilton Head Island, SC, USA, 2002; Transducers Res. Found.: Hilton Head Island, SC, USA, 2002; pp 138-141.
111. Walker, L. M.; Holm, A.; Cooling, L.; Maxwell, L.; Oberg, A.; Sundqvist, T.; El Haj, A. J., Mechanical manipulation of bone and cartilage cells with 'optical tweezers'. *Febs Letters* **1999,** 459, (1), 39-42.
112. MacDonald, M. P.; Spalding, G. C.; Dholakia, K., Microfluidic sorting in an optical lattice. *Nature* **2003,** 426, (6965), 421-424.
113. Fuhr, G.; Glasser, H.; Muller, T.; Schnelle, T., Cell Manipulation and Cultivation under Ac Electric-Field Influence in Highly Conductive Culture Media. *Biochimica Et Biophysica Acta-General Subjects* **1994,** 1201, (3), 353-360.
114. Suehiro, J.; Pethig, R., The dielectrophoretic movement and positioning of a biological cell using a three-dimensional grid electrode system. *Journal of Physics D: Applied Physics* **1998,** (22), 3298-3305.
115. Jones, T. B., *Electromechanics of Particles*. 1st ed.; Cambridge University Press: 1995.
116. Pethig, R., Dielectrophoresis: Using inhomogeneous AC electrical fields to separate and manipulate cells. *Critical Reviews in Biotechnology* **1996,** 16, (4), 331-348.
117. Pohl, H. A., *Dielectrophoresis: The Behavior of Neutral Matter in Nonuniform Electric Fields*. Cambridge University Press: New York, 1978; Vol. XII, p 579.
118. Fiedler, S.; Shirley, S. G.; Schnelle, T.; Fuhr, G., Dielectrophoretic sorting of particles and cells in a microsystem. *Analytical Chemistry* **1998,** 70, (9), 1909-1915.
119. Jones, T. B.; Washizu, M., Multipolar dielectrophoretic and electrorotation theory. *Journal of Electrostatics* **1996,** 37, (1-2), 121-134.
120. Voldman, J. A Microfabricated Dielectrophoretic Trapping Array for Cell-based Biological Assays. Ph. D., MIT, Cambridge, MA, 2002.
121. Liu, J.; Hansen, C.; Quake, S. R., Solving the "world-to-chip" interface problem with a microfluidic matrix. *Analytical Chemistry* **2003,** 75, (18), 4718-4723.
122. Prakash, M.; Gershenfeld, N., Microfluidic Bubble Logic. *Science* **2007,** 315, (5813), 832-835.
123. White, F. M., *Fluid Mechanics*. 4th ed.; WCB McGraw-Hill: Boston, 1999; p 826.
124. Taff, B. M. Design and Fabrication of an Addressable MEMS-Based Dielectrophoretic Microparticle Array. Massachusetts Institute of Technology, Cambridge, MA, 2004.
125. Schwan, H. P., Dielectrophoresis and Rotation of Cells. In *Electroporation and Electrofusion in Cell Biology*, Neumann, E., A. E. Sowers, and C. A. Jordan, Ed. Plenum Press: New York, 1989; pp 3-22.

126. Tziampazis, E.; Kohn, J.; Moghe, P. V., PEG-variant biomaterials as selectively adhesive protein templates: Model surfaces for controlled cell adhesion and migration. *Biomaterials* **2000,** 21, (5), 511-520.
127. Revzin, A.; Tompkins, R. G.; Toner, M., Surface engineering with poly(ethylene glycol) photolithography to create high-density cell arrays on glass. *Langmuir* **2003,** 19, (23), 9855-9862.
128. Irimia, D.; Karlsson, J. O. M., Development of a cell patterning technique using poly(ethylene glycol) disilane. *Biomedical Microdevices* 5, (3), 185-94.
129. Tan, J. L.; Liu, W.; Nelson, C. M.; Raghavan, S.; Chen, C. S., Simple approach to micropattern cells on common culture substrates by tuning substrate wettability. *Tissue Eng* **2004,** 10, (5-6), 865-72.
130. Koo, K. C., T.L. Walzak, and R.D. Davidson In *Corrosion Behaviour of Aluminum Metallization During Aqueous Exposure*, Electronic Packaging Materials Science, 1995; 1995; pp 123-8.
131. Williams, K. R.; Muller, R. S., Etch rates for micromachining processing. *Journal of Microelectromechanical Systems* **1996,** 5, (4), 256-269.
132. Faraasen, S.; Voros, J.; Csucs, G.; Textor, M.; Merkle, H. P.; Walter, E., Ligand-specific targeting of microspheres to phagocytes by surface modification with poly(L-lysine)-grafted poly(ethylene glycol) conjugate. *Pharm Res* **2003,** 20, (2), 237-46.
133. Elbert, D. L.; Hubbell, J. A., Self-assembly and steric stabilization at heterogeneous, biological surfaces using adsorbing block copolymers. *Chem Biol* **1998,** 5, (3), 177-83.
134. Kenausis, G. L.; Voros, J.; Elbert, D. L.; Huang, N.; Hofer, R.; Ruiz-Taylor, L.; Textor, M.; Hubbell, J. A.; Spencer, N. D., Poly(L-lysine)-g-poly(ethylene glycol) layers on metal oxide surfaces: Attachment mechanism and effects of polymer architecture on resistance to protein adsorption. *Journal of Physical Chemistry B* **2000,** 104, (14), 3298-3309.
135. Marie, R.; Beech, J. P.; Voros, J.; Tegenfeldt, J. O.; Hook, F., Use of PLL-g-PEG in micro-fluidic devices for localizing selective and specific protein binding. *Langmuir* **2006,** 22, (24), 10103-8.
136. Chang, J. C.; Brewer, G. J.; Wheeler, B. C., Modulation of neural network activity by patterning. *Biosensors & Bioelectronics* **2001,** 16, (7-8), 527-33.
137. Smith, S. L.; Judy, J. W.; Otis, T. S., An ultra small array of electrodes for stimulating multiple inputs into a single neuron. *Journal of Neuroscience Methods* **2004,** 133, (1-2), 109-14.
138. Happel, J.; Brenner, H., *Low Reynolds Number Hydrodynamics*. Prentice-Hall: Englewood Cliffs, NJ, 1965.
139. Jeffrey, D. J.; Onishi, Y., Calculation of the resistance and mobility functions for two unequal rigid spheres in low-Reynolds-number flow. *Journal of Fluid Mechanics* **1984,** 139, 261-90.
140. Goldman, A. J.; Cox, R. G.; Brenner, H., Slow viscous motion of a sphere parallel to a plane wall. II. Couette flow. *Chemical Engineering Science* **1967,** 22, (4), 653-660.
141. Deen, W. M., *Analysis of Transport Phenomena*. Oxford University Press: New York, 1998.
142. Khoo, B. C.; Le, D. V.; Peraire, J., An immersed interface method for viscous incompressible flows involving rigid and flexible boundaries. *Journal of Computational Physics* **2006,** 220, (1), 109-38.
143. Howe, R. T.; Sodini, C. G., *Microelectronics: An Integrated Approach*. Prentice-Hall: Upper Saddle River, NJ, 1997.
144. Streetman, B. G. a. S. B., *Solid State Electronic Devices*. 5th ed.; Prentice Hall: Upper Saddle River, New Jersey, 2000.
145. Ihle, J. N.; Keller, J.; Henderson, L.; Klein, F.; Palaszynski, E., Procedures for the purification of interleukin 3 to homogeneity. *J Immunol* **1982,** 129, (6), 2431-6.
146. Ahn, K.; Kerbage, C.; Hunt, T. P.; Westervelt, R. M.; Link, D. R.; Weitz, D. A., Dielectrophoretic manipulation of drops for high-speed microfluidic sorting devices. *Applied Physics Letters* **2006,** 88, (2), 24104-1.
147. Hu, X.; Bessette, P. H.; Qian, J.; Meinhart, C. D.; Daugherty, P. S.; Soh, H. T., Marker-specific sorting of rare cells using dielectrophoresis. *Proc Natl Acad Sci U S A* **2005,** 102, (44), 15757-61.
148. Di Carlo, D.; Aghdam, N.; Lee, L. P., Single-cell enzyme concentrations, kinetics, and inhibition analysis using high-density hydrodynamic cell isolation arrays. *Anal Chem* **2006,** 78, (14), 4925-30.
149. Yang, M.; Li, C.-W.; Yang, J., Cell docking and on-chip monitoring of cellular reactions with a controlled concentration gradient on a microfluidic device. *Analytical Chemistry* **2002,** 74, (16), 3991-4001.
150. Pengt, X. Y.; Li, P. C. H., A three-dimensional flow control concept for single-cell experiments on a microchip. 2. Fluorescein diacetate metabolism and calcium mobilization in a single yeast cell as stimulated by glucose and pH changes. *Analytical Chemistry* **2004,** 76, (18), 5282-5292.
151. Li, X.; Li, P. C., Microfluidic selection and retention of a single cardiac myocyte, on-chip dye loading, cell contraction by chemical stimulation, and quantitative fluorescent analysis of intracellular calcium. *Anal Chem* **2005,** 77, (14), 4315-22.

152. Li, P. C.; de Camprieu, L.; Cai, J.; Sangar, M., Transport, retention and fluorescent measurement of single biological cells studied in microfluidic chips. *Lab Chip* **2004,** 4, (3), 174-80.
153. Albrecht, D. R.; Tsang, V. L.; Sah, R. L.; Bhatia, S. N., Photo- and electropatterning of hydrogel-encapsulated living cell arrays. *Lab Chip* **2005,** 5, (1), 111-8.
154. Meynen, H.; Vanden Bulcke, M.; Gonzalez, M.; Harkness, B.; Gardner, G.; Sudbury-Holtschlag, J.; Vandevelde, B.; Winters, C.; Beyne, E. In *Ultra low stress and low temperature patternable silicone materials for applications within microelectronics*, European Workshop on Materials for Advanced Metallization 2004, 7-10 March 2004
Microelectronic Engineering, Brussels, Belgium, 2004/10/, 2004; Elsevier: Brussels, Belgium, 2004; pp 212-18.
155. Vanden Bulcke, M.; Gonzalez, M.; Vandevelde, B.; Winters, C.; Beyne, E.; Larson, L.; Harkness, B. R.; Gardner, G.; Mohamed, M.; Sudbury-Holtschlag, J.; Meynen, H. In *Introducing a silicone under the bump configuration for stress relief in a wafer level package*, Proceedings of the 5th Electronics Packaging Technology Conference (EPTC 2003), 10-12 Dec. 2003, Singapore, 2003//, 2003; IEEE: Singapore, 2003; pp 380-4 BN - 0 7803 8205 6.
156. Shaw, J. M., J. D. Gelorme, N. C. LaBianca, W. E. Conley, and S. J. Holmes, Negative Photoresists for Optical Lithography. *IBM Journal of Research and Development* **1997,** 41, (1/2).
157. Pai, J. H.; Wang, Y.; Salazar, G. T.; Sims, C. E.; Bachman, M.; Li, G. P.; Allbritton, N. L., Photoresist with low fluorescence for bioanalytical applications. *Anal Chem* **2007,** 79, (22), 8774-80.
158. Gauthier, T. D.; Shane, E. C.; Guerin, W. F.; Seitz, W. R.; Grant, C. L., Fluorescence Quenching Method for Determining Equilibrium Constants for Polycyclic Aromatic Hydrocarbons Binding to Dissolved Humic Materials. *Environmental Science and Technology* **1986,** 20, (11), 1162-1166.
159. Hasegawa, M.; Kochi, M.; Mita, I.; Yokota, R., Molecular aggregation and fluorescence spectra of aromatic polyimides. *European Polymer Journal* **1989,** 25, (4), 349-354.
160. Nohta, H.; Yukizawau, T.; Ohkura, Y.; Yoshimura, M., Aromatic glycinonitriles and methylamines as pre-column fluorescence derivatization reagents for catecholamines. *Analytica Chimica Acta* **1997,** 344, (3), 233.
161. Backhus, D. A.; Gschwend, P. M., Fluorescent polycyclic aromatic hydrocarbons as probes for studying the impact of colloids on pollutant transport in groundwater. *Environmental Science and Technology* **1990,** 24, (8), 1214-1223.
162. Nie, S.; Dadoo, R.; Zare, R. N., Ultrasensitive Fluorescence Detection of Polycyclic Aromatic Hydrocarbons in Capillary Electrophoresis. *Analytical Chemistry* **1993,** 65, (24), 3571-3575.
163. Pinto, C. G.; Pavon, J. L. P.; Cordero, B. M., Cloud Point Preconcentration and High-Performance Liquid Chromatographic Determination of Polycyclic Aromatic Hydrocarbons with Fluorescence Detection. *Analytical Chemistry* **1994,** 66, (6), 874-881.
164. Manaresi, N., Romani, A., Medoro, G., Altomare, L., Leonardi, A., Tartagni, M., Guerrieri, R., A CMOS Chip for Individual Cell Manipulation and Detection. *IEEE Journal of Solid-State Circuits* **2003,** 38, (12), 2297-2305.
165. Chiou, P. Y., Ohta, A. T., Wu, M. C., Massively parallel manipulation of single cells and microparticles using optical images. *Nature* **2005,** 436, 370-372.
166. Pardo, O. E.; Lesay, A.; Arcaro, A.; Lopes, R.; Ng, B. L.; Warne, P. H.; McNeish, I. A.; Tetley, T. D.; Lemoine, N. R.; Mehmet, H.; Seckl, M. J.; Downward, J., Fibroblast growth factor 2-mediated translational control of IAPs blocks mitochondrial release of Smac/DIABLO and apoptosis in small cell lung cancer cells. *Mol Cell Biol* **2003,** 23, (21), 7600-10.
167. Green, D.; Kroemer, G., The central executioners of apoptosis: caspases or mitochondria? *Trends Cell Biol* **1998,** 8, (7), 267-71.
168. Docoslis, A.; Kalogerakis, N.; Behie, L. A., Dielectrophoretic forces can be safely used to retain viable cells in perfusion cultures of animal cells. *Cytotechnology* **1999,** 30, (1-3), 133-142.
169. Glasser, H.; Fuhr, G., Cultivation of cells under strong ac-electric field - differentiation between heating and trans-membrane potential effects. *Bioelectrochemistry and Bioenergetics* **1998,** 47, (2), 301-310.
170. Desai, S. P.; Voldman, J. In *Assaying the Physiological Impact of Dielectrophoretic Trapping*, Biomedical Engineering Society Annual Fall Meeting, Los Angeles, CA, 2007; Los Angeles, CA, 2007.
171. Pachernik, J.; Janik, R.; Hofmanova, J.; Bryja, V.; Kozubik, A., Conditions for gene transfection into the HL-60 human leukaemia cell line by electroporation. *Folia Biol (Praha)* **2002,** 48, (4), 154-6.
172. Schakowski, F.; Buttgereit, P.; Mazur, M.; Marten, A.; Schottker, B.; Gorschluter, M.; Schmidt-Wolf, I. G., Novel non-viral method for transfection of primary leukemia cells and cell lines. *Genet Vaccines Ther* **2004,** 2, (1), 1.

173. Loo, L. H.; Wu, L. F.; Altschuler, S. J., Image-based multivariate profiling of drug responses from single cells. *Nat Methods* **2007,** 4, (5), 445-53.
174. Bigi, A.; Cojazzi, G.; Panzavolta, S.; Rubini, K.; Roveri, N., Mechanical and thermal properties of gelatin films at different degrees of glutaraldehyde crosslinking. *Biomaterials* **2001,** 22, (8), 763-8.
175. Blair, D.; Dufresne, E. The MATLAB Particle Tracking Code Repository. http://physics.georgetown.edu/matlab/#contact
176. Kovac, J. R.; Taff, B. M.; Voldman, J., Enabling Technologies for Image-Based Cell Sorting. In *Microdevices in Biology and Medicine*, Nahmias, Y.; Bhatia, S., Eds. Artech House: Norwood, MA, 2008.
177. Barrett, L. M.; Skulan, A. J.; Singh, A. K.; Cummings, E. B.; Fiechtner, G. J., Dielectrophoretic manipulation of particles and cells using insulating ridges in faceted prism microchannels. *Analytical Chemistry* **2005,** 77, (21), 6798-6804.
178. Lapizco-Encinas, B. H.; Simmons, B. A.; Cummings, E. B.; Fintschenko, Y., Dielectrophoretic Concentration and Separation of Live and Dead Bacteria in an Array of Insulators. *Analytical Chemistry* **2004,** 76, (6), 1571-1579.
179. Urbanski, J. P.; Thorsen, T.; Levitan, J. A.; Bazant, M. Z., Fast ac electro-osmotic micropumps with nonplanar electrodes. *Applied Physics Letters* **2006,** 89, (14), 143508-1.
180. Burch, D.; Bazant, M. Z., Design principle for improved three-dimensional ac electro-osmotic pumps. *physical Review E* **2008,** 77, (5), 055303(4).
181. Gitlin, I.; Stroock, A. D.; Whitesides, G. M.; Ajdari, A., Pumping based on transverse electrokinetic effects. *Applied Physics Letters* **2003,** 83, (7), 1486-8.
182. Ajdari, A., Electrokinetic 'ratchet' pumps for microfluidics. *Applied Physics A (Materials Science Processing)* **2002,** A75, (2), 271-4.
183. Sampattavanich, S. In *Matrix-Independent Colony Patterning to Study the Influence of Colony-Colony Interactions on Stem Cell Fate Decision in Murine Embryonic Stem Cells*, International Society for Stem Cell Research Annual Meeting, Philadelphia, PA, June 11-14, 2008; Philadelphia, PA, 2008.
184. Mittal, N.; Rosenthal, A.; Voldman, J., nDEP microwells for single-cell patterning in physiological media. *Lab on a Chip* 7, (9), 1146-53.
185. Albrecht, D. R.; Underhill, G. H.; Wassermann, T. B.; Sah, R. L.; Bhatia, S. N., Probing the role of multicellular organization in three-dimensional microenvironments. *Nat Methods* **2006,** 3, (5), 369-75.
186. Dickinson, T. A.; Michael, K. L.; Kauer, J. S.; Walt, D. R., Convergent, self-encoded bead sensor arrays in the design of an artificial nose. *Analytical Chemistry* **1999,** 71, (11), 2192-2198.
187. Kane, R. S.; Takayama, S.; Ostuni, E.; Ingber, D. E.; Whitesides, G. M., Patterning proteins and cells using soft lithography. *Biomaterials* **1999,** 20, (23-24), 2363-2376.
188. Chen, C. S.; Mrksich, M.; Huang, S.; Whitesides, G. M.; Ingber, D. E., Micropatterned surfaces for control of cell shape, position, and function. *Biotechnology Progress* **1998,** 14, (3), 356-363.